



**ANATOMICAL AND MOLECULAR MAPPING OF THE
HUMAN CARDIAC CONDUCTION SYSTEM – WITH
AIMS TO FURTHER UNDERSTAND ITS FUNCTION**

A thesis submitted to the University of Manchester for the degree of
Doctor of Philosophy

In the Faculty of Biology, Medicine, and Health

2022

Abimbola Juliet Aminu

School of Medical Sciences

Table of Contents

ABBREVIATIONS.....	5
Abstract.....	9
Declaration.....	11
Copyright Statement.....	13
Dedication.....	15
Acknowledgements.....	17
RATIONALE FOR SUBMITTING IN A JOURNAL FORMAT AND HOW THE THESIS HAS BEEN CONSTRUCTED.....	19
CHAPTER 1) INTRODUCTION.....	20
1.1 Introduction to the cardiac anatomy.....	21
1.1.1 The cardiac conduction system.....	21
1.1.2 Function of the sinus node.....	22
1.1.3 Clock mechanisms in the sinus node.....	23
1.1.4 Transcription factors and the sinus node.....	25
1.1.5 Cell markers, the immune system, and the sinus node.....	27
1.2 The biology and therapeutic potential of miRNAs.....	28
1.2.1 miRNAs, mRNAs, markers, and the sinus node.....	29
1.2.2 miRNAs and cardiac development.....	30
1.2.3 miRNAs and cardiac diseases.....	30
1.3 Imaging techniques.....	32
1.3.1 Histology.....	32
1.3.2 Echocardiogram.....	33
1.3.3 Cardiac Magnetic Resonance Imaging.....	33
1.3.4 Computed Tomography and Micro-computed Tomography.....	33
1.4 Obesity and cardiovascular diseases.....	34
1.5 Ageing and cardiovascular diseases.....	35
1.6 Aims.....	36
CHAPTER 2) GENERAL METHODS.....	37
2.1 Human sample details and ethical approval for micro-CT studies.....	38
2.1.2 General principles.....	38
2.1.2.1 Tissue preparation.....	38
2.1.2.2 Basic principles of micro-CT.....	38
2.1.2.3 Image analysis and 3D reconstruction.....	39
2.1.2.4 Basic principles of Masson’s trichrome staining.....	42

2.2 Human sample details and ethical approval for NGS and IPA studies.....	43
2.2.1 General principles	43
2.2.1.1 Tissue preparation	43
2.2.1.2 Basic principles of next-generation sequencing	43
2.2.1.3 Basic principles of Ingenuity Pathway Analysis.....	44
2.3 General principles for bioinformatics	46
2.3.1 RNAseq and qPCR for miRNA.....	46
2.3.2 Prediction of binding sites RNAseq and qPCR for miRNA.....	46
2.3.3 General principles of luciferase reporter gene assay	48
2.3.3.1 Luciferase reporter gene assay experiments.....	48
CHAPTER 3) NOVEL MICRO-COMPUTED TOMOGRAPHY CONTRAST AGENTS TO VISUALISE THE HUMAN CARDIAC CONDUCTION SYSTEM AND SURROUNDING STRUCTURES IN HEARTS FROM NORMAL, AGED, AND OBESE INDIVIDUALS¹.....	50
3.1 Authors' contribution to the paper.....	51
3.2 Hypothesis.....	52
3.3 Aims.....	52
3.4 Materials and methods.....	52
3.4.1 Human sample details.....	52
3.4.2 Whole heart tissue preparation and selection of contrast agents	53
3.4.3 Tissue block preparation.....	53
3.4.4 High-resolution micro-computed tomography.....	54
3.4.5 Segmentation and reconstruction	54
3.4.6 Cryosectioning and histological analysis of tissue blocks containing components of the CCS	55
3.5 Limitations.....	74
Appendix	75
CHAPTER 4) FURTHER INSIGHTS INTO THE MOLECULAR COMPLEXITY OF THE HUMAN SINUS NODE – THE ROLE OF ‘NOVEL’ TRANSCRIPTION FACTORS AND MICRORNAS².....	82
4.1 Authors' contribution to the paper.....	83
4.2 Hypothesis.....	84
4.3 Aims.....	84
4.4 Materials and methods.....	84
4.4.1 Human sample details.....	84
4.4.2 Cryosectioning and histological characterisation of the SN	84
4.4.3 Ingenuity pathway analysis.....	85
4.4.4 Heatmaps, graphs, and statistical analysis	84

4.5 Limitations.....	105
CHAPTER 5) MIR-486-3P AND MIR-938 – IMPORTANT INHIBITORS OF PACEMAKING ION CHANNELS AND/OR MARKERS OF IMMUNE CELLS³	106
5.1 Authors’ contribution to the paper.....	107
5.2 Hypothesis.....	108
5.3 Aims.....	108
5.4 Materials and methods	108
5.4.1 H9C2 cells	108
5.4.2 MiRNAs.....	109
5.4.3 Plasmids	109
5.4.4 Plasmid amplification.....	109
5.4.5 Luciferase reporter gene assay experiments	110
5.4.6 Prediction of binding sites	111
5.5 Limitations.....	124
Appendix	125
CHAPTER 6) IDENTIFICATION OF KEY SMALL NON-CODING MICRORNAS CONTROLLING PACEMAKER MECHANISMS IN THE HUMAN SINUS NODE⁴	133
6.1 Contribution to the paper	134
CHAPTER 7) GENERAL DISCUSSIONS, CONCLUSIONS, LIMITATIONS, FUTURE WORK, AND LIST OF PUBLICATIONS	155
7.1 Discussion.....	156
7.2 Conclusions	160
7.3 Limitations.....	161
7.4 Future work.....	162
7.5 List of publications	163
References.....	166

ABBREVIATIONS

°	degree
°C	degree celsius
μL	microliter
μm	micrometre
2D	2-dimensional
3D	3-dimensional
Ao	aorta
AoR	aortic root
AS	atrial septum
AVN	atrioventricular node
BB	bundle branch
BMI	body mass index
cAMP	cyclic adenosine monophosphate
cm	centimetre
CMRI	cardiac magnetic resonance imaging
CS	coronary sinus
CT	computed tomography
CVD	cardiovascular disease
CCS	cardiac conduction system
cDNA	complementary deoxyribonucleic acid
CN	compact node
CT	crista terminalis
DNA	deoxyribonucleic acid
dNTPs	deoxyribonucleotide triphosphates
EADs	early afterdepolarisations
EF	epicardial fat
GO	graphene oxide
HB	His bundle

HCN	Hyperpolarisation-activated nucleotide-gated channel
HCX	histo-compatibility complex
HLA	human leukocyte antigen
hsa	homosapien
I ₂ KI	iodine potassium-iodide
IAS	interatrial septum
ID	identification
INE	inferior nodal extension
IPA	Ingenuity Pathway Analysis
iPSCs	induced pluripotent stem cells
IVC	inferior vena cava
IVS	interventricular septum
kV	kilovolts
LA	left atrium
LADA	left anterior descending artery
LC	left cusp
LCA	left coronary artery
LCC	left coronary cusp
LCx	left circumflex artery
LV	left ventricle
mRNAs	messenger ribonucleic acid
Micro-CT	micro-computed tomography
MiR/MiRNA/MicroRNA	micro ribonucleic acid
MV	mitral valve
NCC	non-coronary cusp
NGS	next generation sequencing
PA	pulmonary artery
PB	penetrating bundle
PcM	pectinate muscle
PDA	posterior descending artery

PM	papillary muscle
PPM	posterior papillary muscle
PV	pulmonary vein
qPCR	quantitative polymerase chain reaction
RA	right atrium
RCA	right coronary artery
RCC	right coronary cusp
RMA	right marginal artery
RNA	ribonucleic acid
RNA-seq	RNA-sequencing
RV	right ventricle
RyR2	ryanodine receptor type 2
SEM	standard error of mean
SN	sinus node
SND	sinus node dysfunction
SSS	sick sinus syndrome
SVC	superior vena cava
TAVI	transcatheter aortic valve implantation
TbC	trabeculae carneae
TF	transcription factor
TV	tricuspid valve
UTR	untranslated region
VS	ventricular septum
vs.	versus
VSD	ventricular septal defect

Abstract

Anatomical and Molecular Mapping of the Human Cardiac Conduction System – With Aims to Further Understand Its Function

Abimbola Juliet Aminu

The University of Manchester

Doctor of Philosophy

April 2022

Background: Worldwide, cardiovascular diseases (CVDs) remain a leading cause of death, with ageing and obesity being common risk factors. CVDs cause structural and functional remodelling of the heart – hence further cardiac dysfunctions. The cardiac conduction system (CCS) is a collection of specialised cardiomyocytes that work together to regulate and propagate electrical impulses around the heart. The CCS consists of the sinus node (SN, the heart's primary pacemaker), the atrioventricular conduction axis, and the His-Purkinje network. Dysfunction of this system leads to CVDs such as arrhythmia and heart failure.

Therefore, it is vital to further our anatomical understanding of key cardiac structures and the CCS in healthy, aged, and obese hearts. Expanding our current understanding of the human SN's molecular mechanisms is equally vital. Dysfunction of key molecular pathways in the SN results in SN dysfunctions such as bradycardia.

Aims: The studies described in this thesis aimed to contribute to the current understanding of anatomical and molecular interactions of the working myocardium and CCS of the human heart from healthy, aged, and obese individuals. The study aimed to create 3D reconstructions of the whole heart, major blood vessels, valves, and components of the CCS of the human heart from normal (healthy), aged, and obese individuals. Another aim of using healthy human SN samples was to apply bioinformatics to predict interactions between microRNAs, transcription factors (TFs), and cell markers that regulate SN function.

Methods: **1)** Normal, aged, and obese whole hearts and tissue blocks were micro-CT scanned following iodine potassium-iodide (I₂KI) or graphene oxide (GO, a novel contrast agent) staining. Some samples were frozen before sectioning and then stained using Masson's trichrome. **2)** RNA-sequencing and bioinformatics were used to analyse the expression profile and predict interactions of key TFs and cell markers mRNAs with key microRNAs in the healthy adult human SN. **3)** Luciferase assay experiments were performed to validate the predicted significant downregulation of mRNAs by microRNAs.

Results: **1)** Successfully used I₂KI and a novel contrast agent (GO) for high-resolution micro-CT to visualise and create 3D reconstructions of the whole myocardium, major blood vessels, coronary artery network, and valves from whole normal, aged, and obese hearts. Created 3D reconstructions of Purkinje fibres and the region containing the SN from these hearts. **2)** Embryonic TFs (e.g., ISL1) and 'novel' TFs (e.g., RUNX1-2) are significantly more abundant in the SN vs. atrial tissue. These TFs were predicted to regulate HCN4 expression and different cell markers (e.g., COL1A1, a fibroblast marker; and TPSAB1, a mast cell marker) in the SN. Key microRNAs significantly less abundant in the SN (e.g., miR-486-3p and miR-938) were predicted to downregulate mRNAs of pacemaking ion channels. **3)** MiR-486-3p significantly downregulates the luciferase activity of Ca_v1.3, Ca_v3.1, and TPSAB1.

Conclusions: This thesis contributes to and expands the current understanding of myocardium and CCS variations between healthy, aged, and obese individuals. The novel insights into the complex molecular interactions presented in this thesis can be targeted in treating SN dysfunctions. The data presented can aid in developing cardiac models.

Declaration

No portion of the work referred to in the thesis has been submitted in support of an application for another degree or qualification from this or any other university or institution of learning.

Copyright Statement

The author of this thesis (including any appendices and/or schedules to this thesis) owns certain copyright or related rights in it (the “Copyright”), and she has given The University of Manchester certain rights to use such Copyright, including for administrative purposes.

Copies of this thesis, either in full or in extracts and whether in hard or electronic copy, may be made only in accordance with the Copyright, Designs and Patents Act 1988 (as amended) and regulations issued under it or, where appropriate, in accordance with licensing agreements which the University has from time to time. This page must form part of any such copies made.

The ownership of certain Copyright, patents, designs, trademarks, and other intellectual property (the “Intellectual Property”) and any reproductions of copyright works in the thesis, for example, graphs and tables (“Reproductions”), which may be described in this thesis, may not be owned by the author and may be owned by third parties. Such Intellectual Property and Reproductions cannot and must not be made available for use without the prior written permission of the owner(s) of the relevant Intellectual Property and/or Reproductions.

Further information on the conditions under which disclosure, publication and commercialisation of this thesis, the Copyright and any Intellectual Property and/or Reproductions described in it may take place is available in the University IP Policy (see <https://documents.manchester.ac.uk/display.aspx?DocID=24420>), in any relevant Thesis restriction declarations deposited in the University Library, The University Library’s regulations (see <https://www.library.manchester.ac.uk/about/regulations/files/Library-regulations.pdf>) and in The University’s policy on presentation of Theses.

Dedication

TO MY DEAR MOTHER,
OMOLOLA KUDIRAT AMINU

YOUR ABIMBOLA

2022

Acknowledgements

First and foremost, I owe everything to **God Almighty**, who kept me together and infused wisdom, knowledge, understanding, and strength in me throughout this PhD journey.

I am grateful to the British Heart Foundation for their prestigious funding – without which none of this research would have been possible.

I am forever grateful to the best supervisor any PhD student could ask for – **Dr Halina Dobrzynski**. I will never forget your devotion to helping me excel. Thank you for seeing the light in me during my most challenging times; thank you for your constant care, overwhelming support, creative ideas, and constructive criticisms. I must thank my wonderful co-supervisor, **Dr Andrew Atkinson**, your patience and wisdom are qualities that I will always admire. Thank you for teaching me everything I know about micro-CT scanning and image analysis.

I would like to acknowledge **Weixuan Chen** and **Zeyuan Yin**. Thank you for your contribution to this work.

To my dear, **Dr Kenisumo Luwei**. I have been able to endure the writing and formatting of papers and this thesis through your encouragement, insights, and your love. Thank you.

To my family (**Mum, Teju, Michael, Emmanuel, and my Boluwatife**), thank you for being my rock throughout this journey. You may not have been aware of this, but during my intense days and nights in the lab and in front of a computer screen, the thought of going home to you always filled me with hope and joy.

There is no word in the world that I can use to express my deepest gratitude and appreciation to my mother, **Omolola Kudirat Aminu**. Thank you for being my rock, inspiration and well of encouragement. Thank you for motivating me to apply for a PhD. Mum, you always believed in me even when I did not believe in myself. I thank you for never giving up on me, I am eternally grateful, and I dedicate this thesis to you.

RATIONALE FOR SUBMITTING IN A JOURNAL FORMAT AND HOW THE THESIS HAS BEEN CONSTRUCTED

There are three main sections to this PhD project: 1) 3D anatomical reconstruction of cardiac structures and the cardiac conduction system (CCS) from normal, aged, and obese *ex-vivo* human hearts; 2) using next-generation sequencing (NGS) for RNA sequencing and Ingenuity Pathway Analysis (IPA) to predict the expression profile and interaction pathways of molecules within the healthy human sinus node (SN); and 3) using luciferase gene assay experiments to validate some of the predicted interactions. All these three sections were published as separate papers during my PhD (1. Aminu et al., *TRIA*. 2022;**27**:100175; 2. Aminu et al., *Prog Biophys Mol Biol*. 2021;**166**:86-104; and 3. Aminu et al., *Appl Sci*. 2021;**11**:11366). I am the first author in all these papers as all the studies were my PhD project, carried out by me. Therefore, these papers are combined to form this thesis in a journal format.

This thesis has seven main chapters. Chapters 1 (introduction), 2 (general methods), and 7 (general discussion, conclusions, limitations, future work, and list of publications) have been written in traditional thesis format. The remaining chapters belong to each published paper. However, before each paper is presented in its corresponding chapters, I have written a hypothesis, aims, and materials and methods sections. In particular, the materials and methods sections provide further insights into the methods described in the papers by describing troubleshoots and optimisations performed when necessary.

CHAPTER 1) INTRODUCTION

This chapter provides a general introduction, aims, and outline of the three main parts of this thesis: anatomy of the whole heart and its cardiac conduction system; bioinformatics to explore underlying molecular mechanisms within the sinus node; and luciferase assays to validate predicted molecular interactions.

1.1 Introduction to the cardiac anatomy

In the United Kingdom, cardiovascular diseases (CVDs), such as cardiac arrhythmia; heart failure; and myocardial infarction, are responsible for a quarter of all deaths – leading to a healthcare treatment cost of £9 billion [1]. Ageing (60 years and above [2]) and obesity (body mass index (BMI) of 30.0 or higher) are common risk factors for cardiac arrhythmia and heart failure [3]. These CVDs result in anatomical and functional remodelling of the heart – leading to further cardiac dysfunctions such as atrial fibrillation [4], cardiomyopathy, fibrosis, diastolic and systolic dysfunction, and increased epicardial fat [5]. Additionally, the dysfunction of the aforementioned cardiac structures can result in morphological changes and cardiac dysfunction [6]. Based on this, we need to further our anatomical understanding of key cardiac structures such as the working myocardium; pectinate muscles; papillary muscles; aortic root; pulmonary artery root; mitral and tricuspid valves; the coronary arteries; and epicardial fat.

In addition to knowing anatomical variations of the whole heart in healthy, aged, and obese individuals, it is just as important for us to understand the anatomical variations of the cardiac conduction system (CCS) in these individuals. The dysfunction of the CCS leads to CVDs such as arrhythmia, cardiomyopathy, and heart failure.

1.1.1 The cardiac conduction system

The CCS is a collection of specialised cardiomyocytes that work together to regulate and propagate electrical impulses around the heart (Figure 1.1) [7]. It consists of the sinus node (SN, the heart's primary pacemaker), the atrioventricular (AV, which receives electrical impulse from the SN and is the main conduction pathway between the atria and ventricles) conduction axis; and the His-Purkinje network (stems from the AV conduction axis, allowing the rapid conduction of electrical impulses across the ventricles) [8, 9].

The CCS was discovered over a century ago. Yet, we still lack an understanding of the exact anatomies of the CCS within the hearts of healthy, aged, and diseased human individuals. We must know this because remodelling of the CCS occurs in diseased hearts [10-13]. SN dysfunction happens in response to atrial fibrillation, ageing and/or obesity [14]. Approximately 20% of patients that undergo the transcatheter aortic valve implantation

(TAVI) procedure experience AV block or left bundle branch block [15]. This block is due to the close proximity of the aortic valve and the left bundle branch [15]. Purkinje fibres are susceptible to early afterdepolarisations – leading to tachycardia arrhythmia [16, 17]. All arrhythmia associated with CCS dysfunction is discussed in Paper 1, Chapter 3.

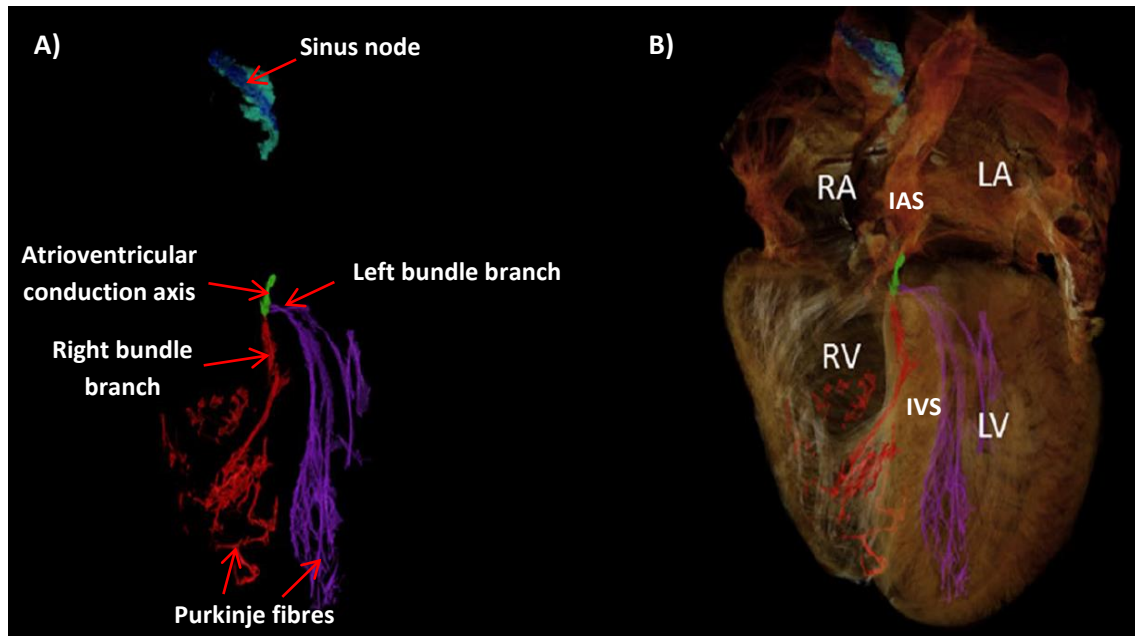


Figure 1. 1. 3D anatomy of the cardiac conduction system in an intact, healthy human heart. Adapted from Stephenson and Atkinson et al., 2017 [36]. A, the cardiac conduction system (CCS) separated from the whole heart and B, the CCS incorporated into the surrounding myocardium, viewed in 4-chamber view. Sinus node = dark blue; atrioventricular conduction axis = green; bundle branches and Purkinje network = red and purple. IAS, interatrial septum; IVS, interventricular septum; LA, left atrium; LV, left ventricle; RA, right atrium; RV, right ventricle.

1.1.2 Function of the sinus node

Since its discovery in 1907 [18], the molecular mechanisms that underlie the pacemaking and cardiac function of the SN (also known as the sinoatrial node) have been an area of great exploration. The SN has a distinctive morphology of a crescent-shaped structure that runs along the crista terminalis [7, 19]. Functioning as the heart's primary pacemaker, the healthy SN has unique pacemaking mechanisms compared to the working myocardium [20]. This function results from the SN's unique expression of ion channels and Ca^{2+} -handling proteins [19]. These channels are responsible for the membrane voltage and Ca^{2+} clocks – the two main mechanisms that maintain the SN's automaticity. Mutation of ion channels can cause

SN dysfunction, such as sick sinus syndrome (SSS, i.e., sinus bradycardia and sinus arrest). Fibrosis is commonly associated with SSS, and ageing is a risk factor for SSS [21]. Increased cardiac fat is associated with ageing [22], and results published in Paper 1; Chapter 3 show that fat replaces the loss of cardiomyocytes observed in the tissue section of the aged SN.

With fibrosis being able to induce abnormalities in the SN's anatomy, it is vital to explore the expression and interactions of molecules that regulate the SN's function.

1.1.3 Clock mechanisms in the sinus node

The membrane voltage clock regulates the spontaneous diastolic depolarisation of the SN myocytes – through the cyclic activation and deactivation of membrane ion channels [23, 24]. Voltage-sensitive membrane currents predominantly mediate this clock mechanism. This mechanism includes the hyperpolarisation-activated current (I_f), created by hyperpolarisation-activated cyclic nucleotide-gated channels HCN1 and HCN4 – with HCN4 being the main isoform highly expressed in the human SN [20]. During phase 4 of the SN's action potential, cyclic adenosine monophosphate (cAMP) activates the hyperpolarisation-activated cyclic nucleotide-gated channels (Figure 1.2) [20].

Now regarding the Ca^{2+} clock. Unlike the working myocardium (i.e. the right atrium), the SN lacks a resting membrane potential (phase 1) – this is because the SN lacks an inward rectifier K^+ current ($I_{k,1}$) due to the low expression of Kir2.1 channels in the SN [19, 20, 25]. Kir2.2 is an inwardly rectifying potassium channel equally expressed in the SN and working myocardium [20]. When Kir2.1 is knocked out of the ventricles, pacemaking activity and characteristics are observed [26]. Compared to the working myocardium, the SN has a slow upstroke at phase 0 of its action potential (Figure 1.2) because the slow L generates it - and T-type Ca^{2+} channels ($I_{Ca,L}$, $I_{Ca,T}$). $I_{Ca,T}$ regulates the late diastole phase of the SN's action potential, and $Ca_v3.1$ – $Ca_v3.3$ are T-type Ca^{2+} channels significantly more expressed in the SN compared to the working myocardium [19, 20]. $I_{Ca,L}$ is the primary current in the SN action potential upstroke and is mainly generated by $Ca_v1.3$ [19, 20]. The higher expression of $Ca_v1.3$ in the SN is responsible for the more prolonged plateau at phase 2, observed in the SN's action potential. $Na_v1.5$ is responsible for the fast inward Na^+ current (I_{Na}) that leads to the action potential upstroke observed in the working atrial and ventricular myocardium [19, 20]. At phase 3 of the SN's action potential, repolarisation occurs as a result of Ca^{2+} inactivation and the subsequent

activation of different K⁺ channels such as K_v1.4 (this channel contributes to the cardiac transient outward K⁺ current, I_{to}), K_v1.5, hERG and K_vLOT (responsible for the ultra-rapidly, rapidly and slowly delayed rectifier K⁺ currents, $I_{K,ur}$, $I_{K,r}$, $I_{K,s}$, respectively) [19, 20].

The spontaneous release of Ca²⁺ from the sarcoplasmic reticulum of SN myocytes is also known as the Ca²⁺ clock [27]. Ca²⁺ is released locally from the sarcoplasmic reticulum through the ryanodine receptor type 2 (RyR2); this causes an increase in the concentration of intracellular Ca²⁺ during phase 4 of the SN's action potential. The release of Ca²⁺ through RyR2 triggers the release of Ca²⁺ by the Na⁺-Ca²⁺ exchanger (NCX), which exchanges 3 Na⁺ ions for every Ca²⁺ ion [27] to generate a net inward current (I_{NCX}) which contributes to the last phase of diastolic depolarisation (phase 4) [19, 20, 25].

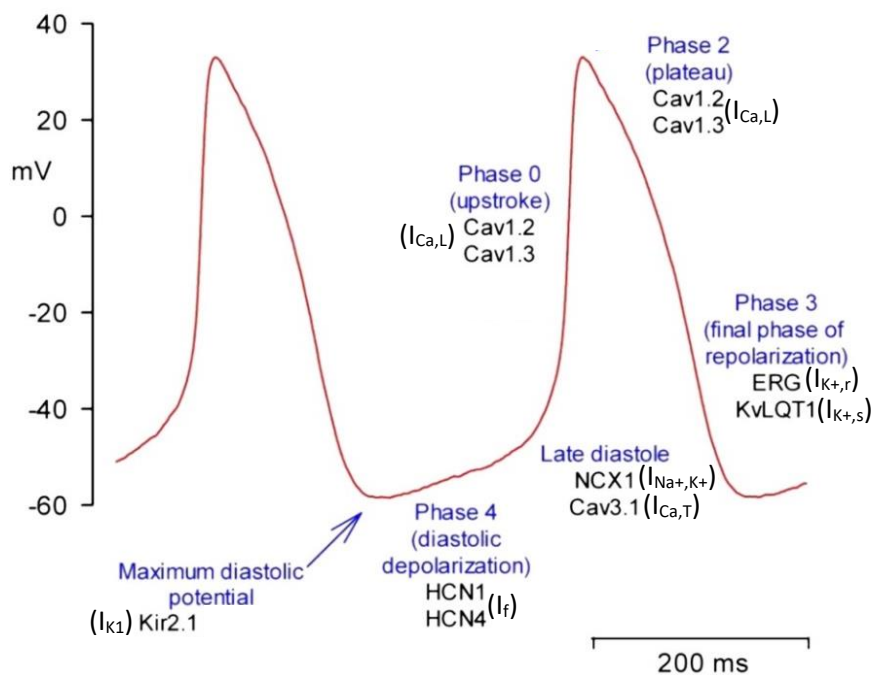


Figure 1. 2. Summarised expression of the key ion channels that regulate phase 0–4 of the sinus node action potential [42]. At maximum diastolic potential, the Kir2.1 ion channel generate the inward rectifier current (I_{K1}). During diastolic depolarisation (phase 4), HCN1 and HCN4 channels generate the funny current (I_f). During late diastole, the sodium-calcium exchanger, NCX1, generates the sodium and potassium ion currents ($I_{Na+,K+}$) and $Ca_v3.1$ generates the T-type calcium current. At phase 0 and phase 2, the calcium channels $Ca_v1.2$ and $Ca_v1.3$ generate the L-type calcium current ($I_{Ca,L}$). At the final phase of repolarisation (phase 3), the ERG potassium ion channel generates the rapid potassium current ($I_{K+,r}$) and the KvLQT1 potassium ion channel generates the slow potassium current ($I_{K+,s}$).

1.1.4 Transcription factors and the sinus node

Transcription factors (TFs) are proteins that regulate the expression of ion channels, Ca^{2+} -handling proteins, and other molecules involved in tissue function - through inhibition, repression, or activation, by binding to their deoxyribonucleic acid (DNA) target sequence [28]. TFs are crucial in embryogenesis and adulthood [29, 30], making them potential therapeutic targets in treating SN dysfunction. T-box TFs - such as TBX2, TBX3, TBX5, and TBX18 - are a group of embryonic TFs involved in the development of the heart and limbs [31].

As shown in Paper 2, Chapter 4, the T-box TFs mentioned above are significantly more expressed in the adult human SN compared to the RA [32].

In mice that lack alleles for TBX2 and TBX3, the development of the AV canal is stunted [33] [34].

Homeodomain TFs are a group of TFs with a 60 amino acid helix-turn-helix DNA-binding domain [35]. Often referred to as 'hox genes', the DNA sequence that codes for the homeodomain TFs are called the 'homeobox'. NKX2-5, ISL1, and SHOX2 are homeodomain TFs. NKX2-5 is highly expressed in early heart progenitor cells, and the lack of NKX2-5 disrupts cardiac development (i.e., disruption of heart tube development and decreased heart growth) [36-38]. ISL1 is crucial in the embryonic development and function of the SN. After embryonic development, the expression of ISL1 is repressed throughout adulthood [39]. In ISL1-mutant cell lines, SN hypoplasia and dysfunction are observed [40]. SHOX2 deactivates the expression of the NKX2-5 promotor, making SHOX2 an important TF in the differentiation of SN pacemaker cells [41]. The role of TFs in the function and dysfunction of the SN is further described in Paper 2, Chapter 4.

This brief explanation of TFs' function highlights their essential contribution to developing and maintaining the SN's pacemaking function. Figure 1.3 shows a summarised regulatory network of TFs in the embryonic development of the SN.

Not only does the SN have a complex mechanism, but it also has a complex morphology. We have previously shown that the SN is embedded in an extensive network of connective tissue [19, 32, 42]. Elastic fibres, macrophages, mast cells, fat cells, fibroblasts, neuronal, endothelial, and epithelial cells lie within this connective tissue, as we have recently reported [32]. miRNAs and TFs regulate the expression of the markers for these fibres and cell types [32].

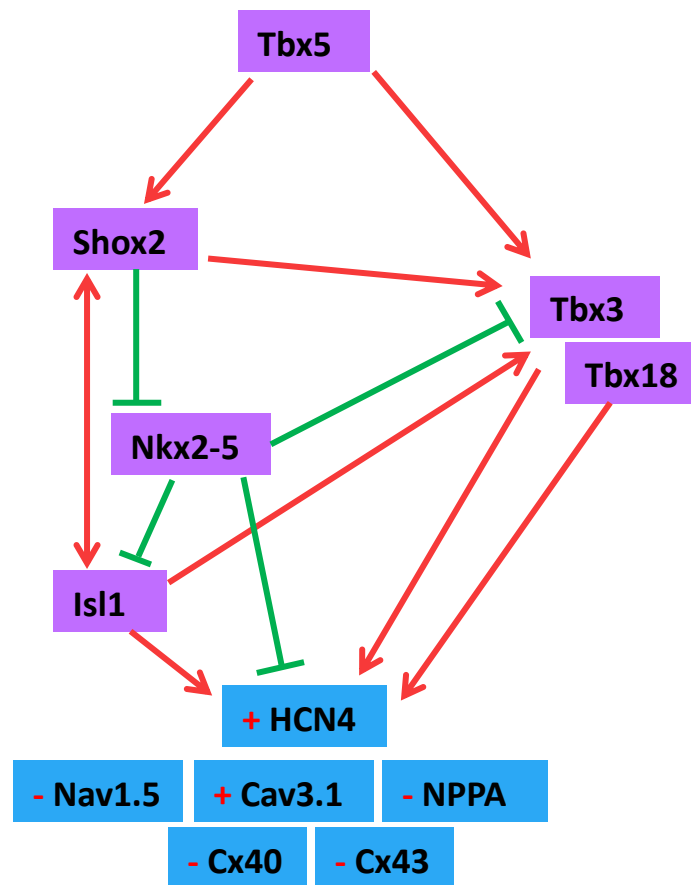


Figure 1. 3. A summarised regulatory network of transcription factors in the embryonic development of the sinus node. Purple box = transcription factors; blue box = target genes/ion channels; red line = upregulation; green line = downregulation. + = expressed in the SN; - = not expressed in the SN. Adapted from Park and Fishman, 2017 [57].

1.1.5 Cell markers, the immune system, and the sinus node

The SN is a structure that is embedded in connective tissue [19, 42]. As mentioned in the introduction of Paper 2, Chapter 4, many non-cardiac cells are contained within the connective tissue, such as macrophages and mast cells (immune cells), fat cells, fibroblasts, endothelial cells, and epithelial cells, amongst others. The specific markers selected for these various cell types and their function is mentioned in Paper 2, Chapter 4. After determining the expression profile of these cell markers in the SN vs. right atrium, *I aimed to use IPA to predict interactions amongst TFs and markers of these various cell types.*

As published in Paper 2, Chapter 4, it was surprising to identify a high abundance of immune cell markers in the SN compared to the right atrium. Interestingly, the immune system plays a crucial role in developing and maintaining the cardiac system and regulating the electrical activity of the CCS [43]. Various immunological mechanisms drive CCS disorders. For example, patients with SSS have higher levels of anti-sinus node antibodies in their plasma [43]. More information on the relationship between the immune system and SN function is presented in the discussion section of Paper 2, Chapter 4.

To further understand the molecular complexity underlying the SN's morphology and function, my PhD research project utilised ingenuity pathway analysis (IPA) to analyse data obtained from next-generation sequencing (NGS) for RNA-sequencing (RNA-seq), as published in Paper 2, Chapter 4. This process involved identifying interactions between key 'novel' and 'embryonic' TFs in the healthy adult human SN vs. right atrium with genes that regulate the SN's pacemaking mechanism. Following this, I aimed to use IPA to identify predicted interactions between TFs, cell markers and miRNAs (that are differentially expressed in the SN vs. right atrium [44]) – hence providing new insights into the treatment of SN dysfunctions. Finally, this research aimed to explore further the relationship between markers of immune cells, key miRNAs, and pacemaking ion channels using luciferase assay experiments.

1.2 The biology and therapeutic potential of miRNAs

MiRNAs have been identified in all animal model systems, with some being highly conserved across species [45, 46], yet new miRNAs are still being discovered.

MiRNAs are a group of non-coding RNAs that regulate gene expression through repression or inhibition and are approximately 22 nucleotides in length. MiRNAs are first transcribed from DNA sequences into primary miRNAs (known as pri-miRNAs) and then processed into precursor miRNAs (also known as pre-miRNAs that are approximately 70 nucleotides long) before finally developing into mature miRNAs.

These mature miRNAs can either be 5 prime (5') or 3 prime (3'). However, the name of the mature miRNA form depends on its directionality. The 5p strand (e.g., miR-486-5p) is from the 5' end of the pre-miRNA hairpin. The 3p strand (e.g., miR-486-3p) is from the 3' end of the pre-miRNA hairpin. These two different stands for the same miRNAs can co-exist and have

similar functions. For example, miR-486-5p is upregulated during congenital heart disease [47], and miR-486-3p is upregulated during bradycardia [44].

MiRNAs post-transcriptionally repress the expression of their target messenger-ribonucleic acid (mRNA) [48]. They commonly do this by binding to complementary sequences on the 3'-prime untranslated region (3'-UTR) of their target mRNA and usually form 'imperfect base heteroduplexes with target sequences' [49]. However, some miRNAs can bind to the 5' UTR, coding domain sequence and gene promoters of their target mRNAs [50, 51]. This precise function of the miRNAs and their ability to regulate a wide range of cellular processes make them key players in gene regulation and interesting therapeutic targets for treating diseases.

The aim of miRNA therapeutics is ultimately to improve health status by altering miR expression. However, the approach of using miRNAs as therapeutic targets is met with some difficulties as a single miRNA can be predicted to target tens to hundreds of genes – and approximately 60% of mRNAs have predicted binding sites for more than one miRNAs in their 3' or 5'UTR [49]. Another challenge that comes with miRNA therapeutics is the fact that most miR modulators are negatively charged. This makes them prone to non-specifically binding to blood proteins, consequently reducing their urinary clearance [52]. Furthermore, only less than 20 miRNA therapeutics (such as miR-29 and miR-122) are in clinical trials – none of which are in phase III [52].

However, there is a promising future for developing miRNA therapeutics as several companies are currently focusing on clinical and large screening studies. The introduction of tail-clamp modifications to the structures of miRNAs inhibitor and plant-derived miRNAs seek to settle some of these challenges [53]. In addition, some miRNA therapeutics are currently on the market, such as a miR-122 inhibitor (Miravirsen) for treating hepatitis C infection in the liver [54].

1.2.1 miRNAs, mRNAs, markers, and the sinus node

The molecules mentioned play a role in the SN's pacemaking function; therefore, this section of my PhD aimed to use luciferase assay experiments to validate predicted interactions. Previous work by Petkova et al. 2020, predicted interactions between key mRNAs (e.g., HCN1, HCN4, Cav1.3, and Cav3.1), TFs (e.g., TBX3 and TBX18), and microRNAs (e.g., miR-486-3p, miR-938, and miR-422a) [50]. Also, during my PhD project, I used bioinformatics software to

predict interactions between key cell markers (such as COL1A1 – a collagen marker, and TPSAB1 – a mast cell marker) and miRNAs.

1.2.2 miRNAs and cardiac development

During cardiac injury or disease (such as heart failure and myocardial infarction), cardiomyocytes are normally lost and the adult heart cannot regenerate [51, 52]. Since their discovery just over 25 years ago, micro-ribonucleic acids (miRNAs) are known to play significant roles in key cardiovascular pathological processes such as arrhythmias, ventricular hypertrophy, and heart failure [53] – all of which can contribute to structural abnormalities of the heart. Improving our understanding of the underlying molecular mechanisms of miRNAs in the cardiogenesis signalling pathways can improve the current treatments of cardiovascular diseases (CVDs).

Studies have shown that a single miRNA can regulate cardiac development and function [55-58]. MiR-1 and miR-133 are significant in cardiac development as miR-1 promotes, while miR-133 inhibits, the differentiation of embryonic stem cells into cardiomyocytes [59-61]. Both miR-1 and miR-133 regulate the activity of the serum response factor (SRF). SRF is important in regulating cardiac and smooth muscle differentiation genes [56, 62]. Tritsch et al. showed that SRF and miR-1 work together to regulate NCX1 (the sodium-calcium exchanger that generates sodium and potassium ion currents (I_{Na^+,K^+}), during the late diastole phase of the SN's action potential, Figure 1.2) [63].

1.2.3 miRNAs and cardiac diseases

CVDs such as SN dysfunction, heart failure, cardiac arrhythmia, and myocardial infarction are the leading cause of death in the United Kingdom [1]. Figure 1.4 summarises some cardiac-specific miRNAs and their targets in cardiovascular diseases.

Ventricular septal defect (VSD, a separation in the ventricular septum) is a condition that is commonly observed in most congenital heart diseases. VSD development correlates with increased levels of GJA1, SOX9 and miR-181c and decreased expression of miR-1-1 [64].

Elevated expression of miR-1, miR-133, miR-208, and miR-499 has been reported in patients with myocardial infarction [65]. On the other hand, miR-133a/b, miR-30b, miR-145, miR-873, and miR-214 are decreased in patients with myocardial infarction [66]. The expression of miR-

873 and miR-2861 has been shown to reduce heart damage by inducing protective signalling [66].

In mouse and human cardiac hypertrophy, the expression of miR-1 and miR-133 is downregulated [67]. MiR-328 targets $Ca_v1.2$ (a calcium channel that generates the L-type calcium current at phase 0 of the SN's action potential) [68]. In the left atrial samples of a canine model of atrial fibrillation and in patients with rheumatic heart disease, the expression of miR-328 is elevated [68].

Therefore, miRNAs can be potential therapeutic targets in the treatment of CVDs. This has previously been demonstrated by Yanni et al. (injected a miR-370 anti-miR into heart failure mice to restore the expression of HCN4 in the SN) [69] and Petkova et al. (injected miR-486-3p into healthy rat tissue to reduce HCN4 expression and thus reduced heart rate) [44].

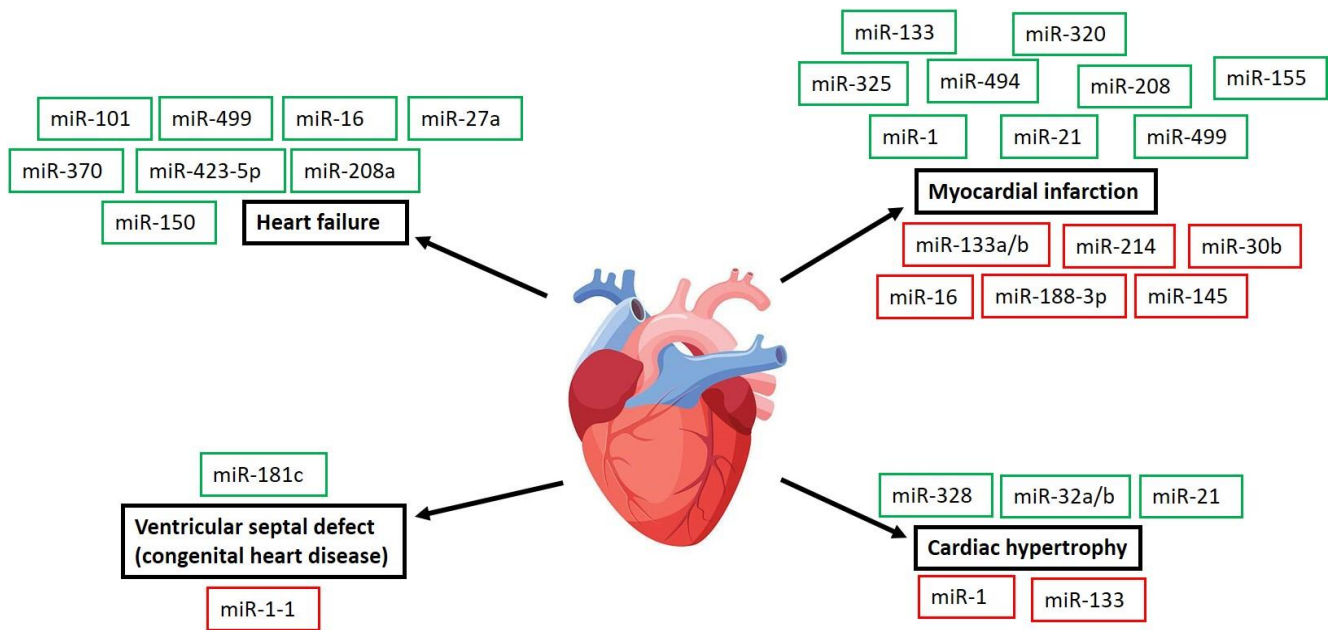


Figure 1. 4. Main miRNAs involved in heart diseases. Green box, upregulated; red box, downregulated.

Adapted from Islas et al. 2018 and Kalayinia et al. 2021. Heart image obtained from (<http://clipart-library.com/clipart/gce5yeaqi.htm>).

1.3 Imaging techniques

Histology, immunohistochemistry, echocardiogram, cardiac magnetic resonance imaging (CMRI), computed tomography (CT), and micro-CT are various imaging techniques used in the anatomical study of the human heart [70-78].

1.3.1 Histology

Histology involves dissecting and staining tissue and examining them under a microscope. In clinical practice, histology contributes to disease study and treatment [79]. Generally, there are five stages involved in histological staining: fixation, processing, embedding, sectioning and staining [80]. Modern histology stains include Toluidine Blue (stains mast cell granules and cartilage), Movat Pentachrome (stains collagen and elastin), and Masson's Trichrome (stains connective tissue, myocytes, and fibrin). In my PhD research project, I performed Masson's trichrome staining on healthy, aged, and obese tissue samples to analyse and study the variation of cardiomyocytes and connective tissue.

1.3.2. Echocardiogram

Because this technique is fast, cheap, and non-invasive, echocardiography is commonly used in clinical practice. It uses sound waves generated by a probe back-recorded from the cardiac tissues to analyse anatomy and function [81]. Although this imaging technique has previously been used for the *in vivo* measurements of myocardial wall thickness and chamber volume [74, 76], it has not yet been used to create 3D reconstructions of the heart.

1.3.3 Cardiac Magnetic Resonance Imaging

CMRI is another imaging technique used for the *in vivo* analysis of the anatomy and function of healthy and diseased hearts. This technique uses a magnetic field and radio waves. It is a highly accurate and reproducible technique commonly used to analyse the anatomy and function of the left ventricle and atria [72, 75, 77]. Kawel et al. (2012) used CMRI to obtain normal reference values for left ventricular wall thickness by manually contouring around regions of interest [72] – a technique utilised in my PhD study.

1.3.4 Computed Tomography and Micro-computed Tomography

CT is a non-invasive and non-destructive imaging technique that uses x-rays that pass through the sample at various angles. The sample rotates through 360° to produce images with voxel sizes of approximately 300 µm, commonly used in clinical settings. Recently, higher-resolution micro-CT (with voxel sizes as low as 0.95 µm) has been used *in vivo* [71, 82] and *ex vivo* [7, 83-85], using contrast agents such as iodine potassium-iodide (I₂KI, to visualise the working myocardium, CCS and blood vessels) [7, 71, 82].

Stephenson and Atkinson et al. 2017 published the first 3D reconstruction of the CCS in an intact, healthy human heart using I₂KI-enhanced micro-CT [7]. Unlike conventional CT, micro-CT works by combining a smaller field of view with a high-resolution detector – resulting in higher-resolution images. The results from my PhD research project are the first to show that graphene oxide (GO) is a viable contrast agent to visualise epicardial fat. This component was previously difficult to visualise using I₂KI.

Based on the variation of attenuation for the contrast agents across the cardiac tissue, it is possible to distinguish between various structures, such as the working myocardium, blood vessels, epicardial fat, and components of the CCS. Compared to the components of the CCS,

the working myocardium has a higher attenuation rate for I₂KI (that is, I₂KI accumulates in the working myocardium, compared to the CCS). This higher attenuation rate is because I₂KI binds to glycogen. Compared to the CCS, there is a higher glycogen content in skeletal muscle (one of the main muscle types in the working myocardium), as discussed in Paper 1, Chapter 3. Histology staining is usually required to confirm images obtained from micro-CT.

Previous studies have used I₂KI contrast agent to stain cardiac tissue for micro-CT scanning and analysis [7, 15, 86-88]. However, these studies did not create and analyse 3D reconstructions of structures within aged and obese hearts. *Therefore, the purpose of this PhD project was to use I₂KI and GO as contrast agents for high-resolution micro-CT to visualise and analyse anatomies of the whole, aged, and obese hearts, including their CCS.*

1.4 Obesity and cardiovascular diseases

Obesity has a direct and indirect link to increased cardiovascular morbidity and mortality. As mentioned earlier, obesity (BMI \geq 30.0) is a common risk factor for cardiac arrhythmia and heart failure [3].

‘Obesity cardiomyopathy’ describes the cardiac remodelling that originates from obesity [89]. Obese patients develop heart failure ten years earlier than patients with a normal BMI [90]. In addition, various haemodynamic changes such as increased cardiac output increased blood volume and reduced systemic vascular resistance that occurs during obesity contributes to hypertension, left ventricular hypertrophy, diastolic dysfunction and heart failure [90].

This dysfunction progresses independently of coronary heart disease, hypertension, heart failure, and other CVDs. The accumulation of fat - notably increased visceral adipose tissue and pericardial fat - leads to the increased cardiac output mentioned above and, eventually, the myocardial wall and/or chambers enlargement to meet the increased energy demands of the myocardial wall and/or chambers obese heart.

Other CVDs manifest because of obesity. Right ventricular hypertrophy (resulting in increased right ventricle end-diastolic volume) is more common in obese individuals than those with normal BMI [91]. Extensive cohort studies have shown a correlation between obesity and increased aortic valve stenosis [92, 93]. The structural and functional remodelling of the atria

and ventricles in the obese heart increases the occurrence of atrial fibrillation in obese individuals [94, 95].

1.5 Ageing and cardiovascular diseases

As mentioned earlier, ageing (60 years and above [2]) is a common risk factor for cardiac arrhythmia, and heart failure – the mean age of patients with SN dysfunction is 68 years [3]. Ageing is associated with cardiac structural and functional remodelling. In aged patients, cardiomyopathy and heart failure are common causes of hospitalisation [96]. A gradual decrease in maximum heart rate is a key feature of ageing in humans and mammals [97]. The most common factor that leads to SN dysfunction is the age-related degeneration of the SN [98]. The proposed reasons for this are a loss in CX43 protein observed in aged guinea pig hearts [99] and the loss of cardiomyocytes (apoptosis) in aged hearts. This apoptosis contributes to aged hearts having smaller mass and volume than healthy and younger hearts [96].

Ageing is linked to a decrease in increased left atrial volume, reduced ventricular volume, and thickened and calcified valves [100]. The structural decline of the ageing heart is associated with fibroblast-extracellular matrix disruption [101]. This disruption results in increased fibrosis as fibroblasts produce fewer ECM proteins and more matrix-degrading metalloproteinase [42, 102].

Obese heart samples and aged heart samples were used in this PhD project on account of the critical effects of obesity and ageing on the development of cardiovascular diseases. We must expand our understanding of the structural differences in obese and aged hearts compared to normal.

1.6 Aims

The overall aim of this research is:

The following aims were established to contribute to the current understanding of the anatomical and molecular mapping of the working myocardium and CCS of the human heart from healthy, obese, and aged individuals,

(1) *As published in Paper 1, Chapter 3, the first aims were to visualise and compare the whole normal, aged, and obese hearts and their CCS components using I₂KI-enhanced micro-CT. The next aim was to visualise epicardial fat within tissue blocks from normal, ageing, and obese hearts, using GO-enhanced micro-CT*

(2) *The following aims were based on the bioinformatics analysis of NGS for RNA-seq dataset for healthy human SN samples to predict key molecular interactions and further understand the molecular complexity of the SN.*

As published in Paper 2, Chapter 4, I aimed to identify 'novel' TFs in the human SN vs. RA, use IPA to predict interactions between these 'novel' TFs and 'embryonic' TFs and predict interactions among key TFs with pacemaking genes. I also aimed to deduce the expression of markers of key cell types and organelles in the SN vs. RA and predict their interaction with key TFs. Finally, I aimed to predict the interaction between these markers and TFs, and recently published key microRNAs [44].

(3) *Again, to further understand the SN's molecular complexity and pacemaking function, the last set of aims was based on the experimental validation of key predicted interactions. As published in Paper 3, Chapter 5, I aimed to use luciferase assay experiments to validate the predicted interactions between microRNAs, key pacemaking ion channels, TFs, and markers for immune (mast) cells and collagen.*

CHAPTER 2) GENERAL METHODS

This chapter provides a general overview of the methods mentioned in this thesis. It also includes the basic principles of these methods.

The methods adopted throughout this PhD project are as follows: human tissue preparation; micro-computed tomography (micro-CT); image analysis; 3D reconstruction; Masson's trichrome staining; bioinformatics; ingenuity pathway analysis; and luciferase reporter gene assays

2.1 Human sample details and ethical approval for micro-CT studies

Five ex vivo human heart specimens were used for micro-CT scanning and analysis, with a patients' age range of 19-97. Specimens were sourced from Prof. Paul Iaizzo (The Visible Heart[®] Laboratories, Minnesota, USA), from Science Care, USA, from Prof. Peter Molenaar (Australia), and from Prof. Filip Perde (Romania), all under local ethical rules. Patient information and specimen source are provided in the methods section of Paper 1, Chapter 3.

2.1.2 General principles

The main methods are summarised in Figure 2.1.

2.1.2.1 Tissue preparation

Formaldehyde is a commonly used fixative in laboratories as a neutral buffered formalin. Formalin is considered a universal fixative because it penetrates tissue quickly, causes less tissue shrinkage compared to other fixatives, and the lipids within the tissue are not made insoluble but are preserved [103]. Therefore, each specimen used for my project was fixed in 4% buffered formalin before micro-CT scanning. Following this, the specimens were stored at room temperature in the Dobrzynski laboratory under the Human Tissue Act (2004). Specimens for cryosectioning and histology were stored at -80 °C, as described in the methods section of Paper 1, Chapter 3.

Before scanning, all specimens were cleared of fixative by immersing them in distilled water for 7-14 days (Figure 2.2) and then immobilised in a container to prevent movement during the scanning process. Scan times ranged from 1 hour - 6 hours.

2.1.2.2 Basic principles of micro-CT

As opposed to other imaging techniques such as histology, micro-CT is a non-destructive imaging technique that produces high-resolution 3D images made from 2D trans-axial projections (otherwise known as '2D slices') of the scanned specimen. Micro-CT produces images with voxel sizes below 1 μm and spatial resolutions of 3 – 100 μm , providing the images with much higher resolution than ultrasound and MRI techniques [104]. The voxel size

depends on the magnification (i.e., the distance between the x-ray source and specimen and between the x-ray source and detector).

During my PhD project, specimens were scanned using the Nikon Metris XTEK XT H 320/225 kV High Flux systems at the Henry Moseley Manchester X-Ray Imaging Facility, University of Manchester, as previously described [7, 15]. This equipment consists of various compartments: an x-ray source/generator, a radiation filter and collimator, a stage to hold and rotate the specimen by 360°, and a phosphor-detector/charge-coupled device camera detects the images (Figure 2.1). 2D projections/slices (number of projections is 2000-4000) of the specimen are created as the specimen rotates on the stage through 360° multiple viewing directions. I then converted these 2D slices to 3D reconstructions (filtered back projection). Additionally, micro-CT allows virtual sectioning and visualisation from any plane, as described in the methods section of Paper 1, Chapter 3.

Visualising images and identifying structures within the micro-CT scanned specimen is based on x-ray attenuation differences, as described in the methods section of Paper 1, Chapter 3. This visualisation corresponds to how much the intensity of the x-ray beam diminishes as it passes through the specimen. Various parts of the myocardium (the working myocardium vs. the CCS) and fat have different x-ray attenuation rates following I₂KI or GO infusion. The working myocardium has a higher attenuation for x-rays. It, therefore, appears light grey-to-white, while the CCS has a lower attenuation and therefore appears dark grey-to-black.

2.1.2.3 Image analysis and 3D reconstruction

I uploaded 2D images/slices obtained following micro-CT scanning of specimens onto Amira v6.5 (Thermo Fischer Scientific). Amira v6.5 refers to 2D slices as 'ortho slices'. The 'volume rendering' function within Amira v6.5 was used to convert the 2D slices to 3D reconstructions. To segment structures such as the working myocardium, atrial and ventricular cavities, components of the CCS; blood vessels; valves; whole tissue block; and epicardial fat, I used the 'segmentation' feature within Amira v6.5. Within this feature, a 'masking' threshold was set. This technique is described in more detail in Paper 1, Chapter 3.

After separating (i.e., segmenting) the region of interest from the surrounding tissue, I reconstructed it into a 3D image using the 'generate volume' function. Volume rendering allows various measurements of the segmented structures, such as volume measurement,

wall thickness, tissue length, and wall width. The location of myocardial wall width measurements is shown in Figure 1 of Appendix A. After segmenting the atrial and ventricular cavities from the normal, aged, and obese whole hearts and creating their 3D reconstructions, I obtained their volumes. I used Graph Pad Prism 8.4.3 (by Dotmatics) software to create the graphs depicting the cavities' volumes, as shown in Figure 4 of Appendix A.

Additionally, the 3D reconstruction of the segmented structures can be manually inserted into other specimens, allowing comparison and further analysis. For example, the segmented SN region from a healthy right atrium tissue block can be inserted into an obese or aged right atrium tissue block or whole heart.

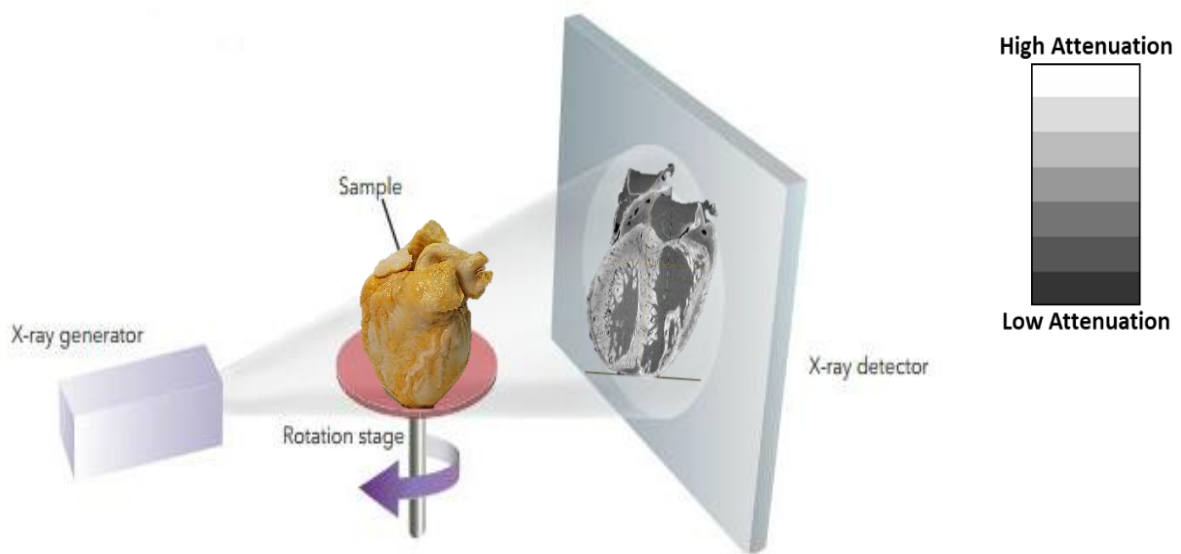


Figure 2. 1. The principal components of a micro-computed tomography scanner. Adapted from <https://www.microphotonics.com/>.

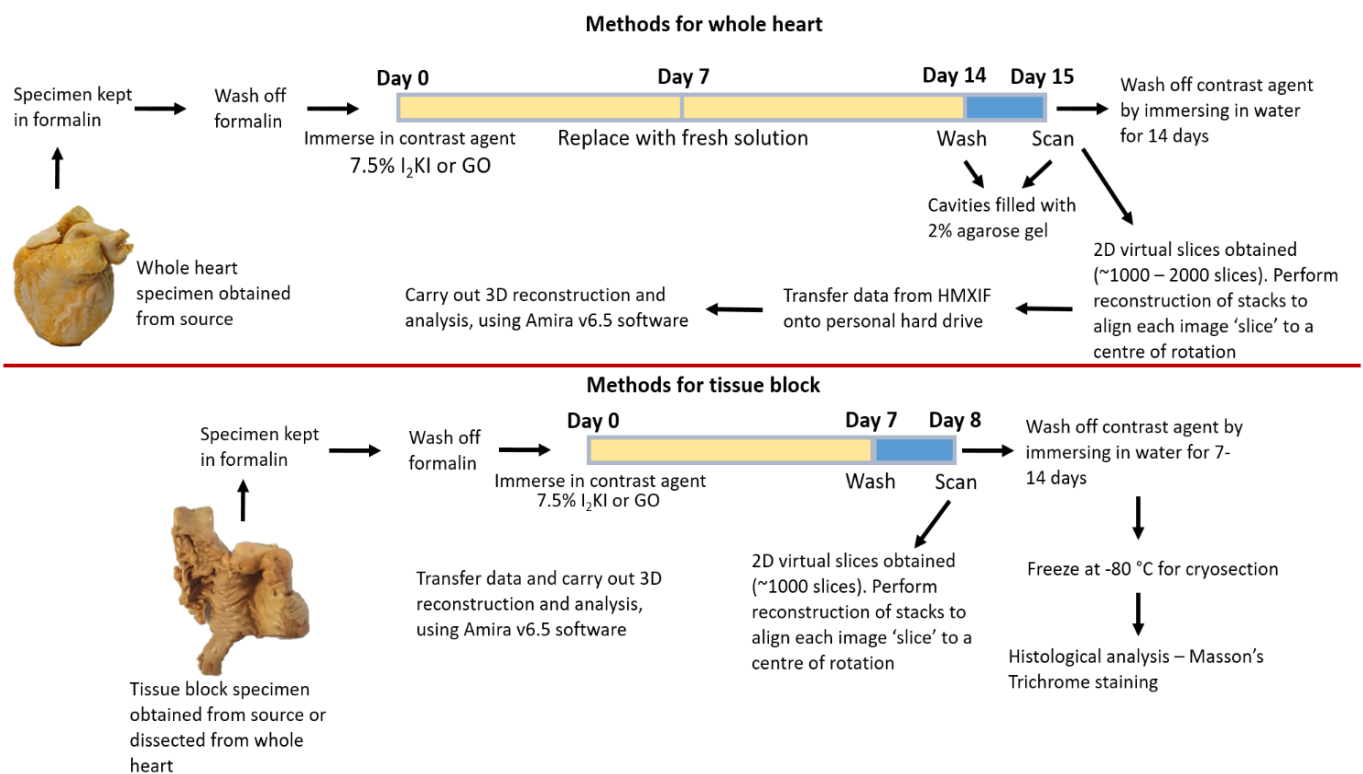


Figure 2. 2. Summary of main methods. GO, graphene oxide; I₂KI, iodine potassium-iodide.

2.1.2.4 Basic principles of Masson's trichrome staining

A detailed description of the cryosectioning of the tissues can be found in the methods section of Paper 1, Chapter 3. I sectioned the tissue blocks containing the AV junction in the direction from the INE to the bundle branches, and tissue blocks containing the SN were cryosectioned from the inferior vena cava to the superior vena cava.

The morphology of tissue sections and the location of specific structures within a tissue can be assessed using histological staining. Stains can be used on their own or in combination with other stains so that multiple components within the tissue section can be visualised simultaneously.

Usually, the negatively charged groups on dyes bind to positively charged groups on the tissue sections (i.e., ionic binding), and the pH of dyes is usually between 1.5 – 3 [105].

The most common fixative used in histology is Bouin's fluid. It works by enhancing the intensity of the stains. In the Masson's trichrome staining I performed during my project, tissue sections on glass slides were initially placed in an oven at ~38°C overnight before immersing in Bouin's fluid. This process was to prevent tissue sections from sliding off the glass slides during the staining process – a common issue that I observed in the early stages of my project.

Masson's trichrome is a common staining method. It consists of celestine blue, Mayer's haematoxylin, acid fuchsin, phosphomolybdic acid, and methylene blue.

Celestine blue is a nuclear stain that is resistant to acid. During Masson's trichrome staining, celestine blue is used to preserve the nuclear staining throughout the staining procedure. Nuclei are stained blue/black (see Figures 8, 10, 11, and 12 in Paper 1, Chapter 3, and Figure 1 in Paper 2, Chapter 4).

Mayer's haematoxylin is a nuclear stain that stains chromatin in nuclei blue/black.

Acid fuchsin is an acidic magenta dye that stains myofilaments red.

Phosphomolybdic acid replaces the stain that is bound to the tissue section.

Methylene blue stains collagen fibres cobalt blue.

2.2 Human sample details and ethical approval for NGS and IPA studies

For next-generation sequencing (NGS) for RNA sequencing (RNA-seq), three *ex vivo* human hearts were obtained as they were deemed unsuitable for transplantation, by collaborators in Australia, under local ethical approval. The patient age range was 19 -54. Upon receiving the samples, they were stored at -80°C in the Dobrzynski laboratory under the Human Tissue Act (2004). Further patient information and specimen source are provided in the methods section of Paper 2, Chapter 4 and Paper 3, Chapter 5.

2.2.1 General principles

2.2.1.1 Tissue preparation

The sinus node (SN) samples were obtained from around the SN artery, and the right atrium (RA) samples were obtained from the pectinate muscle. Dr Halina Dobrzynski carried out this step.

2.2.1.2 Basic principles of next-generation sequencing

The Genomic Technologies Core Technology Facility performed NGS on the samples at the University of Manchester. In principle, during the process of NGS, DNA polymerase catalyses the attachment of fluorescently labelled deoxyribonucleotide triphosphates (dNTPs) to the DNA template strand during the DNA amplification cycles. During each cycle, fluorophore excitation identifies the nucleotides. Multiple screening of the same DNA fragment achieves high accuracy and a high yield of error-free reads.

Generally, there are four basic steps in NGS:

1. Library preparation. This step involves randomly fragmenting the cDNA sample to create smaller sequence strands/fragments. Then DNA ligase joins these smaller strands to specific adapters (short, synthetic DNA fragments that help the cDNA fragments to bind to the complimentary sequence) to the cDNA fragment's 3' and 5' ends [106].

2. Library amplification. After ligation to adapters, the cDNA fragments undergo PCR amplification and gel purification. Higher cDNA abundance produces a stronger signal during amplification, therefore allowing the accurate detection of specific cDNA fragments.

3. Cluster generation. Here, the cDNA library is loaded into optical flow cells. The cDNA fragments are then captured through their adapters binding to complementary surface-bound oligos [106]. Following this, sequencing of the cDNA templates can now occur.

4. Sequencing. A proprietary reversible terminator-based method detects single nucleotide bases on the DNA template strands. The outcome of this is a highly accurate base-to-base sequencing – therefore, it prohibits sequence context-specific errors [106].

Before I began my PhD project, NGS was already carried out on the 3 SN and 3 RA samples by the Genomic Technology Core Facility, University of Manchester. NGS for RNA-seq was performed on total RNA extracted by Dr Dobrzynski from three frozen human SN and RA samples. The NGS dataset contained 2595 mRNAs significantly more or less expressed in the SN vs. RA.

2.2.1.3 Basic principles of Ingenuity Pathway Analysis

I used IPA to identify key and ‘novel’ mRNAs and TFs within the NGS dataset (main methods summarised in Figure 2.3).

As mentioned in the introduction, IPA is an advanced and powerful bioinformatics software that allows the functional analysis, understanding, and integration from RNA-seq and microarray gene expression datasets, as well as miRNA and proteomics datasets [107]. For my PhD project, the NGS dataset was uploaded into the IPA program for a systematic bioinformatic analysis. Within IPA, I identified TFs and mRNAs that were significantly more expressed (\log_2 fold change ≥ 1) and significantly less expressed (\log_2 fold change ≤ -1) in the SN vs. RA. Following this, IPA was used to predict interactions between key TFs, cell markers, miRNAs and mRNAs based on the Ingenuity Knowledge Base of ‘highly-structured, detail-rich biological and chemical findings’ [107]. These findings are linked to original articles constantly reviewed for accuracy by PhD scientists [92] – making IPA unique from other databases.

After identifying predicted targets and interactions, I used various software (<https://cm.jefferson.edu/rna22/> and <http://www.targetscan.org/>) to predict the number of binding sites for the miRNAs on target mRNAs.

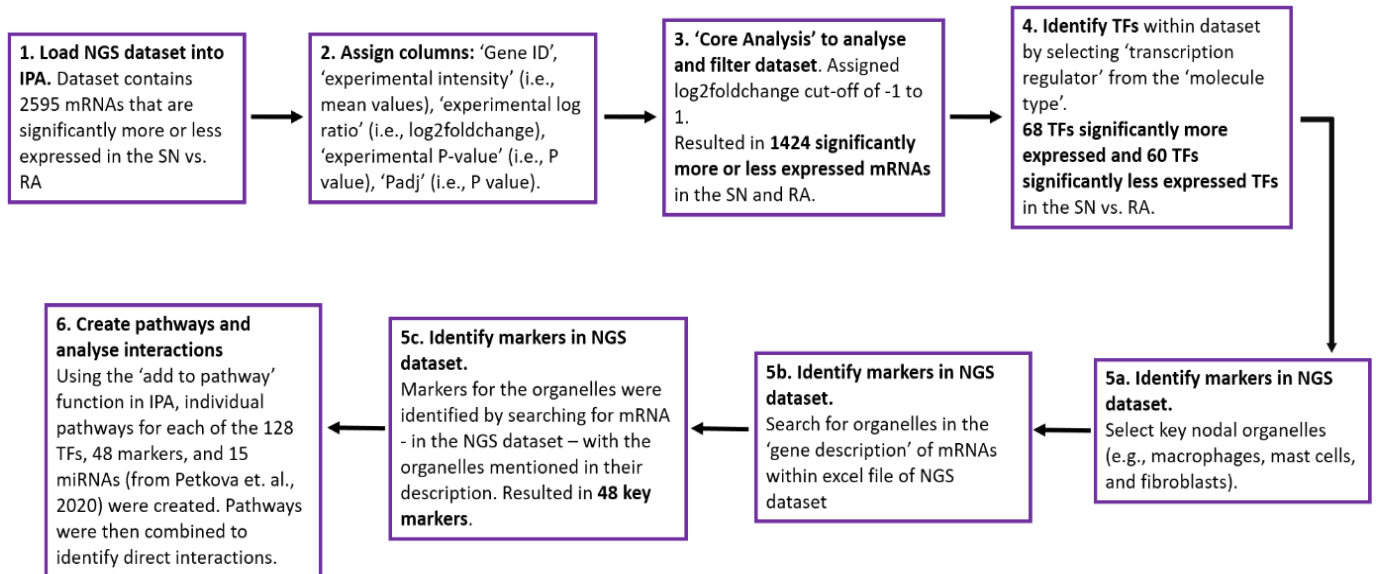


Figure 2. 3. Summary of Ingenuity Pathway Analysis methodology. IPA, Ingenuity Pathway Analysis; mRNAs, messenger ribonucleic acids; NGS, next generation sequencing; RA, right atrium; SN, sinus node; TFs, transcription factors.

2.3 General principles for bioinformatics

2.3.1 RNAseq and qPCR for miRNA

The miRNAs data obtained from previously performed qPCR experiments are what I used for my PhD project. From this, 754 miRNAs were identified - 66 of which were significantly ($\log_2\text{foldchange} \geq$ or ≤ 1) differentially expressed in the sinus node (SN) and right atrium (RA). 18 miRNAs were significantly more expressed in the SN vs. RA, and 48 miRNAs were significantly less expressed in the SN vs. RA. 15 of these 48 miRNAs were predicted to interact with key molecules that regulate the SN's pacemaking function [44]. How these miRNAs were extracted and analysed is described in Petkova et al. (2020) [44].

2.3.2 Prediction of binding sites RNAseq and qPCR for miRNA

After IPA predicted direct interactions between miRNAs and target mRNAs, I used various software to predict the number of binding sites for miRNAs on the target mRNAs.

First, I obtained the sequence for the 3'UTR or the target mRNA from <https://genome.ucsc.edu>. Then, I got the mature sequence for the miRNA from <https://www.mirbase.org>. Following this, the 3'UTR and miRNA sequences were input into RNA22 (<https://cm.jefferson.edu/rna22/>). When IPA predicted interactions but RNA22 predicted no binding sites, TargetScan Human (<http://www.targetscan.org/>) was used to predict the binding sites.

An example of how I predicted binding sites on TPSAB1 for miR-486-3p is described in Figure 2.4.

The miRNAs and mRNAs predicted to have complementary binding sites were chosen for luciferase assay experiments for validation. A list of miRNAs and mRNAs that were 'carried forward' for luciferase experiments and the number of predicted binding sites is shown in Table 1 of Paper 3, Chapter 5. It should be noted that although binding sites for miRNA are predicted to be on their target mRNAs, sometimes no significant downregulation (or even no trend towards downregulation) in the luciferase activity of some target mRNA was observed following miRNA binding, even sometimes after 5 batches of experiments. For example, HCN1 is predicted to have 6 binding sites for miR-486-3p (Table 1 of Paper 3, Chapter 5). However, there was no significant downregulation in the luciferase activity of HCN1 after the addition

2.3.3 General principles of luciferase reporter gene assay

Luciferases are a group of enzymes that produce light when they oxidise luciferin (their substrate), releasing energy. Almost all the energy produced during the oxidation reaction is converted to fluorescent light – making the luciferase reporter gene assay sensitive to changes in gene/protein expression levels [93]. The luciferin-luciferase complex that is formed is found in bacteria (*Vibrio harveyi*), dinoflagellates (*Gonyaulax*), and more commonly, the firefly (*Photinus pyralis*). The firefly luciferase is commonly used in reporter gene assay experiments.

The luciferase gene is cloned downstream of the target DNA sequence (e.g., TFs or mRNAs such as TBX18 or HCN4) into an expression vector before it is transfected into a cell line (e.g., H9C2 rat myoblast cells). In cell culture, the luciferase reporter gene assay is used to determine the expression levels of target genes. It is also used to study the activity of miRNAs on the post-transcriptional repression of their target proteins.

Cells are transfected with the luciferase gene-containing vector and other molecules, such as miRNAs, before incubating the cells for 24 hours. Then the cells are lysed by adding a lysis buffer before the luciferin enzyme. Proteins, including the luciferase protein, are released from the cell culture and interact with luciferin. A bioluminometer detects and quantifies the reaction/amount of light emitted. Luciferase activity is directly proportional to the expression of the target gene because the luciferase gene is fused with the target gene [108]. If the miRNA inhibits its target gene, luciferase intensity is reduced compared to a control assay. A renilla (*Renilla reniformis*) reporter gene internally controls and normalises the luciferase reporter gene results. Renilla also normalises variations that could take place due to transfection efficiency and sample handling.

2.3.3.1 Luciferase reporter gene assay experiments

As mentioned earlier, IPA was used to predict interactions between TFs that are more expressed in the SN vs. RA (e.g., Ca_v1.3 and TPSAB1) and miRNAs that are less expressed in the SN vs. RA (e.g., miR-486-3p and miR-938). Following this, I used various software (<https://cm.jefferson.edu/rna22/> and <http://www.targetscan.org/>) to predict the number of

binding sites for the miRNAs on target mRNAs. 12 mRNAs were predicted to be inhibited by their respective miRNAs.

CHAPTER 3) NOVEL MICRO-COMPUTED TOMOGRAPHY CONTRAST AGENTS TO VISUALISE THE HUMAN CARDIAC CONDUCTION SYSTEM AND SURROUNDING STRUCTURES IN HEARTS FROM NORMAL, AGED, AND OBESE INDIVIDUALS¹

This paper provides detailed descriptions and insights into the use of iodine potassium-iodide (I₂KI) and graphene oxide (GO) as contrast agents for high-resolution micro-computed tomography (micro-CT). The aim is to explore and identify anatomies of normal (i.e., healthy), aged, and obese whole hearts, including their cardiac conduction system (CCS).

The study described in this chapter was conducted on 5 post-mortem human hearts. The use of I₂KI to visualise components of the heart utilises a previously established imaging technique to show 3D reconstructions of whole normal, aged, and obese hearts – for the first time. Uniquely, for the first time, I₂KI is used to produce the first 3D reconstructions of the moderator band, aortic and pulmonary trunk, sinus node (SN) region, and coronary artery network within the normal, aged, and obese hearts. In addition, this chapter provides the first insight into the use of GO to visualise epicardial fat within and surrounding cardiac tissue.

Finally, this chapter describes notable anatomical differences observed in the three heart groups. Therefore, the data obtained in this study provides an outlet to create computational/mathematical models of ageing and obese hearts, to improve surgical outcomes and reduce cardiac morbidities.

At the end of this thesis is an appendix that contains additional data relevant to this study. This appendix was not included in the final publication of the paper.

¹This chapter is directly from the publication: **Aminu, A. J.**, Chen, W., Yin, Z., Kuniewicz, M., Walocha, J., Perde, F., Molenaar, P., Iazzo, P. A., Dobrzynski, H., Atkinson., *Novel micro-computed tomography contrast agents to visualise the human cardiac conduction system and surrounding structures in hearts from normal, aged, and obese individuals*. TRIA. 2022. **27**: p. 100175

3.1 Authors' contribution to the paper

I (Abimbola J. Aminu) carried out the vast majority of the experimental work in this study. This includes creating, writing, and editing the paper. I appreciate the effort and input from all co-authors.

- Abimbola J. Aminu: carried out all graphene oxide-enhanced micro-CT scans; aided Andrew J Atkinson with the I₂KI-enhanced micro-CT scans; analysed all datasets; performed segmentations and created 3D reconstructions of all structures presented in this chapter (Figures 1-13, excluding Figures 4, 11A, 11B, and 12Bii); performed Masson's trichrome staining on healthy SN (Figures 8D and 11Ai), healthy AVN (Figure 10B and 11Bii), and young AVN tissue sections (Figure 12Bi); manuscript planning, writing and editing (original draft and revised/final version); formatting figures and tables; supervision of Weixuan Chen and Zeyuan Yin
- Weixuan Chen: performed segmentations and created 3D reconstructions of all coronary arteries (Figure 4); performed Masson's trichrome staining on obese SN (Figure 11A and 11Aii) and obese AVN (Figure 11B and 11Biii) tissue sections; manuscript editing (original draft)
- Zeyuan Yin: performed Masson's trichrome staining on aged AVN tissue sections (Figure 12Bii)
- Marcin Kuniewicz: manuscript editing (original draft)
- Jerzy Walocha: manuscript editing (original draft)
- Filip Perde: provided specimens (healthy and young AV tissue block)
- Peter Molenaar: provided specimens (healthy SN tissue block); manuscript editing (original draft)
- Paul A. Iazzo: provided specimen (whole, healthy heart); manuscript editing (original draft)
- Halina Dobrzynski: supervision; formatting figures and tables; manuscript planning; manuscript editing (original draft and revised/final version)
- Andrew J. Atkinson: supervision; formatting figures and tables; manuscript planning; manuscript editing (original draft and revised/final version)

3.2 Hypothesis

A previous study by Stephenson and Atkinson et al. (2017) showed that I₂KI is a contrast agent for the micro-CT visualisation of a healthy human heart and SN. If this is possible in a healthy heart, then I₂KI can be used as a contrast agent for the micro-CT visualisation and reconstruction of various structures and CCS components in the healthy human heart, aged human heart, and diseased human heart. No study has been able to carry out the micro-CT visualisation and reconstruction of epicardial fat of the human heart using I₂KI. Therefore, exploring other contrast agents could shed some light on the 3D anatomy of epicardial fat within and around heart samples from these three groups.

3.3 Aims

This study aimed to explore and identify anatomies of normal (i.e., healthy), aged, and obese whole hearts, including their cardiac conduction system (CCS).

I aimed to visualise and compare the whole normal, aged, and obese hearts and their CCS components using I₂KI-enhanced micro-CT. Using GO-enhanced micro-CT, the next aim was to visualise epicardial fat within tissue blocks from normal, aged, and obese hearts.

3.4 Materials and methods

Thorough descriptions of the methods used in this study are provided in the accompanying paper.

3.4.1 Human sample details

I used five ex vivo human hearts in this study with an age range of 19-97. Further details on the specimen information, including the source and cause of death, are provided in Table 1 of Paper 1, Chapter 3. None of the patients died from cardiac-related causes. All the tissue was stored in the Dobrzynski laboratory under the Human Tissue Act 2004.

Before micro-CT scanning, all specimens were fixed in 4% buffered paraformaldehyde. Paraformaldehyde fixation is commonly used for tissue preservation because it forms strong covalent bonds between molecules in the tissue, preventing them from breaking down and preserving their structure.

Some specimens were received as whole hearts before micro-CT scanning or as tissue blocks before micro-CT scanning. However, some whole heart specimens were dissected into tissue blocks after micro-CT scanning (Table 1, Paper 1, Chapter 3).

3.4.2 Whole heart tissue preparation and selection of contrast agents

I₂KI contrast agent was used to visualise the cardiac structure in whole hearts and the CCS in tissue blocks. Before micro-CT scanning, whole hearts were immersed in 7.5% aqueous I₂KI or GO (0.5 mg/mL H₂O) contrast agent solution for 14 days, at day 7, the solution was refreshed. GO contrast agent was used to visualise epicardial fat within and around tissue blocks. The decision to use GO to visualise epicardial fat arose when it became evident that epicardial fat could not be visualised when I₂KI contrast agent was used. On the other hand, when GO was used, visualisation of the CCS and other major cardiac structures was poor.

Warm agarose solution was poured into the cavities in the whole hearts. This solution hardened at room temperature, which was ideal for keeping the cavities open throughout the scanning process. In the instance when agarose was not available, cling film was used for the same purpose.

3.4.3 Tissue block preparation

The healthy tissue block of the right atrium containing the SN region was obtained from Australia, and the healthy tissue block containing the AV junction was obtained from Romania (Table 1, Paper 1, Chapter 3).

After scanning the whole aged and obese hearts, I realised that it was impossible to visualise components of the CCS for segmentation. Therefore, tissue blocks containing components of the CCS were dissected from whole hearts before scanning them individually. Before scanning, tissue blocks were immersed in 7.5% aqueous I₂KI or GO (0.5 mg/mL H₂O) contrast agent solution for 7 days.

Before scanning, the whole hearts and tissue blocks were rinsed with distilled water to remove excess contrast agents and stabilised in a plastic container.

3.4.4 High-resolution micro-computed tomography

As mentioned in the introduction chapter, high-resolution micro-CT produces images with very high resolution (with voxel sizes as low as 0.95 μm) compared to other imaging techniques such as computed tomography and MRI.

All the samples described in this study were scanned using the Nikon Metris XTEK XT H 320/225 V High Flux systems at the Henry Moseley Manchester X-ray Imaging Facility, University of Manchester. The total scan times were between 1 hour - 4 hours.

3.4.5 Segmentation and reconstruction

Figure 3.1 describes how I carried out the segmentation. Generally, areas of interest were manually separated/segmented from the surrounding tissue based on the difference in x-ray attenuations, using the 'brush' tool in the Amira v6.5 software. Areas with high x-ray attenuation rates (i.e., high affinity for the x-ray beams), such as the working myocardium, appeared light grey and regions with lower x-ray attenuation rates (i.e., low affinity for the x-ray beams), such as the components of the CCS, appeared dark grey. In the 'segmentation' section of Amira v6.5, I used the 'masking' tool to assign values to the dark and light areas to make it easier to visualise the region that will be segmented. Then, I used the lasso tool to 'draw' around the region of interest every 10 slices, approximately. Then I used the 'interpolate' function in Amira v6.5 software to fill in the other slices.

It took approximately 8 hours to segment the aorta in one specimen, about 40 hours to segment the SN region from one specimen, and about 80 hours to segment the ventricles from one specimen.

After segmentation was complete, I used the 'volume rendering' function in Amira v6.5 to create a 3D reconstruction of each segmented structure.

In addition to performing segmentations, the myocardial wall thickness and cavities volume was measured for the 3 whole hearts. The 'landmark' location for the wall thickness measurements is shown in Figure 1 of the Appendix.

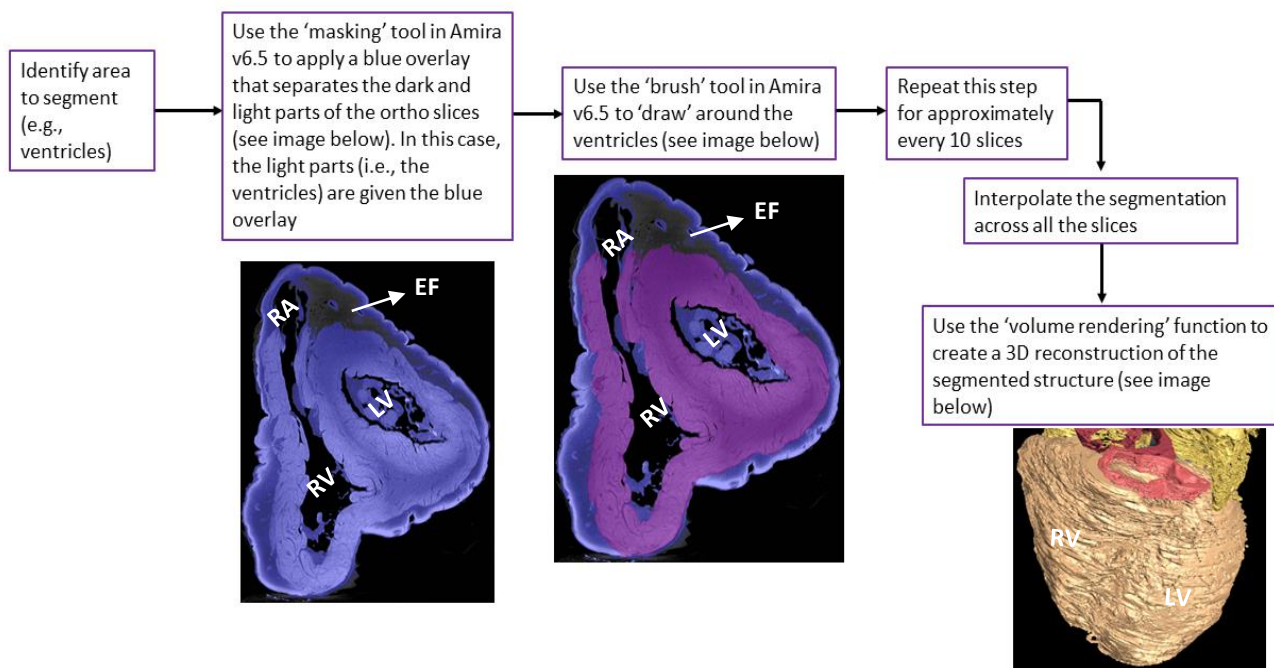


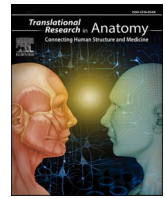
Figure 3.1. Summary of how segmentation and 3D reconstruction were performed. 3D, 3-dimensional; EF, epicardial fat; LV, left ventricle; ortho slices, orthogonal slices; RA, right atria; RV, right ventricle

3.4.6 Cryosectioning and histological analysis of tissue blocks containing components of the CCS

After washing the contrast agents from the tissue blocks using distilled water, I froze the blocks with isopentane before storing them in a $-80\text{ }^{\circ}\text{C}$ freezer. Then I sectioned the tissue blocks using a cryostat in temperatures ranging between -10 and $-20\text{ }^{\circ}\text{C}$ at a thickness of $20\text{--}35\text{ }\mu\text{m}$. Initially, the tissue sections were sliding off the glass slides after overnight immersion in Bouin's fluid – leading to the loss of precious and limited tissue sections. To overcome this, I started storing the glass slides with the tissue sections on them in an oven at a temperature of 48°C overnight because this caused the tissue sections to adhere to the slides firmly. Then Masson's trichrome staining was carried out to identify cardiomyocytes, connective tissue, and fat within the tissues. Further details on this process are provided in paper 1, chapter 3.

This process was successful in the healthy tissue blocks. However, it was challenging to cryosection whole tissue sections from the aged and obese tissue blocks. These tissue blocks were softer than the healthy tissue blocks even though they had been stored under the same conditions. The aged and obese tissue sections kept “folding back” on themselves and

breaking. Various troubleshooting was carried out, such as: reducing the temperature in the cryostat and changing the blades used in the cryostat, but these were to no avail. The partial pieces of tissue section from the obese and aged tissues obtained were stained and are shown in Figure 11 of paper 1, chapter 3.



Novel micro-computed tomography contrast agents to visualise the human cardiac conduction system and surrounding structures in hearts from normal, aged, and obese individuals

Abimbola J. Aminu^a, Weixuan Chen^a, Zeyuan Yin^a, Marcin Kuniewicz^e, Jerzy Walocha^e, Filip Perde^b, Peter Molenaar^{c,f}, Paul A. Iaizzo^d, Halina Dobrzynski^{a,e,1,*}, Andrew J. Atkinson^{a,1}

^a The Division of Cardiovascular Sciences, University of Manchester, United Kingdom

^b National Institute of Legal Medicine, Bucharest, Romania

^c Cardiovascular Molecular & Therapeutics Translational Research Group, University of Queensland, The Prince Charles Hospital, Brisbane, Australia

^d The Visible Heart® Laboratories, Department of Surgery, University of Minnesota, USA

^e Department of Anatomy, Jagiellonian University Medical College, Krakow, Poland

^f School of Biomedical Sciences, Queensland University of Technology, Brisbane, Australia

ARTICLE INFO

Keywords:

Cardiac conduction system
Sinus node
3D reconstruction
Micro-computed tomography
Iodine potassium-iodide graphene oxide

ABSTRACT

Research purpose: The cardiac conduction system (CCS) regulates electrical impulses across the heart and cardiac arrhythmias cause structural remodelling of the CCS. Since its discovery over a century ago, the precise anatomy and differences between the human CCS in healthy, aged, and obese human hearts has remained relatively unknown. Using iodine potassium-iodide (I₂KI) and graphene oxide (GO) as contrast agents for high-resolution micro-computed tomography (micro-CT), we explored and identified the anatomies of whole healthy, aged, and obese hearts, including their CCS.

Basic procedures: Human specimens were obtained from 5 post-mortem hearts, under local ethical rules and stored in the Dobrzynski laboratory, under the Human Tissue Act 2004. Specimens were stained with I₂KI or GO contrast agents before scanning with micro-CT. Data obtained from micro-CT was uploaded onto Amira v6.5 software for analysis, 3-dimensional reconstructions, and segmentation of relevant structures. Following micro-CT analyses, tissue blocks were cryosectioned and stained for histological assessments.

Main findings: There are obvious anatomical structural differences between the healthy, aged and obese hearts. Compared to the healthy heart, the aged heart and obese heart had larger chambers; thicker myocardial walls; thicker blood vessels; more extensive nodal regions and connective tissue; more epicardial fat; and fewer Purkinje fibres.

Our use of I₂KI and GO as contrast agents for high-resolution micro-CT scanning contribute to - and expands - the current understanding of CCS structural variations between healthy, aged and obese human hearts. These current and novel techniques can have key impacts on our anatomical understandings for current treatments for cardiovascular disease and the development of mathematical models of aged and diseased hearts. Thus ultimately aiding in the reduction of cardiac morbidities and reduction of patient death rate.

1. Introduction

The history of the cardiac anatomy has been elegantly reviewed by Roberts et al. [1]. Within the heart, the cardiac conduction system (CCS) is a group of specialised cardiomyocytes that consists of the sinus

node (SN, the heart's primary pacemaker); the atrioventricular (AV) conduction axis (the sole conduction pathway between the atria and ventricles in the healthy heart); and the His-Purkinje network, which allows rapid conduction of action potentials throughout the ventricular chambers [2,3]. Since the discovery of the CCS over 100 years ago, the precise anatomies of the CCS within healthy, aged, and diseased human

* Corresponding author. CTF Building, 46 Grafton Street, Manchester, M13 9NT, UK.

E-mail address: halina.dobrzynski@manchester.ac.uk (H. Dobrzynski).

¹ Equal contribution.

<https://doi.org/10.1016/j.tria.2022.100175>

Received 29 October 2021; Received in revised form 17 January 2022; Accepted 27 January 2022

Available online 14 February 2022

2214-854X/© 2022 The Authors.

Published by Elsevier GmbH. This is an open access article under the CC BY-NC-ND license

(<http://creativecommons.org/licenses/by-nc-nd/4.0/>).

Abbreviations			
2D	2-dimensional	LADA	Left anterior descending artery
3D	3-dimensional	LC	Left cusp
AV	Atrioventricular	LCA	Left coronary artery
CCS	Cardiac conduction system	LCC	Left coronary cusp
CM	Centimetre	LCx	Left circumflex artery
CN	Compact node	Micro-CT	Micro-computed tomography
CT	Computed tomography	MRI	Magnetic resonance imaging
EADs	Early afterdepolarisations	NCC	Non-coronary cusp
GO	Graphene oxide	PB	Penetrating bundle
HB	His bundle	PDA	Posterior descending artery
I ₂ KI	Iodine-potassium iodide	RCA	Right coronary artery
INE	Inferior nodal extension	RCC	Right coronary cusp
		SN	Sinus node
		TAVI	Transcatheter aortic valve implantation

hearts remains poorly understood. Although in recent years, there have been great advancements in our imaging and understanding of the CCS anatomy [4–8], the variation of the CCS anatomy with aging or cardiac disease are relatively unexplored areas.

Knowing the precise anatomies of the CCS in healthy and diseased hearts will further our current understanding of their functions and/or dysfunctions, hence contributing towards improving the treatments of cardiovascular diseases – one of the leading causes of death in the United Kingdom [9] and worldwide [10]. Cardiac arrhythmias and other CCS dysfunctions affects 9% of adults older than 80 years [11,12] and are prevalent in obese patients [13–15].

Previously, we have shown the 3D anatomy of the CCS in animal hearts and the link between the molecular and micro-anatomical remodelling of the CCS observed in disease [6,12,16,17].

1.1. SN anatomy, function, and dysfunction

3D reconstructions show that the SN is commonly a ‘crescent-shaped’ structure located at the junction of the superior vena cava and right atrial appendage, extending along the crista terminalis [8,18,19]. The myocytes of the SN surround the SN artery and are embedded in an extensive network of connective tissue (Fig. 8D).

Chandler et. al. [20] have reported a novel structure named the paranodal area that runs along the SN [20]. Compared to the SN myocytes and atrial myocytes, the myocytes of the paranodal area are loosely packed in fatty tissue and their exact function remains unknown [20,8].

Compared to the working myocardium, the SN has a unique expression of different ion channels, providing it with unique pacemaking mechanisms [21]. Dysfunction of the SN can occur as a result of heart failure, atrial fibrillation, ageing and/or obesity [22].

1.2. AV anatomy, function, and dysfunction

At the base of the atrial septum and top of the ventricular septum within the human heart sits the AV conduction axis (also known as AV junction). The general structure of the AV conduction axis has been likened to a weeping willow [23], consisting of the inferior nodal extension; compact node; penetrating bundle; His bundle; and the left and right bundle branches. After receiving electrical impulses from the SN, the AV conduction axis/junction conducts electrical impulses to the ventricles in a coordinated fashion.

Clinically, when the aortic valve becomes damaged, an aortic valve replacement procedure is deemed required, which could be surgical or a minimally invasive transcatheter aortic valve implantation (TAVI) procedure. But a fair amount of patients that have undergone these procedures tend to experience AV or left bundle branch blocks [24]. These are anatomically due to the close proximity between the aortic valve and

left bundle branch [24]. For example, the current expandable valves used for TAVI are thought to press on the left bundle branch – a result of both varied anatomies and our incomplete understanding of the AV conduction axis anatomy.

1.3. His-Purkinje anatomy, function, and dysfunction

Located at the crest of the ventricular septum, the His bundle divides into the left and right bundle branches [8]. These branches ramify further into what is known as the Purkinje fibres [8]. The His-Purkinje network spreads electrical impulses across the ventricles, allowing contraction to begin at the apex and ventricular emptying. Because Purkinje fibres have a long action potential, they are prone to early afterdepolarisations (EADs) – leading to torsade de pointes arrhythmia (a form of tachycardia arrhythmia) [25,26]).

1.4. Micro-computed tomography

The employment of contrast agents with micro-computed tomography (micro-CT) imaging allows the visualisation of different parts of the myocardium (the atrial and ventricular muscle vs. CCS) and fat, based on differential x-ray attenuation. In this study, we have utilised contrast enhanced micro-CT. Unlike histological techniques, contrast enhanced micro-CT is a non-destructive imaging technique that allows high-resolution 3D visualisation and reconstruction of whole hearts or tissue blocks. Like in previous studies [8,24,27–29], we have also used iodine-potassium iodide (I₂KI) contrast agent to stain the specimens in our study. Following I₂KI infusion, the working myocardium has a higher attenuation for the x-ray beam while the CCS has a lower attenuation for the x-ray beam. High attenuation areas have more accumulation of I₂KI and appear light grey to white and low attenuation areas appear dark grey to black. However, it has always been difficult to visualise epicardial fat with the use of I₂KI. We now present, to the best of our knowledge, the first use of graphene oxide (GO) as a contrast agent for micro-CT to stain specimens and visualise epicardial fat. As well as providing novel insights into the SN and AV regions in human hearts obtained from an obese and an old individual using I₂KI, we now show the differential distributions and reconstructions of epicardial fat in the SN and AV regions of the healthy, aged, and obese heart.

1.5. Other structures within the heart

As well as knowing anatomical variations of the CCS in hearts from healthy, aged, and obese individuals, it is equally important for us to further our anatomical understanding of other structures in the heart, such as: the moderator band; papillary and pectinate muscles; major vessels (such as the aorta and pulmonary artery); and the coronary arteries. This is because the dysfunction of any of these structures has been

linked to their morphological changes, and can affect cardiac function [30–33].

We consider here that the techniques and data present in this study will advance our overall understanding of how the whole cardiac and CCS morphology is modified in heart disease and with ageing. Such finding should also contribute to improving current mathematical models of cardiac arrhythmias.

It should be noted that all heart specimens used in this study are from adult humans. The heart from a healthy/normal adult is referred to as 'normal'; the heart obtained from the obese adult is referred to as 'obese'; and the heart obtained from the aged adult is referred to as 'aged'.

2. Aims

We aimed to use I₂KI-enhanced micro-CT to visualise and compare the whole normal, aged and obese hearts and components of the CCS within each specimen. We also aimed to use GO-enhanced micro-CT to visualise and compare epicardial fat within the tissue blocks from these normal, aged and obese hearts.

3. Materials and methods

3.1. Human sample details and ethical approval

A total of five *ex vivo* human hearts were used in this study. The patients' age range was 19–97. Further specimen information, including cause of death, and source is provided in Table 1. Some of the hearts were initially scanned whole and then dissected into smaller tissue blocks (Table 1). Each specimen was formalin-fixed prior to scanning. Specimen 1 was obtained from The Visible Heart® Laboratories, Minnesota, USA, under local ethical rules: this specimen was from an organ donor and their heart was deemed not viable for transplantation (via LifeSource, Minneapolis, MN) and was immediately perfusion-fixed.

Specimens 2 and 3 were purchased from Science Care, USA and had been frozen prior to fixation. Specimens 4 and 5 were obtained from Australia and Romania, respectively, under local ethical rules. Some specimens from Australia were obtained from organ donors whose hearts were unsuitable for transplantation and the specimens from Romania were obtained from autopsies.

Each specimen was fixed in 4% buffered para-formaldehyde prior to micro-CT scanning. After fixation, specimens were stored at room temperature in the Dobrzynski laboratory, in accordance with the UK Human Tissue Act (2004).

Table 1

Specimen information. CT = computed tomography; F = female; M = male; X = information not provided.

Specimen no.	Specimen type	Age	Gender	BMI	Cause of death	Micro-CT voxel number (μM ³)	Source
1	Whole heart, Purkinje fibres block	54	F	×	Cerebrovascular	<ul style="list-style-type: none"> ●Whole heart: 73 ●Purkinje fibres block: 26.7 	The Visible Heart® Laboratories
2	Whole heart, sinus node block, atrioventricular node block, Purkinje fibres block	56	M	43.9	Pyelonephritis (kidney disease)	<ul style="list-style-type: none"> ●Whole heart: 88 ●Sinus node block: 24.6 ●Atrioventricular node block: 25.9 ●Purkinje fibres block: 36.6 	Science Care, USA
3	Whole heart, sinus node block, atrioventricular node block, Purkinje fibres block	97	F	15.4	Vascular dementia, atherosclerotic vascular disease	<ul style="list-style-type: none"> ●Whole heart: 63 ●Sinus node block: 21.6 ●Atrioventricular node block: 17.9 ● Purkinje fibres block: 29.1 	Science Care, USA
4	Sinus node block	32	F	×	Brain injury/haemorrhage	24.3	The Prince Charles hospital, Australia
5	Atrioventricular node block	19	M	×	Suicide	29.4	National Institute of Legal Medicine, Romania

3.2. Whole heart tissue preparation

Before micro-CT scanning, whole hearts were immersed in 7.5% aqueous I₂KI or GO (0.5 mg/mL H₂O) contrast agent solution at room temperature for 14 days [34,24]. The contrast agent solution was changed on day 7. The heart chambers/cavities were filled with warm agarose solution that becomes gel-like at room temperature or with cling film to prevent the hearts' cavities and major vessels from collapsing.

3.3. Preparation of tissue blocks containing the sinus node, atrioventricular conduction axis and Purkinje fibres for micro-computed tomography

Tissue blocks containing the aged SN, AV conduction axis and Purkinje fibres and the tissue blocks containing the obese/diseased SN, AV conduction axis and Purkinje fibres were dissected from the whole aged heart (Specimen 3, Table 1) and the whole obese heart (Specimen 2, Table 1), respectively. The orange, blue and green boxes in Fig. 5 indicate where the tissue blocks were dissected from. The tissue blocks containing the anatomically normal SN and AV conduction axis were obtained separately from Australia and Romania, respectively (Table 1).

Before micro-CT scanning, the tissue blocks were immersed in 7.5% aqueous I₂KI or GO contrast agent solution at room temperature for 7 days.

3.4. Micro-computed tomography

As previously described, the samples were scanned using the Nikon Metris XTEK XT H 320/225 V High Flux systems at the Henry Moseley Manchester X-ray Imaging Facility, University of Manchester [8,24]. Excess fixative and contrast agent were removed from the samples using distilled water before using a plastic container to hold the specimens to prevent movement during scanning. X-ray energies ranging from 85 to 160 kV were used for the scans. For all the scans, a tungsten target was used with a 1 mm and 0.25 mm aluminium or copper filter (sometimes no filter was used) for the whole hearts and the tissue blocks, respectively.

Total scan times ranged 1 h–4 h, approximately. The acquired data from the scans were reconstructed as previously described [8], with voxel sizes ranging between 63 × 63 × 63 μm³–88 × 88 × 88 μm³ for the whole heart data and between 24 × 24 × 24 μm³–36 × 36 × 36 μm³ for the tissue block data.

3.5. 3-Dimensional anatomical reconstruction

ImageJ 1.45i (<http://rsbweb.nih.gov/ij/>) was used to crop datasets to the area of interest or to remove external blank pixels. 3D anatomical reconstructions of specific regions of interest were created using Amira v6.5 (Thermo Fisher). The segmentation and volume rendering tools available on Amira v6.5 (Thermo Fisher) were used, as previously described [24,34,35].

3.6. Segmentation of specific regions of interest in whole hearts

The differences in the x-ray attenuation of various parts of the hearts lead to them having different detector pixel and voxel intensity values. Based on these differences, the ‘lasso’ tool in Amira v6.5 was used to draw around epicardial fat and the regions containing the CCS; to isolate them from the surrounding tissue. The segmentations of the atria, ventricles, vessels, and valves were carried out based on anatomical position and landmarks in the x, y, and z planes – to isolate them from the surrounding tissue. Segmentations using the lasso tool were carried out manually on approximately every 10 orthogonal (‘ortho’) slices then automatic segmentations were performed to fill in the gaps.

3.7. Segmentation of specific regions of interest in tissue blocks

At the resolution at which the whole hearts were scanned, it was difficult to visualise and segment the conduction tissues. Hence, to increase the resolutions and visibilities, tissue blocks containing the conduction systems were dissected from whole hearts then re-scanned. Following this, segmentations of the regions containing the SN, AV conduction axis and Purkinje fibres were performed based on the x-ray attenuation difference between them and the surrounding myocardium, as described above.

3.8. Preparation of tissue blocks containing the sinus node, atrioventricular conduction axis and Purkinje fibres for cryosectioning and histology

The I₂KI or GO contrast agent solutions were washed from the tissue blocks by immersing the tissue blocks in tap water for 7 days. Then the tissue blocks were snap frozen using cooled isopentane, which had been stored at –80 °C, then wrapped in freezer bags. The frozen SN and AV samples were sectioned at a temperature ranging between –10 and –20 °C using a cryostat at 20–35 µm thickness. Slides were placed in an oven, at 48 °C, for 4 h before fixing in 100% Bouin’s fluid overnight. To distinguish between cardiomyocytes, connective tissue and fat, Masson’s trichrome staining was performed, as previously described [8]. After rinsing in distilled water (5 min), sections were dehydrated through 70%, 90%, and then 100% ethanol. Sections were then immersed in histoclear (Scientific Laboratories Supplies) before mounting with DPX medium (Sigma Aldrich) and covered with glass coverslips. To image the stained sections, a light microscope (Zeiss LSM5) and Axiocam camera (Zeiss) were used. CaseViewer software was used to analyse the obtained images. With this histological stain, myocytes were stained purple and connective tissue green/blue.

4. Results

4.1. The obtained obese heart specimen was remarkably larger than the normal or aged hearts

After scanning the normal, aged, and obese whole hearts using micro-CT, the 2D ortho slices obtained from the scans were uploaded into Amira v6.5 software. This software was then used to create 3D volume rendering (reconstructions) of the whole hearts (Fig. 1). The obese heart was significantly larger than the normal and aged hearts (Fig. 1). In particular, the left ventricle of the obese heart was a huge mass – even leading to the left atrium being displaced (Fig. 1A). This hypertrophy was not limited to just the left ventricle of the obese heart, it was also observed in the right atrium and right ventricle (Fig. 1). On the

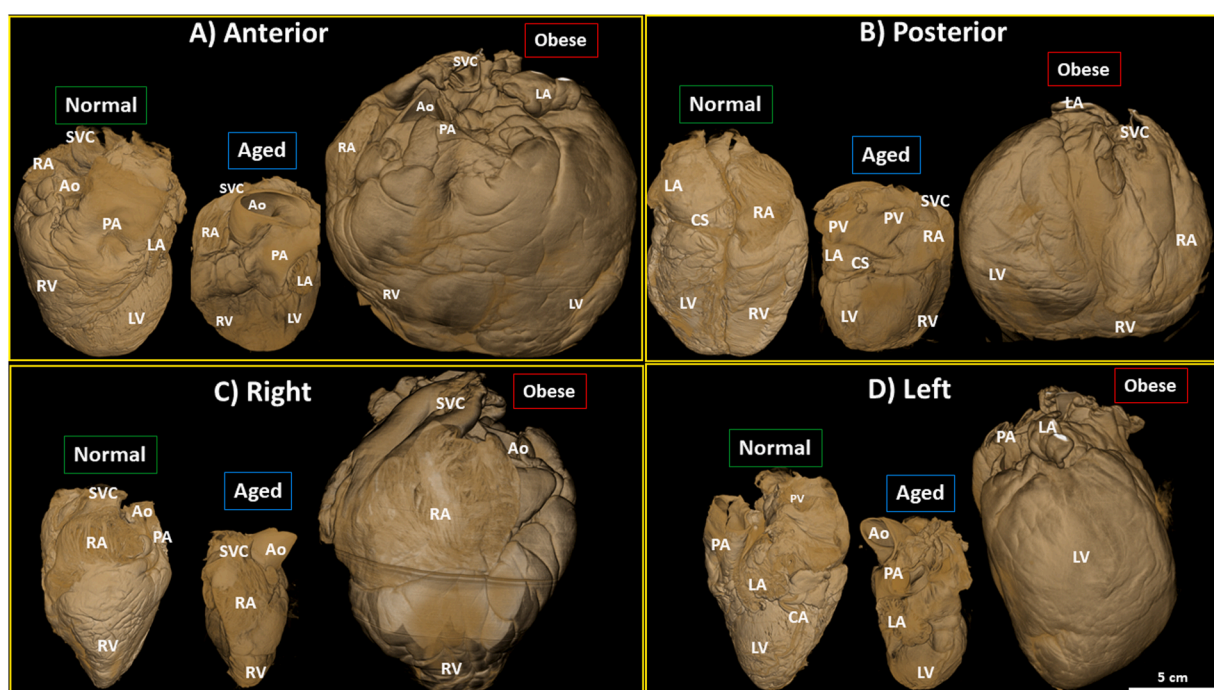


Fig. 1. High resolution volume rendering of the normal, aged and obese hearts. A, anterior view. B, posterior view. C, right view. D, left view. Ao = aorta; CA = coronary artery; CS = coronary sinus; LA = left atrium; LV = left ventricle; PA = pulmonary artery; PV = pulmonary vein; RA = right atrium; RV = right ventricle; SVC = superior vena cava.

other hand, the ventricles of aged heart appeared to be smaller than the normal or obese hearts but the aged right atrium was larger than that of the normal heart (Fig. 1).

4.2. The aortic and pulmonary trunk roots were anatomically intact in the normal and aged hearts, compared to the obese heart

After creating the 3D volume rendering of the whole hearts, the ventricles, and atria (excluding the cavities) and the aortic and pulmonary trunk roots were sub-segmented/separated (Fig. 2). These vessels and their valves appeared as would be expected in the normal and aged hearts, but in the obese hearts, their structure appeared to be distended/enlarged (Fig. 3A and B). The left coronary cusp (LCC), right coronary cusp (RCC) and non-coronary cusp (NCC) of the aortic valve in the normal and aged hearts were clearly visible, but not in the obese heart (Fig. 3B). In the pulmonary trunk root, the left cusp (LC) was visible in the normal and aged hearts were visible, but not in the obese heart (Fig. 3B).

4.3. Coronary artery anatomies were anatomically different in the aged and obese hearts, compared to the normal heart

The major coronary arteries such as: right coronary artery (RCA); right marginal artery (RMA); left coronary artery (LCA); posterior descending artery (PDA); left circumflex artery (LCx); and the left anterior descending artery (LADA) were segmented from the normal, aged and obese hearts: stemming from the aortic root (Fig. 4). These coronary arteries were clearly visible in all three hearts but there were some obvious anatomical differences. In the normal heart, the various bifurcations of the coronary arteries were present (Fig. 4), but there appeared to be fewer bifurcations in the aged heart (Fig. 4) and even more reductions in the obese heart (Fig. 4). In the aged heart, not only was the number of coronary artery bifurcations fewer, but the arteries appear to be thicker than the normal heart's coronary arteries (Fig. 4). The coronary arteries in the obese heart were even thicker than the normal and aged coronary arteries (Fig. 4). The lumen size of the RCA in the obese heart appeared larger than those in the aged heart and normal

heart (Fig. 5, 6Cii).

4.4. There existed more epicardial fat surrounding the obese heart, compared to the normal and aged hearts

From the 3D volume reconstructions, a vast amount of epicardial fat was found to be present in and around the obese heart (Figs. 5C, 6Ci and 6Cii), compared to the normal heart (Figs. 5A, 6Ai and 6Aii) and aged heart (Figs. 5B, 6Bi and 6Bii). Following the analysis of the external structures of the whole hearts, the internal structures were analysed.

4.5. The internal structures of the atria varies between the normal, aged and obese hearts

From the volume renderings of the whole hearts, the atrial cavities in the obese heart (Fig. 6Ci) were much larger than the normal and aged hearts. From the right atrial appendage to the left atrial appendage, the width of the obese atria is approximately 13 cm, 9 cm for the aged atria and 7.5 cm for the normal atria (Fig. 6). In the right atrium of the normal heart, the pectinate muscles were organised and thin (Fig. 6Ai), but in the aged heart, they were less organised (Fig. 6Bi) and even more disorganised and much thicker in the obese heart (Fig. 6Ci).

The crista terminalis of the aged heart was thinner than the normal heart's (Figs. 6Ai and 7A) and the crista terminalis of the obese heart (Figs. 6Aiii, 7Aiii) was much thicker than the normal heart's.

When looking at the internal structures of the atria - particularly the left atria - of the obese heart, it was interesting to see that the left ventricular wall is so hypertrophied that it extends up into the region of the left atrium (Fig. 6Ci).

4.6. The internal structures of the ventricles differ in the normal, aged and obese hearts

The ventricular wall and cavity of the aged heart (Fig. 6Bii) were smaller than the ventricles of the normal heart and the ventricular wall and cavity of the obese heart (Fig. 6Cii) were larger than the normal heart's. From the right ventricle (including epicardial fat) to the left

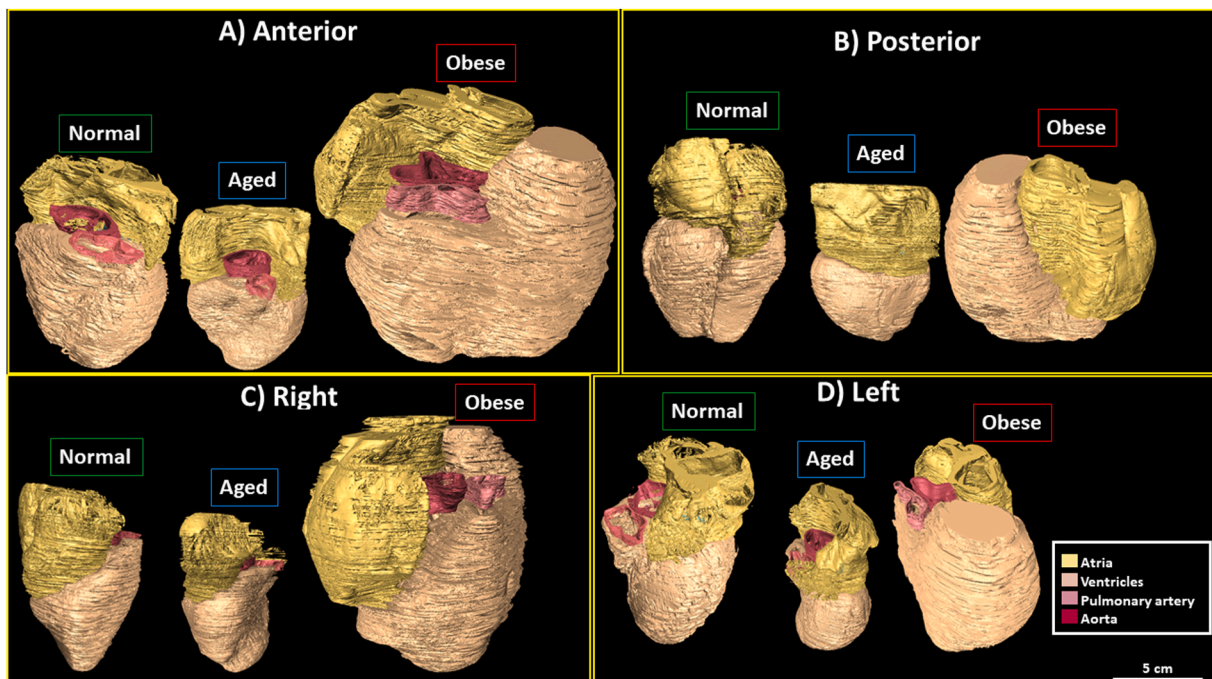


Fig. 2. Segmentation of the chambers, aortic root and pulmonary artery root from the normal, aged and obese hearts. A, anterior view. B, posterior view. C, right view. D left view.

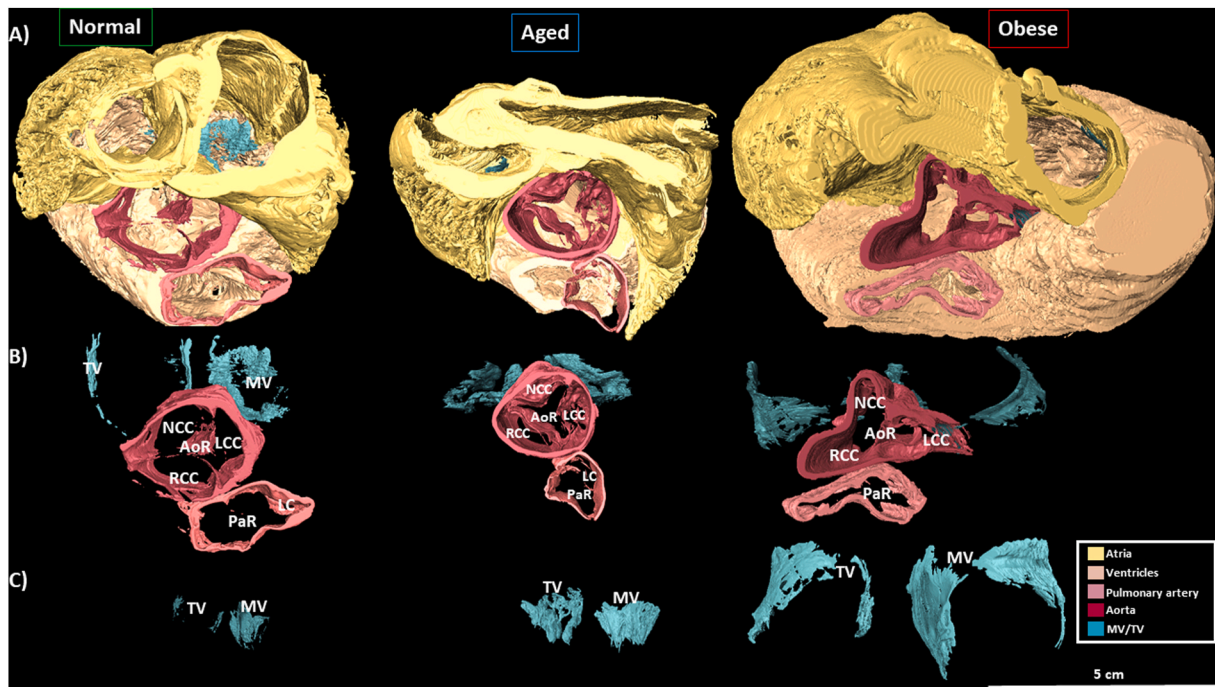


Fig. 3. Short and/or long axis view showing the segmented atria, ventricles, aortic root, pulmonary artery root and valves from the normal, aged and obese heart. A, short axis view of the atria, ventricles and valves. B, short axis view of the valves. C, long axis view of the TV and MV. AoR = aortic root; LC = left cusps; LCC = left coronary cusps; MV = mitral valve; NCC = non-coronary cusps; PaR = pulmonary artery root; RCC = right coronary cusps; TV = tricuspid valve.

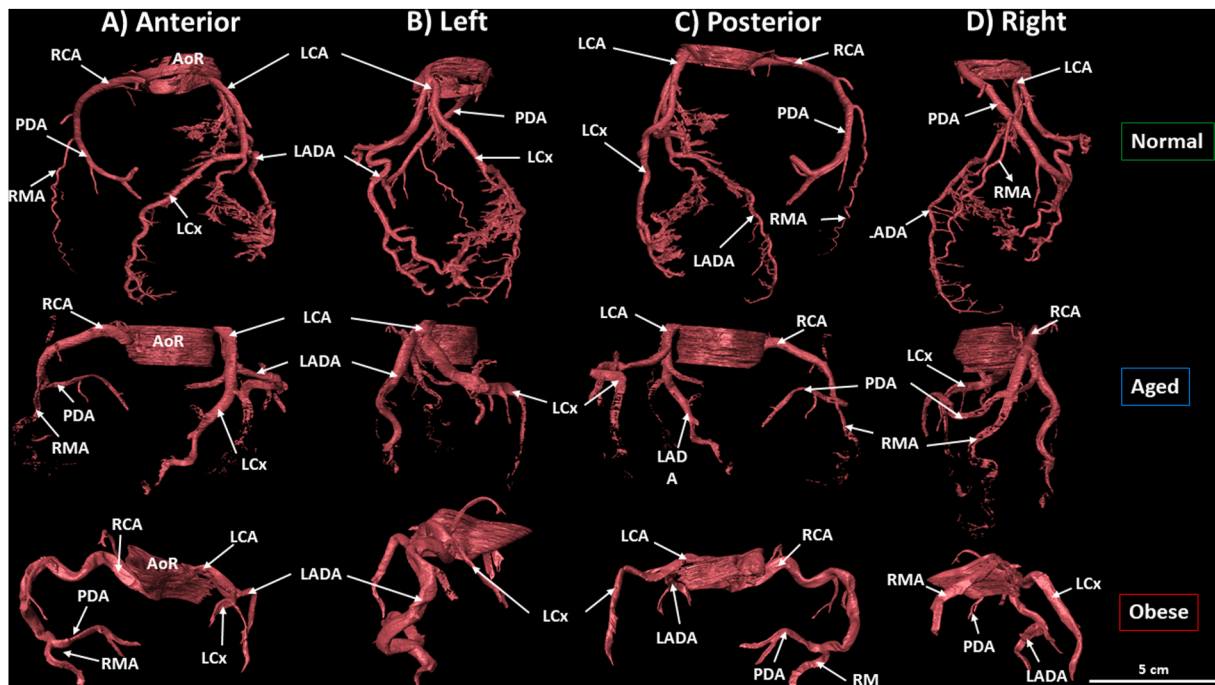


Fig. 4. Segmentation of the coronary artery network from the normal, aged and obese heart. A, anterior view. B left view. C, posterior view. D, right view. AoR = aortic root; LADA = left anterior descending artery; LCA = left coronary artery; LCx = left circumflex artery; PDA = posterior descending artery; RCA = right coronary artery RMA = right marginal artery.

ventricle (including epicardial fat), the width of the obese ventricles was approximately 15 cm, compared to 8 cm for the aged atria and 9 cm for the normal atria (Fig. 6).

Compared to the normal heart, the ventricular septum and ventricular wall (excluding fat) is thicker in the aged and obese hearts, respectively (Figs. 6Aii, Bii, Cii). In the ventricles of the normal heart,

the papillary muscles (particularly the septal, anterior, and posterior papillary muscles) appear as expected (i.e. regular) (Fig. 6Aii), compared to the papillary muscles of the aged (Fig. 6Bii) and obese hearts (Fig. 6Cii). In the obese heart, the number of papillary muscles was drastically lower, compared to the normal and aged papillary muscles. Also, the ventricular cavities of the obese heart appear to lack

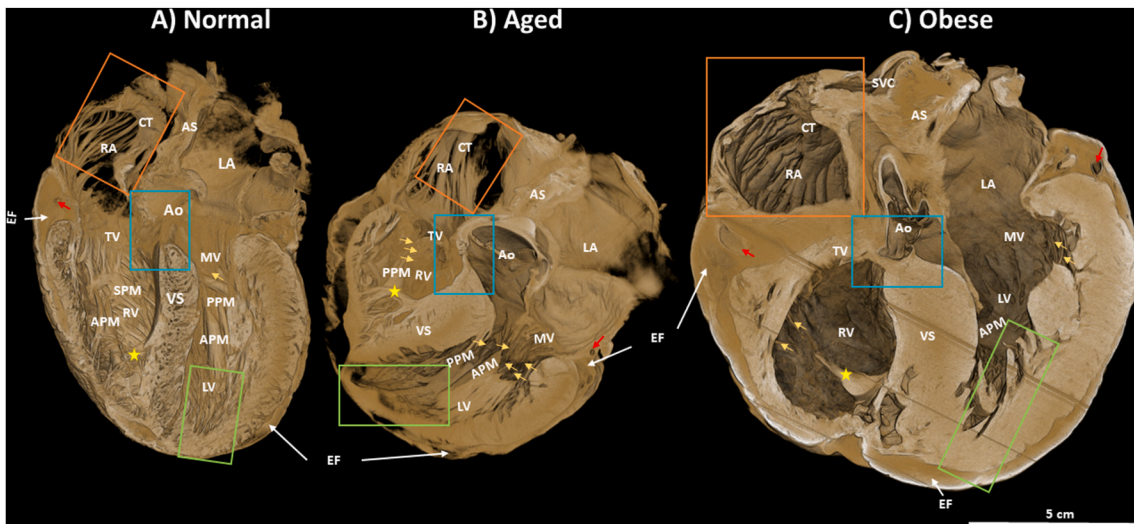


Fig. 5. Long axis four chamber view of the internal structures of the normal, aged and obese hearts. A, normal heart. B, aged heart. C, obese heart. The orange boxes show where the right atrium blocks were dissected for histology of the sinus node. The blue boxes show where the atrial and ventricular septa blocks were dissected for histology of the atrioventricular block segmentations. The green boxes show where the left ventricular apex blocks were segmented for the Purkinje fibres segmentation. The red arrows indicate the coronary arteries. The yellow arrows indicate the chordae tendinae. The yellow stars indicate the moderator band. APM = anterior papillary muscle; Ao = aorta; AS = atrial septum; CT = crista terminalis; EF = epicardial fat; LA = left atrium; LV = left ventricle; MV = mitral valve; PPM = posterior papillary muscle; RA = right atrium; RV = right ventricle; SVC = superior vena cava; VS = ventricular septum. (For interpretation of the references to colour in this figure legend, the reader is referred to the Web version of this article.)

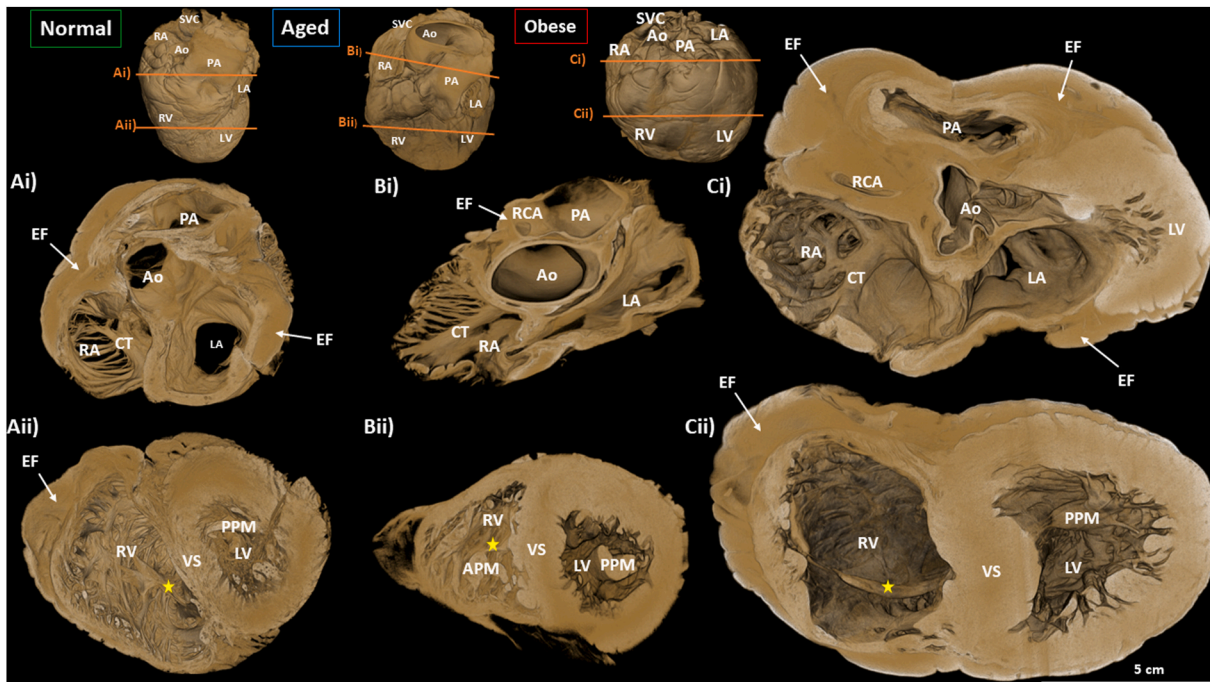


Fig. 6. Short axis views of the internal structures of the normal, aged and obese hearts. A, normal heart. B, aged heart. C, obese heart. Ai, Bi, Ci base view looking into the atrial chambers. Aii, Bii, Cii apex view looking into the ventricular chambers. The view point locations in A, B, C is indicated by the orange lines in the volume rendering in the top panels. The yellow stars indicate the moderator band. APM = anterior papillary muscle; Ao = aorta; CT = crista terminalis; EF = epicardial fat; LA = left atrium; LV = left ventricle; PPM = posterior papillary muscle; RA = right atrium; RV = right ventricle; VS = ventricular septum. (For interpretation of the references to colour in this figure legend, the reader is referred to the Web version of this article.)

some papillary muscles compared to the normal and aged ventricular cavities. Yet, it should be noted that large variabilities in these structures from human heart to human heart have been observed [36].

A moderator band was visible in the right ventricles of each the normal, aged and obese hearts (Figs. 6Aii, Bii, Cii). This band increased in thickness across the normal, aged and obese hearts, respectively. The moderator band appeared to be a wide flat column in the normal heart

(Fig. 6Aii), short and thin in the aged heart (Fig. 6Bii) and, long and thick in the obese heart (Fig. 6Cii).

4.7. The attenuation difference region in the right atrium was extensive in the aged and obese hearts

Tissue blocks containing the right atrium from whole heart

specimens (see orange boxes in Fig. 5) were scanned using micro-CT, after staining with I₂KI contrast medium.

The region of attenuation difference was segmented in orange within the normal, aged and obese right atrium tissue blocks in Fig. 7. The location of the attenuation difference runs along the crista terminalis – the location where the SN would be expected to be. Within this region of attenuation difference lies the SN artery, the SN (Fig. 8) – these structures were confirmed through Masson's trichrome staining of sections from the normal tissue block (Fig. 8D). In the tissue block from the obese heart, the lumen of the sinus node artery was wider (Figs. 8C and 11A). It was found that within the aged and obese tissue blocks, the region of attenuation difference was more extensive, compared to the normal tissue block – with the aged tissue block having the most extensive region of attenuation difference (Fig. 7).

4.8. Graphene oxide contrast agent elicited there was more epicardial fat in the obese right atrium tissue block

After scanning the I₂KI-stained tissue blocks using micro-CT, the contrast medium was washed off before staining the blocks with GO and rescanning. The data obtained revealed epicardial fat within and surrounding the tissue blocks. This was then segmented from the whole block.

It was found that there was more epicardial fat in the obese right atrium tissue block, compared to the normal block (Fig. 7). Looking internally (Fig. 9), there was fat within both the normal and obese tissue blocks but again, there was more fat in the obese tissue block, especially surrounding the region of attenuation difference (Fig. 9B) and surrounding the sinus node artery.

4.9. There are differences in the AV junctional region of the normal, aged and obese heart

Tissue blocks from the AV junctional region (see blue box, Fig. 5) were scanned using micro-CT, after staining with I₂KI contrast medium. Following this, 2D ortho slices were obtained using Amira 6.5 software.

In the AV conduction axis tissue block from the normal heart, it was

possible to identify the AV conduction axis: consisting of the inferior nodal extension (INE), (Fig. 10Bi); compact node (CN) (Fig. 10Bii); penetrating bundle (PB) (Fig. 10Biii) and His bundle (HB) (Fig. 10Biv). However, in the aged and obese AV tissue blocks, the attenuation difference was not very obvious and only the His bundle was visible (data not shown).

4.10. Histology confirms micro-CT observations

Following micro-CT scans, the SN and AV tissue blocks were frozen at –80 °C before cryosectioning. The SN and AV conduction axis blocks from the aged and obese hearts were not easy to be sectioned due to large amount of fibrotic and fat tissue. Therefore only comparable regions of the main part of the SN (the body) and the CN of the AV junction were stained using Masson's trichrome staining.

There were large amounts of epicardial fat surrounding the SN artery on both endocardial and epicardial sides of the obese right atrium tissue block (Fig. 11A). Compared to the normal SN tissue section (Fig. 11Ai), it appeared that in the obese SN tissue sections, the nodal cells were to some degree replaced by fat (Figs. 11A and Aii). As observed in the coronary arteries of the obese whole heart (Fig. 4), the lumen of SN artery in the obese right atrium tissue block was wider (Fig. 11A) than that of the normal SN artery (Fig. 8D).

There was more connective tissue (more blue/green stain) in the aged SN (Fig. 12Aii), compared to the normal/young SN (Fig. 12Ai) and less myocytes (less purple stain). This suggests that in the aged SN, there was increased fibrosis and loss of nodal cells (Fig. 12Aii).

Similar differences were observed in the obese and aged AV tissue blocks, compared to the normal AV tissue block. In the histology section of the obese AV block, there was fat surrounding the CN (Figs. 11B and 11Biii), compared to the normal AV section (Fig. 10Bii, 11Bii). There also appeared to be increased connective tissue (i.e. fibrosis) and loss of CN myocytes in the obese AV section (Fig. 11Biii).

4.11. There are fewer Purkinje fibres observed in the obese and aged apex

Tissue blocks from the LV apex (see green box, Fig. 5) were scanned

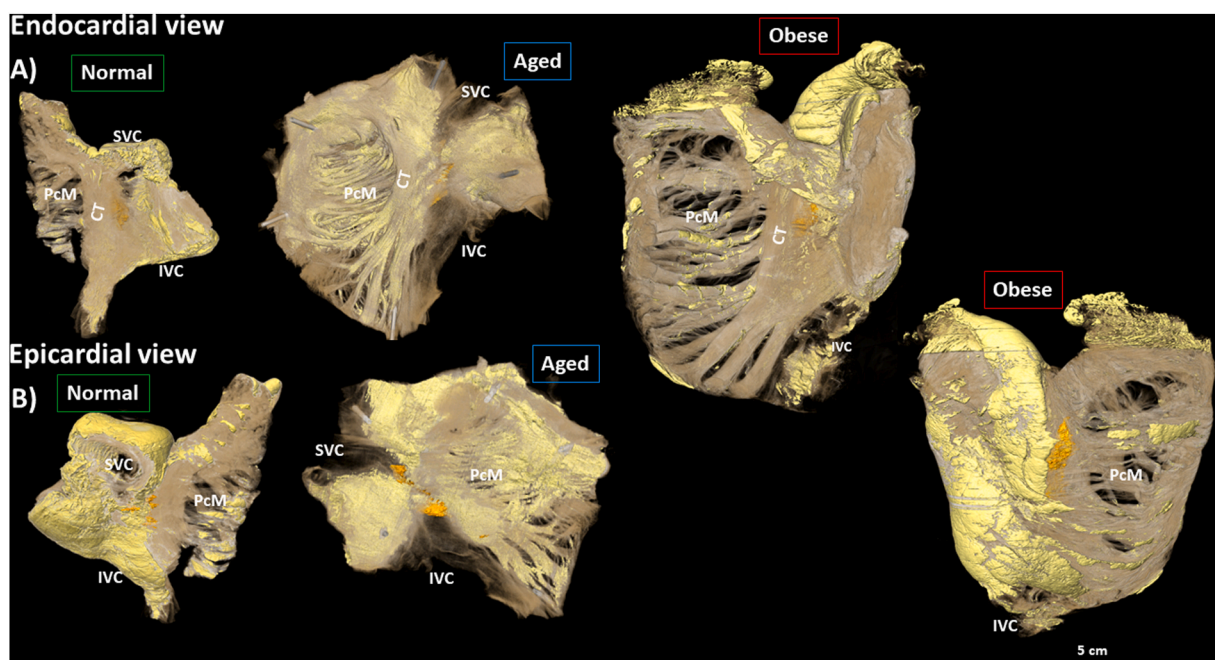


Fig. 7. Segmentation of fat (yellow) and the low attenuation (orange) difference regions in the normal, aged and obese right atrium blocks. Within the orange region is the location of the sinus node. A, endocardial view. B, epicardial view. CT = crista terminalis; IVC = inferior vena cava; PcM = pectinate muscle; SVC = superior vena cava. (For interpretation of the references to colour in this figure legend, the reader is referred to the Web version of this article.)

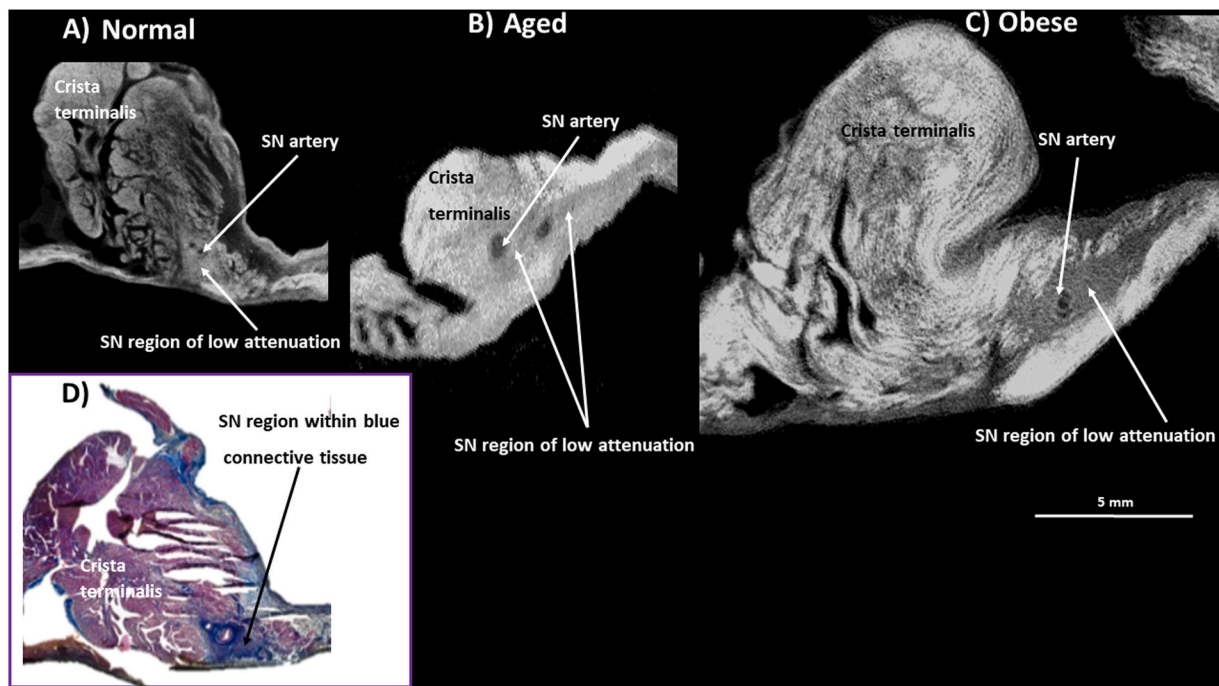


Fig. 8. Visualisation of the human sinus node within the low attenuation regions in the normal, aged and obese right atrium. A, B, C, micro-CT section of the sinus node from the normal (A), aged (B) and obese (C) right atrium with. D, matching histological section for A. SN = sinus node.

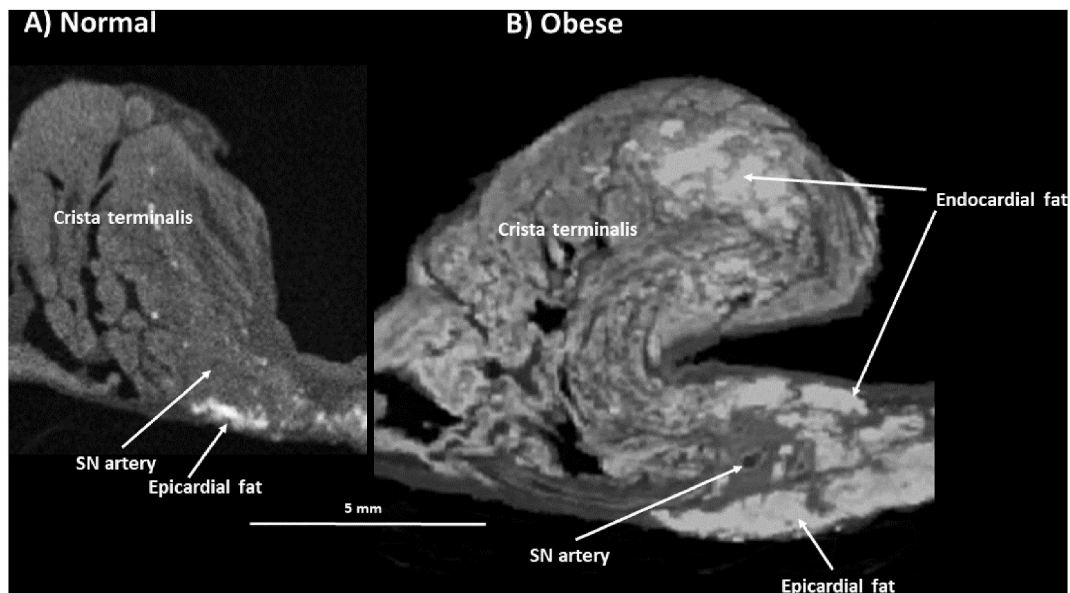


Fig. 9. Visualisation of epicardial fat surrounding the normal and obese sinus node. A, micro-CT section from the normal sinus node. B, micro-CT section from the obese sinus node. SN = sinus node.

using micro-CT, after staining with I_2KI contrast medium. Following this, 2D ortho slices were obtained then converted to 3D volume renderings using Amira 6.5 software.

Purkinje fibres in the normal, aged, and obese apex tissue blocks were segmented (Fig. 13). The network of Purkinje fibres in the aged (Fig. 13B) and obese apex blocks (Fig. 13C) were less dense, compared to the network of fibres in the normal apex block (Fig. 13A). The myocardium and papillary muscles in the obese apex tissue block were thicker (Fig. 13Cii) than the normal apex block (Fig. 13Aii). The papillary muscle in the aged apex tissue block (Fig. 13Bii) appear to be thicker than the normal apex block (Fig. 13Aii) but the myocardial wall

of the aged apex (Fig. 13Bii) was thinner than that of the normal apex block (Fig. 13Aii).

Table 2 is a summary of micro-CT datasets described in sections 4.1 - 4.9 and 4.11.

5. Discussion

In this study, we show that iodine potassium-iodide (I_2KI) and graphene oxide (GO) contrast-enhanced micro-CT is a non-destructive methodology that can be used to produce high-resolution 3D reconstructions of fixed human hearts. This has provided insights into

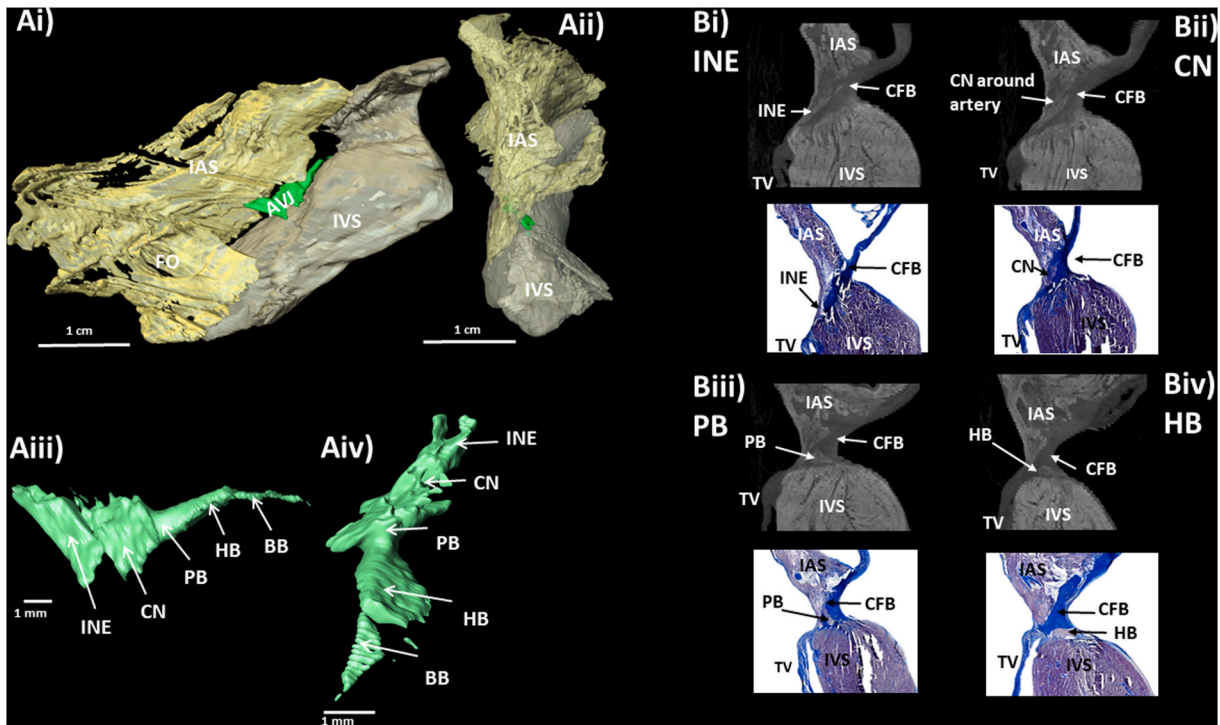


Fig. 10. Visualisation of atrioventricular junction in the normal heart atrioventricular septal region. A, segmentation on the interatrial septum (yellow), atrioventricular junction (green) and interventricular septum (grey). Ai, Aiii, side view, Aii, Aiv, anterior view. B, micro-CT sections from different low attenuation regions of the atrioventricular junction and matching histology sections. AVJ = atrioventricular junction; BB = bundle branch; CFB = central fibrous body; CN = compact node; FO = fossa ovalis; HB = His bundle; IAS = interatrial septum; INE = inferior nodal extension; IVS = interventricular septum; PB = penetrating bundle; TV = tricuspid valve. (For interpretation of the references to colour in this figure legend, the reader is referred to the Web version of this article.)

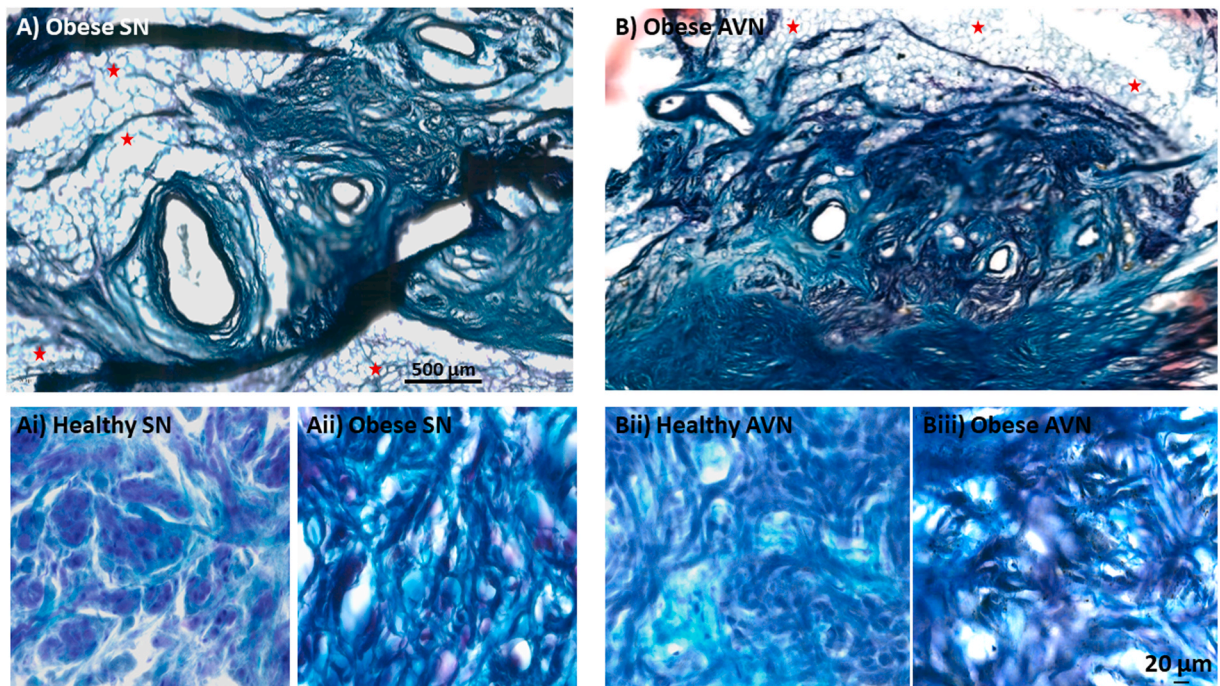


Fig. 11. Replacement of nodal cells by fat within the obese human sinus node and atrioventricular node. A, B, Masson's trichrome stained section through the obese sinus node and atrioventricular node. Ai, Aii, closer view of normal/healthy and obese sinus node. Bi and Bii, closer view of the normal and obese atrioventricular node. Myocytes are stained purple, connective tissue is stained blue and the red stars indicate fat. AVN = atrioventricular node; SN = sinus node. (For interpretation of the references to colour in this figure legend, the reader is referred to the Web version of this article.)

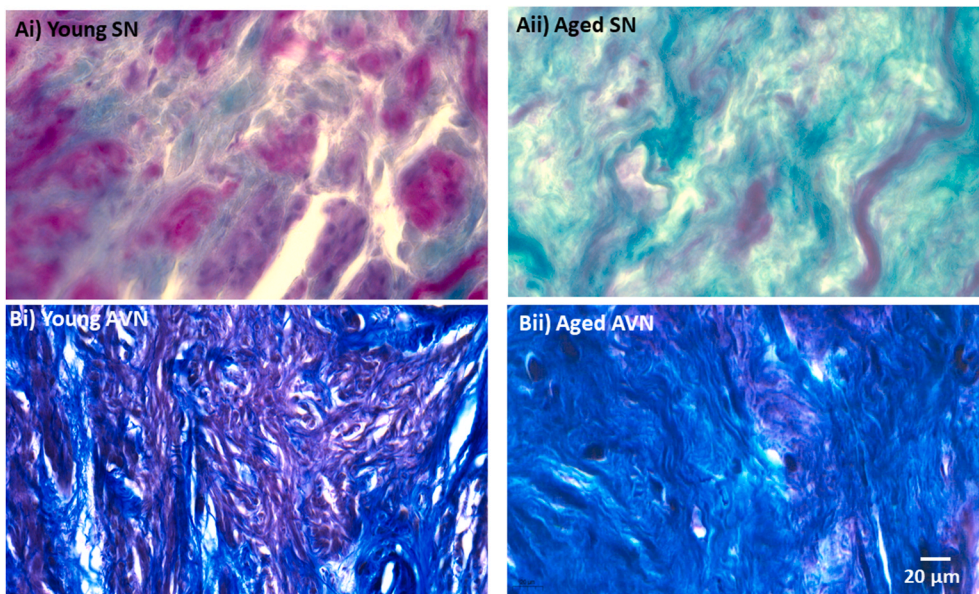


Fig. 12. Fibrosis within the aged human sinus node and atrioventricular node. A,B, Masson's trichrome stained section through the young sinus node (Ai), aged sinus node (Aii), young atrioventricular node (Bi), and aged atrioventricular node (Bii). Myocytes are stained purple, connective tissue is stained green/blue. There is more green/blue signal compared to purple in the aged tissues (Aii and Bii). AVN = atrioventricular node; SN = sinus node. (For interpretation of the references to colour in this figure legend, the reader is referred to the Web version of this article.)

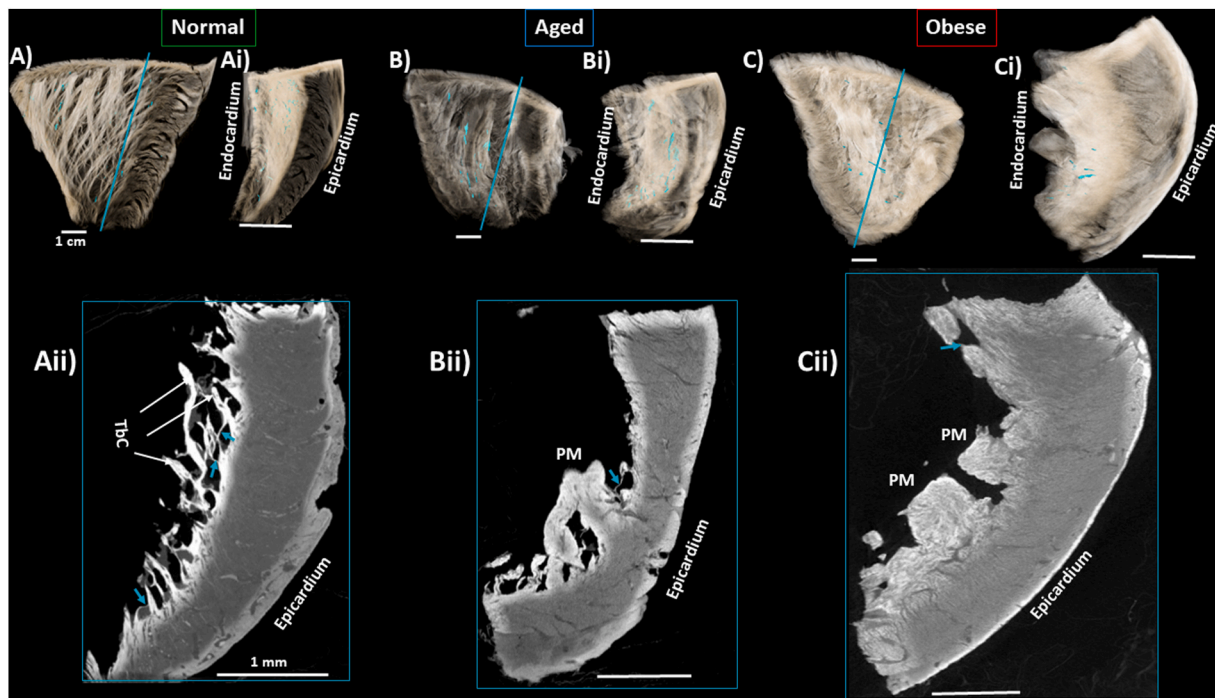


Fig. 13. Segmentation of Purkinje fibres in the normal, aged and obese apex blocks. Purkinje fibres (blue) are segmented and overlaid onto the 3D volume rendering of the apex tissue blocks (A, B, C endocardial views and Ai, Bi, Ci side views). Aii, Bii, Cii, side views of micro-CT sections of the Purkinje fibres. The location of the sections in Aii, Bii and Cii is indicated by the blue lines in the volume rendering in A, B, C. The arrows in Aii, Bii, Cii indicate Purkinje fibres. PM = papillary muscle; TbC = trabeculae carneae. (For interpretation of the references to colour in this figure legend, the reader is referred to the Web version of this article.)

anatomical differences between the normal, aged and obese hearts and can aid in creating mathematical models of these ageing and disease processes. Further, such models can be used to create simulations of arrhythmias, heart failure and other cardiovascular diseases.

The presented data confirms the findings of our previous studies [37–40]. Importantly, the present study is the first to our knowledge to use micro-CT to show 3D reconstructions of the whole normal, aged and obese hearts and the first to show the attenuation difference region that contains the SN in the aged and obese right atrium. Uniquely, the present study provided the 3D reconstructions within the normal, aged and

obese hearts of: 1) the moderator band; 2) the presence or absence of epicardial fat surrounding the right atrium and the SN region; and 3) the coronary artery network.

We observed that the regions of attenuation difference containing the SN in the aged and obese heart were more extensive than in the normal heart – perhaps as a result of extensive fibrosis/fat within these regions within obese and aged hearts, supporting findings in a previous study [41].

Table 2

Summary of normal, aged, and obese specimen information and major differences observed. F = female; M = male.

Specimen no.	Age	Specimen type	Tissue block dissected	Health status	Gender	Segmented structures	Major differences observed (aged vs. normal; obese vs. normal)
1	54	Whole heart	Left ventricular apex	Healthy/normal	F	Figs. 1–3: Atria, ventricles, pulmonary artery, aorta, mitral valve, tricuspid valve Fig. 4: Coronary arteries Fig. 13: Purkinje fibres	x
2	32	Sinus node block	x	Healthy/normal	M	Figs. 7–9: Sinus node region, epicardial fat Fig. 10: Atrioventricular node	x
3	19	Atrioventricular node block	x	Healthy/normal			x
3	97	Whole heart	•Sinus node block •Atrioventricular block •Left ventricular apex	Aged	F	Figs. 1–3: Atria, ventricles, pulmonary artery, aorta, mitral valve, tricuspid valve Fig. 4: Coronary arteries Figs. 7 and 8: Sinus node region, epicardial fat Fig. 13: Purkinje fibres	•Larger right atrium; smaller ventricles •Thicker coronary arteries and less bifurcations •More extensive region of attenuation difference (sinus node region); more connective tissue; fewer cardiomyocytes •Fewer Purkinje fibres
4	56	Whole heart	•Sinus node block •Atrioventricular block •Left ventricular apex	Obese	M	Figs. 1–3: Atria, ventricles, pulmonary artery, aorta, mitral valve, tricuspid valve Fig. 4: Coronary arteries Figs. 7 and 8: Sinus node region, epicardial fat Fig. 13: Purkinje fibres	•Larger chambers; thicker walls; thicker moderator band •Thicker coronary arteries and more bifurcations •More extensive region of attenuation difference (sinus node region); more connective tissue; fewer cardiomyocytes • More fatty tissue •Fewer Purkinje fibres

5.1. The abnormal size of the obese heart's wall and cavities – functional associations

We investigated the myocardial anatomy of the normal, aged and obese hearts to identify anatomical differences that could contribute to the development of cardiovascular diseases.

Obesity is known to be a risk factor for heart failure and it has been shown that a BMI rise of 1 kg/m² increases the risk of heart failure by 5% in men and 7% in women [42]. Volume stress associated with obesity results in anatomical and functional remodelling of the heart – leading to atrial fibrillation [43], cardiomyopathy, fibrosis, diastolic and systolic dysfunction and increased epicardial fat [44].

There are three different types of cardiomyopathy – dilated cardiomyopathy, hypertrophic cardiomyopathy, and restrictive cardiomyopathy. Dilated cardiomyopathy causes dilated and weakened ventricles; hypertrophic cardiomyopathy is an enlargement and thickening of the heart's muscles; and restrictive cardiomyopathy describes stiff and rigid ventricles that are not thickened [45]. The obese heart used in this project (specimen 2, Table 1) was diseased because it had hypertrophic cardiomyopathy, based on its thickened ventricular walls and large cavities (Figs. 1, 2 and 5C, 6Ci, 6Cii).

Using echocardiogram [46], cardiac magnetic resonance [47,48] and computed tomography (CT) [49], research groups have analysed the ventricular wall. However, the images obtained through these methods are of low resolution (1–2 mm), when compared to micro-CT (0.5–1 µM). In this study, we have utilised micro-CT to analyse the tissues at higher resolutions.

Our observations of increased cavity sizes and wall thicknesses in the obese heart (Figs. 1, 2 and 5C, 6Ci, 6Cii) confirms previous descriptions of the fact that obesity commonly causes myocardial hypertrophy – especially left ventricular hypertrophy [37–39]. Our study approach expands on previous works by exploring the 3D volume rendering at various anatomical planes, at higher resolutions; yet additional hearts need to be studied in the future.

Although it is generally noted that the left atrial wall of the obese heart is thicker than the normal heart [32], the anatomic features of atria walls is an area of the heart that is less explored – when compared to the ventricular walls. In our study, we have included visual analyses of the right and left atria and the atrial septum (Figs. 5 and 6) and found

that the atrial walls of the obese heart were thicker than the normal heart's atrial walls and the atrial cavities of the obese heart were more dilated.

5.2. The reduced size of the aged heart likely had an effect on its functional capabilities

We investigated the myocardial anatomy of the normal, ageing and obese hearts to identify anatomical differences that could be associated with the development of cardiovascular dysfunction.

The United Nations, defines individuals that are 60–65 years or over as 'aged' [50]. The aged heart used in this study was from a 97 year-old female (specimen 3, Table 1). A common cause for hospitalisation in patients over 65 years is cardiomyopathy – which can eventually lead to heart failure [51]. It is known that aged hearts generally have smaller mass and volume, compared to a normal heart, as a result of cellular apoptosis (loss of cardiomyocytes) in the working myocardium [51]. This observation of thinner myocardial walls and smaller cavity sizes in the aged heart was confirmed by our high resolution detailed analyses (Figs. 1, 2 and 5B, 6Bi, 6Bii). These reduced cavity sizes and myocardial wall thicknesses of the aged heart increases the prevalence of heart failure and development of dilated cardiomyopathy.

The reduced size of the atrial cavity of the aged heart could be a result of the reduced atrial muscle contraction that is commonly observed in elderly patients [40].

5.3. Anatomical variations of the moderator band in the normal, aged, and obese hearts

We investigated the anatomies of the moderator bands in the normal, aged and obese hearts. The moderator band contains part of the right bundle branch and is a column of muscle that inferiorly extends from the right side of the interventricular septum and attaches to the anterior papillary muscle in the right ventricle. The moderator band is not always observed in all human hearts as noted in other studies [52–54], however the band was observed in the specimens of normal, aged and obese hearts that were used in our study. They were with varying anatomical structures, but the bands were more prominent in the aged and obese hearts compared to the normal, healthy heart (Figs. 5, 6Aii, Bii, Cii).

Previous studies have observed various shapes of the moderator band [53–57]. Across the three different hearts we used in our study, we also observed different shapes of moderator bands. Currently, the moderator band is now gaining recognition for playing a key role in arrhythmias (specifically Purkinje-mediated arrhythmias) when no structural heart disease is observed [30].

5.4. Variation in epicardial fat distribution in normal, aged, and obese tissue blocks

Commonly located between the myocardium and pericardium is varying degrees of epicardial fat – even in a considered functionally healthy heart, a visceral fat deposit can cover up to 80% of the whole heart [58]. Epicardial fat has various physiological functions such as mechanical protection of the coronary arteries; providing an immune barrier for the myocardium and coronary arteries [59]; and provide space for arterial wall expansion in the development of atherosclerosis.

Increasing amounts of epicardial fat has also been associated with obesity and age. The relationship between epicardial fat and obesity has been studied using echocardiogram [60,61] and CT [62]. It is known that epicardial fat increases with age [63–65] and increases by approximately 22% in people over 65 years old, compared to younger patients [66].

Uniquely here, both around and within the whole hearts and tissue blocks, we investigated the extent of fat deposits and epicardial fat. We now show that graphene oxide is a novel contrast agent for micro-CT scanning that can be used to visualise fat and confirm that fat content increases especially in obesity (Figs. 7 and 9).

5.5. Anatomical variations of the pectinate muscles within the right atrium of the normal, aged and obese hearts

Currently, it is not known if the pectinate muscles in the right atrium have a major role in atria contraction but it is known that they stretch when the atria dilates and they prevent the displacement of valve cusps [67]. Our study is the first to present a 3D reconstruction of the pectinate muscles in the aged and obese hearts (Figs. 5B and C, 6Bi, 6Ci, 7). In the right atrium of the obese heart, the pectinate muscles were thicker and disorientated (Figs. 6Ci, 7), compared to the normal heart. This was considered to be partly the result of an overall larger heart and epicardial fat. Importantly, increased heart/bundle size increases the potential for re-entrant arrhythmia to develop [68]. Further, the thickened pectinate muscles – especially the thicker crista terminalis, where the SN is located – may have an effect on electrical conduction across the right atrium.

5.6. Anatomical variations of the papillary muscles within the ventricles of the studied human heart specimens

Mitral regurgitation can be caused by dysfunctions of the papillary muscles in the left ventricle; failing to contract properly, and so the mitral valves fail to close properly. This results in the re-entry of oxygenated blood into the left atrium which can lead to heart failure. From the 3D reconstructions in Figs. 5 and 6, the obese heart appears to have fewer, and thicker papillary muscles, compared to the aged and normal hearts. In Fig. 3C, the tricuspid and mitral valves of the obese heart was larger than the aged and normal hearts. We assume that the significant expansion of the ventricular cavities observed in obese hearts can lead to a loss in the number of papillary muscles and thicker valves. Ventricular hypertrophy causes papillary muscle hypertrophy and weakening, leading to late-systolic intra-left ventricular obstruction during hypertrophic cardiomyopathy [69].

5.7. Anatomical variations of the major vessels of the normal, aged and obese hearts

Previous studies have used CT to create 3D reconstructions of the whole aorta in diseased [70] and normal hearts [71,72]. Stephenson and Atkinson et al. (2017) have used micro-CT to create a 3D reconstruction of the aortic root in an intact normal human heart [8]. However, our study is the first to use micro-CT to visualise and create 3D reconstruction of the aortic root in the aged and obese hearts (Fig. 4).

The aortic root is located at the junction between the aorta and left ventricle – an extension of the left ventricular outflow tract. The aortic valve leaflets (right coronary cusp, left coronary cusp and non-coronary cusp) are located in the aortic root in a crown-like fashion. Aortic root abscess is a complication of the aortic root that requires prosthetic aortic valves [31]. Our data show that the aortic root anatomy was not consistent across the normal, aged and obese hearts. It is known that the blood vessels of the aged heart has a thicker tunica media [73] and in the aged heart used in our study, the aortic root appears thicker (Fig. 3A and B). The aortic root in the obese heart appears even thicker and distorted when compared to the aortic root of the normal heart (Fig. 3A and B). Our research approach to obtain the aortic root reconstructions in this study should aid in improving prosthetic valve design and implantation – particularly in aged and obese hearts. Still today, because the precise anatomies and variations of the aortic root is not well understood, it is common for patients undergoing aortic valve replacements to experience arrhythmia – requiring pacemaker implantation [74]. When the prosthetic valve is implanted below the native valve, the prevalence of cardiac conduction defects increases [75]. Therefore, knowing the precise 3D anatomy of the aortic root and predicting where the conduction system is likely located is crucial in clinics.

5.7.1. Pulmonary trunk/pulmonary artery root

The pulmonary trunk/artery has been reconstructed using magnetic resonance imaging (MRI) [76] and CT [77–79] in normal and diseased hearts; but not in aged hearts. In our study, we show the reconstruction of the normal, aged and diseased pulmonary artery root, using micro-CT (Fig. 3A and B). This novel data can further our current understanding of pulmonary artery anatomical variations in order to improve the current designs and implantations of prosthetic pulmonary valves, for the treatment of pulmonary regurgitation.

5.7.2. Coronary arteries

To understand the development of coronary artery diseases and atherosclerotic plaques and how they alter the anatomy of coronary arteries, it is important to know the 3D anatomy of the arteries in normal, aged and diseased hearts. Previous studies have used x-ray [80] and CT angiography [81,82] to either study a bifurcation of the coronary arteries or a section of one coronary artery in diseased and normal/healthy patients.

Our study provides new methodologies of using micro-CT to both visualise and create 3D reconstructions and models of the coronary artery network in normal, aged and obese patients. In this small sample of specimens we observed that the number of coronary arteries reduces in the aged and obese hearts, and their thickness increases, respectively (Fig. 4). Arterial wall thickening that occurs during the heart's ejection period is described as systolic wall thickening. It is reported that systolic wall thickness increases as myocardial blood flow increases [83]. We can assume that the heart from the obese patient had an increased heart rate and blood flow (due to its thickened myocardial walls and increased cavity size) – this would explain the increased coronary artery size and thickness.

5.8. Anatomical variations of the normal, aged and obese sinus node and atrioventricular conduction axis/node

CT has previously been used to visualise and segment the SN and AV

conduction axis in aged hearts [5]. In whole hearts however, the resolution of the CCS region have to date been considered low, making visualisation difficult, hence why we dissected tissue blocks containing the CCS regions from the whole hearts and then rescanned the blocks. We have previously used micro-CT to visualise and segment the SN and AV conduction axis in normal tissue blocks [8]. In our current study, we provided high resolution contrast-enhanced micro-CT imaging that could be used to visualise the SN and AV junction region in aged and obese tissue blocks (Fig. 8B and C, 9, 11).

5.8.1. Sinus node

In the normal, healthy right atrium, fatty tissue and fibrosis are landmarks of the SN region and these structures provide support and insulation to the nodal tissue [84]. However, the occurrences of extensive fibrosis and fatty tissue can be functionally problematic. Confirming previous studies [33,41,85–87], our data show that loss of myocytes and extensive fibrosis occurs in the aged nodal tissue (Fig. 12Aii). It has been suggested that extensive fibrosis plays a key role in the development of SN dysfunction, abnormal SN automaticity, abnormal SN conduction and SN re-entry [88–90] and this has been confirmed in the aged mouse [91].

SN dysfunction is associated with obesity [92] and there is a strong correlation between obesity and increased cardiac fibrosis [93,94] - confirmed in our obese nodal tissue (Figs. 11A and Aii). In ageing and obesity, the size of the atria and ventricles increases to meet the heart's contractile demands [84]. The implication of increased atrial size (Figs. 5–7) and increased fibrotic content (Figs. 11A and 12Aii) in the aged and obese hearts on the functional demands of the SN is not well established. But a proposed explanation is that the extended SN region within a bigger, stretched atrial tissue requires more insulation as a protective mechanism against the electrical and mechanical load of the larger atria [95].

5.8.2. Atrioventricular node

Following micro-CT scanning of normal AV tissue block, the components of the AV conduction axis were obvious in the ortho slices and could be segmented (Fig. 10). However, this was not the case for the aged and obese tissue blocks. This could be a result of extensive fibrosis in the aged and obese AV region - making visualisation of the AV conduction axis difficult.

The risk of AV or heart block increases with older age and obesity [96], leading to prolonged PR interval [21]. This could have a positive correlation with the increased fibrosis in the AV region of the aged and obese tissue blocks.

5.9. Anatomical variation of the Purkinje fibres in the left apex of the normal, aged and obese hearts

It is known that Purkinje fibres are remodelled during heart failure, therefore are pro-arrhythmic [6,97,98]. Therefore, it is important to understand the anatomies and potential variations of the Purkinje network in normal, aged and diseased hearts. We have previously used micro-CT to visualise and reconstruct the Purkinje fibre network in the intact normal human heart [8] and heart failure rabbits [6]. A previous study used optical coherence microscopy and light microscope to visualise the Purkinje fibre network of the left ventricle of the sheep heart [99]. Other studies have used MRI to visualise the Purkinje fibre network in the left ventricle of pig heart [7] and whole rabbit heart [4].

Our current study provides evidence that high resolution micro-CT can be used to scan a tissue block taken from a small part of the left ventricle apex from normal, aged, and obese hearts to visualise Purkinje fibres (Fig. 13). From this, we show that the number of Purkinje fibres reduces in the aged and obese ventricles, compared to the normal ventricle (Fig. 13).

As mentioned above, Purkinje fibres are prone to early after-depolarisation (EADs) - leading to torsade de pointes arrhythmia and

ventricular tachycardia [25,26,100]. It is reported that the structural and electrical remodelling that occurs in aged [101] and obese hearts [102] is associated with the increased prevalence of ventricular tachycardia observed in these patients.

In the human cerebellum, it has been shown that loss of Purkinje fibre branches is indicative of Alzheimer's disease [103]. However, in the human heart, the implications of Purkinje fibre loss on cardiac function has not yet been explored. We propose that the loss of Purkinje fibres observed in the left ventricular apex of the aged and obese heart is a result of increased myocardium size and thickness and could contribute to the prevalence of Purkinje fibre dysfunction.

6. Limitations

In the normal right atrium and AV junction blocks, the SN and AV region was obvious and separate from the surrounding region (Figs. 8A and 10). However, it was difficult for us to confidently distinguish the SN and AV region in the aged and obese tissue blocks. As mentioned in the introduction, the visualisation of the SN and AV conduction axis in the normal heart is more obvious due to a difference in attenuation rates between the SN, AV conduction axis and the surrounding myocardium after immersion in I₂KI contrast agent. High attenuation areas have more accumulation of I₂KI. I₂KI binds to glycogen, therefore it localises in areas of high glycogen content such as skeletal muscle (a major muscle type in the working myocardium) - resulting in a lighter grey appearance in the 2D ortho slices. Because the SN and AV region of the aged and obese contain more connective tissue (compared to normal), they contain even less glycogen, therefore appear even darker - making visualisation of the precise SN and AV region difficult.

The cryosectioning of the frozen aged and obese tissue blocks was difficult. This was particularly due to the extensive fatty tissue within and around the blocks, the tissue blocks were too soft (even after freezing at -80 °C and sectioning at temperatures ranging between -10 and -20 °C) and the full tissue sections repeatedly folded.

Unfortunately, we had limited number of specimens (3 normal specimens; 1 aged specimen and 1 obese specimen), making it difficult to carry out statistical comparisons and semi-quantitative analysis, identify anomalies and to draw robust conclusions. Ideally, for qualitative and quantitative studies, a minimum sample size of 12 and 40 is recommended, respectively [104–106]. *Ex-vivo* human specimens are incredibly difficult to obtain and having at least 3 normal, 3 aged, and 3 obese specimens would have allowed us to make firm conclusions about the differences we have observed. However, wherever possible, we have confirmed our observations with what is known in published literature. We hope that the data obtained and reported using the imaging techniques presented here can be transferred to mathematical modellers (and 3D printers) to simulate disease (e.g. cardiac arrhythmia) observed in aged and diseased/obese hearts. We have previously shown that we can do the simulation of cardiac electrical activation in a healthy human heart [8] and re-entry arrhythmia around the human SN [41].

7. Conclusions

We present here that micro-CT has clear useful applications for cardiac imaging and advancement in our current understanding of the CCS anatomy and variation in normal, aged and obese situations. Our use of I₂KI and GO as contrast agents for micro-CT scanning contribute to - and expands - the current understanding of structural variations in normal, aged and obese hearts.

These current and novel techniques can have key impacts on current cardiovascular disease treatments such as the TAVI procedure and electronic pacemaker implantation, and the development of mathematical models of aged and diseased hearts. Thus aiding in the reduction of cardiac morbidities and reduction of patient death rate.

Funding

This work was supported by the British Heart Foundation program grant FS/17/67/33483 and the Leducq Foundation (THE FANTASY 19CVD03).

CRediT authorship contribution statement

Abimbola J. Aminu: Data collection (conducted all segmentations and reconstructions, normal SN and AVN histology staining), Formal analysis, creating figures and tables, Methodology, Formal analysis, Visualization, Investigation, manuscript planning and writing – original and final draft. **Weixuan Chen:** data collection (conducted coronary arteries segmentation and reconstruction, obese SN/AVN and healthy SN/AVN histology staining), manuscript editing, and commentary. **Zeyuan Yin:** data collection (conducted aged SN and AVN histology staining). **Marcin Kuniewicz:** manuscript editing, and commentary. **Jerzy Walocha:** manuscript editing, and commentary. **Filip Perde:** provided human specimens. **Peter Molenaar:** provided human specimens, manuscript editing, and commentary. **Paul A. Iaizzo:** provided human specimens, manuscript editing, and commentary. **Halina Dobrzynski:** research conceptualisation, Funding acquisition, Project administration, Supervision, contributed to manuscript planning, Formal analysis, formatting figures and tables, manuscript editing, and commentary. **Andrew J. Atkinson:** research conceptualisation, Project administration, Supervision, contributed to manuscript planning, Formal analysis, formatting figures and tables, manuscript editing, and commentary.

Declaration of competing interest

The authors declare no conflict of interest.

Acknowledgements

We acknowledge the Engineering and Physical Science Research Council (EPSRC) for funding the Henry Moseley X-ray Imaging Facility, which has been made available through the Royce Institute for Advanced Materials through grants (EP/F007906/1, EP/F001452/1, EP/I02249X, EP/M010619/1, EP/F028431/1, EP/M022498/1 and EP/R00661X/1).

References

- [1] W. Roberts, S. Salandy, G. Mandal, M.K. Holda, K.A. Tomaszewski, J. Gielecki, R. S. Tubbs, M. Loukas, 'Across the centuries: piecing together the anatomy of the heart, *Transl. Res. Anat.* 17 (2019) 100051–110059.
- [2] R.M. Boyett, 'And the beat goes on' the cardiac conduction system: the wiring system of the heart, *Exp. Physiol.* 94 (2009) 1035–1049.
- [3] D. Sanchez-Qunitana, H.S. Yen, 'Anatomy of cardiac nodes and atrioventricular specialized conduction system, *Rev. Esp. Cardiol.* 56 (2003) 1085–1092 (*English Version*).
- [4] M.-S. Hwang, K.E. Odening, B.-R. Choi, G. Koren, S.J. Blackband, J.R. Forder, 'Non-invasive visualization of the complete cardiac conduction system using magnetic resonance microscopy, *J. Cardiovasc. Magn.* 13 (2011) M1.
- [5] T. Kawashima, F. Sato, 'First in situ 3D visualisation of the human cardiac conduction system and its transformation associated with heart contour and inclination, *Sci. Rep.* 11 (2021) 8636.
- [6] S.J.R.J. Logantha, X.J. Cai, J. Yanni, C.B. Jones, R.S. Stephenson, L. Stuart, G. Quigley, O. Monfredi, S. Nakao, I.I.-Y. Oh, T. Starborg, A. Kitmitto, A. Vohra, R.C. Hutcheon, A.F. Corno, J.C. Jarvis, H. Dobrzynski, M.R. Boyett, G. Hart, 'Remodeling of the purkinje network in congestive heart failure in the rabbit, *Circulation: Heart Fail.* 14 (2021), e007505.
- [7] J. Magat, A. Fouillet, M. Constantin, K. Haliot, J. Naulin, D. El Hamrani, D. Benoist, S. Charron, R. Walton, O. Bernus, B. Quesson, '3D magnetization transfer (MT) for the visualization of cardiac free-running Purkinje fibres: an ex vivo proof of concept, *Magma* 34 (2021) 605–618.
- [8] S.R. Stephenson, A. Atkinson, P. Kottas, F. Perde, F. Jafarzadeh, M. Bateman, A. P. Iaizzo, J. Zhao, H. Zhang, H.R. Anderson, C.J. Jarvis, H. Dobrzynski, 'High resolution 3-dimensional imaging of the human cardiac conduction system from microanatomy to mathematical modeling, *Sci. Rep.* 7 (2017) 1–13.

- [9] BHF, CVD Statistics - BHF UK Factsheet, 2017. Accessed 25th January 2018. [file:///nask.man.ac.uk/home\\$/bhf-cvd-statistics—uk-factsheet.pdf](file:///nask.man.ac.uk/home$/bhf-cvd-statistics—uk-factsheet.pdf).
- [10] WHO, WHO Reveals Leading Causes of Death and Disability Worldwide: 200–2019, 2020. <https://www.who.int/news/item/09-12-2020-who-reveals-leading-causes-of-death-and-disability-worldwide-2000-2019>. (Accessed October 2021). Accessed 19th.
- [11] R.V. de Castroviejo, J.M. Bellido, C.L. Cabezas, A.R. Moreno, M.G. Herrera, A. T. Casrellani, A.F. Pineda, B.J. Araque, B.A. Lechuga, C.P. Vilardebo, 'Analysis of the Frequency of Cardiac Arrhythmias and Conduction Disturbances from a Health-Care Perspective, 58, *Revista Espanola de Cardiologia (English Edition)*, 2005, pp. 657–665.
- [12] K.H. Yiu, H.F. Tse, 'Hypertension and cardiac arrhythmias: a review of the epidemiology, pathophysiology and clinical implications, *J. Hum. Hypertens.* 22 (2008) 380–388.
- [13] J.C. Lavie, V.R. Milani, O.H. Ventura, Obesity and cardiovascular disease: risk factor, paradox, and impact of weight loss, *JACC (J. Am. Coll. Cardiol.)* 53 (2009) 1925–1932.
- [14] B.F. Ortega, J.C. Lavie, N.S. Blair, 'Obesity and cardiovascular disease, *Circ. Res.* 118 (2016) 1752–1770.
- [15] P. Poirier, D.T. Giles, A.G. Bray, Y. Hong, S.J. Stern, X. Pi-Sunyer, H.R. Eckel, Obesity and cardiovascular disease: pathophysiology, evaluation, and effect of weight loss, *Circulation* 113 (2006) 898–918.
- [16] J. Roh, J. Rhee, V. Chaudhari, A. Rosenzweig, The role of exercise in cardiac aging, *Circ. Res.* 118 (2016) 279–295.
- [17] Y. Song, Q. Yao, J. Zhu, B. Luo, S. Liang, 'Age-related variation in the interstitial tissues of the cardiac conduction system; and autopsy study of 230 Han Chinese, *Forensic Sci. Int.* 104 (1999) 133–142.
- [18] N. Chandler, O. Aslanidi, D. Buckley, S. Inada, S. Birchall, A. Atkinson, D. Kirk, O. Monfredi, P. Molenaar, R. Anderson, V. Sharma, D. Sigg, H. Zhang, M. Boyett, H. Dobrzynski, 'Computer three-dimensional anatomical reconstruction of the human sinus node and a novel paranodal area, *Anat. Rec.* 294 (2011) 970–979.
- [19] H. Dobrzynski, R.M. Boyett, H.R. Anderson, 'New insights into pacemaker activity - promoting understanding of sick sinus syndrome, *Circulation* 115 (2007) 1921–1932.
- [20] J.N. Chandler, D.I. Greener, O.J. Tellez, S. Inada, H. Musa, P. Molenaar, D. DiFrancesco, M. Baruscotti, R. Longhi, H.R. Anderson, R. Billeter, V. Sharma, C.D. Sigg, R.M. Boyett, H. Dobrzynski, 'Molecular architecture of the human sinus node insights into the function of the cardiac pacemaker, *Circulation* 119 (2009) 1562–1575.
- [21] H. Dobrzynski, H.R. Anderson, A. Atkinson, Z. Borbas, A. D'Souza, F.J. Fraser, S. Inada, J.R.J.S. Logantha, O. Monfredi, M.G. Morris, M.F.A. Moorman, T. Nikolaidou, H. Schneider, V. Szuts, P.I. Temple, J. Yanni, R.M. Boyett, 'Structure, function and clinical relevance of the cardiac conduction system, including the atrioventricular ring and outflow tract tissues, *Pharmacol. Therapeut.* 139 (2013) 260–288.
- [22] H. Zhang, A.V. Holden, I. Kodama, M. Honjo, M. Lei, T. Varghese, R.M. Boyett, 'Mathematical models of action potentials in the periphery and center of the rabbit sinoatrial node, *Am. J. Physiol.* 279 (2000) 397–421.
- [23] S. Tawara, The Conduction System of the Mammalian Heart, Imperial College Press, 2000.
- [24] S.R. Stephenson, R.M. Boyett, G. Hart, T. Nikolaidou, Xue Cai, F.A. Corno, N. Alphonso, N. Jeffery, C.J. Jarvis, 'Contrast enhanced micro-computed tomography resolves the 3-dimensional morphology of the cardiac conduction system in mammalian hearts, *PLoS One* 7 (2012), e35299.
- [25] Ben, E. Caref, M. Boutjdir, H.D. Himel, N. El-Sherif, 'Role of subendocardial Purkinje network in triggering torsade de pointes arrhythmia in experimental long QT syndrome, *Eurospace* 10 (2008) 1218–1223.
- [26] G. Schram, M. Pourrier, P. Melnyk, S. Nattel, Differential distribution of cardiac ion channel expression as a basis for regional specialization in electrical function, *Circ. Res.* 90 (2002) 939–950.
- [27] O.V. Aslanidi, T. Nikolaidou, J. Zhao, B.H. Smaill, S.H. Gilbert, A.V. Holden, T. Lowe, P.J. Withers, R.S. Stephenson, J.C. Jarvis, J.C. Hancox, M.R. Boyett, H. Zhang, 'Application of micro-computed tomography with iodine staining to cardiac imaging, segmentation, and computational model development, *IEEE Trans. Med. Imag.* 32 (2012) 8–17.
- [28] A. Atkinson, S. Inada, J. Li, J.O. Tellez, J. Yanni, R. Sleiman, E.A. Allah, R. H. Anderson, H. Zhang, M.R. Boyett, H. Dobrzynski, 'Anatomical and molecular mapping of the left and right ventricular His-Purkinje conduction networks, *J. Mol. Cell. Cardiol.* 51 (2011) 689–701.
- [29] S. Nakao, A.J. Atkinson, T. Motomochi, D. Fukunaga, H. Dobrzynski, 'Common arterial trunk in a cat: a high-resolution morphological analysis with micro-computed tomography, *J. Vet. Cardiol.* 34 (2012) 8–15.
- [30] M. Barber, J. Chinitz, R. John, 'Arrhythmias from the right ventricular moderator band: diagnosis and management, *Arrhythmia Electrophysiol. Rev.* 8 (2019) 294–299.
- [31] K. Kirali, S. Sarikaya, D. Gokse def, Chapter 26 - Aortic Root Replacement, Academic Press, 2018.
- [32] M.R. Movahed, Y. Saito, 'Obesity is associated with left atrial enlargement, E/A reversal and left ventricular hypertrophy, *Exp. Clin. Cardiol.* 13 (2008) 89–91.
- [33] G.J. Seidman, C. Seidman, The genetic basis for cardiomyopathy: from mutation identification to mechanistic paradigms, *Cell* 104 (2001) 557–567.
- [34] J.C. Jarvis, R. Stephenson, 'Studying the microanatomy of the heart in three dimensions: a practical update, *Front. Pediatr.* 1 (2013) 1–6.
- [35] T. Nikolaidou, X.J. Cai, R.S. Stephenson, J. Yanni, T. Lowe, A.J. Atkinson, C. B. Jones, R. Sardar, A.F. Corno, H. Dobrzynski, P.J. Withers, J.C. Jarvis, G. Hart, M.R. Boyett, 'Congestive heart failure leads to prolongation of the PR interval and

- atrioventricular junction enlargement and ion channel remodeling in the rabbit, *PLoS One* 10 (2015), e0141452.
- [36] M.G. Bateman, J.L. Quill, A.J. Hill, P.A. Iaizzo, 'The clinical anatomy and pathology of the human atrioventricular valves: implications for repair or replacement, *J. Cardiovasc. Transl. Res.* 6 (2013) 155–165.
- [37] E. Avelar, T.V. Cloward, J.M. Walker, R.J. Farney, M. Strong, R.C. Pendleton, N. Segerson, T.D. Adams, R.E. Gress, S.C. Hunt, S.E. Litwin, 'Left ventricular hypertrophy in severe obesity - interactions among blood pressure, nocturnal hypoxemia, and body mass, *Hypertension* 49 (2006) 34–39.
- [38] P. Ballo, A. Motto, S. Mondillo, S.A. Faraguti, Impact of obesity on left ventricular mass and function in subjects with chronic volume overload, *Obesity* 15 (2007) 2019–2026.
- [39] M.P. de la Maza, A. Estevez, D. Bunout, C. Klenner, M. Oyonarte, S. Hirsch, 'Ventricular mass in hypertensive and normotensive obese subjects, *Obes. Relat. Metab. Disord.* 18 (1994) 193–197.
- [40] M. Steenman, G. Lande, Cardiac aging and heart disease in humans, *Biophys. Rev.* 9 (2017) 131–137.
- [41] R.S. Kharache, E. Vigmond, R.I. Efimov, H. Dobrzynski, 'Computational assessment of the functional role of sinoatrial node exit pathways in the human heart, *PLoS One* 12 (2017), e0183727.
- [42] S. Kenchaiah, J.C. Evans, D. Levy, P.W.F. Wilson, E.J. Benjamin, M.G. Larson, W. B. Kannel, R.S. Vasan, 'Obesity and the risk of heart failure, *N. Engl. J. Med.* 347 (2002) 305–313.
- [43] G. Novo, D. Guttilla, G. Fazio, D. Cooper, S. Novo, 'The role of the renin-angiotensin system in atrial fibrillation and the therapeutic effects of ACE-Is and ARBS, *Br. J. Clin. Pharmacol.* 66 (2008) 345–351.
- [44] E.D. Abel, S.E. Litwin, G. Sweeney, Cardiac remodeling in obesity, *Physiol. Rev.* 88 (2008) 389–419.
- [45] H. Sisakian, 'Cardiomyopathies: evolution of pathogenesis concepts and potential for new therapies, *World J. Cardiol.* 6 (2014) 478–494.
- [46] R.B. Devereux, G. de Simone, T.G. Pickering, J.E. Schwartz, M.J. Roman, 'Relation of left ventricular midwall function to cardiovascular risk factors and arterial structure and function, *Hypertension* 31 (1998) 929–936.
- [47] N. Kawel, B.E. Turkbey, J.J. Carr, J. Eng, S.A. Gomes, G.W. Hundley, C. Johnson, C.S. Masri, R.M. Prince, J.R. van der Geest, C.A.J. Lima, A.D. Bluemke, Normal left ventricular myocardial thickness for middle aged and older subjects with SSFP cardiac MR: the Multi-Ethnic Study of Atherosclerosis, *Circ. Cardiovasc. Imag.* 5 (2012) 500–508.
- [48] J. Webb, A. Villa, I. Bekri, J. Shome, T. Teall, S. Claridge, T. Jackson, B. Porter, F. T. Ismail, K. Di Giovine, A.C. Rinaldi, G. Carr-Whitw, K. Al-Fakih, R. Razavi, A. Chiribiri, 'Usefulness of cardiac magnetic resonance imaging to measure left ventricular wall thickness for determining risk scores for sudden cardiac death in patients with hypertrophic cardiomyopathy, *J. Cardiol.* 119 (2017) 1450–1455.
- [49] L. Hindso, A. Fuchs, T.J. Kuhl, P.J. Nilsson, E.P. Sigvardsen, L. Kober, G. B. Nordestgaard, F.K. Kofoed, Normal values of regional left ventricular myocardial thickness, mass and distribution-assessed by 320-detector computed tomography angiography in the Copenhagen General Population Study, *Int. J. Cardiovasc. Imag.* 33 (2017) 421–429.
- [50] UN, Department of economic and social affairs, population division (2019), in: *World Population Ageing 2019: Highlights, 2019. ST/ESA/SER.A/430*.
- [51] A. Biernacka, G.N. Frangogiannis, Aging and cardiac fibrosis, *Aging Dis* 2 (2011) 158–173.
- [52] J.-Y. Lee, M.-S. Hur, 'Morphological classification of the moderator band and its relationship with the anterior papillary muscle, *Anat. Cell Biol.* 52 (2019) 38–42.
- [53] M. Loukas, Z. Klaasen, R.S. Tubbs, T. Derderian, D. Paling, D. Chow, S. Patel, R. H. Anderson, 'Anatomical observations of the moderator band, *Clin. Anat.* 23 (2010) 443–450.
- [54] A.Y. Raghavendra, K.A. Kavitha, P. Tarvadi, C.R. Harsha, 'Anatomical Study of the Moderator Band, 3, *Nitte Univ J Health Sci*, 2013, pp. 78–81.
- [55] S.T. Bandeira, G.C. Wafae, C. Ruiz, S.R. Nascimento, J.R. Fernandes, N. Wafae, Morphological classification of the septomarginal trabecula in humans, *Folia Morphol. (Wars.)* 70 (2011) 300–304.
- [56] A. Kosinski, D. Kozlowski, J. Nowinski, E. Lewicka, A. Dabrowska-Kugacha, G. Raczak, M. Grzybiak, 'Morphogenetic aspects of the septomarginal trabecula in the human heart, *Arch. Med. Sci.* 6 (2010) 733–743.
- [57] P. Shenoy, M. Lucas, K.V. Vinay, A. Ramos, 'Morphometric study of septomarginal trabeculae (moderator band), *Int. J. Anat. Res.* 4 (2016) 3302–3308.
- [58] S.W. Rabkin, 'Epicardial fat: properties, function and relationship to obesity, *Obes. Rev.* 8 (2007) 253–261.
- [59] A. Schäffler, J. Schölmerich, Innate immunity and adipose tissue biology, *Trends Immunol.* 31 (2010) 228–235.
- [60] G. Iacobellis, H.J. Wilens, G. Barbaro, A.M. Sharma, 'Threshold values of high-risk echocardiographic epicardial fat thickness, *Obesity* 16 (2008) 887–892.
- [61] J.-S. Kim, S.W. Kim, J.S. Lee, S.K. Lee, R. Abbott, K.Y. Lee, H.E. Lim, K.-C. Sung, G.-Y. Cho, K.K. Koh, C. Shin, S.H. Kim, Association of pericardial adipose tissue with left ventricular structure and function: a region-specific effect? *Cardiovasc. Diabetol.* 20 (2021) 26.
- [62] P.M. Gorter, A.S. van Lindert, A.M. de Vos, M.F. Meijis, Y. van der Graaf, P. A. Doevendans, M. Prokop, F.L.J. Visseren, 'Quantification of epicardial and pericardial fat using cardiac computed tomography; reproducibility and relation with obesity and metabolic syndrome in patients suspected of coronary artery disease, *Atherosclerosis* 197 (2008) 896–903.
- [63] N. Alexopoulos, D.S. McLean, M. Janik, C.D. Arepalli, A.E. Stillman, P. Raggi, 'Epicardial adipose tissue and coronary artery plaque characteristics, *Atherosclerosis* 210 (2010) 150–154.
- [64] C.S. Fox, P. Gona, U. Hoffmann, S.A. Porter, C.J. Salton, J.M. Massaro, D. Levy, M. G. Larson, R.B. D'Agostino, C.J. O'Donnell, W.J. Manning, 'Pericardial fat, intrathoracic fat, and measures of left ventricular structure and function: the Framingham Heart Study, *Circulation* 119 (2009) 1586–1591.
- [65] A. Silaghi, M.-D. Piercecchi-Marti, M. Grino, G. Leonetti, M.C. Alessi, K. Clement, F. Dadoun, A. Dutour, 'Epicardial adipose tissue extent: relationship with age, body fat distribution, and coronaropathy, *Obesity* 16 (2008) 2424–2430.
- [66] S. Abbata, J.C. Desai, R.C. Cury, J. Butler, K. Nieman, V. Reddy, 'Mapping epicardial fat with multi-detector computed tomography to facilitate percutaneous transeptal arrhythmia ablation, *Eur. J. Radiol.* 57 (2006) 417–422.
- [67] J. Shirani, J. Alaeddini, 'Structural remodeling of the left atrial appendage in patients with chronic non-valvular atrial fibrillation: implications for thrombus formation, systemic embolism, and assessment by transesophageal echocardiography, *Cardiovasc. Pathol.* 9 (2000) 95–101.
- [68] J.L. Cox, J.P. Boineau, R.B. Schuessler, K.M. Kater, T.B. Ferguson, M.E. Cain, B. D. Lindsay, J.M. Smith, P.B. Corr, C.B. Hogue, 'Electrophysiologic basis, surgical development, and clinical results of the maze procedure for atrial flutter and atrial fibrillation, *Adv. Card. Surg.* 6 (1995) 1–67.
- [69] E.C. Madu, I.A. D'Cruz, 'The vital role of papillary muscles in mitral and ventricular function: echocardiographic insights, *Clin. Cardiol.* 20 (1997) 93–98.
- [70] F. Bocalandro, B. De La Guardia, W.R. Smalling, 'Rotational aortogram with three-dimensional reconstruction in a case of repaired aortic coarctation, *Circulation* 104 (2001) 620–621.
- [71] B.J. Doyle, L.G. Morris, A. Callanan, D.A. Vorp, T.M. McLaughlin, '3D reconstruction and manufacture of real abdominal aortic aneurysms: from CT scans to silicone model, *J. Biomech. Eng.* 130 (2008), 034501.
- [72] A. Hossien, S. Gelsomino, B. Mochtar, J.G. Marsden, P.S. Nia, 'Novel multi-dimensional modelling for surgical planning of acute aortic dissection type A based on computed tomography scan, *Eur. J. Cardio. Thorac. Surg.* 48 (2015) e95–101.
- [73] F. Paneni, C.D. Cañestro, P. Libby, T.F. Lüscher, G.G. Camici, 'The aging cardiovascular system: understanding it at the cellular and clinical levels, *J. Am. Coll. Cardiol.* 69 (2017) 1952–1967.
- [74] S. Dawkins, A.R. Hobson, P.R. Kalra, A.T. Tang, J.L. Monro, K.D. Dawkins, 'Permanent pacemaker implantation after isolated aortic valve replacement: incidence, indications, and predictors, *Ann. Thorac. Surg.* 85 (2008) 108–112.
- [75] N. Piazza, P. de Jaegere, C. Schultz, A.E. Becker, P.W. Serruys, R.H. Anderson, 'Anatomy of the aortic valve complex and its implications for transcatheter implantation of the aortic valve, *Cardiovasc. Interv.* 1 (2008) 74–81.
- [76] M.W. Vannier, S. Gronemeyer, F.R. Gutierrez, C.E. Canter, J.C. Laschinger, R. H. Knapp, 'Three-dimensional magnetic resonance imaging of congenital heart disease, *Radiographics* 8 (1988) 857–871.
- [77] L.E. Hirsig, P.G. Sharma, N. Verma, D.A. Rajderkar, 'Congenital pulmonary artery anomalies: a review and approach to classification, *J. Clin. Imag. Sci.* 8 (2018) 1–10.
- [78] S. Speggin, S. Durairaj, B. Mimic, A.F. Corno, 'Virtual 3D modelling of airways in congenital heart defects, *Front. Pediatr.* 4 (2016) 116.
- [79] M.L. Tomov, A. Cetnar, K. Do, H. Bauser-Heaton, V. Serpooshan, 'Patient-specific 3-dimensional-bioprinted model for in vitro analysis and treatment planning of pulmonary artery atresia in tetralogy of fallot ad major aortopulmonary collateral arteries, *JAHA* 8 (2019), e0144490.
- [80] F. Galassi, M. Alkhalil, R. Lee, P. Martindale, R.K. Kharbanda, K.M. Channon, V. Grau, R.P. Choudhury, '3D reconstruction of coronary arteries from 2D angiographic projections using non-uniform rational basis splines (NURBS) for accurate modelling of coronary stenoses, *PLoS One* 13 (2018), e0190650.
- [81] V.I. Kigka, G. Rigas, A. Sakellarios, S. Panagiotis, I.O. Andrikos, T.P. Exarchos, D. Loggitsi, C.D. Anagnostopoulos, L.K. Michalis, D. Neglia, G. Pelosi, O. Parodi, D.I. Fotiadis, '3D reconstruction of coronary arteries and atherosclerotic plaques based on computed tomography angiography images, *Biomed. Signal Process Control* 40 (2018) 286–294.
- [82] W. Wu, S. Samant, G. de Zwart, S. Zhao, B. Khan, M. Ahmad, M. Bologna, Y. Watanabe, Y. Murasato, F. Burzotta, E.S. Brilakis, G. Dangas, Y. Louvard, G. Stankovic, G.S. Kassab, F. Migliavacca, C. Chiastra, Y.S. Chatzizisis, '3D reconstruction of coronary artery bifurcations from coronary angiography and optical coherence tomography: feasibility, validation, and reproducibility, *Sci. Rep.* 10 (2020) 18049.
- [83] K.P. Gallagher, M. Matsuzaki, J.A. Koziol, W.S. Kemper, J. Ross Jr., 'Regional myocardial perfusion and wall thickening during ischemia in conscious dogs, *Am. J. Physiol. Heart Circ. Physiol.* 247 (1984) H727–H738.
- [84] D. Sanchez-Quintana, H.R. Anderson, A.J. Cabrera, V. Climent, R. Martin, J. Farre, Y.S. Ho, The terminal crest: morphological features relevant to electrophysiology, *Heart* 88 (2002) 406–411.
- [85] Y.S. Ho, 'Anatomy and myoarchitecture of the left ventricular wall in normal and in disease, *Eur. J. Echocardiogr.* 10 (2009) 113–117.
- [86] K.M. Keller, S.E. Howlett, 'Sex differences in the biology and pathology of the aging heart, *Can. J. Cardiol.* 32 (2016) 1065–1073.
- [87] A. Sheydina, R.D. Riordan, R.K. Boheler, 'Molecular mechanisms of cardiomyocyte aging, *Clin Sci (Lond)*. 121 (2011) 315–329.
- [88] D.G. Benditt, S. Sakaguchi, M.A. Goldstein, K.G. Lurie, C.C. Gornick, S.W. Adler, 'Sinus node dysfunction: pathophysiology, clinical features, evaluation, and treatment, in: D.P. Zipes, J. Jalide (Eds.), *Cardiac Electrophysiology: from Cell to Bedside*, WB Saunders Company, Philadelphia, 1995.
- [89] A.V. Glukhov, L.T. Hage, B.J. Hansen, A. Pedraza-Toscano, P. Vargas-Pinto, R. L. Hamlin, R. Weiss, C.A. Carnes, G.E. Billman, V.V. Fedorov, 'Sinoatrial node reentry in a canine chronic left ventricular infarct model: the role of intranodal

- fibrosis and heterogeneity of refractoriness, *Circ. Arrhythm. Electrophysiol.* 6 (2013) 984–994.
- [90] W.E.J. Sanders, R.A. Sorrentino, R.A. Greenfield, H. Shenasa, M.E. Hamer, J. M. Wharton, 'Catheter ablation of sinoatrial node reentrant tachycardia, *J. Am. Coll. Cardiol.* 23 (1994) 926–934.
- [91] X. Hao, X. Zhang, M. Nirmalan, L. Davies, D. Konstantinou, F. Yin, H. Dobrzynski, x. Wang, A. Grace, H. Zhang, M. Boyett, C.L. Huang, M. Lei, 'TGF-beta1-mediated fibrosis and ion channel remodeling are key mechanisms in producing the sinus node dysfunction associated with SCN5A deficiency and aging, *Circ. Arrhythm. Electrophysiol.* 4 (2011) 397–406.
- [92] J. Yanni, J.O. Tellez, P.V. Sutyagin, M.R. Boyett, H. Dobrzynski, 'Structural remodelling of the sinoatrial node in obese old rats, *J. Mol. Cell. Cardiol.* 48 (2010) 653–662.
- [93] M.A. Alpert, J. Omran, A. Mehra, S. Ardhanari, 'Impact of obesity and weight loss on cardiac performance and morphology in adults, *Prog. Cardiovasc. Dis.* 56 (2014) 391–400.
- [94] C. Gonzalez-Quesada, M. Cavalera, A. Biernacka, P. Kong, D.-W. Lee, A. Saxena, O. Frunza, M. Dobaczewski, A. Shinde, N.G. Frangogiannis, 'Thrombospondin-1 induction in the diabetic myocardium stabilizes the cardiac matrix in addition to promoting vascular rarefaction through angiotensin-2 upregulation, *Circ. Res.* 113 (2013) 1331–1344.
- [95] R.W. Joyner, F.J. van Capelle, 'Propagation through electrically coupled cells. How a small SA node drives a large atrium, *Biophys. J.* 50 (1986) 1157–1164.
- [96] R. Shan, Y. Ning, Y. Ma, S. Liu, J. Wu, X. Fan, J. Lv, B. Wang, S. Li, L. Li, 'Prevalence and risk factors of atrioventricular block among 15 million Chinese health examination participants in 2018: a nation-wide cross-sectional study, *BMC Cardiovasc. Disord.* 21 (2021) 289.
- [97] W. Han, D. Chartier, D. Li, S. Nattel, 'Ionic remodelling of cardiac Purkinje cells by congestive heart failure, *Circulation* 104 (2001) 2095–2100.
- [98] S. Nattel, A. Maguy, S. Le Bouter, Y.H. Yeh, 'Arrhythmogenic ion-channel remodeling in the heart: heart failure, myocardial infarction, and atrial fibrillation, *Physiol. Rev.* 87 (2007) 425–456.
- [99] M.-J. Cha, J.-W. Seo, H. Kim, M. Kim, J. Choi, D.-H. Kang, S. Oh, 'Visualization of left ventricular Purkinje fiber distribution using widefield optical coherence microscopy, *Int. J. Clin. Exp. Pathol.* 13 (2020) 3013–3020.
- [100] D.O. Arnar, J.R. Bullinga, J.B. Martins, 'Role of the Purkinje system in spontaneous ventricular tachycardia during acute ischemia in a canine model, *Circulation* 96 (1997) 2421–2429.
- [101] A.B. Curtis, R. Karki, A. Hattoum, U.C. Sharma, 'Arrhythmias in patients ≥ 80 years of age, *J. Am. Coll. Cardiol.* 71 (2018) 2041–2057.
- [102] R. Samantha, J. Pouliopoulos, S. Kumar, A. Narayan, F. Nadri, P. Qian, S. Thomas, G. Sivagangabalan, P. Kovoor, A. Thiagalingam, 'Influence of BMI on inducible ventricular tachycardia and mortality in patients with myocardial infarction and left ventricular dysfunction: the obesity paradox, *Int. J. Cardiol.* 15 (2018) 148–154.
- [103] I.A. Mavroudis, D.F. Fotiou, L.F. Adipepe, M.G. Manani, S.D. Njau, D. Psaroulis, V. G. Costa, S.J. Baloyannis, Morphological changes of the human Purkinje cells and deposition of neuritic plaques and neurofibrillary tangles on the cerebellar cortex of Alzheimer's disease, *AJADD* 25 (2010) 585–591.
- [104] R. Budiu, K. Moran, How many participants for quantitative usability studies: a summary of sample-size recommendations, in: Nielsen Normal Group, 2021.
- [105] V. Clarke, V. Braun, *Successful Qualitative Research: a Practical Guide for Beginners*, SAGE, California, US, 2013.
- [106] A.J. Fugard, H.W. Potts, 'Supporting thinking on sample sizes for thematic analyses: a quantitative tool, *Int. J. Soc. Res. Methodol.* 18 (2015) 669–684.

3.5 Limitations

This study used a very limited sample size (3 healthy/normal specimens, 1 aged specimen, and 1 obese specimen). It would have been ideal to use more healthy, aged, and obese samples from both males and females.

It was impossible to explore if gender would influence the extent of fat accumulation, the size of the SN or AVN region and the anatomy of the whole myocardium and major blood vessels. However, the fact that the healthy and aged samples were from females somewhat eliminates gender influence as there were apparent differences in the anatomy and microanatomy of these specimen groups.

The whole, healthy heart was from a 54-year-old individual. While ageing is classed as 60 years and above [2]), 54 years old is close to 60; therefore, it may be difficult to confidently class 54 as 'young' (even though it technically is). Consequently, it would be ideal to obtain whole heart samples from a younger cohort to confidently conclude the anatomical differences between young/healthy/normal and aged.

The small sample size makes it difficult to make robust conclusions and conduct statistical, semi-quantitative and qualitative analyses. However, where possible, the observations reported in this study have been confirmed with published reports.

The nodal regions of these specimens contained much less-than-normal glycogen content. This low glycogen content explains why these regions in the aged and obese specimens appeared very dark and challenging to distinguish confidently from the surrounding tissue (Figure 6 of Appendix).

Appendix

Wall thickness and cavity volume measurements; atrioventricular (AV) junction; and paranodal area from normal, aged, and obese hearts

In addition to carrying out visual analyses and comparisons of the myocardial wall and cavities in normal, aged, and obese hearts, I carried out additional measurements. These measurements included: wall thickness/width measurements, segmentation of ventricular and atrial cavities, calculating the volumes of cavities; segmentation of the paranodal area; and analysis of the AV region in the aged and obese tissue block. To measure wall thickness, I took measurements in the coronal plane (4-chamber view) (Figure 1, 2). As a 'landmark', the hearts were split mid-way, at the point where the aortic valve starts to appear. To calculate the volume of the atrial and ventricular cavities, they were first segmented (i.e., separated) from the whole hearts using Amira v6.5 (Figure 3). Then the volume of the segmented cavities was calculated (Figure 4). The ventricular and atrial walls of the obese heart were thicker than those of the normal heart and aged heart (Figure 1). The aged heart's atrial septum was more expansive than the normal and obese heart's (Figure 1). The volume of the atria and ventricular cavities of the obese heart was higher than the normal heart's and aged heart's.

Chandler et al. (2011) first reported the paranodal area [109]. This area runs alongside the sinus node (SN) and has atrial and nodal properties, although its exact function remains unknown [109]. The region of attenuation difference (that possibly contained the SN) in the normal, aged, and obese atrial tissue blocks has been segmented (Figure 7 in Paper 1, Chapter 3). I segmented the paranodal area from the normal, aged, and obese tissue blocks (Figure 5, 6). In the right atrium tissue blocks from the aged and obese hearts, the area of attenuation difference is extended/greater. This observation may not necessarily mean the SN region is extended (because nodal myocytes have been replaced with fat in obese and aged atrial tissue, as shown in Paper 1, Chapter 3). The extended region of attenuation difference instead suggests an increase in fibrosis, as shown in Paper 1, Chapter 3.

In Paper 1, chapter 3, it was mentioned that the region of attenuation difference containing the atrioventricular (AV) junction was not apparent in the aged and obese AV tissue blocks. Only the His bundle was visible in the aged and obese tissue blocks (Figure 7).



Healthy heart_reconstruction.mp4

Movie 1. 3D reconstruction of the normal heart, its chambers, major vessels, and valves. Double-click on the icon to play it.

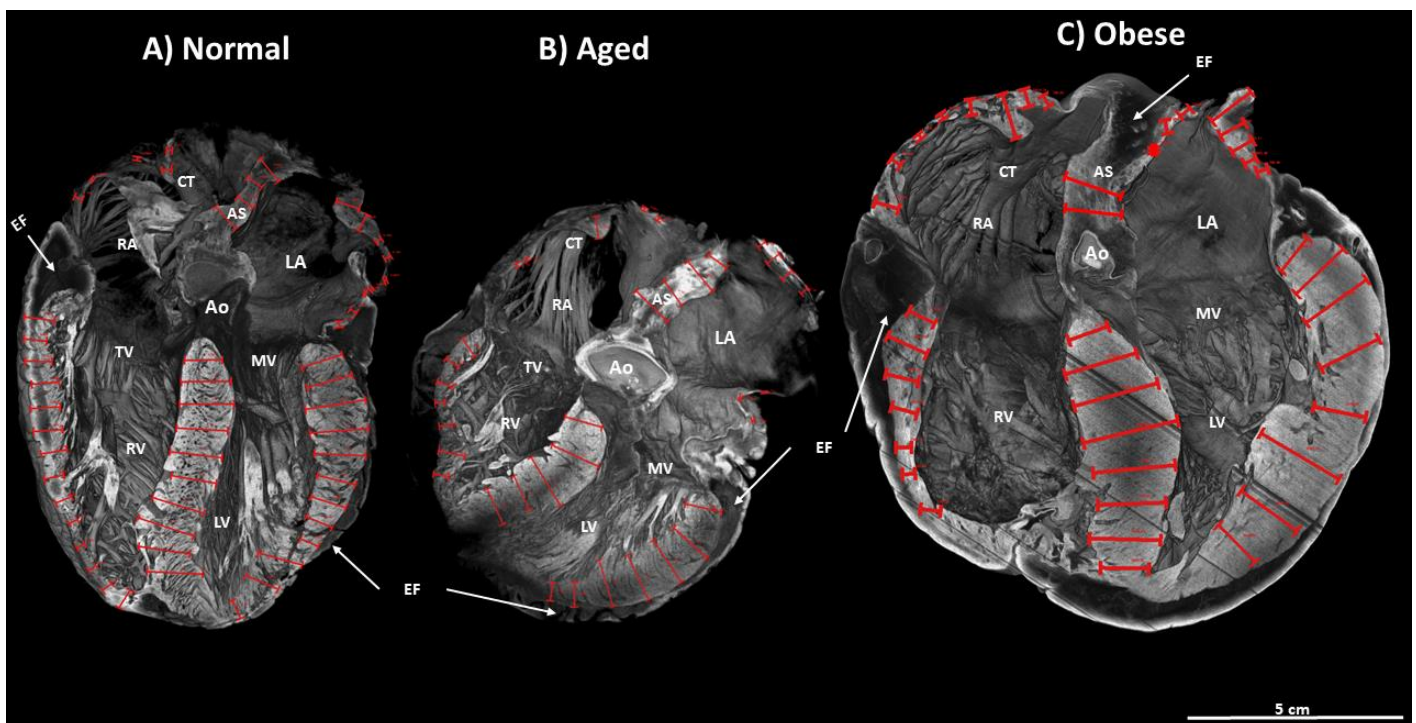


Figure 1. Long axis four chamber view of the normal, aged and obese hearts, showing the location of the myocardial wall width measurements. (A), normal heart. (B), aged heart. (C), obese heart. Red lines indicate location and position of measurements. n=1 normal heart; n=1 aged heart; n=1 obese heart. Ao = aorta; AS = atrial septum; CT = crista terminalis; EF = epicardial fat; LA = left atrium; LV = left ventricle; MV = mitral valve; PPM = posterior papillary muscle; RA = right atrium; RV = right ventricle; VS = ventricular septum.

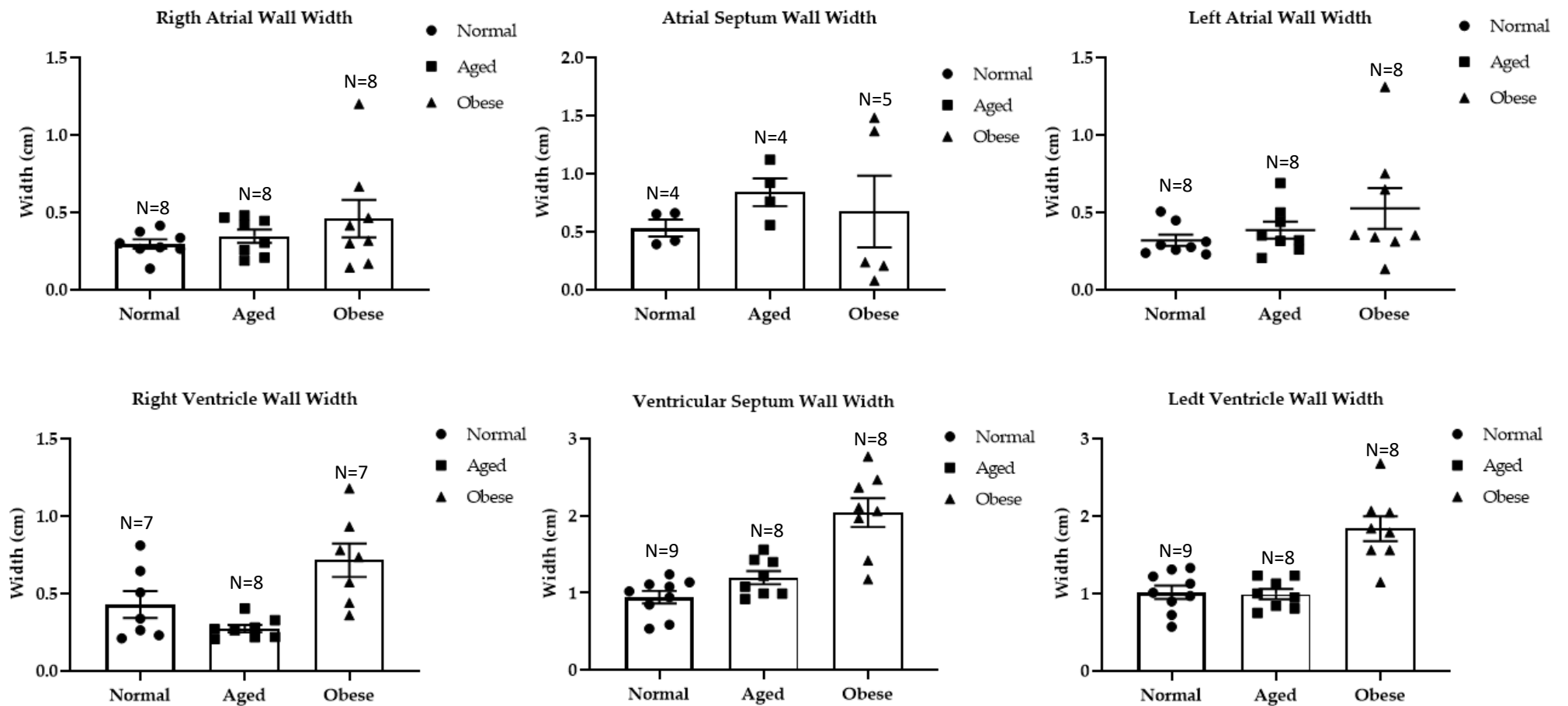


Figure 2. Myocardial wall width measurements from normal, aged, and obese hearts. (A) Right atrial wall width, (B) Atrial septum wall width, (C) Left atrial wall width, (D) Right ventricle wall width, (E) Ventricular septum wall width, and (F) Left ventricle wall width. Data are shown as mean \pm SEM. N numbers on the graph indicate the number of measurements that were taken for the corresponding bar.

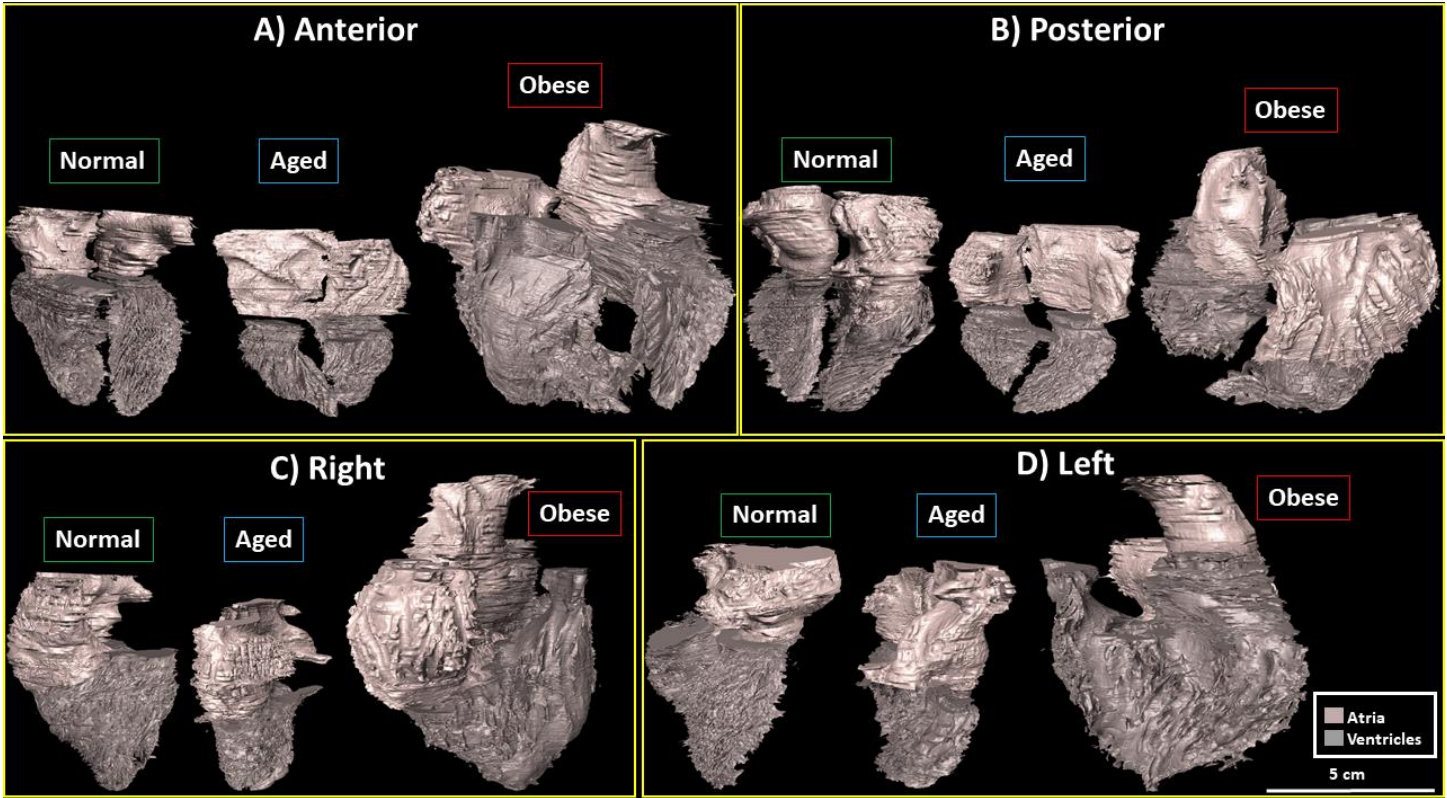


Figure 4. Segmentation of the atrial and ventricular cavities from the normal, aged and obese hearts. (A) Anterior view. (B), Posterior view. (C) Right view. (D) Left view.

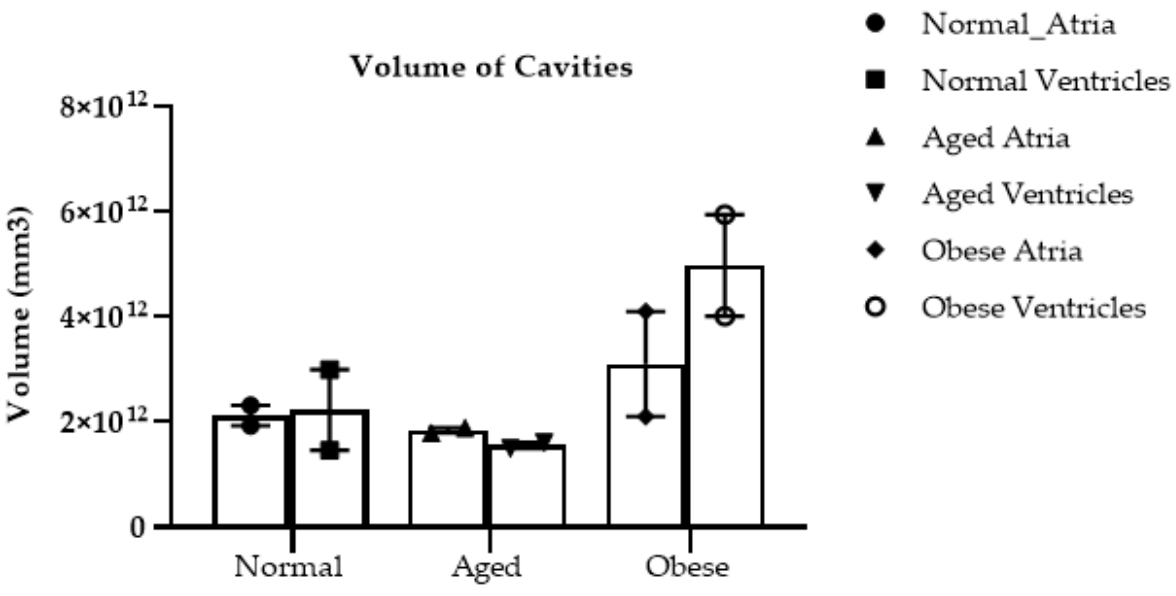


Figure 3. Volume of segmented cavities from normal, aged, and obese hearts. Data are shown as mean ± SEM.

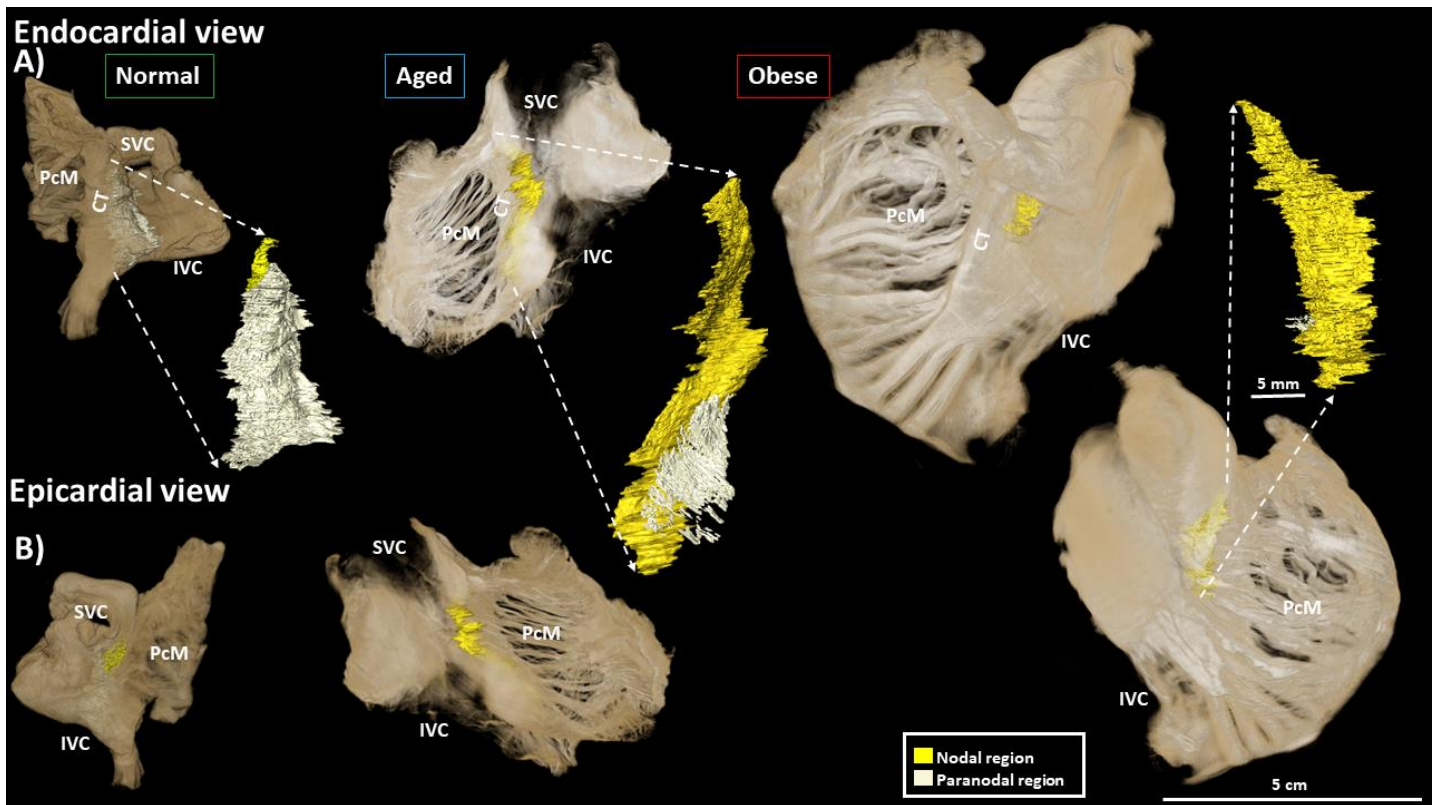


Figure 5. Segmentation of paranodal area (white) and the low attenuation (yellow) difference regions in the normal, aged and obese right atrium blocks. Within the yellow region is the location of the sinus node. (A) Endocardial view. (B) Epicardial view. CT = crista terminalis; IVC = inferior vena cava; PcM = pectinate muscle; SVC = superior vena cava.

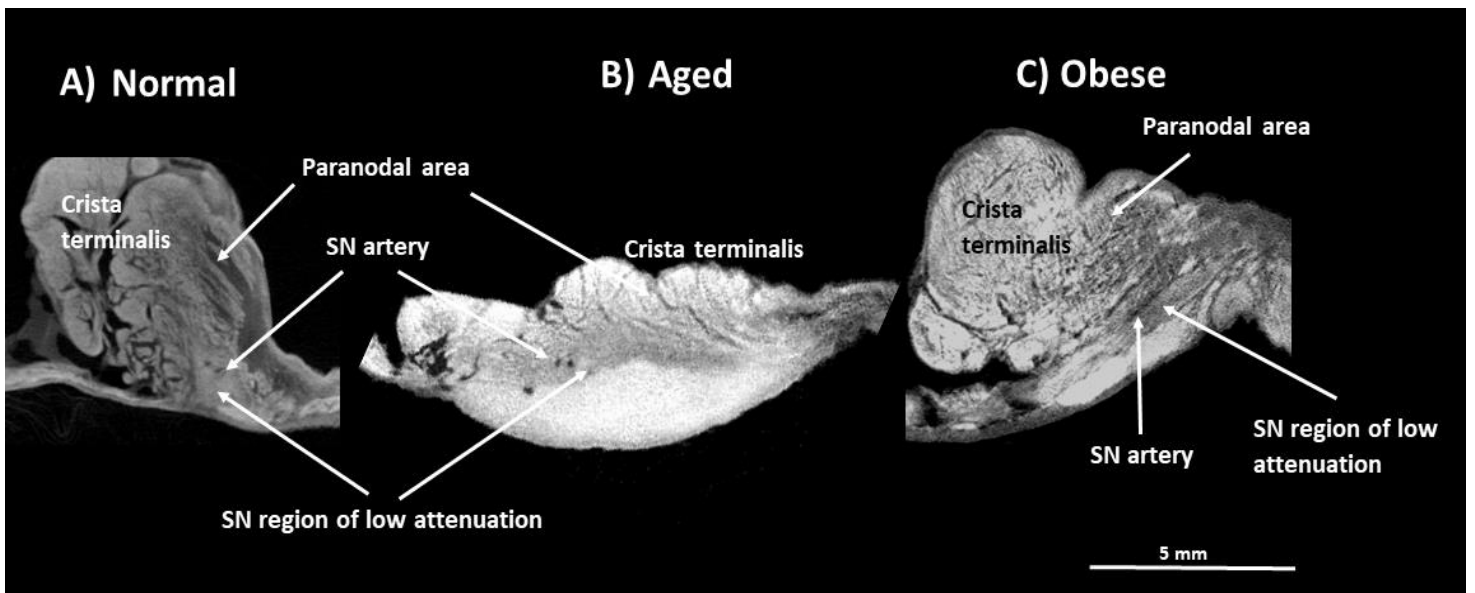


Figure 6. Visualisation of the human paranodal area and sinus node within the low attenuation regions in the normal, aged and obese right atrium. A, B, C, micro-CT section of the sinus node from the normal (A), aged (B) and obese (C) right atrium with. SN = sinus node.

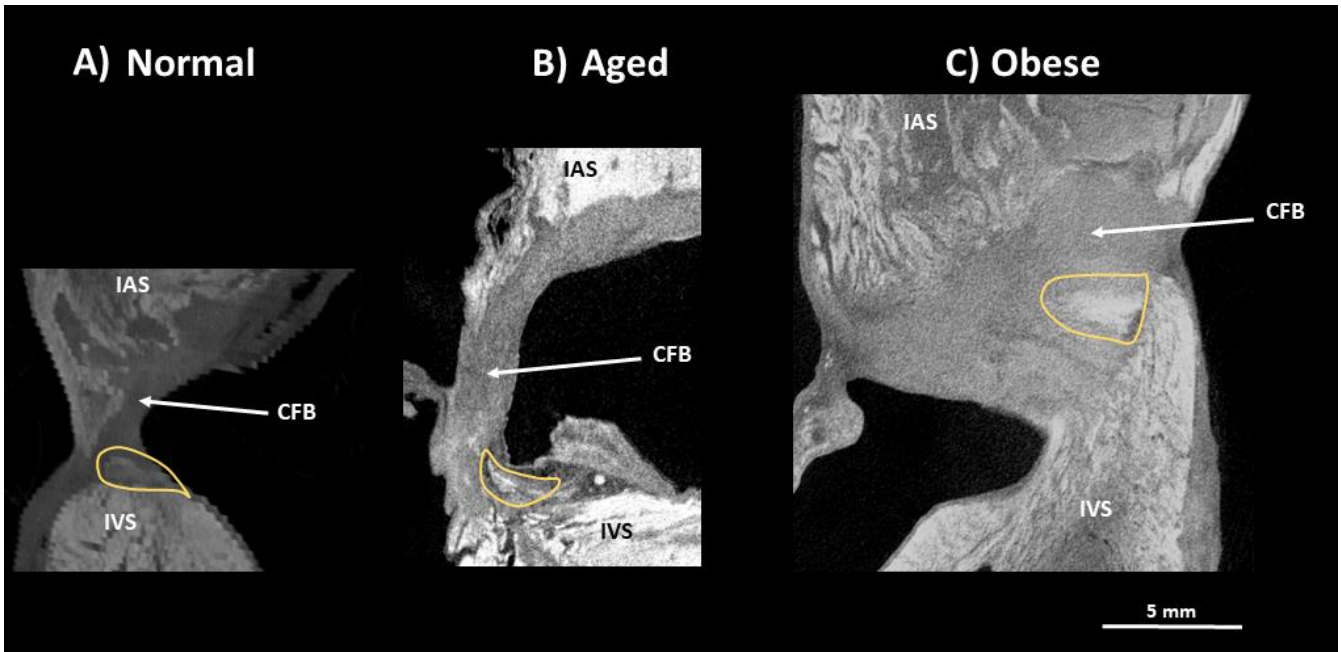


Figure 5. Micro-CT sections of the His bundle in the normal heart atrioventricular septal region. Yellow outline identifies the region of low attenuation region containing the His bundle. **A, B, C,** micro-CT section of the sinus node from the normal (**A**), aged (**B**), and obese (**C**) atrioventricular tissue block. CFB = central fibrous body; IAS = interatrial septum; INE = inferior nodal extension; IVS = interventricular septum.

CHAPTER 4) FURTHER INSIGHTS INTO THE MOLECULAR COMPLEXITY OF THE HUMAN SINUS NODE – THE ROLE OF ‘NOVEL’ TRANSCRIPTION FACTORS AND MICRORNAS²

Expanding the current understanding of anatomical differences of various structures in healthy, aged, and obese human hearts is essential. However, it is equally important to expand our current understanding of the molecular interactions that underlie the first component of the CCS – the SN. This is because the underlying interactions between molecules such as miRNAs, mRNAs, TFs, and cell markers within the healthy human SN correspond to its anatomical structure. Alterations to these intricate molecular interactions contribute to dysfunctions such as sick sinus syndrome and arrhythmia, which can contribute to structural modifications of the SN and other parts of the heart.

This chapter further explains the incredibly complex morphological, molecular, and functional characteristics that underlie the human sinus node (SN). The aim was to use next generation sequencing (NGS) for RNA-sequencing (RNAseq) and Ingenuity Pathway Analysis (IPA) to analyse the expression profile of transcription factors (TFs), microRNAs (miRs), and cell markers in the healthy adult human SN, compared to the right atrial (RA) tissue. The aim was also to predict interactions of key ‘novel’ TFs and cell markers with key miRs in the healthy adult human SN, compared to the RA. Therefore, providing new insight into the treatment of SN dysfunction (SND) – an increasing occurrence in an increasingly ageing population.

A total of 10 samples were collected from the SN region and the pectinate muscles (i.e., remote from the SN region). 3 of these samples were used for NGS for RNA-seq, and 7 were used for qPCR analysis. The NGS dataset contained key known and ‘novel’ TFs and cell markers significantly more/less expressed in the SN vs. RA. IPA was used to analyse interaction networks between TFs, cell markers, and miRs previously reported to interact with key molecules involved in the SN’s pacemaking function (Petkova et al. 2020).

The novel observations reported in this chapter - especially the uniquely high expression of immune cell markers in the SN vs. RA and their interaction with key TFs and miRs – allow for developing therapeutic targets in the treatment of SND.

²This chapter is directly from the publication: **Aminu, A. J.**, Petkova, M., Atkinson, A. J., Yanni, J., Morris, A. D., Simms, R. T., Chen, W., Yin, Z., Kuniewicz, M., Holda, M. K., Kuzmin, V. S., Perde, F., Molenaar, P., Dobrzynsk, H., *Further insights into the molecular complexity of the human sinus node – the role of ‘novel’ transcription factors and microRNAs.* Prog. Biophys. Mol. Biol. 2021. **166**: p. 86-104

4.1 Authors' contribution to the paper

I (Abimbola J. Aminu) performed most of this study's bioinformatics (particularly IPA). I also wrote and edited the paper. I appreciate the effort and input from all co-authors.

- Abimbola J. Aminu: analysis of NGS dataset; analysis and creation of network interactions using IPA; histology; created all figures and tables; manuscript planning, writing, and editing; supervision of Weixuan Chen and Zeyuan Yin
- Maria Petkova: contributed to cryosectioning; histology; RNA extraction; NGS analysis
- Andrew J. Atkinson: contributed to RNA extraction; cryosectioning; histology; and supervision
- Joseph Yanni: contributed to RNA extraction; supervision
- Alex D. Morris: contributed to cryosectioning and histology
- Robert T. Simms: contributed to NGS and IPA analysis
- Weixuan Chen: contributed to morphological analysis; NGS, and IPA analysis as part of her training while I supervised
- Zeyuan Yin: contributed to NGS and IPA analysis as part of his training while I supervised
- Mateusz K. Holda: manuscript editing (original draft)
- Marcin Kuniewicz: manuscript editing (original draft)
- Filip Perde: provided specimens
- Peter Molenaar: provided specimens; manuscript editing (original draft)
- Halina Dobrzynski: supervision; data analysis; formatted figures and tables; manuscript planning, writing, and editing

4.2 Hypothesis

Previous data obtained from NGS for RNA-seq for 3 healthy human SN samples showed varying expression levels of key miRNAs, mRNAs, and TFs, compared to the RA [44]. If these molecules have different expression levels in the SN, then they must be interacting with one another. These varying expression levels must play a role in regulating the molecular and functional characteristics of the SN.

4.3 Aims

The aims were based on the bioinformatics analysis of NGS for RNA-seq dataset for healthy human SN samples to predict key molecular interactions and further understand the molecular complexity of the SN. As published in Paper 2, Chapter 4, I aimed to identify 'novel' TFs in the human SN vs. RA; use IPA to predict interactions between these 'novel' TFs and 'embryonic' TFs and predict interactions among key TFs with pacemaking genes; deduce the expression of markers of key cell types and organelles in the SN vs. RA and predict their interaction with key TFs; and finally, predicted the interaction between these markers and TFs, and recently published key microRNAs [44].

4.4 Materials and methods

Thorough descriptions of the methods used in this study are provided in the accompanying paper.

4.4.1 Human sample details

Human hearts that were unsuitable for heart transplants were obtained from collaborators in Romania and Australia (as shown in Table 1, Paper 2, Chapter 4). They were stored in the Dobrzynski laboratory under the Human Tissue Act 2004. 3 samples (age range 19-54) were used for NGS for RNAseq.

4.4.2 Cryosectioning and histological characterisation of the SN

One tissue specimen was cryosectioned at a thickness of 10–30 μm and frozen at $-80\text{ }^{\circ}\text{C}$ before Masson's trichrome staining. This staining was carried out to identify cardiomyocytes, connective tissue, and fat within the tissues. Following this, the Genomics department at the University of Manchester carried out NGS for RNAseq on the 3 RA and SN samples. Further details on this process are provided in paper 2, chapter 4.

4.4.3 Ingenuity pathway analysis

In depth-description of the use of IPA to analyse the NGS dataset and to create interaction pathways is provided in paper 2, chapter 4.

Initially, knowing how to use the IPA software was difficult as no one in the laboratory group had experience with it. To overcome this, I attended various tutorial sessions organised by the Genomics department at the University of Manchester and reached out to Qiagen representatives. This increased my competence with the software, allowing me to explore the NGS datasets in-depth.

4.4.4 Heatmaps, graphs, and statistical analysis

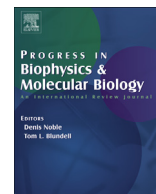
I used heatmaps to visualise the similarities and differences in the distribution of the molecules in the SN and atrial tissue. After searching various software, I settled on Heatmapper (<http://www.heatmapper.ca/expression/>). This software was relatively straightforward to use. However, it was challenging to navigate how to select colour schemes. I settled on using green and red colour schemes as this matched the colour schemes of the pathways generated using IPA.

All graphs and statistical analyses were created using GraphPad Prism 8.4.3 software.



Contents lists available at ScienceDirect

Progress in Biophysics and Molecular Biology

journal homepage: www.elsevier.com/locate/pbiomolbio

Further insights into the molecular complexity of the human sinus node – The role of ‘novel’ transcription factors and microRNAs



Abimbola J. Aminu^a, Maria Petkova^a, Andrew J. Atkinson^a, Joseph Yanni^a, Alex D. Morris^a, Robert T. Simms^a, Weixuan Chen^a, Zeyuan Yin^a, Marcin Kuniewicz^{a,e}, Mateusz K. Holda^{a,e}, Vladislav S. Kuzmin^f, Filip Perde^b, Peter Molenaar^{c,d}, Halina Dobrzynski^{a,e,*}

^a The Division of Cardiovascular Sciences, University of Manchester, United Kingdom

^b National Institute of Legal Medicine, Bucharest, Romania

^c School of Biomedical Sciences, Queensland University of Technology, Brisbane, Australia

^d Cardiovascular Molecular & Therapeutics Translational Research Group, University of Queensland, The Prince Charles Hospital, Brisbane, Australia

^e Department of Anatomy, Jagiellonian University Medical College, Krakow, Poland

^f Department of Human and Animal Physiology, Lomonosov Moscow State University, Moscow, Russia

ARTICLE INFO

Article history:

Received 2 February 2021

Received in revised form

26 April 2021

Accepted 29 April 2021

Available online 15 May 2021

Keywords:

Transcription factors
microRNAs
Sinus node dysfunction
Immune cells
Funny channel
Heart rate

ABSTRACT

Research purpose: The sinus node (SN) is the heart's primary pacemaker. Key ion channels (mainly the funny channel, HCN4) and Ca²⁺-handling proteins in the SN are responsible for its function. Transcription factors (TFs) regulate gene expression through inhibition or activation and microRNAs (miRs) do this through inhibition. There is high expression of macrophages and mast cells within the SN connective tissue. ‘Novel’/unexplored TFs and miRs in the regulation of ion channels and immune cells in the SN are not well understood. Using RNAseq and bioinformatics, the expression profile and predicted interaction of key TFs and cell markers with key miRs in the adult human SN vs. right atrial tissue (RA) were determined.

Principal results: 68 and 60 TFs significantly more or less expressed in the SN vs. RA respectively. Among those more expressed were ISL1 and TBX3 (involved in embryonic development of the SN) and ‘novel’ RUNX1-2, CEBPA, GLI1-2 and SOX2. These TFs were predicted to regulate HCN4 expression in the SN. Markers for different cells: fibroblasts (COL1A1), fat (FABP4), macrophages (CSF1R and CD209), natural killer (GZMA) and mast (TPSAB1) were significantly more expressed in the SN vs. RA. Interestingly, RUNX1-3, CEBPA and GLI1 also regulate expression of these cells. MiR-486-3p inhibits HCN4 and markers involved in immune response.

Major conclusions: In conclusion, RUNX1-2, CSF1R, TPSAB1, COL1A1 and HCN4 are highly expressed in the SN but not miR-486-3p. Their complex interactions can be used to treat SN dysfunction such as bradycardia. Interestingly, another research group recently reported miR-486-3p is upregulated in blood samples from severe COVID-19 patients who suffer from bradycardia.

© 2021 The Authors. Published by Elsevier Ltd. This is an open access article under the CC BY license (<http://creativecommons.org/licenses/by/4.0/>).

1. Introduction

The sinus node (SN) is the heart's primary pacemaker because of its unique morphological, molecular and functional properties (Dobrzynski et al., 2013). Anatomical studies show that the human

SN is an extended complex crescent-shaped structure that is located at the superior vena cava and right atrium junction, extending along the crista terminalis (Stephenson et al. 2012, 2017; Chandler et al., 2009).

Since the discovery of the SN in 1907 (Keith and Flack 1907), the molecular mechanisms that regulate the pacemaking and conduction function of the SN remain an area of intense exploration. The SN has a unique expression of ion channels, Ca²⁺ handling proteins previously analysed in the human SN by our group (Chandler et al., 2009). These ion channels and Ca²⁺ handling

* Corresponding author. Address: CTF Building, 46 Grafton Street, Manchester, M13 9NT, UK.

E-mail address: halina.dobrzynski@manchester.ac.uk (H. Dobrzynski).

proteins are responsible for the membrane voltage and Ca^{2+} clocks - two main mechanisms that are involved in maintaining the SN automaticity which has recently been elegantly summarised by DiFrancesco, D., 2020 in his mini review (DiFrancesco 2020).

An interesting “funny journey” involved in the so-called membrane clock, started with Brown, DiFrancesco and Noble in the late 70's when they discovered the “funny” current (I_f) (Brown et al. 1979). Since then I_f has been extensively studied by DiFrancesco and colleagues (see DiFrancesco D. 2020 for all relevant references) (DiFrancesco 2020). This current is generated by hyperpolarisation-activated cyclic nucleotide-gated channels, activated by cyclic adenosine monophosphate (cAMP), during phase 4 of the SN's action potential. The main isoform of the funny channel, HCN4, is highly expressed in the human SN (Dobrzynski et al., 2013).

Through activation or inhibition of their targets, transcription factors (TFs) regulate the expression of ion channels, Ca^{2+} -handling proteins and other molecules involved in SN function. T-box factors (TBX3, TBX5 and TBX18) and homeodomain factors (SHOX2, ISL1 and NKX2-5) are crucial TFs that are well established to be involved in the development of the SN, heart embryogenesis and are also expressed in adulthood (Petkova et al., 2020; Hoogaars et al., 2007; Christoffels et al., 2010). In the SN, these TFs enhance the expression of genes that are more abundant in the SN (e.g., HCN4) and suppress those that are less expressed in the SN (e.g. cardiac Na^+ channel, SCN5A/ $\text{Na}_v1.5$ and main cardiac gap junctional channel, Cx43) (Park and Fishman 2017).

In many tissues including the heart, small non-coding RNA molecules (microRNAs, miRs) regulate the post-transcriptional expression of many protein-coding genes (Thum et al., 2007; Callis and Wang 2008).

We have recently shown that there is complex expression of key miRs involved in pacemaking mechanisms and we confirmed that miR-486-3p regulates HCN4 expression leading to bradycardia when upregulated in the rodent SN (Petkova et al., 2020).

The SN is embedded in an extensive connective tissue as we have previously shown (Chandler et al., 2009; Kharche et al., 2017). Within this connective tissue, there are many elastic fibres and non-cardiac cell types such as fibroblasts, macrophages, mast, fat, neuronal, endothelial and epithelial. Due to a low abundance of mitochondria and contractile/cytoskeletal proteins, nodal cardiomyocytes are referred to as “empty” (Choudhury et al. 2015; Boyett et al. 2000).

The SN is characterised by its complex morphology and mechanisms. Therefore, to bring more fun to the “funny” journey, we aimed to: use next generation sequencing (NGS) to identify other key unexplored ‘novel’ TFs in the human SN vs. RA; use ingenuity pathway analysis (IPA) to identify predicted interactions amongst ‘novel’ TFs and ‘embryonic’ TFs (well known to be involved in the embryonic development of the SN) described by (van Eif et al., 2018) and identify any predicted interactions amongst key TFs with those genes involved in pacemaker mechanisms - especially the funny channel; determine the expression of key markers of different cells type as well as organelles in the SN vs. RA and identify any predicted interactions amongst TFs and markers; identify predicted interactions of TFs, markers and recently published key miRs (Petkova et al., 2020).

The dysfunction of the two clock pacemaker mechanisms as well as changes to tissue morphology (e.g., in fibrosis) contribute to the development of sinus node dysfunction (SND), which is characterised by tachycardia and bradycardia, sinus pauses, sinus arrest, sinoatrial exit block etc – a common problem in ageing, heart failure, obesity and atrial arrhythmias (Dobrzynski et al., 2013; Zhang et al., 2000).

Interestingly, it has recently been shown, that in severe COVID-19 patients who suffer from bradycardia (Amaratunga et al., 2020;

Capoferri et al., 2020), miR-486-3p is shown to be elevated in their RBC-depleted whole blood due to immune system response (Tang et al., 2020). Furthermore, in the mouse atrioventricular node (AV node), an unusually high expression of immune cells (such as macrophages) has been discovered by (Hulsmans et al., 2017). They noticed that depletion of macrophages in mice results in AV block and bradycardia (Hulsmans et al., 2017). They also noticed that HCN4-expressing cardiomyocytes in the AV node frequently interperse with macrophages (Hulsmans et al., 2017). Could this upregulation of circulating miR-486-3p in the coronavirus disease 2019 (COVID-19) patients lead to downregulation of HCN4 hence reduced heart rate via immune response?

This study seeks to contribute further to our understanding of the morphological, molecular and functional characteristics of the human heart's primary pacemaker and we hope that this will set a scene for this funny journey to continue for 40 more years and beyond, and thus provide new insight into the treatment of SND.

2. Materials and methods

2.1. Specimens' information

Human specimens were obtained, dissected and frozen by co-authors in Romania (FP) and Australia (PM) under their local ethical approval procedures. Specimens from Australia (Table 1, specimens 6, 7, 10) were obtained for research from hearts that were unsuitable for heart transplantation (Ethics Approval EC256, The Prince Charles Hospital Ethics Committee). Written authorisation for removal and use of tissue was obtained from the available Senior Next of Kin. Post-mortem specimens from Rumania (Table 1, specimens 2–5, 8, 9) were from suicide and road traffic accidents people and no informed consent was required for FP to remove and use the tissue for research. After transfer to the University of Manchester, specimens were stored under the Human Tissue Act 2004. The age of patients ranged between 19 and 54. Further information can be found in Table 1 and in (Petkova et al., 2020). The quality and quantity of RNA was also assessed in (Petkova et al., 2020).

2.2. Sectioning and histology

Ten frozen tissue blocks were sectioned perpendicular to the crista terminalis and superior vena cava (SVC) and cryosections were 10–30 μm thick.

Masson's trichrome histological staining was used to confirm the location of the SN. This is our preferred staining method for the SN identification, because nodal cells (stained purple) are embedded into significant amounts of connective tissue (stained blue) as previously described (Chandler et al., 2009) and can be seen in Fig. 1A–C.

Table 1
Patient information.

Specimen Number	Patient Age	Patient Gender	Cause of death
1	29	M	Road accident
2	22	M	Road accident
3	66	M	Suicide
4	19	M	Suicide
5	60	M	Sudden death
6	54	M	Intracranial haemorrhage
7	42	M	Subarachnoid haemorrhage
8	19	M	Suicide
9	21	M	Suicide
10	54	M	Intracranial haemorrhage

2.3. Next generation sequencing for mRNA and qPCR for miRs

Ten SN samples were collected from the area around the SN artery (Fig. 1) and RA samples from the pectinate muscles remote from the SN region as described by (Petkova et al., 2020). NGS for RNA-sequencing (RNA-seq) was performed on RNA samples from 3 SN, 3 RA (Table 1, specimens 8, 9, 10) and qPCR for miRs was performed on RNA samples from 7 SN, 7 RA (Table 1, specimens 1–7) as described in our recently published study (Petkova et al., 2020).

We used Bcl2fastq software (2.17.1.14) to generate mRNA expression database for the SN vs. RA as individual values as well as mean values, Log2fold change, P values, adjusted P values and calculated percent as shown in Table 2 – 4 from the SN and RA specimens. Our published principal component analysis confirmed the SN samples are similar and different from RA samples (Petkova et al., 2020).

2.4. Bioinformatics

2.4.1. Ingenuity Pathway Analysis

The Ingenuity Pathways Analysis (IPA; Ingenuity systems, Qiagen) knowledge-base contains information about experimentally validated genes, origin and function of which can be found in the published scientific literature and other databases such as TarBase, miRBase (<http://www.mirbase.org/>), Genome (<https://genome.ucsc.edu>), RNA22 (<https://cm.jefferson.edu/rna22/>) and TargetScan Human (<http://www.targetscan.org/>). Identification of the transcription factors/transcription regulators (TFs), which were significantly more expressed (\log_2 fold change > 1), or significantly less expressed (\log_2 fold change < -1) in the SN vs. RA in our data set was performed using IPA software. Our NGS dataset that was uploaded into IPA and contained the gene ID of 2595 mRNAs significantly less or more expressed in the SN vs. RA, gene ID, base mean values ('experimental intensity'), \log_2 fold change

('experimental log ratio'), P value ('experimental P-value') and adjusted P value ('Padj'). The uploaded dataset was 'analysed/filtered' by performing 'Core Analysis' to compare our dataset to IPA knowledge base. This allowed us to identify 1424 mRNAs significantly more/less expressed mRNAs in the SN vs. RA within our data set. A Log2foldchange cut-off of -1.5 to 1.5 was selected in order to narrow down and select only significantly expressed molecules in our dataset.

In order to identify TFs from 1424 significantly more/less expressed mRNAs in the SN vs. RA, within IPA, we selected the 'transcription regulator' option from the 'molecule type' drop-down menu and performed analysis. We identified 68 TFs that were significantly more expressed in the SN vs. RA and 60 TFs that were significantly less expressed in the SN vs. RA (see Tables 2 and 3).

After identifying all 128 differentially expressed TFs, we were interested in investigating how these TFs regulate different cell types and organelles in the SN vs. RA. In order to do this, key markers for each cell types and organelles (see Table 4) were selected from our NGS dataset, based on their gene description. The estimation of NGS-based expression of key markers was correlated with the TFs pattern. In total, 48 key markers were selected from our NGS dataset (Table 4). The reliability of selected genes as markers of each cell type and/or organelles (see Results section for further information) was confirmed on the basis of published literature and IPA data).

2.4.2. Creating and analysing interactions/networks in IPA

For each TF identified, individual pathways' network was created. In total 128 individual pathways were created and predicted targets ranged in individual networks from 0 to 153. Out of 128 only 27 TFs were identified to show interactions amongst each other. We also searched for interactions of 27 TFs with 48 selected markers of cells/organelles and 11 TFs were identified as directly

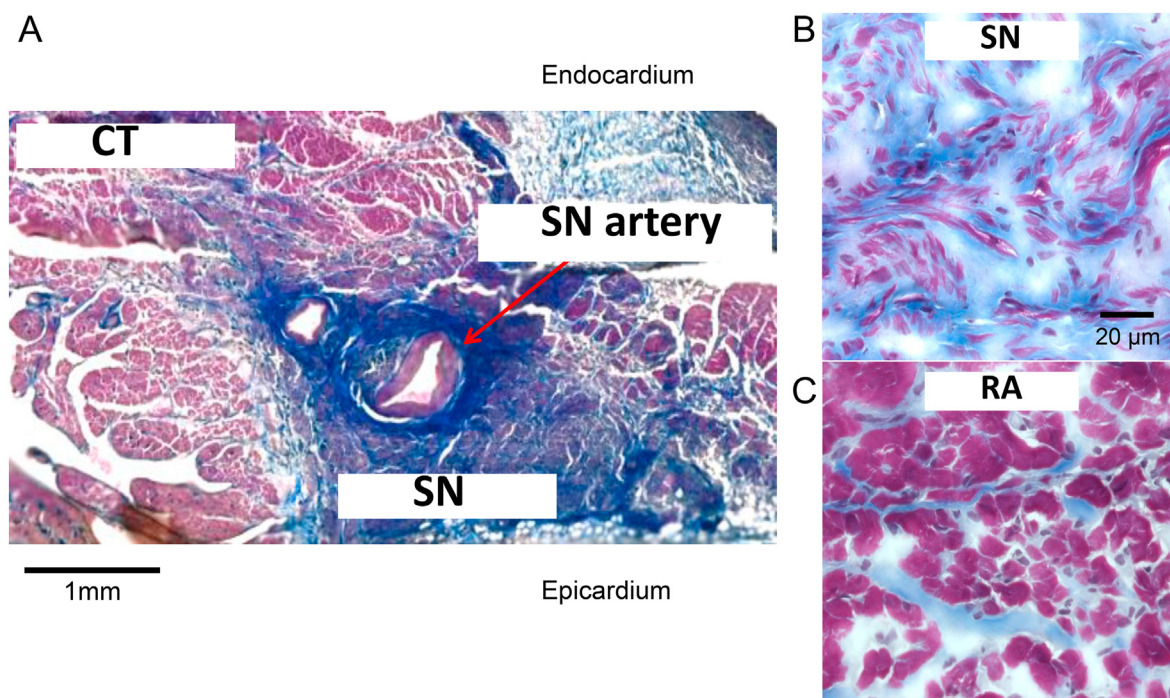


Fig. 1. Morphology of the sinus node in comparison to right atrium. A, Masson trichrome stained section through the sinus node showing nodal myocytes around the sinus node artery. Myocytes are stained purple and connective tissue is stained blue. The sinus node tissue is evident by the extensive connective tissue region. B and C, closer view of the sinus node (B) and right atrium (C). CT = crista terminalis; SN = sinus node.

Table 2

Transcription factors that significantly more expressed in the sinus node vs. right atrium. The table shows gene names of 68 transcription factors; expression in the SN and RA \pm SEM; log₂foldchange; adjusted P value (all calculated using the Bcl2fastq software 2.17.1.14); and % of each transcription factor in the SN/RA (where 100% expression is in the RA).

Transcription factor (gene name)	SN mean	SN \pm SEM	RA mean	RA \pm SEM	Log2fold change	Adjusted P value	% (SN/RA)
AKNA	677.906	142.210	319.611	57.408	1.055	1.134E-03	47.147
ATF5	540.281	69.534	247.840	41.619	1.127	1.312E-03	45.872
BACH2	226.331	59.842	97.960	20.395	1.130	9.556E-03	43.282
BATF	61.748	22.495	11.799	6.641	2.674	3.648E-04	19.109
BCL11B	39.23	22.307	8.633	6.676	2.608	5.776E-03	22.006
CEBPA	282.356	65.316	52.355	24.256	2.653	1.464E-08	18.542
CERS5	896.236	87.785	433.370	61.242	1.054	1.014E-03	48.354
CIITA	398.745	111.455	149.505	36.256	1.381	7.075E-05	37.494
DLX1	108.905	48.375	20.363	11.822	2.433	1.883E-04	18.698
DLX2	48.099	20.607	8.451	4.757	2.738	2.228E-03	17.570
DTX1	249.000	39.096	74.937	20.187	1.793	8.086E-06	30.095
FOXD3	385.436	175.537	84.572	47.553	2.199	5.883E-07	21.942
GLI1	183.878	38.227	57.936	7.130	1.607	1.140 E-03	31.508
GLI2	347.127	75.203	137.196	19.863	1.283	3.754E-03	39.523
HDAC10	38.406	10.630	6.879	1.777	2.465	4.688E-03	17.912
HEY2	457.506	13.418	165.326	11.391	1.463	1.335E-05	36.136
HIC1	1362.142	353.431	521.178	112.365	1.323	1.587E-05	38.262
HLX	782.153	165.116	306.64	117.080	1.468	1.079E-05	39.205
HOXA3	122.178	35.992	18.937	3.932	2.610	6.601E-06	15.500
HOXA5	61.832	13.331	12.492	4.679	2.387	6.226E-04	20.203
HOXB2	776.382	153.160	166.100	53.351	2.319	1.204E-12	21.394
HOXB3	440.507	40.289	76.885	29.006	2.722	1.332E-10	17.454
HOXB4	221.93	24.513	37.187	24.114	3.091	1.103E-08	16.756
HOXC4	107.812	34.363	15.536	3.518	2.723	1.052E-06	14.411
HOXD8	85.567	7.471	26.220	9.035	1.852	3.520E-03	30.642
HR	419.256	156.295	151.074	40.595	1.249	3.728 E-03	36.034
IER2	5491.416	1798.91	2118.285	678.573	1.361	6.376E-07	38.574
IKZF1	189.948	118.644	46.666	22.659	1.792	9.265E-05	24.568
IRF7	493.157	124.674	213.957	75.260	1.256	4.397E-04	43.385
ISL1	208.879	83.062	0.000	0.000	12.140	9.242E-05	0.479
KCNIP3	389.946	148.584	138.006	68.334	1.607	6.986E-06	35.391
KLF2	6750.78	1240.935	2732.485	295.238	1.253	1.599E-05	40.477
LBH	2394.91	443.351	1091.937	135.245	1.093	4.424E-03	45.594
LMO2	687.174	86.682	319.748	115.363	1.280	5.251E-03	46.531
LYL1	379.379	41.071	181.422	9.254	1.038	6.576E-03	47.821
LZTS1	234.963	59.310	76.747	13.548	1.572	2.987E-04	32.664
MAF	1475.905	276.728	548.679	102.208	1.418	1.014E-06	37.176
MEOX1	1350.634	629.078	662.000	360.592	1.108	3.625E-04	49.014
MLXIPL	234.667	80.361	79.937	22.441	1.522	5.286E-04	34.064
MSC	1603.090	546.664	490.110	191.398	1.798	1.287E-09	30.573
MYCN	61.499	5.4330	10.308	4.002	2.689	2.365E-04	16.762
NFKBIZ	870.258	184.484	329.93	38.444	1.338	9.408E-04	37.912
NLRC5	341.150	66.534	136.747	23.483	1.303	4.248E-04	40.084
NUPR1	5710.273	179.142	2548.803	440.630	1.199	1.857E-04	44.635
PHOX2B	74.570	23.194	10.887	6.165	3.131	3.272E-05	14.600
PRDM16	456.732	25.624	137.165	9.657	1.727	6.020E-07	30.032
PYCARD	301.691	77.164	101.776	6.302	1.475	2.029E-04	33.735
RUNX1	412.141	61.976	112.900	13.806	1.841	1.892E-06	27.393
RUNX2	101.047	16.069	25.667	3.726	1.959	4.618E-04	25.401
RUNX3	97.062	41.225	25.676	14.122	2.041	3.027E-04	26.453
SHOX2	1039.710	260.04	223.735	78.368	2.250	1.719E-08	21.519
SMARCD2	1516.491	365.786	742.922	193.867	1.030	5.407E-04	48.990
SOX10	2026.732	753.631	662.197	179.093	1.394	6.052E-05	32.673
SOX13	1369.973	110.721	631.294	47.328	1.104	2.6400E-04	46.081
SOX17	584.337	39.839	290.279	85.723	1.101	2.817E-03	49.677
SOX2	153.772	53.947	21.604	6.022	2.776	1.521E-08	14.049
SOX9	3348.057	108.482	1507.809	373.240	1.231	5.124E-04	45.035
SPI1	381.480	186.713	119.83	69.676	1.799	5.273E-07	31.412
SREBF1	4927.952	1336.040	2308.654	325.077	1.001	1.191E-03	46.848
TBX1	131.445	67.297	36.094	25.787	2.261	2.286E-03	27.459
TBX18	1190.75	86.23333	470.920	64.5568	1.345	4.956E-05	39.548
TBX2	1749.702	175.142	658.368	122.010	1.434	8.247E-05	37.627
TBX3	1972.733	469.804	543.995	115.281	1.845	7.316E-07	27.576
TGFB111	2466.217	284.716	872.904	75.898	1.477	1.511E-06	35.394
TSC22D3	9758.316	3669.472	4380.536	1004.956	1.030	2.313E-03	44.891
TWIST1	377.545	84.672	143.105	42.079	1.470	9.327E-05	37.904
VAV1	107.197	57.514	24.553	11.685	1.912	3.517E-03	22.904
VENTX	98.187	15.838	10.922	3.750	3.294	7.27E-08	11.123

Table 3

Transcription factors significantly less expressed in the sinus node vs. right atrium. The table shows gene names of 60 transcription factors; expression in the SN and RA \pm SEM; log₂foldchange; adjusted P value (all calculated using the Bcl2fastq software 2.17.1.14); and % of each transcription factor in the SN/RA (where 100% expression in is the RA).

Transcription factor (gene name)	SN mean	SN \pm SEM	RA mean	RA \pm SEM	Log2fold change	Adjusted P value	% (SN/RA)
ACTN2	21634.431	7833.845	59256.856	5474.155	-1.662	1.398E-04	36.510
ASB15	123.674	37.790	1739.861	474.424	-3.848	8.954E-45	7.108
ASB4	23.684	6.879	70.022	13.042	-1.645	8.560 E-03	33.824
ASB5	16.300	7.161	133.294	23.129	-3.233	4.37E-09	12.228
ASB8	637.596	50.060	1291.190	48.396	-1.037	7.061E-04	49.380
BRCA1	126.173	10.455	282.040	60.510	-1.120	4.219E-03	44.736
CAND2	590.303	136.063	1630.819	216.947	-1.539	4.103E-07	36.197
CASKIN1	98.435	21.743	370.275	36.706	-1.973	1.854E-06	26.584
CBX4	602.128	129.064	1333.066	241.324	-1.186	5.616E-04	45.169
CERS6	1222.011	380.239	3551.558	784.415	-1.665	4.948E-07	34.408
CHCHD3	1259.526	186.752	2966.429	190.626	-1.273	1.240E-04	42.459
COPS5	794.737	79.793	1980.436	268.256	-1.315	5.682E-05	40.129
DCAF6	2723.082	396.688	9437.394	312.369	-1.836	7.386E-10	28.854
FEM1A	1145.289	200.935	2378.667	319.940	-1.088	1.098E-03	48.148
FHL2	4488.626	1459.722	12576.092	7584.572	-1.173	7.422E-03	35.692
GRIP1	68.755	20.714	197.073	92.005	-1.422	4.884 E-03	34.888
GTF2I	466.899	108.962	1313.898	292.866	-1.514	3.536E-07	35.535
GTF3A	2393.535	216.862	5320.791	640.947	-1.153	3.186E-04	44.985
HAND1	6.150	1.766	56.440	19.813	-3.029	9.348E-05	10.897
HDAC9	258.074	32.224	549.930	51.861	-1.112	7.917E-04	46.928
HIVEP2	538.440	57.714	1286.742	295.821	-1.201	3.419E-03	41.845
HLF	737.032	112.679	1921.831	194.315	-1.416	7.18E-07	38.350
HMGA1	420.776	54.922	856.277	41.092	-1.058	2.286E-03	49.140
HOPX	194.455	62.767	1157.648	446.288	-2.549	7.699E-18	16.797
HSF2	422.250	19.749	1691.197	128.986	-2.009	3.853E-13	24.968
KANK1	2571.452	526.933	6727.928	204.166	-1.458	1.868E-06	38.221
KAT2B	1121.328	73.391	3010.476	471.115	-1.408	1.318E-05	37.247
KCTD1	401.470	33.964	1268.950	310.905	-1.602	1.537E-06	31.638
MEF2A	2578.413	233.194	7634.998	757.997	-1.577	6.563E-09	33.771
MITF	598.513	213.906	1802.958	727.443	-1.578	7.884E-07	27.112
MKL2	956.58	331.959	2660.534	1659.107	-1.075	3.840E-04	35.954
MLIP	1407.866	431.711	6203.713	1222.175	-2.268	1.195E-13	22.694
MLX	969.099	65.291	1959.077	140.850	-1.026	4.594E-04	49.467
MYT1	3.126	2.298	32.681	10.734	-3.899	4.566E-04	9.566
NCOA2	835.154	95.142	1727.300	381.213	-1.018	1.960E-03	48.350
NCOA4	3405.760	431.596	8749.216	571.405	-1.389	4.000E-07	38.926
NFE2L1	10964.520	1829.637	28663.931	4334.959	-1.400	6.824E-07	38.252
NKX2-5	1116.112	308.341	5549.073	1761.584	-2.287	1.198E-10	20.113
NOCT	43.806	0.646	159.363	65.339	-1.663	1.464E-03	27.488
NPAS2	736.022	124.618	1503.172	308.439	-1.017	6.937E-03	48.965
PBX3	1224.393	47.244	3027.975	201.759	-1.314	5.361E-06	40.436
PPARGC1A	858.408	314.360	2627.464	651.225	-1.814	6.539E-05	32.671
PPP1R13 L	859.854	207.086	3018.562	350.626	-1.900	3.963E-10	28.486
PROX1	514.407	198.737	1897.360	415.061	-2.021	9.071E-09	27.112
RFX2	352.593	55.933	918.063	340.632	-1.133	7.258E-03	16.797
SALL1	9.075	3.795	67.701	33.401	-2.798	4.02E-04	13.405
SATB1	493.157	124.674	213.957	75.260	1.256	2.947E-04	45.573
SFMBT1	138.972	33.019	327.697	65.700	-1.285	2.152E-03	42.409
SMYD1	1604.484	589.106	5358.148	819.541	-1.960	3.263E-06	29.945
STAT4	140.858	42.809	581.692	74.953	-2.153	4.961E-08	24.215
TBX20	400.478	52.818	2094.381	304.501	-2.392	3.222E-13	19.122
TBX5	2894.793	967.928	9297.928	1916.888	-1.825	8.549E-07	31.134
TCEA3	828.140	135.026	1736.017	182.424	-1.098	9.300E-04	47.703
TEAD1	2063.731	110.694	4656.889	513.296	-1.174	6.386E-05	44.316
TRIM24	400.102	64.223	875.524	95.024	-1.160	3.398E-04	45.699
VGLL2	32.552	29.600	60.589	25.769	-2.293	5.569E-03	43.727
YAF2	766.448	115.140	1719.524	37.999	-1.211	1.716E-04	44.573
YBX3	6104.641	277.970	13980.831	1611.231	-1.191	2.562E-05	43.664
ZBTB20	158.281	30.758	626.103	388.802	-1.494	7.478E-04	25.280
ZNF189	453.549	22.899	1185.676	426.572	-1.228	1.061E-03	38.252

interacting with 6 different key markers. In addition, we identified those TFs that directly and/or indirectly regulate the key genes involved in pacemaking.

Previously we predicted 15 miRs, which interact with the key molecules involved in the SN's pacemaking (Petkova et al., 2020). Therefore, we were interested if these key 15 miRs interact with differentially expressed TFs and markers. The interaction for 27 TFs

and 48 markers with 15 miRs was tested using IPA and identified interaction is shown in Table 5.

2.4.3. Binding sites identification

For all mRNAs, the sequence of their 3'-untranslated regions (UTR) were obtained using Genome (<https://genome.ucsc.edu>). The sequence of all miRs were obtained using miRBase (<http://www>.

Table 4

Markers for different cell types and organelles expressed in the sinus node vs. right atrium. The table shows gene names of markers (see Fig. 11); expression in the SN and RA \pm SEM; log2foldchange; adjusted p value (all calculated using the Bcl2fastq software 2.17.1.14); and % of each marker in the SN/RA (where 100% expression in the RA).

Marker (gene name)	SN mean	SN \pm SEM	RA mean	RA \pm SEM	Log2fold change	Adjusted P value	% (SN/RA)
ACTG2	1242.990	432.331	269.4733	41.119	2.050	3.678E-08	461.266
ACTN2	21634.430	7833.845	59256.86	5474.156	-1.662	1.398E-04	36.510
CD209	219.460	125.490	76.090	50.976	1.581	5.850E-04	288.436
CD44	2595.847	604.517	1277.290	291.791	1.035	2.819 E-03	203.230
CERCAM	3012.570	893.747	1013.453	329.419	1.550	9.575E-08	297.258
COL14A1	9472.997	1597.945	4242.62	953.404	1.183	1.971E-03	223.282
COL1A1	25501.240	4503.298	7930.85	1311.630	1.665	1.013E-09	321.545
COL1A2	58118.510	10427.945	23600.197	3021.211	1.271	1.182E-05	246.263
COL3A1	27758.890	8618.337	11647.983	2840.022	1.181	2.198E-05	238.315
COL5A1	4966.340	1553.434	2086.927	430.746	1.128	2.188 E-04	237.974
COL5A3	2761.960	915.702	1141.823	348.382	1.187	8.693E-05	241.890
COL6A1	25169.030	5652.913	12218.197	2535.694	1.025	6.598E-04	205.996
COL6A2	46818.51	6355.024	20505.690	4243.743	1.224	1.013E-04	228.320
COL8A2	600.92	163.656	197.187	34.931	1.515	8.104E-04	304.747
COL9A2	322.08	104.366	88.167	15.339	1.715	5.012E-05	365.308
COL9A3	682.560	288.143	210.997	56.040	1.390	1.507E-03	323.493
CSF1R	874.533	395.078	274.083	108.957	1.838	2.752E-09	353.943
DES	112041.9	40572.007	202808.3	17832.319	-1.141	0.0071819	55.245
DMD	2411.157	277.11	8679.833	1901.656	-1.808	4.415E-08	27.779
EMILIN1	3317.597	360.138	1381.06	302.828	1.316	2.127E-05	240.221
FABP4	1802.743	350.257	316.377	79.730	2.539	9.571E-11	569.809
GZMA	59.184	41.363	8.052	2.872	2.387	3.830E-04	735.000
HLA-DMA	829.197	77.720	328.510	65.641	1.369	2.325E-05	252.411
HLA-DMB	197.270	34.208	64.797	13.501	1.620	2.046E-04	304.445
HLA-DOA	281.580	59.060	78.817	18.096	1.849	1.412E-06	357.259
HLA-DPA1	3574.673	333.741	1565.163	94.958	1.172	6.401E-05	94.958
HLA-DPB1	2027.295	407.980	931.253	128.927	1.275	1.321E-05	217.695
HLA-DQA1	672.007	98.565	231.413	39.456	1.535	1.76E-06	290.392
HLA-DQB1	1358.700	119.051	592.570	82.459	1.202	2.075E-04	229.289
HLA-DRA	4667.940	808.427	2002.060	235.036	1.182	6.295E-05	233.157
HLA-DRB1	4042.847	630.230	1702.450	104.091	1.202	5.656E-05	237.472
HLA-DRB5	1214.300	777.612	520.970	302.671	1.128	6.960E-04	233.084
INA	61.443	18.434	7.337	6.157	3.770	1.962E-04	837.483
MRPL15	1129.537	234.793	2254.08	289.964	-1.044	7.607E-03	50.111
MRPL33	1310.670	180.021	2891.307	306.905	-1.161	5.854E-04	45.331
MRPL35	1054.260	163.380	2374.223	25.602	-1.220	1.458E-04	44.404
MRPL39	449.207	36.865	985.8433	149.484	-1.118	9.678E-04	45.5666
MRPL50	540.197	47.376	1071.587	32.518	-1.009	1.225 E-03	50.411
MRPS23	674.4633	103.967	1396.073	128.115	-1.081	5.398E-04	48.311
MRPS30	667.847	79.874	1635.447	133.496	-1.316	7.679E-06	40.836
MRPS33	721.797	49.514	1461.570	210.658	-1.005	3.432E-03	49.385
MRPS36	539.670	44.411	1313.953	210.581	-1.264	2.877E-03	41.072
MRPS9	865.430	123.524	1804.787	260.927	-1.070	4.472E-03	47.952
MUC1	99.317	24.787	29.730	7.725	1.710	1.691E-03	334.062
MYH6	217807.900	83862.528	1066895.000	115574.238	-2.528	7.279E-13	20.415
TNNT2	52996.690	15892.935	144599.200	21446.601	-1.560	1.099E-04	36.651
TPSAB1	408.170	60.284	54.140	5.871	2.889	1.147E-16	753.916
TTN	27820.200	8702.962	154512.700	72399.518	-2.376	5.388E-08	18.005

mirbase.org/). The sequence of the miRs and their predicted target mRNAs were uploaded into RNA22 (<https://cm.jefferson.edu/rna22/>) or TargetScan Human (<http://www.targetscan.org/>). The number of miRs binding sites on their predicted mRNAs is summarised in Table 5.

2.4.4. Heat maps

Heat maps were created using Heatmapper (<http://www.heatmapper.ca/expression/>). To do this, a dataset containing gene names and the normalised count of each gene expressed in each SN sample ($n = 3$, Tables 2–4) or RA sample ($n = 3$, Tables 2–4) was uploaded. Greener represents higher while redder represents lower expression in the SN vs. RA. Z-score of -1 indicates that a sample is one standard deviation below the mean value; and a Z-score of 1 indicates a sample is one standard deviation above the mean value (see Tables 2–4 for mean values).

2.4.5. Graphs and statistical analysis

GraphPad Prism 8.4.3. software was used for statistical analysis and for making graphs. Data are shown as mean \pm SEM in Tables 2–4 and graphs are plotted as % SN/RA. Significant differences were identified with one-way ANOVA test; differences were assumed as significant at $P < 0.001$.

3. Results

3.1. The sinus node region is characterised by extensive connective tissue and fewer myocytes

To confirm the location of the SN, Masson's trichrome staining was performed as shown in Fig. 1 as previously shown by (Chandler et al., 2011; Stephenson et al., 2017; Petkova et al., 2020). The SN myocytes (in purple) surround the SN artery and are embedded in a network of connective tissue (in blue).

Table 5

Predicted microRNA-transcription factor and microRNA-marker interactions. This data is based on the expression of microRNAs from our previous study by [Petkova et al. \(2020\)](#) and the expression of transcription factors and markers from this study. From left to right, the columns show miR name; expression of each miRs in the sinus node vs. the right atrium; predicted targets according to RNA22 and TargetScan Human; expression profile of each target in the sinus node vs. the right atrium; the number of binding sites on the target according to RNA22 and TargetScan Human. Bold represents those that are upregulated in the sinus node compared to the right atrium. -, no predicted marker targets. TF = Transcription factor; HCX = Histo-compatibility complex. All predicted interactions from IPA were chosen for this table that were functionally validated.

miRNA	miRNA expression in SN vs. RA based on Petkova et al. (2020)	Gene name of predicted target	mRNA expression based on this study	Total no. of binding sites for each miRNA on predicted target P<0.05 and P>0.05
hsa-miR-10b-5p	↑	TBX5 (TF)	↓	1
hsa-miR-30c-5p	↓	COL1A1 (Collagen)	↑	0
		RUNX2 (TF)	↑	2
		COL1A2 (Collagen)	↑	0
		COL9A3 (Collagen)	↑	1
		COL5A1 (Collagen)	↑	0
hsa-miR-133a-3p	↓	COL1A1 (Collagen)	↑	1
		RUNX2 (TF)	↑	0
		HLA-DOA (HCX)	↑	0
		TPSAB1 (Mast cells marker)	↑	1
		COL9A2 (Collagen)	↑	0
hsa-miR-153-3p	↑	MITF (TF)	↓	1
		MEF2A (TF)	↓	1
		PPARGC1A (TF)	↓	1
hsa-miR-215-5p	↑	NKX2-5 (TF)	↓	1
hsa-miR-422a	↓	TBX3 (TF)	↑	2
		GLI2 (TF)	↑	3
hsa-miR-429	↓	SOX2 (TF)	↑	1
hsa-miR-486-3p	↓	LBH (TF)	↑	1
		LZTS1 (TF)	↑	12
		SOX13 (TF)	↑	3
		CERCAM (Endothelial cell marker)	↑	1
		TPSAB1 (Mast cell marker)	↑	2
		CD209 (Macrophage cell marker)	↑	1
		HLA-DRA (HCX)	↑	2
		HLA-DRB5 (HCX)	↑	1
		HLA-DRB1 (HCX)	↑	1
hsa-miR-512-5p	↑	NKX2-5 (TF)	↓	0
hsa-miR-938	↓	LBH (TF)	↑	2
		SOX2 (TF)	↑	2
hsa-miR-1225-3p	↑	NKX2-5 (TF)	↓	2
hsa-miR-483-3p	↓	LBH (TF)	↑	1
hsa-miR-1-3p	↓	–	–	–
hsa-miR-198	↑	–	–	–
hsa-miR-204-5p	↑	–	–	–

3.2. Identification of 'novel'/unexplored transcription factors in the sinus node vs. right atrium

Tables 2 and 3 list all transcription factors (TFs) that are significantly more or significantly less expressed in the SN vs. RA. Using IPA, we have identified 68 significantly more expressed and 60 significantly less expressed TFs in the SN vs. RA. The position of these TFs is shown in Fig. 2 (A, B) on Volcano plots. Most identified TFs are within a range of 0 to +5 or 0 to -5 log₂Foldchange with the exception of ISL1 (well known to be involved in the embryonic development of the SN) which is > 10 log₂Fold change.

The heat maps in Figs. 3A and 4A show expression profiles of TFs in individual SN and RA samples. As expected, there is some inter-individual variation in the expression of TFs within the range of 0–1 and 0 to -1 Row Z-score.

TF expression profiles are shown as percent in the SN/RA (Figs. 3B and 4B and Tables 2 and 3). It is interesting to observe that ISL1 is the most abundant TF in the adult human SN (Fig. 3B).

Amongst well known TFs (important for the embryonic development of the SN), TBX3 and SHOX2 are highly expressed in the adult SN compared to other TFs. Many 'novel'/unexplored TFs in the adult SN, were identified to be highly expressed e.g., FOXD3 (known to regulate cardiac neural crest progenitors in the mouse heart - (Nelms et al. 2011), DLX2 (known to regulate lymphocyte development - (Sunwoo et al., 2008), PHOX2B (known to be associated with congenital heart disease in humans (Lombardo et al., 2018), VENTX (known to promote myeloid cell differentiation that may differentiate into macrophages (Leitoguinho et al., 2019), SOX2 (known to be involved in stem cell preservation and self-renewal (Mallanna et al., 2010) and a few HOX-TFs members (e.g. HOXA3, HOXB4 and HOXC4) that play a major role in heart development and are highly relevant to human pathology (Lescroart and Zaffran 2018).

Interestingly, NKX2-5 and TBX5 (key embryonic TFs) are <50% expressed in the adult human SN vs. RA (Fig. 4B). Amongst 'novel' TFs that are least abundant in the human SN are ASB5 and ASB15

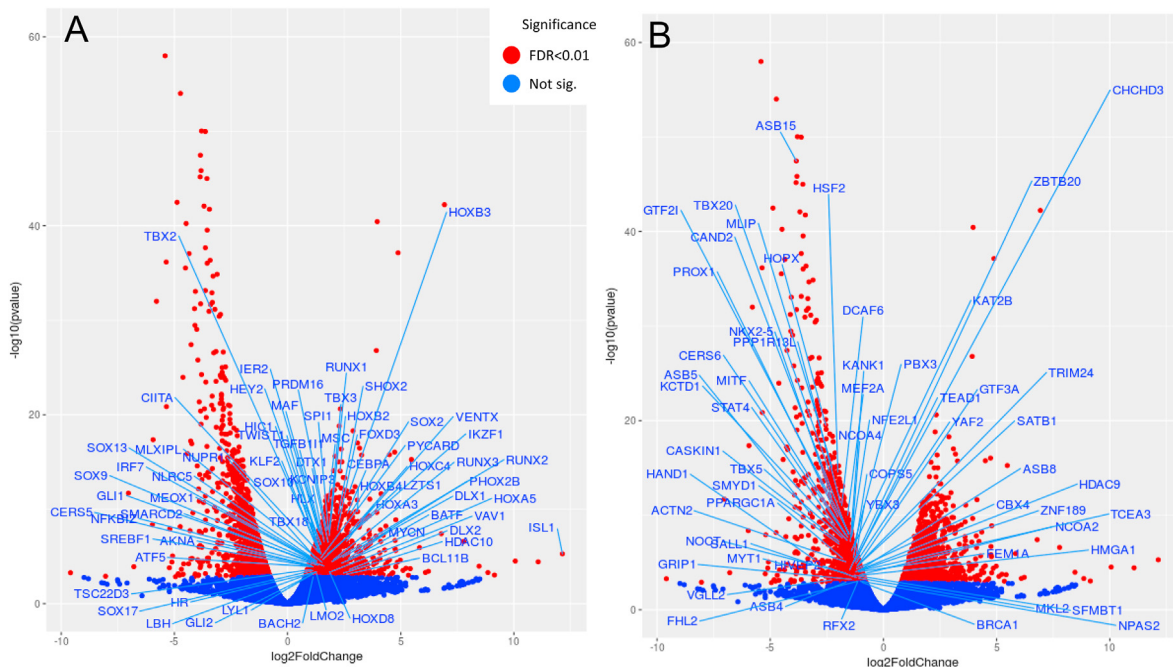


Fig. 2. Volcano plot of significantly more and significantly less expressed transcription factors in the sinus node vs. right atrium. **A**, location of 68 transcription factors that are significantly more highly expressed in the sinus node compared to right atrium. **B**, location of 60 transcription factors that are significantly less expressed in the sinus node, compared to the right atrium. See Tables 1 and 2 for details. Red = significantly more/less expressed mRNA; blue = non-significantly expressed mRNAs.

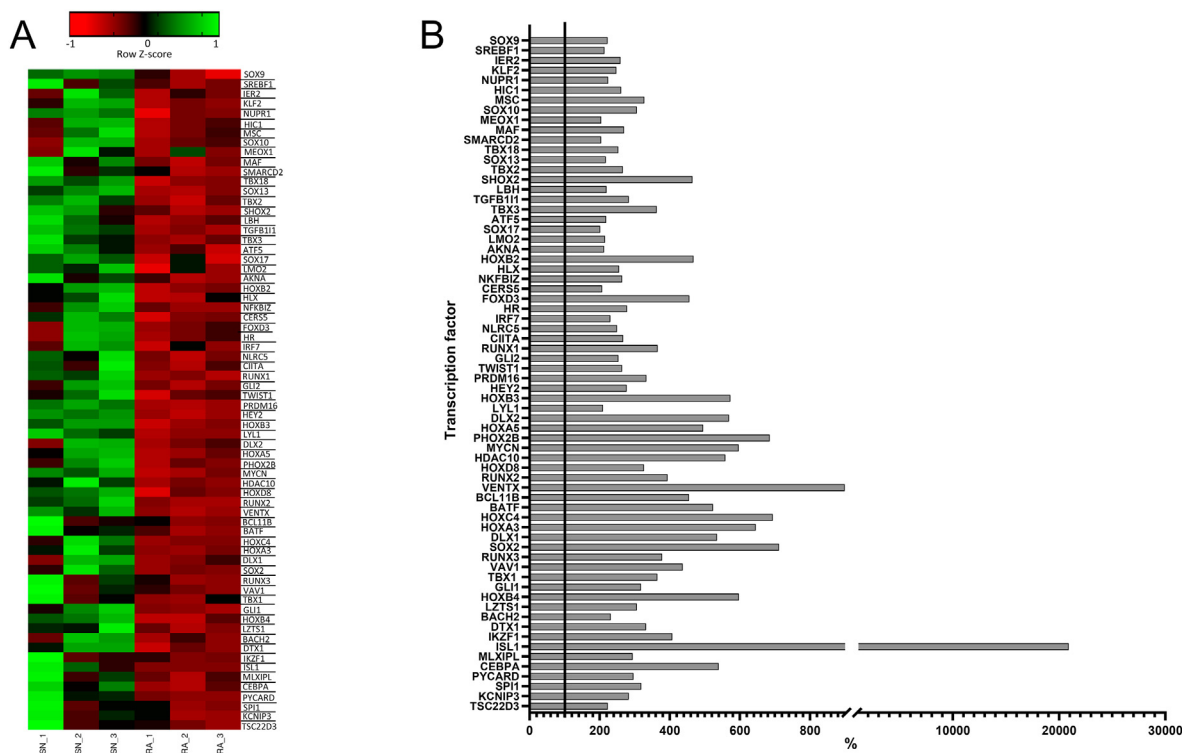


Fig. 3. Expression profile of 68 transcription factors that are significantly more expressed in the adult human sinus node vs. right atrial muscle. **A**, heat map shows inter-individual expression of each transcription factor in each sinus node (SN1 – SN3) and right atrium (RA1 – RA3) samples. **B**, mean expression of transcription factors in the sinus node vs. right atrium (n = 3) plotted as % SN/RA (see Table 2 for details). The black line at 100% represents the transcription factors expression in the right atrium (i.e., basal level). SN = sinus node; RA = right atrium.

(known to be associated with skeletal muscle growth (McDaneld et al. 2004) MYT1, known to promote neuronal cell differentiation, (Vasconcelos et al., 2016); HAND1, known to be associated

with cardiac cell differentiation, (Riley et al. 1998); SALL1, known to be associated with early heart development, (Morita et al., 2016); RFX2 (known to maintain brain development HOPX (known to

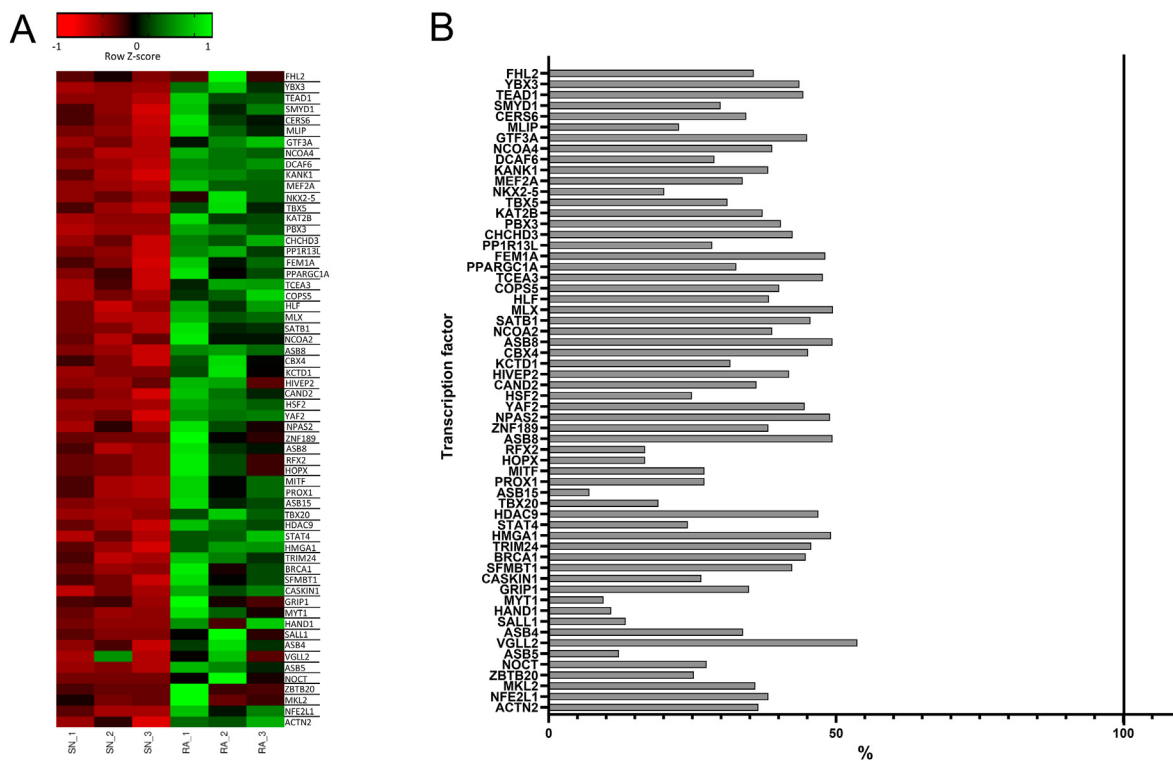


Fig. 4. Expression profile of 60 transcription factors that are significantly less expressed in the adult human sinus node compared vs. right atrial muscle. **A**, heat map shows inter-individual expression of each transcription factor in each sinus node (SN1 – SN3) and right atrium (RA1 – RA3) samples. **B**, mean expression of transcription factors in the sinus node vs. right atrium (n = 3) plotted as % SN/RA (see Table 3 for details). The black line at 100% represents the transcription factors expression in the right atrium (i.e., basal level). SN = sinus node; RA = right atrium.

regulate hypertrophy and maturation of cardiomyocytes (Friedman et al., 2018) (Fig. 4B).

3.3. Prediction of interactions amongst transcription factors and their predicted role in regulating HCN4 and Ca²⁺ proteins

One of the main aims of this study was to predict the interaction of the key ‘novel’ TFs with each other and with TFs known to be involved in the embryonic development of the heart (ISL1, TBX3, TBX5, NKX2-5, SHOX2) as well as to gain further insight into their relationship with HCN4 and Ca²⁺ handling proteins (RYR2, Na²⁺-Ca²⁺ exchanger, NCX1 and SERCA2A). An example of IPA-based interaction network is shown in Fig. 5 which includes well known TFs. ISL1 and TBX3 facilitate while NKX2-5 and TBX5 inhibit the expression of HCN4, and Ca²⁺ channels, Ca_v3.1 and Cav3.1, (Park and Fishman 2017). HCN4, RYR2, NCX1 and SERCA2A have previously been shown by our group to be differentially expressed in the SN vs. RA (Chandler et al., 2011): HCN4 more and both RYR2 and SERCA2A less expressed in the adult human SN vs. RA.

Using IPA, we can appreciate the complexity of interactions of many TFs that can directly and/or indirectly control the function of the pacemaker of the heart. IPA analysis revealed that besides HCN4, ISL1 (the most abundant TF in our adult human SN) activates ‘novel’ TFs RUNX3 (known to maintain the differentiation of mesenchymal cells during heart development (Fu et al., 2011) and RUNX1 (known to be involved in cardiac repair following myocardial infarction (McCarroll et al., 2018). Oppositely, ISL1 is activated by RUNX2 (known to be involved in osteoblast differentiation (Alfieri et al., 2010), whereas GLI1 (known to regulate the coordination of the heart and lung (Park et al., 2000)) activates RUNX2 and SOX2 (Figs. 5A and 3B) activates TBX3. Together they activate the expression of HCN4. Interestingly, the most targeted TF is RUNX2 with 6 activators (Fig. 5A).

Out of those TFs that are less abundant in the SN but more abundant in the RA, TBX5 is shown to interact with NKX2-5 and HOPX (one the novel TFs to be least expressed in the adult human SN (Figs. 4B and 5B). TBX5 activates NCX1, RYR2 and SERCA2A and NKX2-5 activates RYR2 (Fig. 5B). MEF2A (another novel TF more abundant in the adult human RA, known to regulate the mammalian cardiomyocyte differentiation (Desjardins and Naya 2016), like TBX5, activates SERCA2A (Fig. 5B). MEFA2A also activates ASB4 (known to be expressed in murine embryonic vasculature (Bode et al., 2011) and PPARGC1A (a regulator of mitochondrial biogenesis (Duncan and Finck 2007) (Fig. 5B).

3.4. Markers for key cell types and organelles more abundant in the sinus node compared to the right atrium

Fig. 1 shows the SN is characterised by more connective tissue than surrounding RA. We therefore aimed to identify other cell types’ markers that are present within its connective tissue. From our NGS dataset we identified, and then selected at least one marker of each cell type: ACTG2 for the smooth muscle cells (Wangler et al., 2014); CSF1R and CD209 for macrophages (Rojo et al., 2019) (Ortiz et al., 2008); FABP4 for fat/adipocytes cells (Queipo-Ortuno et al., 2012); INA for neuronal cells (Baum and Garriga 1997); MUC1 for epithelial cells (Dhar and McAuley 2019); TPSAB1 for mast cells (Lyons et al., 2017); CERCAM for endothelial cells (Starzyk et al., 2000); COL1A1 for fibroblasts (Wong et al., 2020); CD44 for mesenchymal stem cells (Maleki et al., 2014), widely investigated for many therapies including creation of a biological pacemaker (Hu et al., 2019); GZMA for natural killer cells (Cursons et al., 2019) and EMILIN1 for elastic fibres (Zanetti et al., 2004).

Table 4 lists markers and their mean ± SEM expression profile in 3 SN and 3 RA. The heat map shows their expression profile in each

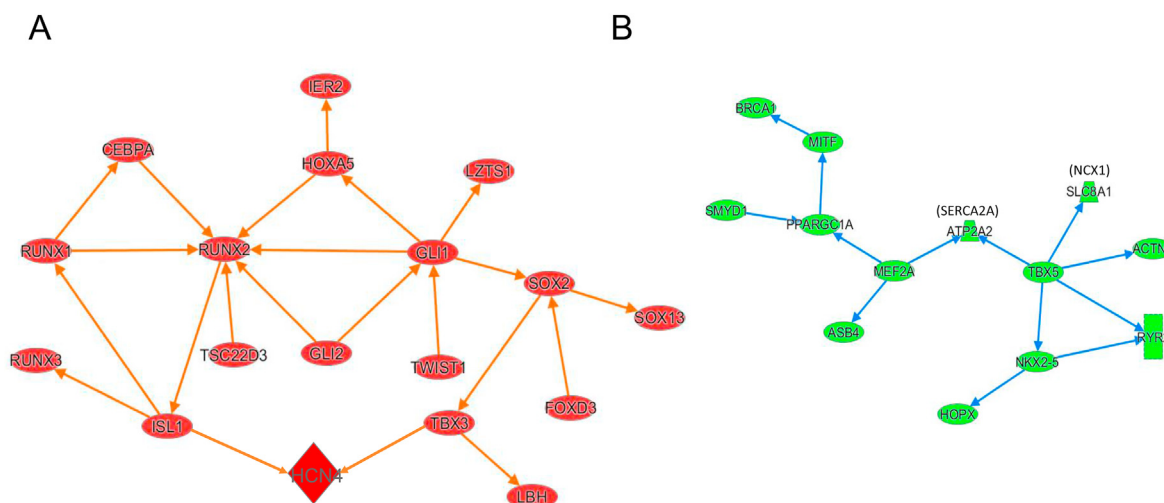


Fig. 5. Ingenuity Pathway Analysis predictions of interactions amongst ‘novel’ and well-known transcription factors (to be involved in embryonic development of the heart) and their predicted role in controlling HCN4 and Ca²⁺ handling proteins. **A**, transcription factors that were more abundant in the sinus node vs. right atrium. **B**, transcription factors that were less abundant in the sinus node vs. right atrium. Arrows = predicted activation. Oval shape = transcription factors; trapezoid shape = calcium-handling proteins; diamond shape = HCN4, hyperpolarisation-activated nucleotide-gated channel 4; NCX1 = Na⁺/Ca²⁺ exchanger; SERCA2A = sarcoplasmic reticulum Ca²⁺-ATPase. Red nodes represent molecules significantly more expressed in the SN. Green nodes represent molecules that are significantly less expressed in the SN (i.e., significantly more expressed in the RA).

sample (Fig. 6A). Their expression as % SN over RA is also included in Table 4 and shown graphically in Fig. 6B. As expected, there is some inter-individual variation in the expression of these cell markers within range of 0–1 and 0 to –1 Row Z-score. Each marker is abundantly expressed in the SN samples compared to the RA (Fig. 6B). Considering that the SN is highly innervated by the autonomic nervous system (ANS) (Alboni et al., 2007) not surprisingly, the most expressed marker was INA (log2foldchange of 3.77, Table 4) and percentage difference of 837% (Fig. 6B). It was interesting to observe that the immune cell marker (TPSAB1) is highly

expressed in the adult human SN (754%, Fig. 6B). Similarly to TPSAB1, the natural killer marker (GZMA) is also highly expressed in the adult human SN. In addition, the fat, smooth muscle, macrophage and mesenchymal stem cell markers are highly expressed in the human adult SN (Fig. 6B: FABP4, ACTG2, CSF1R/CD209 and CD44 are markers for these cells, respectively).

As well as the immune cells such as the mast, macrophages and natural killer being highly abundant in the adult human SN (Fig. 6), we noticed that 10 human leukocyte antigens (HLA, encoded by the major histocompatibility complex genes involved in regulation of

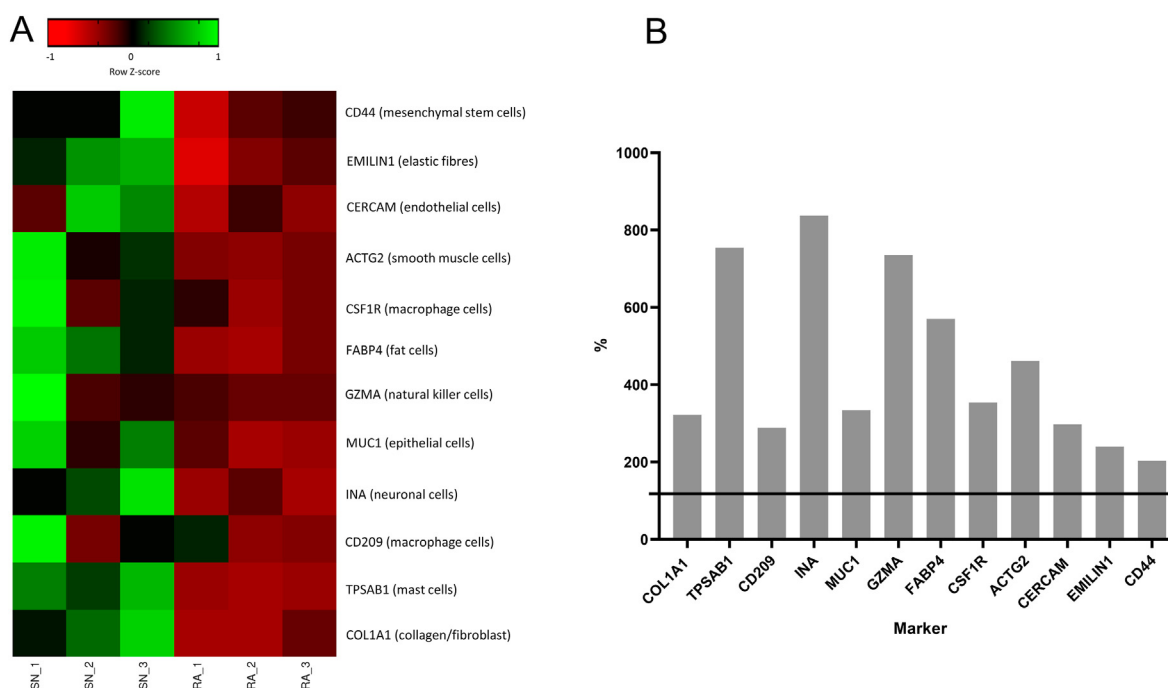


Fig. 6. Expression profile of markers for different cell types in the human adult sinus node vs. right atrial muscle. **A**, heat map shows inter-individual expression of each marker in each sinus node (SN1 – SN3) and right atrium (RA1 – RA3) samples. **B**, mean expression of cell markers in the sinus node vs. right atrium (n = 3) plotted as % SN/RA (see Table 4 for details). The black line at 100% represents the markers expression in the right atrium (i.e., basal level). SN = sinus node; RA = right atrium.

the immune system) were more highly expressed in the adult human SN (Fig. 7B). Table 4 lists those HLA markers and their mean \pm SEM expression profile in 3 SN and 3 RA. Their expression as % SN over RA is also included in Table 4 and shown graphically in Fig. 6B. The heat map shows their expression profile in each sample (Fig. 7A).

The high expression of HLAs together with high expression of macrophages, mast and natural killer cells in the adult human SN is of great interest as may be related to slower heart rates in COVID19 patients (Amaratunga et al., 2020; Capoferri et al., 2020). As already mentioned in the introduction, the importance of macrophages in maintaining HR and rhythm has been explored by (Hulsmans et al., 2017).

Table 4 lists collagen isoforms and their mean \pm SEM expression profiles in 3 SN and 3 RA. The heat map shows their expression profile in each sample (Fig. 8A). Their expression as % SN over RA is also included in Table 4 and shown graphically in Fig. 8B. Collagens are linked to cardiac fibrosis (Dobrzynski et al., 2013; Zhang et al., 2000; Wynn 2009). We have identified 11 collagen isoforms that are highly expressed in the SN compared to RA (Fig. 8). Out of the 11-collagen isoforms, COL9A2 (365% SN/RA is most abundant), however, COL9A3, COL8A2 and COL1A1 are also highly abundant in the human adult SN (Fig. 8B).

3.5. Contractile apparatus and related markers and mitochondria markers are less expressed in the adult human SN vs. right atrium

Table 4 lists markers for the contractile apparatus and mitochondria and their mean \pm SEM expression profiles in 3 SN and 3 RA. The heat maps show their expression profile in each sample (Figs. 9A and 10A). Their expression as % SN/RA is also included in Table 4 and shown graphically in Figs. 9B and 10B. Each marker is abundantly less in the SN samples compared to the RA (Figs. 9B and 10B).

The SN myocytes are not contractile cells and are known to be 'empty' due to poor expression of the contractile machinery

(Choudhury et al. 2015; James et al., 1966; Boyett et al. 2000). All contractile markers: actin (ACTN2), myosin heavy chain 6 (MYH6), titin (TTN), troponin T (TNNT2), as well as, desmin (DES (Yamamoto et al., 2011); and dystrophin (DMD (Williams and Bloch 1999); are less expressed in the human adult SN vs. RA. MYH6, a well-established marker for atrial cells (Gelb and Chin 2012; Ching et al., 2005), is approximately 80% less expressed in the SN/RA (Fig. 10B).

The SN cells also contain less mitochondria (James et al., 1966). We observed that various isoforms of mitochondria (MRPs) are less abundant in the adult human SN compared to RA (Fig. 9B). All of these isoforms were similarly twice less expressed in the SN (around 50%) to that of RA.

We summarised the expression profiles of the markers of cells, collagen, HLA, mitochondria and contractile machinery in the SN according to their log2foldchange to show their clustering (Fig. 11). The markers for the non-cardiac cell types (smooth muscle, macrophage, fat, neuronal, epithelial, mast, endothelial, natural killer, mesenchymal stem cells) are mostly expressed in the SN and they cluster together (Fig. 11). The least expressed markers in the SN also cluster together (Fig. 11).

3.6. Prediction of interactions of novel transcription factors and markers for cell types and contractile machinery

After identifying novel TFs within our dataset and quantification of various cell markers/organelles, we aimed to use IPA to determine if any of the key 'novel' TFs activate/inhibit the key markers specific to the SN. Several cross-control pathways were identified with IPA and are shown in Fig. 12A and B. Both RUNX1 and RUNX3 are activating mast cells; RUNX1 is also activating macrophages along with CEBPA. CEBPA also activates fat cells and RUNX2 activates fibroblasts (Fig. 12A). The TFs, GLI1 activates RUNX2, fibroblasts and CD44 (Fig. 12A). MEFA2A (more expressed in the RA) activates MYH6 (atrial myocyte marker which is more expressed in the RA vs. SN).

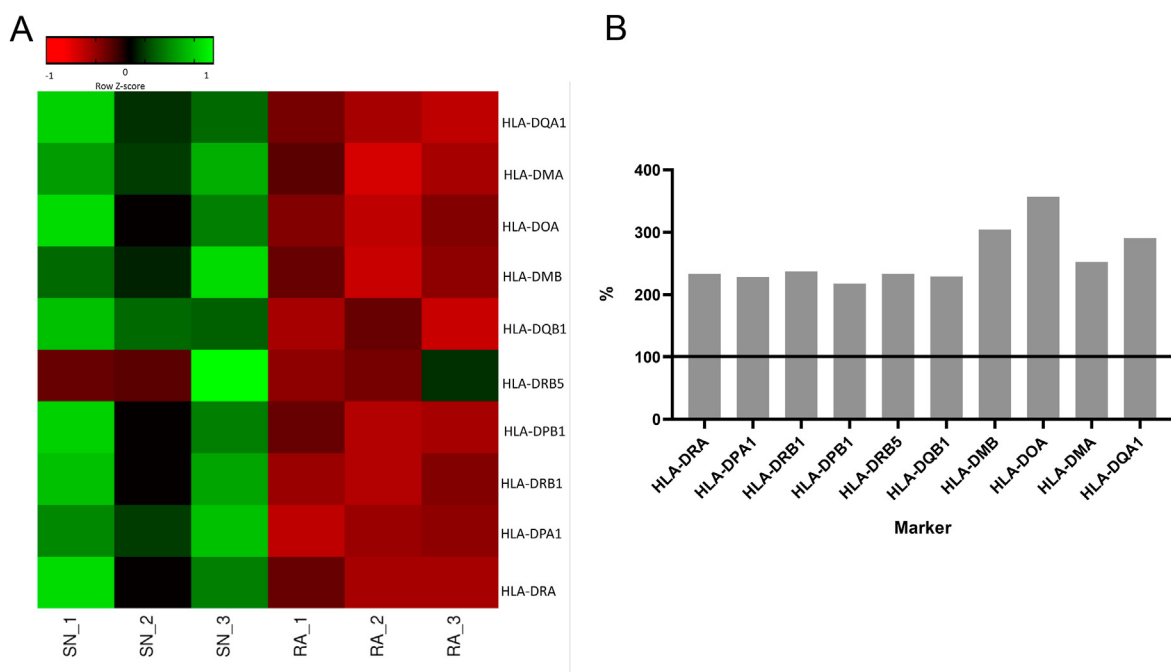


Fig. 7. Expression profile of human leukocyte antigen markers in the human sinus node vs. right atrium. A, heat map shows inter-individual expression of HLA markers in each sinus node (SN1 – SN3) and right atrium (RA1 – RA3) samples. B, mean expression in the sinus node vs. right atrium (n = 3) plotted as % SN/RA (see Table 4 for details). The black line at 100% represents HLA expression in the right atrium (i.e., basal level). SN = sinus node; RA = right atrium; HLA = human leukocyte antigen (major histocompatibility complex class I).

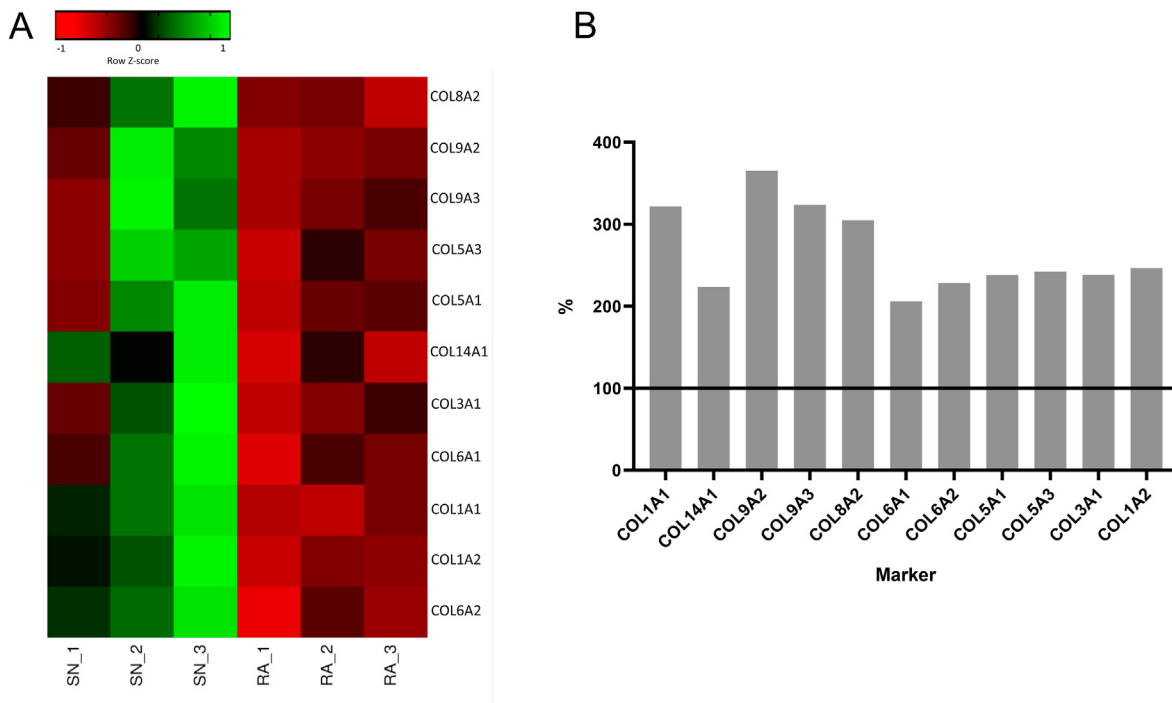


Fig. 8. Expression profile of collagen isoforms expressed in the adult human sinus node vs. right atrial muscle. **A**, heat map shows inter-individual expression of various collagen markers in each sinus node (SN1 – SN3) and right atrium (RA1 – RA3) samples. **B**, mean expression in the sinus node vs. right atrium (n = 3) plotted as % SN/RA (see Table 4 for details). The black line at 100% represents collagens expression in the right atrium (i.e., basal level). SN = sinus node; RA = right atrium; COL = collagen.

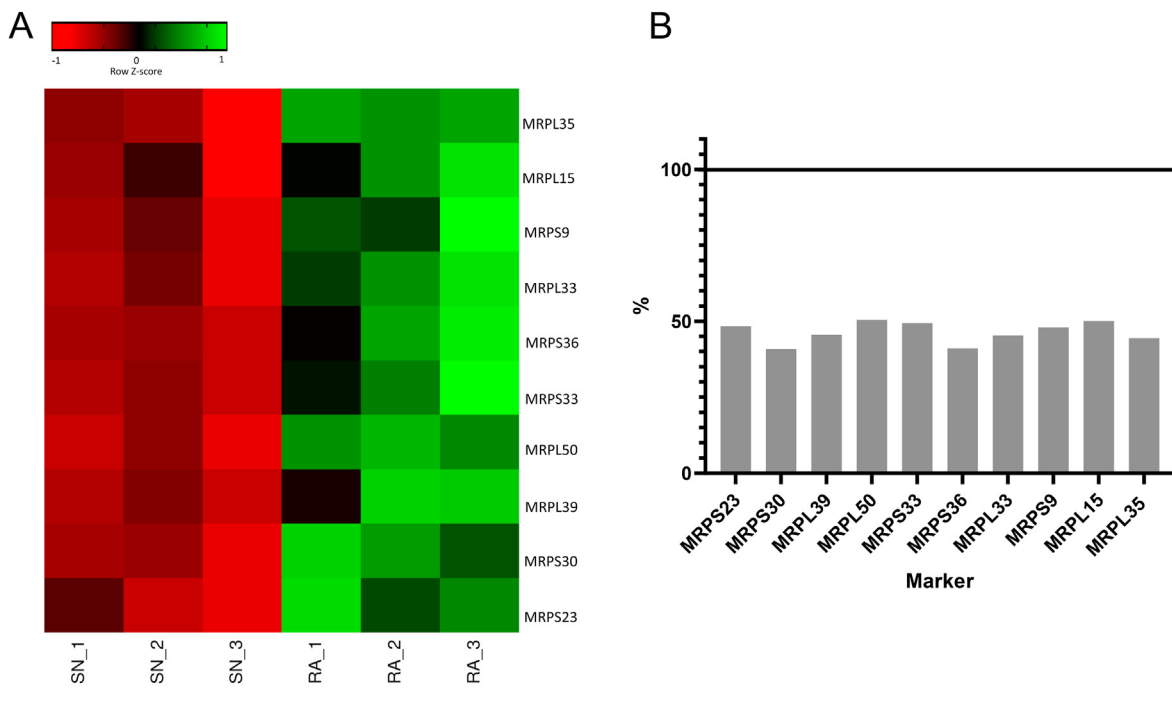


Fig. 9. Expression profile of contractile mitochondria markers in the adult human sinus node vs. right atrial muscle. **A**, heat map shows inter-individual expression of various mitochondria markers in each sinus node (SN1 – SN3) and right atrium (RA1 – RA3) samples. **B**, mean expression in the sinus node vs. right atrium (n = 3) plotted as % SN/RA (see Table 4 for details). The black line at 100% represents mitochondria markers expression in the right atrium (i.e., basal level). MRP = mitochondrial ribosomal protein; SN = sinus node; RA = right atrium.

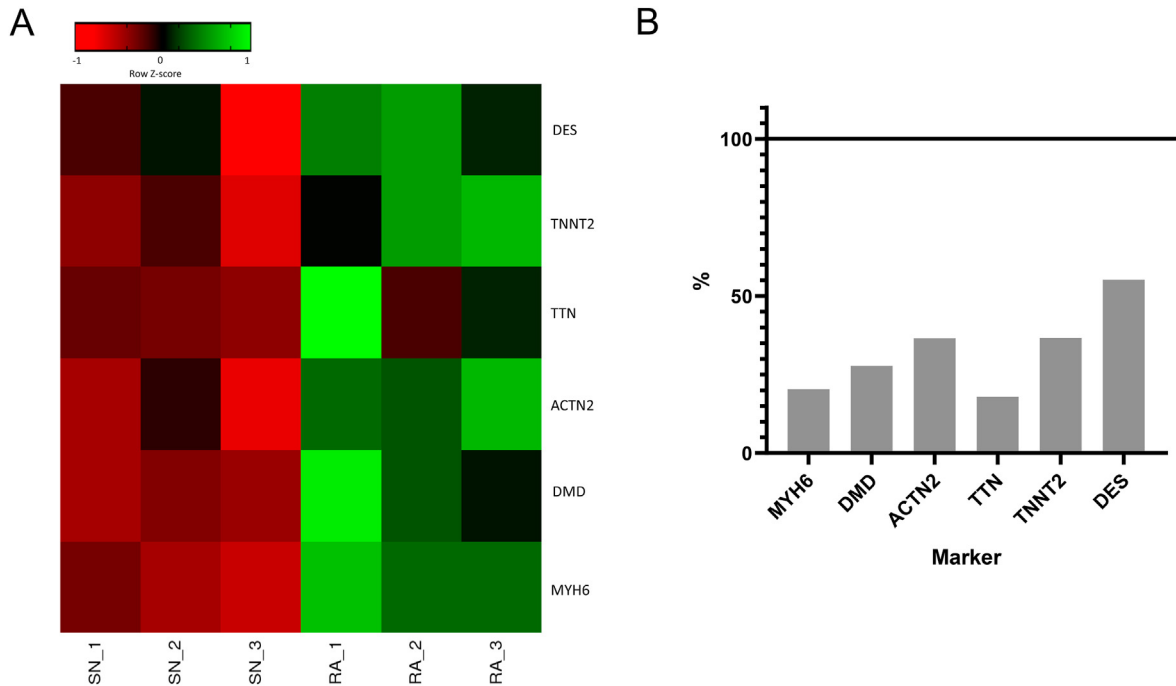


Fig. 10. Expression profile of contractile apparatus/cytoskeletal markers the adult human sinus node vs. right atrial muscle. **A**, heat map shows inter-individual expression of various contractile/cytoskeletal markers in each sinus node (SN1 – SN3) and right atrium (RA1 – RA3) samples. **B**, mean expression in the sinus node vs. right atrium (n = 3) plotted as % SN/RA (see Table 4 for details). The black line at 100% represents contractile/cytoskeletal markers expression in the right atrium (i.e., basal level). ACTN2 = actinin alpha 2; DES = desmin; DMD = dystrophin; MYH6 = myosin heavy chain 6; RA = right atrium; SN = sinus node; TTN = titin; TNNT2 = troponin T2.

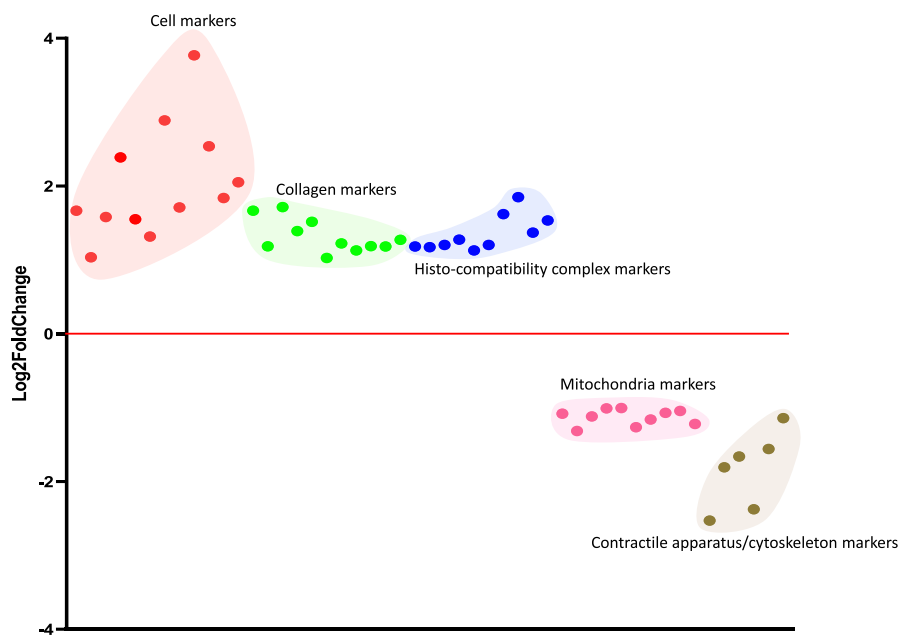


Fig. 11. Summary of expression of all markers as fold change. log2foldchange expression of markers. Log2foldchange>1 = significantly more expressed in the sinus node vs. right atrium; log2foldchange<1 = significantly less expressed in the sinus node vs. right atrium (see Table 4 for details).

3.7. Interaction of key microRNAs with key transcription factors and key cell markers

We have recently published miR profiles of the human adult SN vs. RA (Petkova et al., 2020). We predicted that 15 key miRs are involved in regulation of the two clocks responsible for pacemaking (Petkova et al., 2020). Furthermore, we validated that the funny

channel HCN4 is inhibited by miR-486-3p. If miR-486-3p is up-regulated that leads to HCN4 downregulation resulting in bradycardia.

Fig. 13 is summarises our key findings on our new predicted interaction. The number of binding sites on the targets interacting with miRs are listed in Table 5. The predicted interactions need to be validated in the future as we did in our recent study by (Petkova

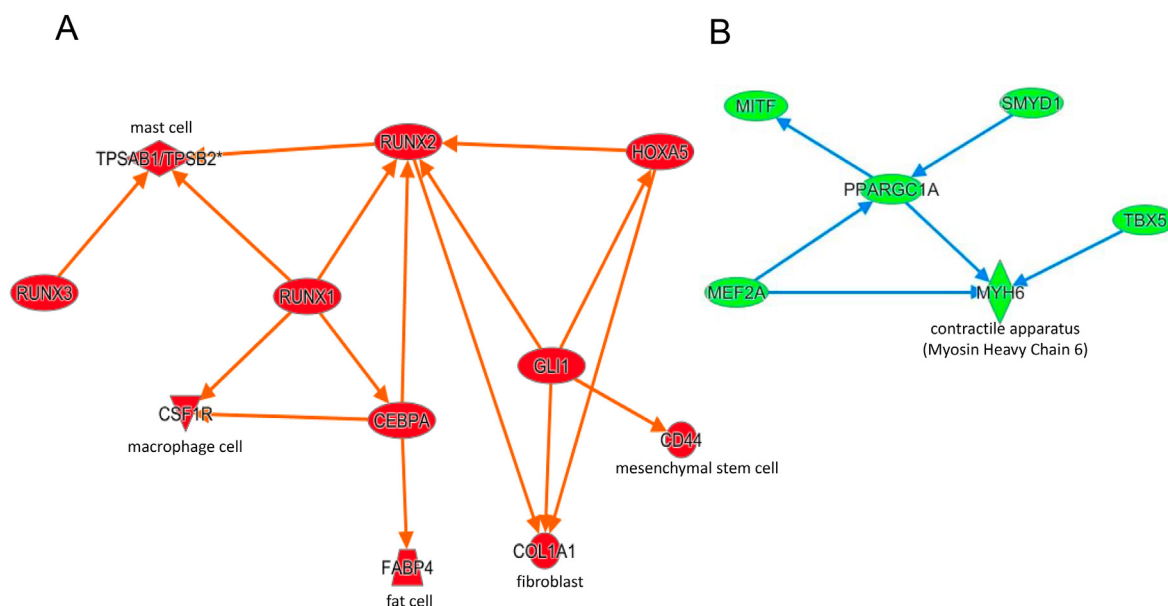


Fig. 12. Ingenuity Pathway Analysis of predicted interactions amongst ‘novel’ transcription factors and markers. **A**, transcription factors and markers more abundant in the sinus node vs. right atrium. **B**, transcription factors and markers less abundant in the adult human sinus node vs. right atrium. Arrows = predicted activation; oval shape = transcription factors. Red nodes represent molecules significantly more expressed in the SN. Green nodes represent molecules that are significantly less expressed in the SN (therefore significantly more expressed in the RA).

et al., 2020) for HCN4 and miR-486-3p.

Fig. 13 shows that miR-486-3p interacts with the mast cell marker, TPBAB1, macrophage cell marker, CD209, and other immune system markers (HLAs) as well as endothelial cell marker, CERCAM, (Fig. 13). MiR-133a-3p also inhibits the mast cells and COL1A (Fig. 13). Interestingly, some ‘novel’ TFs (LZTS1, SOX13, LBH, SOX2, RUNX2 and GLI2), which are highly expressed in the human adult SN are predicted to inhibit those microRNAs that are less expressed in the SN including miR-486-3p, miR-133a-3p, miR-938, miR-429, miR-422a, miR-30c-5p, miR-483-3p (Fig. 13).

It can be suggested that in the SN, RUNX2 activates COL9A3 via inhibition of miR-30c-5p, whereas LZTS1, LBH and SOX13 are activate immune markers via inhibiting miR-486-3p (Fig. 13). It can also be suggested that those miRs that are highly expressed in the SN namely miR-10 b-5p, miR-215-5p miR-1225-3p and miR153-3p inhibit the expression of TBX5, NKX2-5, MIF, MEF2A and PPARGC1A (Fig. 13).

We also hypothesise that increased circulating miR-486-3p in severe COVID-19 patients (Tang et al., 2020) may be responsible for decreased HR (Amaratunga et al., 2020; Capoferri et al., 2020) via inhibition of HCN4 and/or immune markers.

4. Discussion

4.1. The role of ‘novel’ transcription factors in the sinus node and their predicated interactions with TBX3 and ILS1

In this study we investigated the expression profile of known/‘embryonic’ and unexplored/‘novel’ TFs in the human adult SN vs. RA. We explored the interaction pathways of all significantly expressed TFs and their potential role in controlling SN function and structure by interacting with different cell types in this specialised tissue of the heart. Furthermore, we explored the interaction pathways of key miRs with key TFs and markers of different cells.

It is known that TBX3 and ILS1 are important during the embryonic development of the SN (van Eif et al., 2019). These TFs are also expressed in the SN of adult rodent heart (Liang et al., 2015) as

well as adult human heart (Petkova et al., 2020; Chandler et al., 2009). Nothing is known about overexpression of these TFs in the adult mammalian SN but TBX3 overexpression in the ventricles of adult mice can induce pacemaker characteristics (Bakker et al., 2012).

Many other ‘novel’ TFs present in the adult human SN are predicted to interact with TBX3 and ISL1 to regulate the expression of the funny channel, HCN4, (Fig. 5A). It is well known that HCN4 downregulation is responsible for SND and its upregulation can promote atrial arrhythmias (Zicha et al., 2005). ISL1 (the most abundant TF in the human adult SN; Figs. 2 and 3, Table 1), if mutated, can cause sinus bradycardia and sinus arrhythmia (Tessadori et al., 2012; Hoffmann et al., 2013).

As can be seen in Fig. 5A, some ‘novel’ TFs namely RUNX2 directly activates ISL1 whereas SOX2 activates TBX3 (Fig. 5A). It can therefore be hypothesised that changes to RUNX2 or SOX2 expression (the direct activators of ILS1 and TBX3 respectively; Fig. 5) could also result in SND. RUNX2 (an osteogenic TF) has been detected in the heart, where its overexpression caused significantly lower heart rate in mice (Nakayama et al., 2018). This could be mediated via ISL1 (Fig. 5) or immune cells (Fig. 12) discussed later. SOX2 (one of the most highly expressed TFs in the SN vs. RA; Figs. 2A and 3B, Table 2) is reported to be important for hiPSC generation into diverse cardiac cells from human fibroblasts, which are then further differentiated into pacemaker cells (Schweizer et al., 2017). It has also been reported that overexpression of SOX2 can increase number of differentiated myocytes in mice (Koyanagi et al., 2010).

The precise role of RUNX2 and SOX2 in the SN is not yet understood but their higher expression in the SN and predicted direct interactions with ISL1 and TBX3 can help to maintain the SN structure and function.

Other ‘novel’ TFs activate ISL1 via RUNX2 to activate HCN4 (Fig. 5A) and GLI1 via SOX2 activates TBX3 to also activate HCN4. Of interest are the following ‘novel’ TFs: 1). GLI1 (known to be up-regulated in diseased mouse heart and is involved in the hedgehog pathway (Xiao et al., 2012); 2). GLI2 is also involved in signalling

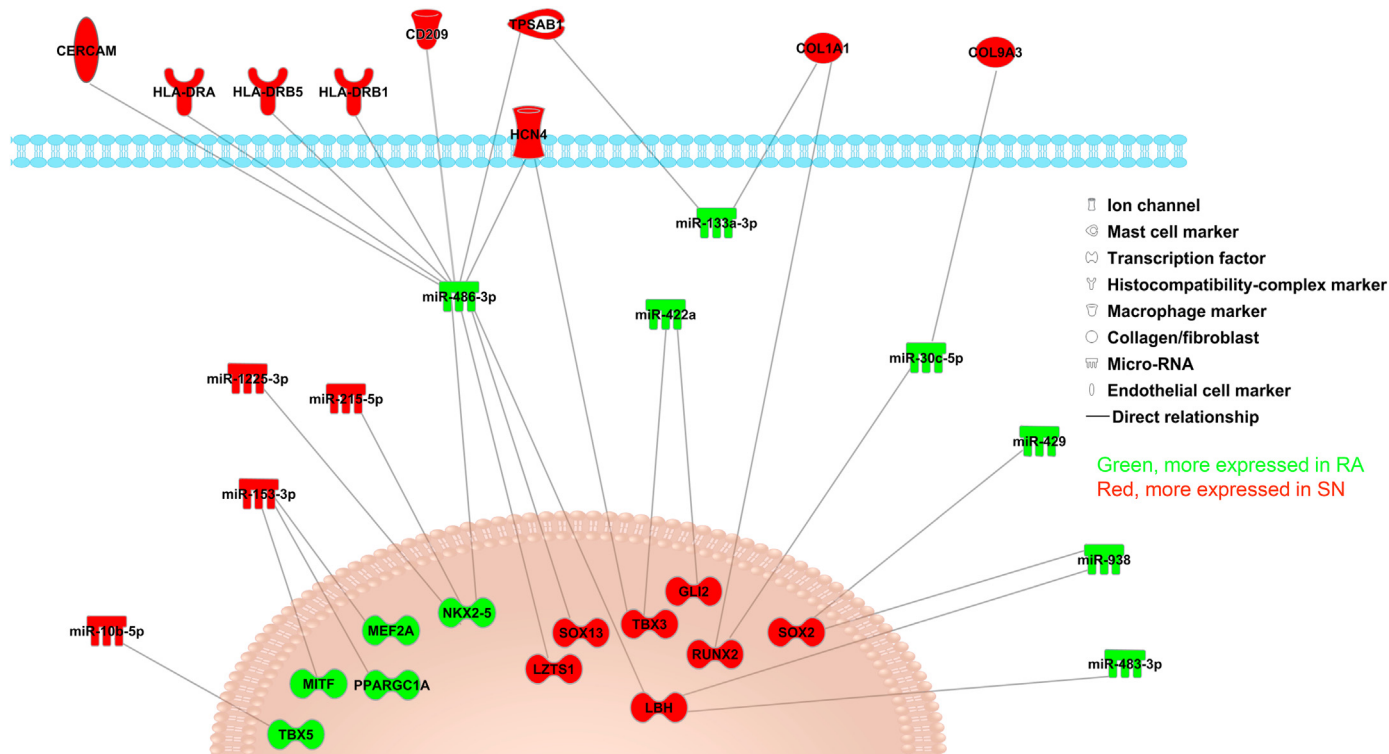


Fig. 13. Ingenuity Pathway Analysis predicted interactions amongst microRNAs, ‘novel’ transcription factors and markers. Markers are represented by different shapes. Mast cell marker (TPSAB1), macrophage cell marker (CD209), endothelial cell marker (CERCAM), collagen markers (CLO1A1, COL9A3), human leukocyte antigen markers (HLAs) are within ECM. HCN4, funny channel is within the plasma membrane. miRNAs are in the cytoplasm and transcription factors are shown in the nucleus. Red = more expressed in the SN vs. RA; green = more expressed in the RA vs. SN. ECM = extracellular matrix; miR = microRNAs.

pathways in the heart (Qin et al., 2019); 3). RUNX1 if lost in zebrafish enhances heart regeneration (Koth et al., 2020). Interestingly, ISL1, RUNX2 and TBX3 are also known to be involved in this Sonic hedgehog pathway (Lin et al., 2006; Dunaeva and Waltenberger 2017; Ludtke et al., 2016). TBX3 expression in mouse lungs depends on Sonic hedgehog signalling (Ludtke et al., 2016). RUNX1 depletion results in an altered expression of ISL1 in cancer research (van der Deen et al., 2012).

The ‘novel’ aforementioned TFs together with TBX3 and ILS1 may help with biological pacemaker formation strategies, human embryonic stem cell differentiation and use as novel therapeutic targets in regenerative medicine.

The role of ‘novel’ transcription factors in the sinus node and their predicated interactions with markers of immune, fat and fibroblast cells.

Interestingly some of these novel TFs e.g., RUNX1, RUNX2, RUNX3 and CEBPA also activate immune cells (Fig. 12A). This information may be of importance and may suggest that there might be an interaction between immune and nodal cells because both cells types are predicted to be activated by the TFs involved in the same signalling pathways.

We found that the markers for macrophages (CSF1R/CD209, Fig. 6) and the major histocompatibility complex (MHC) components (Fig. 7) are more expressed in the adult human SN compared to RA. Macrophages not only clear foreign antigens and cellular debris but also they are involved in the regeneration of the damaged myocardium through their interaction with other cardiac cells (Pinto et al. 2014). The HLA (human leukocyte antigen) complex is a group of related proteins that are encoded by the MHC and they are cell-surface proteins involved in the regulation of the immune system and are well known as transplantation antigens (Choo 2007). It is well known that CSF1R is important for

macrophage development, growth and survival by CEBPA (Zriwil et al., 2016) and RUNX1 (Himes et al., 2005). RUNX3 was also shown to be an important mediator of immune cell development and maturation (Boto et al. 2018).

At gestation, immune cells are recruited into the heart and remain there for life; therefore the immune system is essential for the development and maintenance of the heart. In response to infection or after myocardial infraction, immune cells are essential for repairing the damaged tissue (Swirski and Nahendorf 2018). In the mouse AV node a high expression of macrophages was discovered by (Hulsmans et al., 2017) that are electrically coupled with AV node cells via Cx43. The depletion of macrophages in mice results in AV block and lower heart rate (Hulsmans et al., 2017). This research group also noticed that HCN4-expressing cardiomyocytes in the AV node frequently scattered with macrophages (Hulsmans et al., 2017).

It is likely that the depletion of immune cells in diseased SN can cause lower heart rate via Cx45 dysregulation (the main gap junction channel in the human SN; Chandler et al., 2009).

RUNX2, GLI1 and HOXA5 activate fibroblasts, CEBPA activates fat cells and GLI1 also activates mesenchymal stem cells (Fig. 12A). We have previously shown that there is an increase in connective tissue (mainly collagen content - an indicator of fibrosis) as well as fat in the aged cardiac conduction system (Kharche et al., 2017; Saeed et al., 2018; Csepe et al., 2015). Ageing is a risk factor of SND, and increased fibrosis is observed in sick sinus syndrome (Csepe et al., 2015). When activated fibroblasts secrete excessive extracellular matrix, which can lead to pathological fibrosis and organ failure (Zhang et al., 2019). In our current study, we observed a high expression profile of 11 different isoforms of collagens (Fig. 8A) and FABP4 (a fat cell marker - Fig. 6B) in the adult human SN. Highly expressed collagen 1A1 is predicted to be activated by RUNX2, GLI1

and HOXA5. HOXA5 is known to be expressed in fibroblasts and its upregulation depends on GLI1-dependent Hedgehog signalling (Zhang et al., 2019; Katoh and Katoh 2005) and RUNX2 has also been shown to be involved in fibrosis (Hsu et al., 2017).

An increase in fat content can also contribute to SND (Shiraishi et al., 1992), therefore it would be interesting to know if CEBPA and FABP4 are also increased in the diseased SN. It has recently been reported that they are involved in adipogenesis and FABP4 is expressed in the mature fat cells (Bahrami-Nejad et al., 2020).

Collectively our data suggests that similar TFs are involved in regulation of different cell types in the SN (namely immune, nodal, fat and fibroblasts) in health. RUNX1 is of particular interest because it not only regulates key TFs involved in the regulation of primary pacemaker cell (Fig. 5) activity but are also involved in regulation of other cell types present in the SN (Fig. 12) and perhaps can offer new treatment for SND. In fact, RUNX1 has recently been reported to offer a new emerging target for treatment for cardiovascular diseases (Riddell et al., 2020).

The SN is non-contractile tissue and has fewer myofilaments and fewer mitochondria than in RA (Bleeker et al., 1980; Marvin et al., 1984; Boyett et al. 2000; Christoffels et al., 2010). Therefore, as expected, there is a lower expression of contractile machinery and mitochondria in the adult human SN compared to the RA (Figs. 9 and 10). TFs, MEFA2A, TBX5 and NKX2-5 are activating Ca^{2+} handling proteins in the RA (Fig. 5B), which are less expressed in the SN (Chandler et al., 2009). It is reported that the knock-out of NKX2-5 in mouse heart resulted in the repression of RYR2 (Briggs et al., 2008). Interestingly MEFA2A (known to regulate structural proteins – (Guo et al., 2014)), together with TBX5 activates MYH6 (involved in the contractile machinery in the working atrial muscle) (Fig. 12B).

4.2. The role of microRNAs in the sinus node and their predicted interactions with transcription factors and other markers

Interestingly, Fig. 13 shows that lower expression of MEFA2A and NKX2-5 in the SN may be due to higher expression of miR-153-3p and miR-1225-3p, which are also predicted to inhibit RYR2 and $Na_v1.5$ respectively which are less expressed in the SN (Petkova et al., 2020; Chandler et al., 2009).

The 'novel' TFs namely: SOX2, RUNX2 and LBH inhibit the expression of e.g., miR-30c-5p, miR-938 in the SN hence explain the higher expression of $Ca_v1.3$ (Petkova et al., 2020; Chandler et al., 2009) and COL9A3 (Fig. 13).

The TFs LZTS1, SOX13 and LBH, which are highly expressed in the adult human SN vs. RA, and are predicted to inhibit miR-486-3p, which can explain higher expression of HCN4 and immune markers in the SN vs. RA (Fig. 13). LZTS1 has as many as 12 binding sites for miR-486-3p (Table 5); therefore it is also possible that miR-486-3p is inhibiting LZTS1 expression in the RA. LZTS1 is a TF that plays a role in the regulation of cell growth and proliferation and deficiency of this TF is reported to cause cancer in human cell lines (Cabeza-Arvelaiz et al., 2001).

It has already been mentioned that sinus bradycardia in COVID-19 patients has recently been reported by (Amaratunga et al., 2020; Capoferri et al., 2020), which has been postulated to be caused by hypoxia and inflammatory damage of the SN cells. It has also been recently reported that circulating miR-486-3p is upregulated in COVID-19 patients, which may result in immune response dysregulation (Tang et al., 2020). It is possible that upregulation of miR-486-3p can cause changes in the connective tissue flora via mast and macrophage cells and HLAs dependent pathological conditions in the SN in addition to the direct HCN4 suppression leading to sinus bradycardia (Fig. 13). Furthermore, SND can also be attributed to changes in immune response and fibrosis via changes in miR-

133a-3p and RUNX2 (Fig. 13).

The interactions of miR-486-3p and miR-133a-3p with immune and/or fibroblast markers and 'novel' TFs (Fig. 13) requires further validation.

All this puzzling information on the high expression of immune markers' in the SN vs. RA and their complex interactions with TFs and miRs leads to the question "why does the SN require such high expression of immune response markers"? (Hulsmans et al., 2017) showed that macrophages are involved in healthy functioning of the mouse AV node. Here we report that the immune system is likely to be important for the maintenance of a healthy functioning human SN. The high expression of innate immune system natural killer cells, macrophages and HLAs (present on the surface of most cells) in the SN may play an important role in the immune response to foreign material (Fig. 13). It is possible that this high expression of HLAs, natural killer and macrophage cells rapidly respond to virus infections and other pathological stimuli in the SN may cause an obstacle for the development of biological pacemakers (Hu et al., 2014; Kapoor et al., 2013; Kapoor et al. 2011). The development and delivery of TFs and/or miRNAs as biological pacemakers is a difficult task, primarily due to the fact that the SN induces a rapid immune response against foreign matter. Hu et al. studied the adenoviral vector-delivery of TBX18 (expressed in the adult human SN (Petkova et al., 2020);) in a swine model of total heart block where the pacemaking activity was stabilised but after day 7 the heart rate started to decrease due to an immune response by the host tissue (Hu et al., 2014). Thus our results and the studies carried out by other groups confirm significance of the immune system cells in the SN functioning.

5. Conclusion

The morphology and mechanisms of the adult human SN are incredibly complex. There is a unique expression of 'novel' TFs in the adult human SN tissue that most likely work together with TBX3 and ISL1 to regulate the expression of the funny channel as well as immune cells in health and could contribute to SND. Our study provides novel insights into the complex underlying mechanisms that control molecular, morphological and functional characteristics of the tissue that makes our heartbeat. It also provides novel perception into the importance of the immune response that contributes to functioning of the primary pacemaker of the heart. In an increasing global ageing population, the occurrence of SND is increasing, therefore key 'novel' TFs, immune marker cells and miRs identified in this study should be explored for functional validation and for potential therapeutic management of SND.

Authors' statement/contribution

Abimbola J Aminu (AJA): contributed to planning and manuscript writing, analysis of NGS data, bioinformatics, histology; creating all figures and tables; discussed with HD on format of manuscript and figures. Maria Petkova (MP): contributed to cryosectioning, histology, RNA extraction, NGS analysis and bioinformatics. Andrew J Atkinson (AJA): contributed to RNA extraction, cryosectioning, histology and supervision of MP, ADM, RTS. Joseph Yanni (JY): contributed to RNA extraction and supervision of MP. Alex D Morris (ADM): contributed to cryosectioning and histology. Robert T Simms (RTS): contributed to NGS analysis and bioinformatics. Weixuan Chen (WC): contributed to morphological and NGS analysis and bioinformatics. Zeyuan Yin (ZY): contributed to NGS analysis and bioinformatics. Mateusz K. Holda (MKH): provided comments on the manuscript. Marcin Kuniewicz (MP): provided interesting ideas related to revision of the manuscript.

Vladislav S. Kuzmin (VSK): contributed to editing and writing manuscript. Filip Perde (FP): provided human specimens. Peter Molenaar (PM): provided human specimens, edited the manuscript and provided comments on Figures and Tables. Halina Dobrzynski (HD): conceived research, obtained funding, supervised AJA, MP, ADM, RTS, WC, ZY, contributed to planning and writing of manuscript, analysis of data, formatting figures and tables. All authors approved the manuscript.

Source of funding

This work was supported by the British Heart Foundation program grant FS/17/67/33,483 and the Leducq Foundation (THE FANTASY 19CVD03).

Disclosures

None.

Declaration of competing interest

The authors declare no conflict of interest.

Acknowledgment

We would like to thank Ian Donaldson for his help with NGS analysis and plotting volcano plots.

References

- Alboni, P., Filippi, L., Pirani, R., De Lorenzi, E., Masoni, A., 2007. The role of the autonomic nervous system on sinus node function in patients with intermittent sinoatrial block. *J. Electrocardiol.* 17, 25–32.
- Alfieri, C.M., Cheek, J., Chakraborty, S., Yutzey, K.E., 2010. Wnt signalling in the heart development and osteogenic gene induction. *Dev. Biol.* 338, 127–135.
- Amaratunga, E.A., Corwin, S.D., Moran, L., Snyder, R., 2020. Bradycardia in patients with COVID-19: a calm before the storm? *Cureus* 12, e8599.
- Bahrami-Nejad, Z., Chen, T., Tholen, S., Rabiee, A., Zhao, M.L., Bielczyk-Maczynska, E., Braemer, F.B., Teruel, M.N., 2020. The Highly Expressed Lipid Buffer FABP4 Enforces Adipocyte Cell Identity by Driving the Initial Cell Differentiation Process.
- Bakker, M.L., Boink, J.J.G., Boukens, J.B., Verkerk, O.A., van den Boogaard, M., den Haan, D.A., Hoogaars, H.M.W., p Buermans, H., 2012. T-box transcription factor TBX3 reprogrammes mature cardiac myocytes into pacemaker-like cells. *Cardiovasc. Res.* 94, 439–449.
- Baum, P.D., Garriga, G., 1997. Neuronal migrations and axon fasciculation are disrupted in ina-1 integrin mutants. *Neuron* 19, 51–62.
- Bleeker, W.K., Mackaay, A.J., Masson-Pevet, M., Jongasma, H.J., Bouman, L.N., Becker, A.E., 1980. Functional and morphological organization of the rabbit sinus node. *Circ. Res.* 46, 11–22.
- Bode, M., Wu, Y., Pi, X., Lockyer, P., Dechyapirom, W., Portbury, A.L., Patterson, C., 2011. Regulation of ASB4 expression in the immortalized murine endothelial cell lines MS1 and SVR: a role for TNF- α and oxygen. *Cell Biochem. Funct.* 29, 334–341.
- Boto, P., Csuth, T.I., Szatmari, I., 2018. Runx3-mediated immune cell development and maturation. *Crit. Rev. Immunol.* 38, 63–78.
- Boyett, M.R., Honjo, H., Kodama, I., 2000. The sinoatrial node, a heterogeneous pacemaker structure. *Cardiovasc. Res.* 47, 658–687.
- Briggs, E.L., Takeda, M., Cuadra, E.A., Wakimoto, H., Marks, H.M., Walker, J.A., Seki, T., Oh, P.S., Lu, T.J., Summers, C., Raizada, K.M., Horikoshi, N., Weinberg, O.E., Yasui, K., Ikeda, Y., Chien, R.K., Kasahara, H., 2008. Perinatal loss of Nkx2-5 results in rapid conduction and contraction defects. *Circ. Res.* 103, 580–590.
- Brown, H.F., DiFrancesco, D., Noble, S.J., 1979. How does adrenaline accelerate the heart? *Nature* 280, 235–236.
- Cabeza-Arvelaiz, Y., Sepulveda, J.L., Lebovitz, R.M., Thompson, T.C., Chinault, C.A., 2001. Functional identification of LZTS1 as a candidate prostate tumor suppressor gene on human chromosome 8p22. *Oncogene* 20, 4169–4179.
- Callis, E.T., Wang, D.-Z., 2008. Taking microRNAs to heart. *Trends Mol. Med.* 14, 254–260.
- Capoferri, G., Oshoff, M., Egli, A., Stoeckle, M., Bassetti, S., 2020. Relative Bradycardia in Patients with COVID-19. CMI.
- Chandler, J.N., Greener, D.I., Tellez, O.J., Inada, S., Musa, H., Molenaar, P., DiFrancesco, D., Baruscotti, M., Longhi, R., Anderson, H.R., Billeter, R., Sharma, V., Sigg, C.D., Boyett, R.M., Dobrzynski, H., 2009. Molecular architecture of the human sinus node insights into the function of the cardiac pacemaker. *Circulation* 119, 1562–1575.
- Chandler, N., Aslanidi, O., Buckley, D., Inada, S., Birchall, S., Atkinson, A., Kirk, D., Monfredi, O., Molenaar, P., Anderson, R., Sharma, V., Sigg, D., Zhang, H., Boyett, M., Dobrzynski, H., 2011. Computer three-dimensional anatomical reconstruction of the human sinus node and a novel paranodal area. *Anat. Rec.* 294, 970–979.
- Ching, Y.H., Ghosh, T.K., Cross, S.J., Packham, E.A., Honeyman, L., Loughna, S., Robinson, T.E., Dearlove, A.M., Ribas, G., Bonser, A.J., Thomas, N.R., Scotter, A.J., Caves, L.S.D., Tyrrell, G.P., Newbury-Ecob, R.A., Munnich, A., Bonnet, D., Brook, D.J., 2005. Mutation in myosin heavy chain 6 causes atrial septal defect. *Nat. Genet.* 37, 423–428.
- Choo, S.Y., 2007. The HLA system: genetics, immunology, clinical testing, and clinical implications. *Yonsei Med. J.* 48, 11–23.
- Choudhury, M., Boyett, R.M., Morris, M.G., 2015. Biology of the sinus node and its disease. *Arrhythmia Electrophysiol. Rev.* 4, 28–34.
- Christoffels, V.M., Smits, G.J., Kispert, A., Moorman, A.F.M., 2010. Development of the pacemaker tissues of the heart. *Circ. Res.* 106, 240–254.
- Csepe, T.A., Kalyanasundaram, A., Hansen, B.J., Zhao, J., Federov, V.V., 2015. Fibrosis: a structural modulator of sinoatrial node physiology and dysfunction. *Front. Physiol.* 6, 37.
- Cursons, J., Souze-Fonseca-Guimaraes, F., Foroutan, M., Anderson, A., Hollande, F., Hediye-Zadeh, S., Behren, A., Huntington, D., Davis, M.J., 2019. A gene signature predicting natural killer cell infiltration and improved survival in melanoma patients. *Cancer Immunol Res* 7, 1162–1174.
- Desjardins, C.A., Naya, F.J., 2016. The function of the MEF2 family of transcription factors in cardiac development, cardiogenomics, and direct reprogramming. *J. Cardiovasc. Dev Dis* 3, 26.
- Dhar, P., McAuley, J., 2019. The role of the cell surface mucin MUC1 as a barrier to infection and regulator of inflammation. *Front. Cell Infect. Microbiol.* 9, 117.
- DiFrancesco, D., 2020. A brief history of pacemaking. *Front. Physiol.* 10, 1599.
- Dobrzynski, H., Anderson, H.R., Atkinson, A., Borbas, Z., D'Souza, A., Fraser, F.J., Inada, S., Logantha, J.R.J.S., Monfredi, O., Morris, M.G., Moorman, M.F.A., Nikolaidou, T., Schneider, H., Szuts, V., Temple, P.I., Yanni, J., Boyett, R.M., 2013. Structure, function and clinical relevance of the cardiac conduction system, including the atrioventricular ring and outflow tract tissues. *Pharmacol. Therapeut.* 139, 260–288.
- Dunaeva, M., Waltenberger, J., 2017. Hh signaling in regeneration of the ischemic heart. *Cell. Mol. Life Sci.* 74, 3481–3490.
- Duncan, J.G., Finck, B.N., 2007. The PPAR α -PGC-1 α axis Controls Cardiac Energy Metabolism in Healthy and Diseased Myocardium. *PPAR Research*, pp. 1–10, 2008.
- Friedman, C.E., Nguyen, Q., Lukowski, S.W., Helfer, A., Chiu, H.S., Miklas, J., Levy, S., Suo, S., Han, J.-D., J., Osteil, P., Peng, G., Jing, N., Baillie, G.J., Senabouth, A., Christ, A.N., Bruxner, T.J., Murry, C.E., Wong, E.S., Ding, J., Wang, Y., Hudson, J., Ruohola-Baker, H., Bar-Joseph, Z., Tam, P.P.L., Powell, J.E., Palpant, N.J., 2018. Single-cell transcriptome analysis of cardiac differentiation from human PSCs reveals HOPX-dependent cardiomyocyte maturation. *Cell Stem Cell* 23, 586–598.
- Fu, Y., Chang, A.C.Y., Fournier, M., CHnag, L., Niessen, K., Karsan, A., 2011. RUNX3 maintains the mesenchymal phenotype after termination of the Notch signal. *J. Biol. Chem.* 286, 11803–11813.
- Gelb, B.D., Chin, S.E., 2012. Genetics of congenital heart disease. *Muscle. Academic Press.*
- Guo, Y., Kuhl, S.J., Pftser, A.S., Cizelsky, W., Denk, S., Beer-Molz, L., Kuhl, M., 2014. Comparative analysis reveals distinct and overlapping functions of Mef2c and Mef2d during cardiogenesis in *Xenopus* larvae. *PLoS One* 9, e83294.
- Himes, S.R., Cronau, S., Mulford, C., Hume, D.A., 2005. The Runx1 transcription factor controls CSF-1-dependent and -independent growth and survival of macrophages. *Oncogene* 24, 5278–5286.
- Hoffmann, S., Berger, I.M., Glaser, A., Bacon, C., Li, L., Gretz, N., Steinbeisser, H., Rottbauer, W., Just, S., Rappold, G., 2013. Islet1 is a direct transcriptional target of the homeodomain transcription factor Shox2 and rescues the Shox2-mediated bradycardia. *Basic Res. Cardiol.* 108, 339.
- Hoogaars, W.M.H., Engel, A., Brons, J.F., Verkerk, A.O., de Lange, F.J., Wong, L.Y.E., Bakker, M.L., Clout, D.E., Wakker, V., Barnett, P., Ravesloot, J.H., Moorman, A.F.M., Verheijck, E.E., Christoffels, V.M., 2007. Tbx3 controls the sinoatrial node gene program and imposes pacemaker function on the atria. *Genes Dev.* 21, 1098–1112.
- Hsu, C.-K., Lin, H.-H., Harn, H.I., Ogawa, R., Wang, Y.-K., Ho, Y.-T., Chen, W.-R., Lee, Y.-C., Lee, J.Y.-Y., Shieh, S.-J., Cheng, C.-M., McGrath, J.A., Tang, M.-J., 2017. Caveolin-1 controls hyperresponsiveness to mechanical stimuli and fibrogenesis-associated Runx2 activation in keloid fibroblasts. *J. Invest. Dermatol.* 138, 208–218.
- Hu, Y.F., Dawkins, H.C., Cho, E., Marban, E., Cingolani, E., 2014. Biological pacemaker created by minimally invasive somatic reprogramming in pigs with complete heart block. *Sci. Transl. Med.* 6, 254ra94.
- Hu, Y., Li, N., Liu, L., Zhang, H., Xue, X., Shao, X., Zhang, Y., Lang, X., 2019. Genetically modified porcine mesenchymal stem cells by lentiviral tbx18 create a biological pacemaker. *Stem Cell. Int.* 7, 3621314.
- Hulsmans, M., Clauss, S., Xiao, Aguirre, D.A., King, R.K., Hanley, A., Hucker, J.W., Wulfers, M.E., Seemann, G., Courties, G., Iwamoto, Y., Sun, Y., Savol, J.A., Sager, B.H., Lavine, J.K., Fishbein, A.G., Capen, E.D., Da Silva, N., Miquero, L., Wakimoto, H., Seidman, E.C., Seidman, G.J., Sadreyev, I.R., Xaverova, K., Mitchell, N.R., Brown, D., Libby, P., Weissleder, R., Swirski, K.F., Kohl, P., Vinegoni, C., Milan, J.D., Ellinor, T.P., Nahrendorf, M., 2017. Macrophages

- facilitate electrical conduction in the heart. *Cell* 169, 510–522.
- James, T.N., Sherf, L., Fine, G., Morales, A.R., 1966. Comparative ultrastructure of the sinus node in man and dog. *Circulation* 34, 139–163.
- Kapoor, N., Liang, W., Marban, E., Cho, H.C., 2013. Direct conversion of quiescent cardiomyocytes to pacemaker cells by expression of Tbx18. *Nat. Biotechnol.* 31, 54–62.
- Kapoor, N., Marban, E., Cho, H.C., 2011. Biological pacemaker induced in vivo by focal Tbx18 gene transfer in the Guinea-pig left ventricle. *Circulation* 124, A15845.
- Katoh, Y., Katoh, M., 2005. Hedgehog signaling pathway and gastric cancer. *Canc. Biol. Ther.* 4, 1050–1054.
- Keith, A., Flack, M., 1907. The form and nature of the muscular connections between the primary divisions of the vertebrate heart. *J Anat Physiol* 41, 172–189.
- Kharache, R.S., Vigmond, E., Efmov, R.I., Dobrzynski, H., 2017. Computational assessment of the functional role of sinoatrial node exit pathways in the human heart. *PLoS One* 12, e0183727.
- Koth, J., Wang, X., Killen, A.C., Stockdale, W.T., Potts, H.G., Jefferson, A., Bonkhofer, F., Riley, P.R., Patient, K.R., Gottgens, B., Mommersteeg, M.T., 2020. Runx1 promotes scar deposition and inhibits myocardial proliferation and survival during zebrafish heart regeneration. *Development* 147, dev186569.
- Koyanagi, M., Iwasaki, M., Rupp, S., Tedesco, S.F., Yoon, C.-H., Boeckel, J.-N., Trauth, J., Schutz, C., Ohtani, K., Goetz, R., Lekushi, K., Bushoven, P., Momma, S., Mummery, C., Passier, R., Henschler, R., Akintuerk, H., Schranz, D., Urbich, C., Galvez, G.B., Cossu, G., Zeiher, A., Dimmeler, S., 2010. Sox2 transduction enhances cardiovascular repair capacity of blood-derived mesoangioblasts. *Circ. Res.* 106, 1290–1302.
- Leitoguinho, A.R., Ng, E., Stanley, E., Elefanty, A., 2019. The role of ventx homeobox gene during human haematopoietic development. *Exp. Hematol.* 76, 573.
- Lescroart, F., Zaffran, S., 2018. Hox and Tale transcription factors in heart development and disease. *Int. J. Dev. Biol.* 62, 11–12.
- Liang, X., Zhang, Q., Cattaneo, P., Zhuang, S., ong, X., Spann, N.J., Jiang, C., Cao, X., Zhao, X., Zhang, X., Bu, L., Wang, G., Chen, H.S., Zhaung, T., Yan, J., Geng, P., Luo, L., Banerjee, I., Chen, Y., Glass, C.K., Zamboni, A.C., Chen, J., Sun, Y., Evans, S.M., 2015. Transcription factor ISL1 is essential for pacemaker development and function. *J. Clin. Invest.* 125, 3256–3268.
- Lin, L., Bu, L., Cai, C.-L., Zhang, X., Evans, S., 2006. Isl1 is upstream of sonic hedgehog in a pathway required for cardiac morphogenesis. *Dev. Biol.* 295, 756–763.
- Lombardo, R.C., Porollo, A., Cnota, J.F., Hopkin, R.J., 2018. Congenital heart disease and aortic arch variants associated with mutation in PHOX2B. *Genet. Med.* 20, 1538–1543.
- Ludtke, T.H., Rudat, C., Wojahn, I., Weiss, A.-C., Kleppa, M.-J., Kurz, J., Farin, H., Moon, A., Christoffels, V.M., Kispert, A., 2016. Tbx2 and Tbx3 act downstream of Shh to maintain canonical Wnt signalling during branching morphogenesis of the murine lung. *Dev. Cell* 39, 239–253.
- Lyons, J.J., Yu, X., Hughes, J.D., Le, Q.T., Jamil, A., Bai, Y., Ho, N., Zhao, M., Liu, Y., O'Connell, M.P., Trivedi, N.N., Nelson, C., DiMaggio, T., Jones, N., Matthews, H., Lewis, K.L., Oler, A.J., Carlson, R.J., Arkwright, P.D., Hong, C., Agama, S., Wilson, T.M., Tucker, S., Zhang, Y., McElwee, J.J., Pao, M., Glover, S.C., Rothenberg, M.E., Hohman, R.J., Stone, K.D., Caughey, G.H., Heller, T., Metcalfe, D.D., Biesecker, L.G., Schwartz, L.B., Milner, J.D., 2017. Elevated basal serum tryptase identifies a multisystem disorder associated with increased TPSAB1 copy number. *Nat. Genet.* 48, 1564–1569.
- Maleki, M., Ghanbarvand, F., Behzad, R.M., Ejtemaei, M., Ghadirkhomi, E., 2014. Comparison of mesenchymal stem cell markers in multiple human adult stem cells. *Int J Stem Cells* 7, 118–126.
- Mallanna, S.K., Ormsbee, B.D., Iacovino, M., Gilmore, J.M., Cox, J.L., Kyba, M., Washburn, M.P., Rizzino, A., 2010. Proteomic analysis of Sox2-associated proteins during early stages of mouse embryonic stem cell differentiation identifies Sox21 as a novel regulator of stem cell fate. *Stem Cell.* 28, 1715–1727.
- Marvin Jr., J.W., Chittick, L.V., Rosenthal, K.J., Sandra, A., Atkins, L.D., Hermsmeyer, K., 1984. The isolated sinoatrial node cell in primary culture from the newborn rat. *Circ. Res.* 55, 253–260.
- McCarroll, C.S., He, W., Foote, K., Bradley, A., Mcglynne, K., Vidler, F., Nixon, C., Nather, K., Fattah, C., Riddell, A., Bowman, P., Elliott, E.B., Bell, M., Hawksby, C., MacKenzie, S.M., Morrison, L.J., Terry, A., Blyth, K., Smith, G.L., McBride, M.W., Kubin, T., Braun, T., Nicklin, S.A., Cmaeron, E.R., Loughrey, C.M., 2018. Runx1 deficiency protects against adverse cardiac remodeling after myocardial infarction. *Circulation* 137, 57–70.
- McDaneld, T.G., Hancock, D.L., Moody, D.E., 2004. Altered mRNA abundance of ASB15 and four other genes in skeletal muscle following administration of β -adrenergic receptor agonists. *Physiol. Genom.* 16, 275–283.
- Morita, Y., Andersen, P., Hotta, A., Sasagawa, N., Kurokawa, J., Tsukahara, Y., Hayashida, N., Koga, C., Nishikawa, M., Evans, S.M., Furukawa, T., Koshiba-Takeuchi, K., Nishinakamura, R., Yoshida, Y., Kwon, C., Takeuchi, J.K., 2016. Sall1 transiently marks undifferentiated heart precursors and regulates their fate. *J. Mol. Cell. Cardiol.* 92, 158–162.
- Nakayama, H., Hamatani, T., Kumagai, S., Tonegawa, K., Yamashita, T., Fujo, Y., 2018. Cardiac-specific overexpression of Runx2 mediates cardiac hypertrophy and dysfunction in mice. *Circ. Res.* 111, A241.
- Nelms, B.L., Pfaltzgraff, E.R., Labosky, P.A., 2011. Functional interaction between foxd3 and pax3 in cardiac neural crest development. *Genesis* 49, 10–23.
- Ortiz, M., Kaessmann, H., Zhang, K., Bashirova, A., Carrington, M., Quintana-Murci, L., Telenti, A., 2008. The evolutionary history of the CD209 (DC-SIGN) family in humans and non-human primates. *Gene Immun.* 9, 483–492.
- Park, D.S., Fishman, G.L., 2017. Development and function of the cardiac conduction system in health and disease. *J Cardiovasc Dev Dis*, 2017.
- Park, H.L., Bai, C., Platt, K.A., Matisse, M.P., Beeghly, A., Hui, C.C., Nakashima, M., Joyner, A.L., 2000. Mouse Gli1 mutants are viable but have defects in SHH signalling in combination with a Gli2 mutation. *Development* 127, 1593–1605.
- Petkova, M., Atkinson, J.A., Yanni, J., Stuart, L., Aminu, J.A., Ivanova, D.A., Pustovit, B.K., Geraghty, C., Feather, A., Li, N., Zhang, Y., Oceandy, D., Perde, F., Molenaar, P., D'Souza, A., Fedorov, V.V., Dobrzynski, H., 2020. Identification of key small non-coding microRNAs controlling pacemaker mechanisms in the human sinus node. *J Am Heart Assoc* 9, e016590.
- Pinto, A.R., Godwin, J.W., Rosenthal, N.A., 2014. Macrophages in cardiac homeostasis, injury responses and progenitor cell mobilisation. *Stem Cell Res.* 13, 705–714.
- Qin, X., Jiang, Q., Miyazaki, T., Komori, T., 2019. Runx2 regulates cranial suture closure by inducing hedgehog, Fgf, Wnt and Pthlh signaling pathway gene expressions in suture mesenchymal cells. *Hum. Mol. Genet.* 28, 896–911.
- Queipo-Ortuno, M.I., Escote, X., Ceperuelo-Mallafre, V., Garrido-Sanchez, L., Miranda, M., Clemente-Postigo, M., Perez-Perez, R., Peral, B., Cardona, F., Fernandez-Real, J.M., Tinahones, F.J., Vendrell, J., 2012. FABP4 dynamics in obesity: discrepancies in adipose tissue and liver expression regarding circulating plasma levels. *PLoS One* 7, e48605.
- Riddell, A., McBride, M., Braun, T., Nicklin, S.A., Cameron, E., Loughrey, C.M., Martin, T.P., 2020. Runx1: an emerging therapeutic target for cardiovascular. *Cardiovasc. Res.* 116, 1410–1423.
- Riley, P., Anson-Cartwright, L., Cross, J.C., 1998. The Hand1 bHLH transcription factor is essential for placenta and cardiac morphogenesis. *Nat. Genet.* 18, 271–275.
- Rojo, R., Raper, A., Ozdemir, D.D., Lefevre, L., Grabert, K., Wollscheid-Lengeling, E., Bradford, B., Caruso, M., Gazova, I., Sanchez, A., Lisowski, Z.M., Alves, J., Molina-Gonzalez, I., Davtyan, H., Lodge, R.J., Glover, J.D., Wallace, R., Munro, D.A.D., David, E., Amit, I., Miron, V.E., Priller, J., Jenkins, S.J., Hardingham, G.E., Blurton-Jones, M., Mabbott, N.A., Summers, K.M., Hohenstein, P., Hume, D.A., Pridans, C., 2019. Deletion of a Csf1r enhancer selectively impacts CSF1R expression and development of tissue macrophage populations. *Nat. Commun.* 10, 11053–11058.
- Saeed, Y., Temple, I.P., Atkinson, A., Yanni, J., Maczewski, M., Aly, M., Logantha, S.J.R.J., Garratt, C.J., Dobrzynski, H., 2018. Structural and functional remodeling of the atrioventricular node with aging in rate: the role of hyperpolarization-activated cyclic nucleotide-gated and ryanodine 2 channels. *Heart Rhythm* 15, 752–760.
- Schweizer, A.P., Darce, F.F., Ullrich, D.N., Geschwill, P., Greber, B., Rivinius, R., Seyler, C., Muller, D.K., Draguhn, A., Utikal, J., Koenen, M., Katus, A.H., Thomas, D., 2017. Subtype-specific differentiation of cardiac pacemaker cell clusters from human induced pluripotent stem cells. *Stem Cell Res. Ther.* 8, 229.
- Shiraishi, I., Takamatsu, T., Minamikawa, T., Onouchi, Z., Fujita, S., 1992. Quantitative histological analysis of the human sinoatrial node during growth and aging. *Circulation* 85, 176–184.
- Starzyk, R.M., Rosenow, C., Frye, J., Leismann, M., Rodzinski, E., Putney, S., Tuomanen, E.I., 2000. Cerebral cell adhesion molecule: a novel leukocyte adhesion determinant on blood-brain barrier capillary endothelium. *J. Infect. Dis.* 181, 181–187.
- Stephenson, S.R., Atkinson, A., Kottas, P., Perde, F., Jafarzadeh, F., Bateman, M., Iaizzo, A.P., Zhao, J., Zhang, H., Anderson, H.R., Jarvis, C.J., Dobrzynski, H., 2017. High resolution 3-dimensional imaging of the human cardiac conduction system from microanatomy to mathematical modeling. *Sci. Rep.* 7, 1–13.
- Stephenson, S.R., Boyett, R.M., Hart, G., Nikolaidou, T., Cai, Xue, Corno, F.A., Alphonso, N., Jeffery, N., Jarvis, C.J., 2012. Contrast enhanced micro-computed tomography resolves the 3-dimensional morphology of the cardiac conduction system in mammalian hearts. *PLoS One* 7, e35299.
- Sunwoo, J.B., Kim, S., Yang, L., Naik, T., Higuchi, A.D., Rubenstein, L.J., Yokoyama, W.M., 2008. Distal-less homeobox transcription factors regulate development and maturation of natural killer cells. *Proc. Natl. Acad. Sci. Unit. States Am.* 105, 10877–10882.
- Swirski, K.F., Nahendorf, M., 2018. Cardioimmunology: the immune system in cardiac homeostasis and disease. *Nat. Rev. Immunol.* 18, 733–744.
- Tang, H., Gao, Y., Li, Z., Miao, Y., Huang, Z., Liu, X., Xie, L., Wen, W., Zheng, Y., Su, W., 2020. The noncoding and coding transcriptional landscape of the peripheral immune response in patients with COVID-19. *Clin. Transl. Med.* 10, e200.
- Tessadori, F., van Weerd, H.J., Burkhard, B.S., Verkerk, O.A., de Pater, E., Boukens, J.B., Vink, A., Christoffels, M.V., Bakkers, J., 2012. Identification and functional characterization of cardiac pacemaker cells in zebrafish. *PLoS One* 7, e47644.
- Thum, T., Galuppo, P., Wolf, C., Fiedler, J., Kneitz, S., van Laake, L.W., Doevendans, A.P., Mummery, C.L., Borlak, J., Haverich, A., Gross, C., Engelhardt, S., Ertl, G., Bauersach, J., 2007. MicroRNAs in the human heart: a clue to fetal gene reprogramming in heart failure. *Circulation* 17, 258–267.
- van der Deen, M., Akech, J., Lapointe, D., Gupta, S., Young, W.D., Montecino, A.M., Galindo, M., Lian, B.J., Stein, L.J., Stein, S.G., van Wijnen, J.A., 2012. Genomic promoter occupancy of runt-related transcription factor RUNX2 in osteosarcoma cells identifies genes involved in cell adhesion and motility. *J. Biol. Chem.* 287, 4503–4517.
- van Eif, V.W.W., Stefanovic, S., van Duijvenboden, K., Bakker, M., Wakker, V., de Gierde Vries, C., Zaffran, S., Verkerk, A.O., Boukens, B.J., Christoffels, V.M., 2019. Transcriptome analysis of mouse and human sinoatrial node cells reveals a conserved genetic program. *Development* 146, dev173161.
- van Eif, V.W.W., Devalla, D.H., Boink, J.J.G., Christoffels, M.V., 2018. Transcriptional regulation of the cardiac conduction system. *Nat. Rev. Cardiol.* 15, 1–14.

- Vasconcelos, F.F., Sessa, A., Laranjeira, C., Raposo, A.A.S.F., Teixeira, V., Hagey, D.W., Tomaz, D.M., Muhr, J., Broccoli, V., Castro, D.S., 2016. MyT1 counteracts the neural progenitor program to promote vertebrate neurogenesis. *Cell Rep.* 17, 469–483.
- Wangler, M.F., Gonzaga-Jauregui, C., Gambin, T., Penney, S., Moss, T., Chopra, A., Probst, F.J., Xia, F., Yang, Y., Werlin, S., Eglite, I., Kornejeva, L., Bacino, A.C., Baldrige, D., Neul, J., Lehman, E.L., Larson, A., Beuten, J., Muzny, D.M., Jhangiani, S., B-HCMG, Gibbs, R.A., Lupski, J.R., Beaudet, A., 2014. Heterodysgenic de novo and inherited mutations in the smooth muscle actin (ACTG2) gene underlie megacystis-microcolon-intestinal hypoperistalsis syndrome. *PLoS Genet.* 10, e1004258.
- Williams, M.W., Bloch, R.J., 1999. Differential distribution of dystrophin and beta-spectrin at the sarcolemma of fast twitch skeletal muscle fibres. *J. Muscle Res. Cell Motil.* 20, 383–393.
- Wong, H.H., Seet, S.H., Bascom, C.C., Isfort, R.J., Bard, F., 2020. Red-COLA1: a human fibroblast reporter cell line for type I collagen transcription. *Sci. Rep.* 10, 1–12.
- Wynn, T.A., 2009. Cellular and molecular mechanisms of fibrosis. *J. Pathol.* 214, 199–210.
- Xiao, Q., Hou, N., Wang, Y.-P., Zhang, G.-P., Yi, Q., Liu, S.-M., Chen, M.-S., Luo, J.-D., 2012. Impaired sonic hedgehog pathway contributes to cardiac dysfunction in type 1 diabetic mice with myocardial infarction. *Cardiovasc. Res.* 95, 507–516.
- Yamamoto, M., Abe, S.-I., Rodriguez-Vazquez, J.F., Fajimiya, M., Murakami, G., Ide, Y., 2011. Immunohistochemical distribution of desmin in the human fetal heart. *J. Anat.* 219, 253–258.
- Zanetti, M., Braghetta, P., Sabatelli, P., Mura, I., Doliana, R., Colombatti, A., Volpin, D., Bonaldo, P., Bressan, G.M., 2004. EMILIN-1 deficiency induces elastogenesis and vascular cell defects. *Mol. Cell Biol.* 24, 638–650.
- Zhang, H., Holden, A.V., Kodama, I., Honjo, M., Lei, M., Varghese, T., Boyett, R.M., 2000. Mathematical models of action potentials in the periphery and center of the rabbit sinoatrial node. *Am. J. Physiol.* 279, 397–421.
- Zhang, H., Tian, L., Shen, M., Tu, C., Wu, H., Gu, M., Paik, D.T., Wu, J.C., 2019. Generation of quiescent cardiac fibroblasts from human induced pluripotent stem cells for in vitro modeling of cardiac fibrosis. *Circ. Res.* 125, 552–566.
- Zicha, S., Fernandez-Velasco, M., Lonardo, G., L'Heureux, N., Nattel, S., 2005. Sinus node dysfunction and hyperpolarization-activated (HCN) channel subunit remodelling in a canine heart failure model. *Cardiovasc. Res.* 66, 472–481.
- Zriwil, A., Boiers, C., Wittmann, L., Green, J.C.A., Woll, P.S., Jacobsen, S.E.W., Sitnicka, E., 2016. Macrophage colony-stimulating factor receptor marks and regulates a fetal myeloid-primed B-cell progenitor in mice. *Blood* 128, 217–226.

4.5 Limitations

The three specimens used in this study were aged 19, 21, and 54. Although principal component analysis showed that the SN samples from these age groups were like each other and different from the RA samples from the same groups, it would be ideal to compare comparing another sample from an age group similar to 19 to 21. A similar age group would eliminate any potential age-related anomalies.

CHAPTER 5) MIR-486-3P AND MIR-938 – IMPORTANT INHIBITORS OF PACEMAKING ION CHANNELS AND/OR MARKERS OF IMMUNE CELLS³

The study described in Chapter 4 provided novel insights into predicted interactions between key miRNAs, mRNAs, and cell markers – particularly markers of immune cells. It was interesting to see that both miR-486-3p and miR-133a-3p inhibit the mRNAs of Ca²⁺ ion channels and a mast cell marker (TPSAB1). It is important to experimentally validate these interesting, predicted interactions that underlie the molecular mechanisms of the healthy human SN.

This chapter provides insights into the interaction between key miRNAs and mRNAs that play key roles in the sinus node (SN).

This study identifies potential therapeutic targets for treating SN dysfunctions (SND). This study aimed to validate previously predicted interactions between miRNAs and mRNAs of key pacemaking Ca²⁺ ion channels and mRNA of TPSAB1 using luciferase assay experiments. These predicted interactions were mentioned in the previous chapter.

Previous studies (Petkova et al. 2020, Aminu et al. 2021) show Ca_v1.3, Ca_v3.3 or TPSAB1 are upregulated, and miR-486-3p and miR-938 (a novel miRNA highly expressed in the human right atrium) are downregulated in the human SN, compared to the surrounding right atrium. Using bioinformatics software, we predicted these mRNAs to be inhibited by these miRNAs. To validate these predictions, rat cardiac H9C2 were transfected with either Ca_v1.3, Ca_v3.3, or TPSAB1, along with miR-486-3p or miR-938 in a luciferase reporter gene assay. The study showed that miR-486-3p significantly downregulates Cav1.3, Cav3.3, and TPSAB1-mediated luciferase activity is significantly downregulated by miR-938.

This chapter provides novel insights into the interaction between key miRNAs, ion channels, and immune cell markers in H9C2 cells. Therefore, it provides a basis for the further exploration of these miRNAs and their effect on cardiac function/dysfunction.

At the end of this thesis is an appendix that contains additional data relevant to this study. This appendix was not included in the final publication of the paper.

³ This chapter is directly from the publication: **Aminu, A. J.**, Petkova, M., Chen, W. C., Yin, Z., Kuzmin, V. S., Atkinson, A. J., Dobrzynski, H., *MiR-486-3p and miR-938-important inhibitors of pacemaking ion channels and/or markers of immune cells.* Appl. Sci., 2021. **11**: p. 11366

5.1 Authors' contribution to the paper

I (Abimbola J. Aminu) performed most of the experiments in this study. I also wrote and edited the paper. I appreciate the effort and input from all co-authors.

- Abimbola J. Aminu: performed all luciferase assay experiments; analysis of all datasets; created all figures, graphs, and tables; manuscript planning, writing, and editing; supervision of Weixuan Chen and Zeyuan Yin
- Maria Petkova: contributed to bioinformatics and luciferase assay experiments
- Weixuan Chen: contributed to luciferase assay experiments (i.e., performed some methods as part of her training while I supervised); manuscript editing (original draft)
- Zeyuan Yin: contributed to luciferase assay experiments (i.e., performed some methods as part of his training while I supervised)
- Vlad S. Kuzmin: manuscript editing (original draft)
- Andrew J. Atkinson: supervision
- Halina Dobrzynski: supervision; data analysis; formatted figures and tables; manuscript review and editing

5.2 Hypothesis

The *in-silico* prediction of interactions between key miRNAs (e.g., miR-486-3p) and key mRNAs (e.g., $Ca_v1.3$) in the adult human SN required further exploration. If it is predicted that these key miRNAs have binding sites on their target mRNAs, then experimental validation should prove this

5.3 Aims

The aims were based on the experimental validation of key predicted interactions. As published in Paper 3, Chapter 5, I aimed to use luciferase assay experiments to validate the predicted interactions between microRNAs, key pacemaking ion channels, TFs, markers for immune (mast) cells, and collagen.

This study identifies potential therapeutic targets for treating SN dysfunctions (SND). The aim was to use luciferase assay experiments to validate previously predicted interactions between miRNAs and mRNAs of key pacemaking Ca^{2+} ion channels and mRNA of TPSAB1 (a mast cell marker). These predicted interactions were mentioned in the previous chapter.

5.4 Materials and methods

Thorough descriptions of the methods used in this study are provided in the accompanying paper.

5.4.1 H9C2 cells

Rat cardiac H9C2 cells were purchased from ATCC, LGC Limited, Middlesex, UK. Upon arrival, they were stored in a liquid nitrogen storage freezer. When needed, they were defrosted in a water bath at a temperature of 37°C before storing in DMEM containing 10% feline bovine serum (FBS), 1% penicillin-streptomycin, and 1% nonessential amino acids (this made up the cell culture medium). The cells were then stored in a 37°C incubator. This initial passage was passage 1. After splitting the cells a few times (up to a passage number of 4), some cells were frozen in separate vials at 1 million cells per 1 ml of freezing media (containing 1 mL dimethyl sulfoxide, 5 mL FBS, and 4 mL cell culture medium). For the luciferase assay experiments, the cells were used at passage numbers ranging between 4 and 20 or until the structure of the cells started to disintegrate following microscopic observation.

Following the laboratory practice of the department, the cells were routinely tested for mycoplasma infection. Contamination of cell cultures can cause major problems such as: altering the DNA and protein synthesis of the cells, halting experimental procedures for weeks, and infecting other cell cultures that are kept in the same incubator, to name a few.

5.4.2 MiRNAs

MiRNA mimics arrived from Horizon Discovery (UK) in a powder form in a 96-well plate. These miRNAs were: miR-1-3p; miR-30c-5p; miR-486-3p; miR-133a-3p; miR-938; miR-429; and miR-422a. A non-functional scrambled miRNA from the *c. elegans* family was also purchased to serve as a control miRNA. The plates were spun at 2000 rpm for approximately 30 seconds to ensure that all the powder was suspended at the bottom of each well. The powder was diluted using 20 µl 1X siRNA buffer to a concentration of 5 µM. The plate was then sealed before storing in a -20 °C freezer.

The first time I performed this, I noticed that the solution had evaporated by the time I wanted to use the miRNAs for luciferase experiments. I realised that the plate was not sealed tightly enough – causing the solution to evaporate while it was stored in the freezer. To overcome this issue, after the powder was diluted in 20 µl 1X siRNA buffer to a concentration of 5 µM, each solution was transferred to a 1 mL microcentrifuge tube. These tubes were then stored in a -20 °C freezer.

5.4.3 Plasmids

All the human-3'UTR-containing plasmids were purchased from GeneCopoeia (Rockville, MD, USA) or LabOmics (UK). These plasmids were Ca_v1.3, Ca_v3.1, HCN1, HCN4, TBX3, TBX18, TPSAB1, COL1A1, LZTS1, LBH, and HLA-DRA.

These plasmids were predicted to interact with the miRNAs mentioned above. The predicted miRNA-mRNA interactions were based on the studies described in Chapter 4.

5.4.4 Plasmid amplification

1 µL of each plasmid was taken up in 20 µL of supercompetent cells before placing them on ice and heat shocking them for approximately 30 seconds. The solution was put on ice again before spreading on an agar plate containing carbenicillin (under sterile conditions). This plate was then stored overnight in a 37°C incubator.

The following day, a single colony was picked using a glass 'picker' and placed into a solution of 3 mL LB medium and 3 µL carbenicillin (both sterile) (100 µg/µL), then placed in a shaker overnight at a speed of 120 rpm at 37°C. The following day, the solution was cloudy – indicating that the colony had multiplied. However, the solution was not cloudy on some occasions, and the colony had not multiplied. To overcome this, 2 or 3 colonies were picked (rather than 1) and placed into the LB medium and carbenicillin solution. 1 mL of the cloudy solution was then added to a 200 mL LB medium solution and 200 µL carbenicillin in a shaker overnight at a speed of 200 rpm at 37°C.

The following day, a Purelink Plasmid Kit (Thermo Fisher Scientific, Altrincham, UK) was used to extract and purify the plasmid DNA according to the manufacturer's protocol.

5.4.5 Luciferase reporter gene assay experiments

On day 1, rat cardiac H9C2 cells were seeded into a 96-well plate at a density of 50,000 cells per well in 250 µL media for 24 h, stored in an incubator at 37 °C and 5% CO₂. The following day, the media was replaced with 225 µL fresh media. Cells were then transfected with 0.25 µg human plasmid (i.e., mRNA) (from a stock solution of 1 µg/µL) and with 1.25 µL miRNA (from a stock solution of 5 µM). The plasmid and miRNA were diluted in 11 µL optiMEM, and 0.75 µL Lipofectamine 2000 (ThermoScientific, Altrincham, UK) was diluted in 11.75 µL optiMEM. This brought the total solution to 25 µL. This 25 µL solution of diluted plasmid, miRNA and lipofectamine was mixed and incubated at room temperature for approximately 5 minutes. The solution was then added to the well containing the 225 µL media. The plate was then stored in an incubator at 37 °C and 5% CO₂ for 24 h.

The following day, the media was aspirated from the cells, then 50 µL lysis buffer was added, and the plate was placed on a rocker for approximately 20 minutes to detach (i.e., 'lyse') the cells from the well. Following this, 10 µL of each lysate was added into a 96-well plate, in duplicates, for luciferase and renilla readings, from a GloMax Luminometer (Promega, Southampton, UK). This luminometer injected 50 µL of luciferase or renilla from injectors 1 or 2. Luciferase activity was normalised to renilla, and bioluminescence was read as a normalised ratio of $\frac{\text{luciferase}}{\text{renilla}}$. This ratio was input into GraphPad Prism 8. The number of luciferase assay experiments per plasmid/miRNA ranged between 3-5. Statistical significance was calculated in GraphPad Prism 8 and identified using an unpaired t-test. $P \leq 0.05$ indicated statistical significance.

5.4.6 Prediction of binding sites

The 3'UTR sequence of the target human mRNAs was obtained from Genome (<https://genome.ucsc.edu/>), and the miRNA sequence was obtained from miRbase (<https://www.mirbase.org/>). TargetScan Human (https://www.targetscan.org/vert_72/) and RNA22 (<https://cm.jefferson.edu/rna22/interactive/>) were used to predict the number of binding sites on the target mRNA for the miRNA.

Article

MiR-486-3p and MiR-938—Important Inhibitors of Pacemaking Ion Channels and/or Markers of Immune Cells

Abimbola J Aminu ¹, Maria Petkova ¹, Weixuan Chen ¹ , Zeyuan Yin ¹ , Vlad S Kuzmin ², Andrew J Atkinson ¹ 
and Halina Dobrzynski ^{1,3,*} 

¹ Cardiovascular Sciences, School of Medicine, University of Manchester, Manchester M13 9PL, UK; abimbola.akerele@postgrad.manchester.ac.uk (A.J.A.); petkova4656@gmail.com (M.P.); weixuan.chen@postgrad.manchester.ac.uk (W.C.); zeyuan.yin@postgrad.manchester.ac.uk (Z.Y.); andrew.atkinson-2@manchester.ac.uk (A.J.A.)

² Biological Faculty, Department of Human and Animal Physiology, Leninskie Gory 1, Building 2, Lomonosov Moscow State University, 119991 Moscow, Russia; ku290381@gmail.com

³ Department of Anatomy, Jagiellonian University Medical College, Świętej Anny 12, 31-008 Krakow, Poland

* Correspondence: halina.dobrzynski@manchester.ac.uk; Tel.: +44-1612751182

Abstract: The sinus node (SN) is the heart's primary pacemaker and has a unique expression of pacemaking ion channels and immune cell markers. The role of microribonucleic acids (miRNAs) in control of ion channels and immune function of the sinus node is not well understood. We have recently shown that hsa-miR-486-3p downregulates the main pacemaking channel HCN4 in the SN. In addition, we recently demonstrated that immune cells are significantly more abundant in the SN compared to the right atrium. The aim of this study was to validate the previously predicted interactions between miRNAs and mRNAs of key Ca²⁺ ion channels (involved in peacemaking) and mRNA of TPSAB1—a mast cells marker) using luciferase assay. We now show that miR-486 significantly downregulates Ca_v1.3, Ca_v3.1, and TPSAB1-mediated luciferase activity, while miR-938 significantly downregulates only TPSAB1-mediated luciferase activity. This makes miR-486-3p a potential therapeutic target in the treatment of SN dysfunctions.

Keywords: miR-486-3p; miR-938; Ca_v1.3; Ca_v3.1; TPSAB1; sinus node; pacemaking channels; mast cells; cardiovascular diseases



Citation: Aminu, A.J.; Petkova, M.; Chen, W.; Yin, Z.; Kuzmin, V.S.; Atkinson, A.J.; Dobrzynski, H. MiR-486-3p and MiR-938—Important Inhibitors of Pacemaking Ion Channels and/or Markers of Immune Cells. *Appl. Sci.* **2021**, *11*, 11366. <https://doi.org/10.3390/app112311366>

Academic Editor: Michal Sobkowski

Received: 4 November 2021

Accepted: 26 November 2021

Published: 1 December 2021

Publisher's Note: MDPI stays neutral with regard to jurisdictional claims in published maps and institutional affiliations.



Copyright: © 2021 by the authors. Licensee MDPI, Basel, Switzerland. This article is an open access article distributed under the terms and conditions of the Creative Commons Attribution (CC BY) license (<https://creativecommons.org/licenses/by/4.0/>).

1. Introduction

As part of the cardiac conduction system (CCS), the sinus node (SN) is the primary pacemaker of the heart and is located at the junction of the superior vena cava and right atrium. The SN is a crescent-shaped structure that extends along the crista terminalis [1,2]. Compared to the surrounding working myocardium, the SN has distinctive molecular and functional properties—owing to its unique expression of ion channels and Ca²⁺-handling proteins, both responsible for the membrane voltage and Ca²⁺ clocks—as we have previously described [1].

Hyperpolarization-activated cyclic nucleotide-gated channels 1 and 4 (HCN1, HCN4) are the key ion channels responsible for the SN's myocytes' diastolic depolarization also known as the pacemaker potential, with HCN4 being the main isoform that is highly expressed in human SN [3,4]. The Ca_v3.1 ion channel carries the T-type calcium current (I_{Ca,T}) at the late diastole phase of the pacemaker potential, and Ca_v1.3 carries the L-type calcium current (I_{Ca,L}) at the upstroke phase of the action potential [3]. We have previously shown that these key ion channels are highly expressed in the human SN, compared to the atrial muscle [1,4]. The SN dysfunction of these ion channels contribute to the development of SN-related rhythm abnormalities such as bradycardia, tachycardia, sinus arrest, etc. [3,5].

Small noncoding RNA molecules (miRNAs) have been extensively studied and are known to regulate the post-transcriptional expression of protein-coding genes, through

inhibition [6] by binding to complementary 3 prime untranslated region (3'UTR) of their target messenger-ribonucleic acids (mRNAs). This regulation plays key roles in the development of cardiac diseases such as cardiac arrhythmia, hypertrophy, fibrosis, and heart failure [7–9].

Our previous studies have shown that 18 microRNAs are significantly more expressed, and 48 microRNAs are significantly less expressed in the SN vs. right atrium [1,4]. Among these microRNAs, seven microRNAs (miR-1-3p, miR-30c-5p, miR-133a-3p, miR-429, miR-4220, miR-486-3p, and miR-938) were predicted to inhibit key pacemaking ion channels (HCN1, HCN4, $Ca_v1.3$, and $Ca_v3.1$) [4], key transcription factors (TFs) (TBX3 and TBX18) [4], a mast cell marker (TPSAB1—a tryptase isoenzyme), and macrophage cell marker CD209 [10], which are significantly more expressed in the SN compared to the right atrium [10]. We have also shown that miR-486-3p reduces the beating rate of rat SN via inhibition of HCN4 [4].

To further our understanding of the SN's pacemaking and immune response function, the aim of this work was to validate the previously predicted interactions between six miRNAs and key ion channels, transcription factors, immune cell markers, and collagen using luciferase assay experiments. A reduction in bioluminescence indicated that the inhibition of miRNA's target is taking place. Renilla reporter gene is used to normalize values produced by the luciferase reporter gene. We found that out of the seven microRNAs that are predicted to inhibit key pacemaking channels and mast cell marker, some microRNAs did or did not downregulate their predicted targets.

2. Materials and Methods

Main methods are summarized in Figure 1.

2.1. MiRNAs

MiRNA mimics were ordered from the Dharmacon Cherry Pick library (Horizon Discovery) and arrived in a powder form in a 96-well plate. This was then resuspended in 1X siRNA buffer (diluted from 5X buffer Dharmacon using RNase-free water). All miRNAs were diluted to a final concentration of 5 μ M. Plates were spun down, at a speed of 2000 rpm for 30 s, before adding 20 μ L of 1X siRNA buffer to each well and storing at -20 °C. As one of the control experiments, scrambled miRNA (a nonfunctional miRNA) was used.

2.2. Plasmids

Human $Ca_v1.3$ (NCBI Reference Sequence: NM_000720.2; HmiT054373-MT06); HCN4 (NCBI Reference Sequence: NM_005477.2; HmiT088528-MT06); and TBX18 (NCBI Reference Sequence: NM_001080508.1; HmiT022062-MT06)—3'UTR-containing plasmids were purchased from GeneCopoeia (Rockville, MD, USA).

Human $Ca_v3.1$ (NCBI Reference: NM_001256324.1; HmiT055094-MT06); TPSAB1 (NCBI Reference Sequence: NM_003294.3; HmiT018221-MT06); TBX3 (NCBI Reference Sequence: NM_005996.4; HmiT117945-MT06); HCN1 (NCBI Reference Sequence: NM_021072.4; HmiT117946a-MT06); COL1A1 (NCBI Reference Sequence: NM_000088.4; HmiT127385-MT06); LZTS1 (NCBI Reference Sequence: NM_001362884.1; HmiT091521-MT06); LBH (NCBI Reference Sequence: NM_030915.4; HmiT127384-MT06); and HLA-DRA (NCBI Reference Sequence: 019111.4; HmiT100191-MT06)—3'UTR-containing plasmids were purchased from LabOmics, UK. The plasmids were delivered in pEZX-MT06 with reporter genes for firefly luciferase and tracking genes for renilla luciferase, in a 30–50 μ L solution. A generic vector information provided for all plasmids is shown in Figure 2. Further information regarding predicted interactions between miRNAs and mRNA is shown in Table 1.

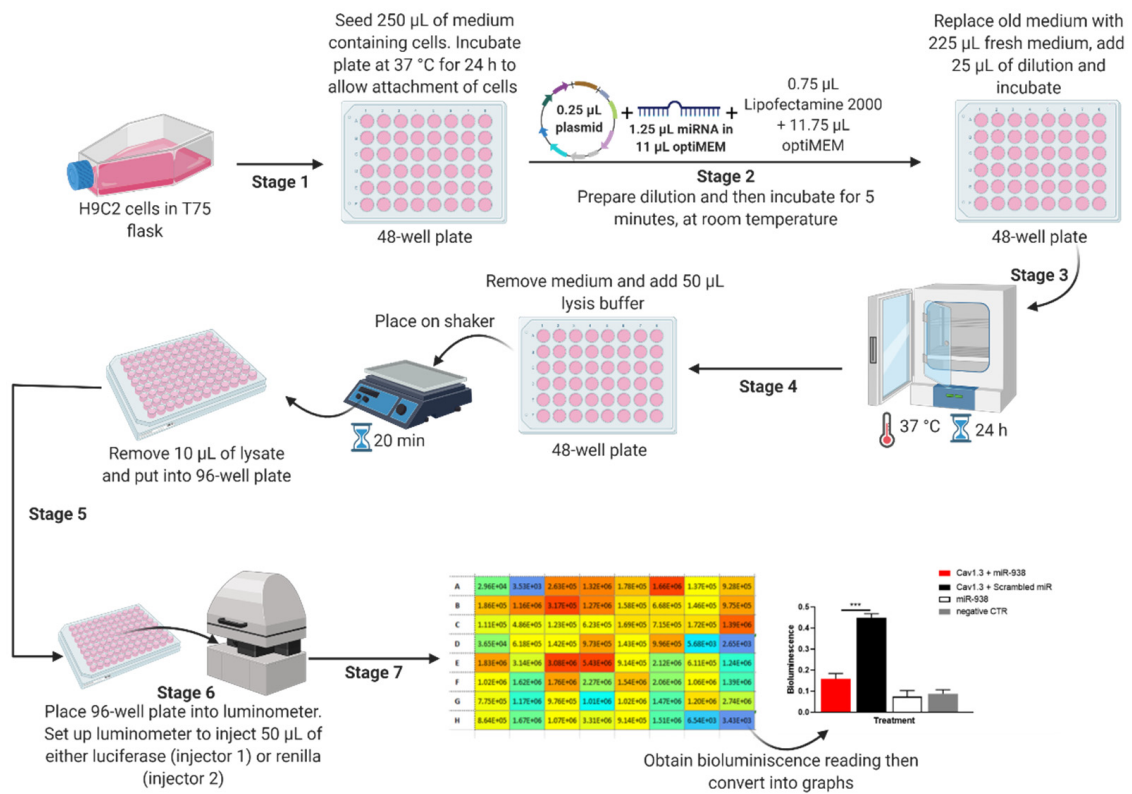


Figure 1. Summary of main methods. H9C2, a rat cardiomyoblast cell line; OptiMEM (Life Technologies, Inc., Gaithersburg, MD, USA), minimal essential medium; and miRNA, microribonucleic acid. Created with BioRender.com.

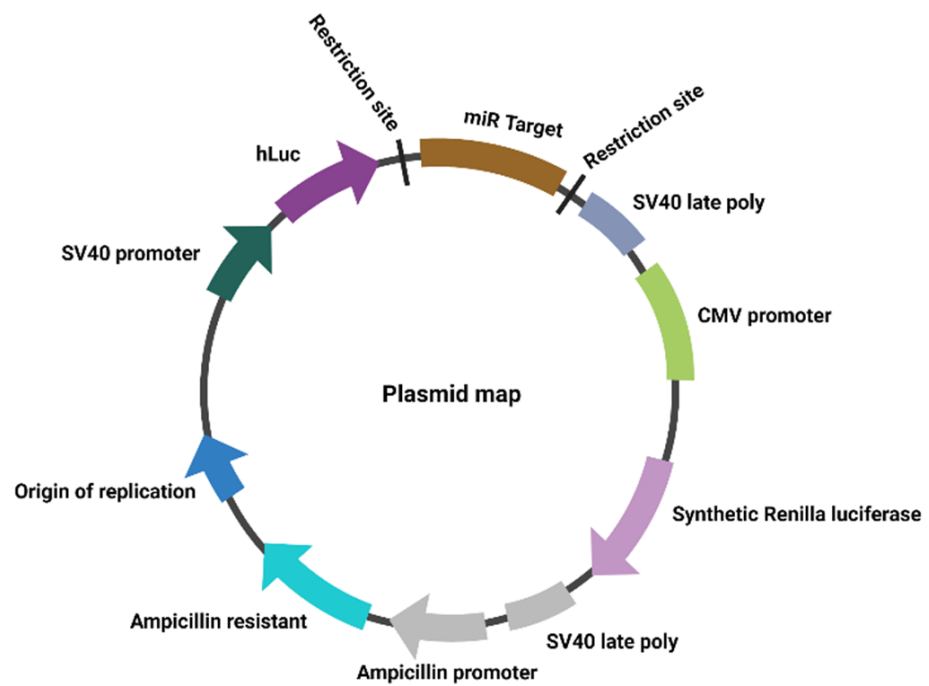


Figure 2. Generic vector map for all human plasmids used. SV40, Simian Virus 40 promoter; CMV, cytomegalovirus; hLuc, Firefly luciferase reporter gene. Modified from GeneCopoeia (Rockville, MD, USA) and LabOmics, Nivelles, Belgium.

2.3. Plasmid Amplification

In total, 1 μL of plasmid was taken up in 20 μL of supercompetent cells (XL1-Blue, Agilent Technologies) and placed on ice for 3 min before heat-shocking for 30 s. The solution was placed on ice again before spreading 21 μL solution on an agar gel plate (containing carbenicillin) and incubating at 37 °C overnight. Then, a single bacterial colony transfected with the plasmid was added to a solution containing 3 mL sterile LB medium and 3 μL carbenicillin (100 $\mu\text{g}/\mu\text{L}$) overnight at 37 °C, shaking at a speed of 120 rpm. Following this, 1 mL of the resulting culture was mixed with a solution containing 200 mL LB medium and 200 μL carbenicillin (100 $\mu\text{g}/\mu\text{L}$) overnight at 37 °C, shaking at a speed of 120 rpm. The remaining 2 mL of culture was added to 200 μL 50% glycerol and stored at -80 °C for future use. The next day, the plasmid DNA was extracted and purified using Purelink Plasmid Kit (Thermo Fisher Scientific, Altrincham, UK), according to manufacturer's protocol. Concentration of plasmids was determined using a NanoDrop ND-1000 spectrophotometer (ThermoScientific, Altrincham, UK). The plasmid concentrations ranged between 0.3 and 2.3 $\mu\text{g}/\mu\text{L}$.

Table 1. Predicted microRNA-mRNA interactions. MicroRNA expression data are based on our previous studies [4,10]. Significant change in the expression of mRNA and microRNA is classed as $p \leq 0.05$. Red represents significantly more expressed mRNA in the SN vs. right atrium. Green represents significantly less expressed microRNA in the SN vs. right atrium. HCN1, HCN4, $\text{Ca}_v1.3$, and $\text{Ca}_v3.1$ are pacemaking ion channels (see text for details); LZTS1, LBH, TBX3, and TBX18 are transcription factors; COL1A1 is a collagen marker; TPSAB1 is a mast cell marker; HLA-DRA is histocompatibility complex marker; and CD209 is a macrophage cell marker. N = no; Y = yes; Hsa = homospaien.

Hsa-miRNA	Hsa-miRNA Sequence	Predicted Target mRNA	Number of Binding Sites for Hsa-miRNA on Hsa-mRNA
Hsa-miR-1-3p	UGGAAUGUAAAAGAAGUAUGUAU	HCN1	1
		HCN4	1
		TBX3	1
Hsa-miR-30c-5p	UGUAAACAUCUACACUCUCAGC	HCN1	1
		HCN4	1
		COL1A1	0
Hsa-miR-486-3p	CGGGGCAGCUCAGUACAGGAU	HCN1	6
		HCN4	7
		$\text{Ca}_v3.1$	1
		$\text{Ca}_v1.3$	6
		LZTS1	12
		LBH	1
		TPSAB1	2
		HLA-DRA	2
		CD209	1
Hsa-miR-133a-3p	UUUGGUCCCCUUAACCAGCUG	HCN4	5
		COL1A1	1
		TPSAB1	1
Hsa-miR-938	UGCCCUUAAAGGUGAACCCAGU	$\text{Ca}_v1.3$	9
		LBH	1
Hsa-miR-429	UAAUACUGUCUGGUAACCGU	TBX18	1
Hsa-miR-422a	ACUGGACUUAGGGUCAGAAGGC	TBX3	1

2.4. Luciferase Reporter Gene Assay

Rat cardiac H9C2 cells (cell line purchased from ATCC, LGC Limited, Middlesex, UK) were maintained in DMEM (Life Technologies, Inc., Gaithersburg, MD, USA) containing 10% feline bovine serum (Life Technologies, Inc., Gaithersburg, MD), 1% penicillin-streptomycin (Life Technologies, Inc., Gaithersburg, MD), and 1% nonessential amino acids (Thermo Fisher Scientific, Altrincham, UK). At day 1, cells were plated in 48-well plates

at a density of 50,000 cells in a volume of 250 μL of media for 24 h. Following this, the medium was removed and replaced with 225 μL of fresh medium. Cells were transfected with 0.25 μg plasmid (from a 1 $\mu\text{g}/\mu\text{L}$ stock solution) with 1.25 μL miRNA (from a 5 μM stock) in 11 μL of optiMEM (Life Technologies, Inc., Gaithersburg, MD). Lipofectamine 2000 (ThermoScientific, Altrincham, UK) was diluted in optiMEM (0.75 μL lipofectamine 2000 with 11.75 μL optiMEM). Then, the diluted lipofectamine 2000, diluted miRNA, and diluted plasmid were mixed (see Figure 1 for details) and allowed to incubate for 5 min at room temperature before adding to the cells in each well. The cells were then incubated at 37 $^{\circ}\text{C}$ and 5% CO_2 for 24 h before luciferase activity was measured.

Following this, renilla and luciferase substrate and buffers (Promega) were thawed at room temperature. Here, 1X cell culture lysis was prepared from 5X cell culture lysis reagent (Promega), using milliQ water to dilute. Medium was aspirated from the cells before washing with PBS, and then 50 μL lysis buffer was added and placed on a rocker for 20–25 min. In addition, 10 μL of each lysate was added into a 96-well plate in duplicate for both renilla and luciferase assay readings. A GloMax Luminometer (Promega, Southampton, UK) was set up to inject 50 μL of either luciferase (from injector pump 1) or renilla (from injector pump 2) per well. Luciferase assay activity was normalized to renilla assay activity to obtain a ratio than was then inputted in GraphPad Prism 8. Batches of experiments ranged between 3 and 6.

2.5. Statistical Analysis

In Tables 2 and 3 and Figures 3–5 mean \pm SEM values are shown. All statistical analysis was carried out using GraphPad Prism 8. Significant differences were identified using unpaired t test. Significant difference was assumed at $p \leq 0.05$.

Table 2. Nonsignificant downregulation of hsa-mRNAs by hsa-miRNAs in H9C2 cells, observed following luciferase assay experiments. Mean \pm SEM values are shown. Red represents significantly more expressed mRNA in the SN vs. right atrium whereas green represents significantly less expressed microRNA in the SN vs. right atrium, as shown in our previous publications [4,10].

Hsa-miRNA	Predicted Target hsa-mRNA	Hsa-miRNA Plus hsa-mRNA Mean \pm SEM	Scrambled hsa-miRNA Plus hsa-mRNA Mean \pm SEM	Hsa-miRNA No mRNA Mean \pm SEM	No hsa-miRNA and No hsa-mRNA (Negative Control) Mean \pm SEM
Hsa-miR-1-3p	HCN1	0.789 \pm 0.205	0.686 \pm 0.211	-	-
	HCN4	0.558 \pm 0.144	0.422 \pm 0.103	-	-
	TBX3	0.686 \pm 0.244	0.586 \pm 0.189	-	-
Hsa-miR-30c-5p	HCN1	0.955 \pm 0.248	0.686 \pm 0.211	-	-
	HCN4	0.689 \pm 0.024	0.422 \pm 0.103	-	-
	COL1A1	0.800 \pm 0.232	0.626 \pm 0.292	-	-
Hsa-miR-486-3p	HCN1	0.554 \pm 0.157	0.686 \pm 0.211	0.593 \pm 0.344	0.580 \pm 0.313
	LZTS1	0.326 \pm 0.178	0.556 \pm 0.178	0.707 \pm 0.398	0.589 \pm 0.310
	LBH	0.343 \pm 0.142	0.604 \pm 0.228	0.7065 \pm 0.398	0.589 \pm 0.310
	HLA-DRA	0.672 \pm 0.228	0.944 \pm 0.359	0.593 \pm 0.344	0.580 \pm 0.313
Hsa-miR-133a-3p	HCN4	0.457 \pm 0.111	0.422 \pm 0.103	-	-
	COL1A1	0.334 \pm 0.094	0.542 \pm 0.186	0.255 \pm 0.126	0.666 \pm 0.369
	TPSAB1	0.814 \pm 0.300	0.743 \pm 0.372	0.255 \pm 0.126	0.6666 \pm 0.369
Hsa-miR-938	LBH	0.276 \pm 0.109	0.575 \pm 0.190	0.081 \pm 0.035	0.093 \pm 0.024
Hsa-miR-429	TBX18	0.593 \pm 0.048	0.558 \pm 0.229	-	-
Hsa-miR-422a	TBX3	0.512 \pm 0.171	0.586 \pm 0.179	-	-

Table 3. Significant downregulation of hsa-mRNAs by hsa-miRNAs in H9C2 cells, observed following luciferase assay experiments. Mean \pm SEM values are shown. Red represents significantly more expressed mRNA in the SN vs. right atrium, whereas green represents significantly less expressed miRNA in the SN vs. right atrium, as shown in our previous publications [4,10]. *p* values are shown in Figures 3–5.

Hsa-miRNA	Predicted Target hsa-mRNA	Hsa-miRNA Plus hsa-mRNA Mean \pm SEM	Scrambled hsa-miRNA Plus hsa-mRNA Mean \pm SEM	Hsa-miRNA No mRNA Mean \pm SEM	No hsa-miRNA and No hsa-mRNA (Negative Control) Mean \pm SEM
Hsa-miR-486-3p	Ca _v 3.1	0.511 \pm 0.111	1.188 \pm 0.281	0.596 \pm 0.344	0.567 \pm 0.318
	Ca _v 1.3	0.211 \pm 0.039	0.449 \pm 0.019	0.057 \pm 0.020	0.083 \pm 0.026
	TPSAB1	1.049 \pm 0.256	2.240 \pm 0.032	0.593 \pm 0.344	0.580 \pm 0.313
Hsa-miR-938	Ca _v 1.3	0.159 \pm 0.025	0.449 \pm 0.019	0.074 \pm 0.020	0.087 \pm 0.020

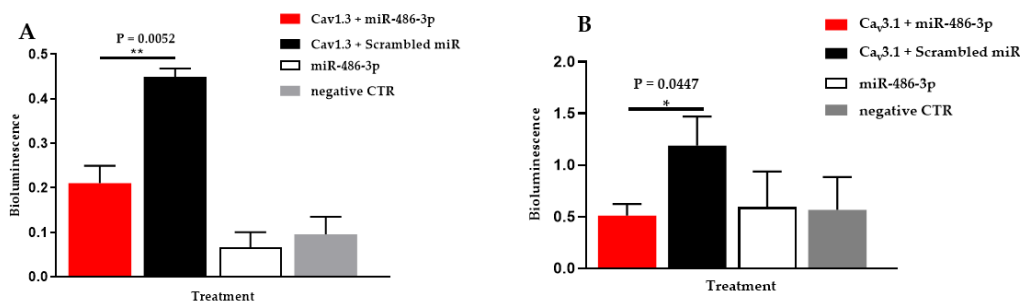


Figure 3. Luciferase bioluminescence after transfection of H9C2 cells with hsa-miR-486-3p and plasmids. Bioluminescence was recorded 24 h after transfecting H9C2 cells with 0.25 μ g of (A) Ca_v1.3'- or (B) Ca_v3.1—3'-untranslated region-containing plasmid and 1.25 μ L hsa-miR-486-3p or scrambled hsa-miRNA. Two control groups did not include the luciferase reporter gene, and cells were transfected with only hsa-miR-486-3p or remained untransfected (i.e., contained an equivalent volume of culture medium to replace the hsa-miRNAs or 3'-untranslated region-containing plasmid). Data are shown as mean \pm SEM ($n = 3$ batches of experiments were plotted for Ca_v1.3; $n = 6$ batches of experiments were plotted for Ca_v3.1; * $p \leq 0.05$, ** $p \leq 0.005$).

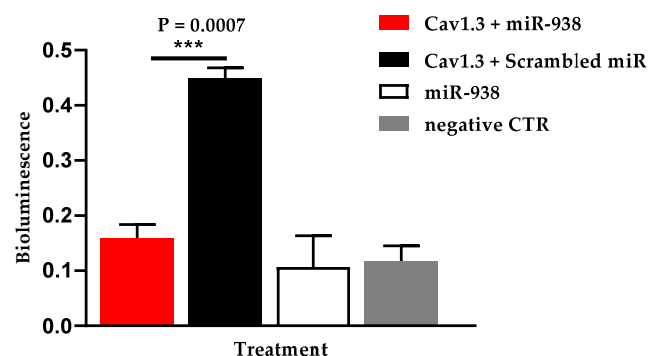


Figure 4. Luciferase bioluminescence after transfection of H9C2 cells with hsa-miR-938 and hsa-Ca_v1.3. Bioluminescence was recorded 24 h after transfecting H9C2 cells with 0.25 μ g of hsa-Ca_v1.3—3'-untranslated region-containing plasmid and 1.25 μ L hsa-miR-938 or scrambled miRNA. Two control groups did not include the luciferase reporter gene, and cells were transfected with only hsa-miR-938 or remained untransfected (i.e., contained an equivalent volume of culture medium to replace the miRNAs or Ca_v1.3). Data are shown as mean \pm SEM shown ($n = 3$ batches of experiments; *** $p \leq 0.0010$).

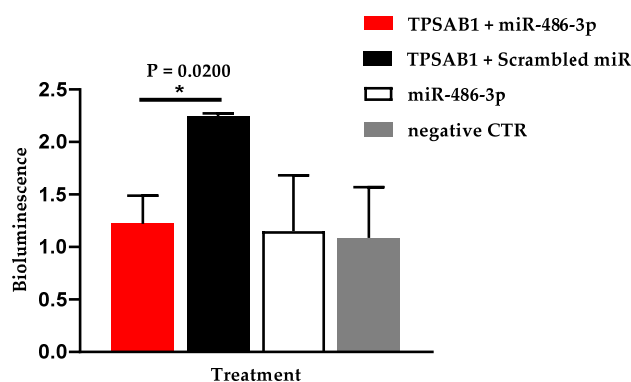


Figure 5. Luciferase bioluminescence after transfection of H9C2 cells with hsa-miR-486-3p and hsa-TPSAB1. Bioluminescence was recorded 24 h after transfecting H9C2 cells with 0.25 μ g of hsa-TPSAB1 3'-untranslated region-containing plasmid and 1.25 μ L has-miR-486-3p or scrambled miRNA. Two control groups did not include the luciferase reporter gene, and cells were transfected with only hsa-miR-486-3p or remained untransfected (i.e., contained an equivalent volume of culture medium to replace the miRNAs or hsa-TPSAB1). Data are shown as mean \pm SEM shown ($n = 3$ batches of experiments; * $p \leq 0.05$).

2.6. Binding Sites Prediction

Genome (<https://genome.ucsc.edu> accessed on 25 November 2021) was used to obtain the 3'UTR sequence for the target mRNAs. MirBase (<https://www.mirbase.org> accessed on 25 November 2021) was used to obtain the sequence for the microRNAs. The microRNA sequence and the 3'UTR sequence for their target mRNA were uploaded into RNA22 v2 (<https://cm.jefferson.edu/rna22/interactive/> accessed on 25 November 2021) or TargetScan Human (http://www.targetscan.org/vert_72/ accessed on 25 November 2021) in order to predict the number of binding sites on the mRNAs for their corresponding microRNAs and identify predicted binding sites (Table 1).

3. Results

Out of the 12 hsa-mRNAs that had been predicted to be inhibited by their respective has-miRNAs, we did not observe a significant decrease in luciferase activity with eight hsa-mRNAs and their respective hsa-miRNAs (Table 2). However, we observed a significant decrease in luciferase activity with four hsa-mRNAs and their respective hsa-miRNAs (Table 3, Figures 3–5), suggesting the presence of interaction between the hsa-mRNAs and hsa-miRNAs. Therefore, we can assume a reduction in the expression of the genes and proteins encoded by these genes, based on these observed interactions.

3.1. Hsa-miR-486-3p Significantly Downregulates Hsa-Ca_v1.3

Hsa-Ca_v1.3 is predicted to have six binding sites for hsa-miR-486-3p (Table 1). Hsa-Ca_v1.3-mediated luciferase activity was significantly reduced by hsa-miR-486-3p when compared to cells transfected with hsa-Ca_v1.3 and scrambled miR, hsa-miR-486-3p only, or negative control cells (culture media only) (Table 2 and Figure 3).

3.2. Hsa-miR-486-3p Significantly Downregulates Hsa-Ca_v3.1

Hsa-Ca_v3.1 is predicted to have one binding site for hsa-miR-486-3p (Table 1). Hsa-Ca_v3.1-mediated luciferase activity was significantly reduced by hsa-miR-486-3p, when compared to cells transfected with hsa-Ca_v3.1 and scrambled miR, hsa-miR-486-3p only, or negative control cells (culture media only) (Table 2 and Figure 3).

3.3. Hsa-miR-938 Significantly Downregulates Hsa-Ca_v1.3

Hsa-Ca_v1.3 is predicted to have nine binding sites for hsa-miR-938 (Table 1). Hsa-Ca_v1.3-mediated luciferase activity was significantly reduced by hsa-miR-938, when com-

pared to cells transfected with hsa -Ca_v1.3 and scrambled miR, hsa-miR-938 only, or negative control cells (culture media only) (Table 2 and Figure 4).

3.4. Hsa-miR-486-3p Significantly Downregulates Hsa-TPSAB1

Hsa-TPSAB1 is a marker for mast cells, involved in immune system regulation, and is predicted to have two binding sites for hsa-miR-486-3p (Table 1). Hsa-TPSAB1-mediated luciferase activity was significantly reduced by hsa-miR-486-3p, when compared to cells transfected with hsa-TPSAB1 and scrambled miR, hsa-miR-486-3p only, or negative control cells (culture media only) (Table 2 and Figure 5).

4. Discussion

Following our previously predicted interactions between key hsa-miRNAs and key hsa-mRNAs [4,10], it was important for us to experimentally verify these predictions. It should be noted that the experimental validation of miRNA-mRNA interaction is still a challenging feat. The reason why some predicted microRNA-mRNA interactions have been confirmed (through observations of significantly reduced bioluminescence/luciferase activity) and some interactions could not be confirmed could be due to several factors such as: thermodynamic stability and binding site accessibility—as recently reviewed by Riolo et. al., 2021 [11].

The current study focuses on two microRNAs (hsa-miR-486-3p and hsa-miR-938) that significantly reduces the luciferase of the mRNAs encoding for Ca²⁺ ion channels (Ca_v1.3 and Ca_v3.1) and a mast cell marker (TPSAB1) in H9C2 cells (Table 3). This suggests that an interaction between these mRNAs and their respective microRNAs is taking place; therefore, this could result in a reduction in expression of Ca_v1.3, Ca_v3.1, and TPSAB1.

In our previous study, we have shown that the direct binding of hsa-miR-486-3p to hsa-HCN4 significantly reduces HCN4-mediated luciferase activity and reduces the beating rate in the rat SN preparations [4]. We now provide evidence that hsa-miR-486-3p also significantly downregulates the luciferase activity of mRNAs encoding hsa-Ca_v1.3, hsa-Ca_v3.1, and hsa-TPSAB1 (Figures 3–5).

4.1. Hsa-miR-486-3p

Hsa-miR-486-3p is less expressed in the SN, which explains why the pacemaking ion channels and other related transcripts are more expressed in this specialized tissue of the heart [4]. In human SN during heart failure, hsa-miR-486-3p is upregulated [12]. The other predicted targets for hsa-miR-486-3p are hsa-Ca_v1.3, hsa-Ca_v3.1, hsa-TPSAB1, hsa-HCN1, hsa-HCN4, LZTS1, LBH, HLA-DRA, and TBX18 [4,10]—all of which we explored through luciferase assay experiments. Interestingly, we observed that hsa-miR-486-3p can significantly reduce the luciferase activity of three key target mRNAs (hsa-Ca_v1.3, hsa-Ca_v3.1, and hsa-TPSAB1) (Figures 3 and 5). In acute myocardial infarction patients, their serum hsa-miR-486-3p levels is increased [13,14]. The expression of hsa-miR-486-3p is also elevated during ventricular hypertrophy [15] and in patients with congenital heart diseases [16]. Not only does hsa-miR-486-3p inhibit hsa-TPAB1 (a mast cell marker), it also inhibits hsa-CD209 (a macrophage marker) [10]. We have pilot data that show a trend toward hsa-miR-486-3p inhibiting hsa-CD209 (data not shown). Hulsmans et. al. (2017) noticed a high expression of immune cells in the atrioventricular node (AV) of mice [17]. They also observed AV block and bradycardia in mice that had reduced macrophage expression [17]. Incidentally, severe COVID-19 patients suffer from bradycardia [18,19], and the expression of hsa-miR-486-3p in their blood is increased due to an immune response to the virus [20].

Based on our studies and many other studies described above, hsa-miR-486-3p can be a principal therapeutic target in the treatment of cardiac dysfunction.

4.2. *Hsa-Ca_v1.3 and Hsa-miR-486-3p*

Ca_v1.3 is a voltage-gated L-type Ca²⁺ channel that is important in the regulation of the SN's pacemaking function. When this channel is deactivated in mice, bradycardia and sinoatrial arrhythmia are observed [21,22]. We have recently shown that hsa-miR-486-3p is predicted to indirectly inhibit hsa-Ca_v1.3—with hsa-Ca_v1.3 being predicted to have six binding sites for hsa-miR-486-3p [4]. Our luciferase assay experiment confirms this prediction because the binding of hsa-miR-486-3p significantly reduces hsa-Ca_v1.3-mediated bioluminescence (Figure 3).

4.3. *Hsa-Ca_v3.1 and Hsa-miR-486-3p*

Ca_v3.1 is a voltage-gated T-type Ca²⁺ channel that also plays a key role in regulating the pacemaking function of the SN. Mangoni et al. (2006) demonstrated that the knockout of Ca_v3.1 in mice led to the lack of transitory I_{Ca,T} current and slowed down the SN pacemaker activity and AV conduction and reduced their heart rate [23]. We have recently shown that hsa-miR-486-3p is predicted to indirectly inhibit hsa-Ca_v3.1—with Ca_v3.1 being predicted to have one binding site for hsa-miR-486-3p [4]. Our luciferase assay experiment confirms this prediction because the binding of hsa-miR-486-3p significantly reduces hsa-Ca_v3.1-mediated bioluminescence (Figure 3).

4.4. *Hsa-TPSAB1 and Hsa-miR-486-3p*

In the early phase of myocardial infarction, inflammatory cells migrate to the infarction in order to aid cardiac repair [24]. It has been shown that a dysfunction of the immune and inflammatory pathways may contribute to the development of various cardiovascular diseases, including heart failure and arrhythmia [25,26]. Mast cells are involved in the immune response pathways, and TPSAB1—the main tryptase isoenzyme that is expressed in mast cells—plays a role in immunity [27].

Tryptase is the enzymatic activator of membrane protease-activated receptor 2 (PAR-2)—a receptor that is expressed by cardiomyocytes [28]. These PAR-2 receptors are connected to ERF kinases that mediate survival and hypertrophic signals. It could be assumed that hsa-miR-486-3p suppresses the tryptase/PAR-2/ERK hypertrophy pathway in the SN, preventing myocyte hypertrophy and therefore supporting the SN's spindle-like neonatal-like morphology. In addition, tryptase belong to the serine proteases family [29], and they all have very conservative 3-UTRs with a unique secondary structure that is crucial to mRNA stability.

We recently reported that hsa-TPSAB1 is significantly expressed in the adult human SN and is predicted to be directly inhibited by hsa-miR-486-3p [10]. The function of TPSAB1 in the SN is unknown, but it is interesting to see its high expression in the SN. The binding of hsa-miR-486-3p significantly reduces hsa-TPSAB1-mediated bioluminescence (Figure 5). It is possible that the immune system is important for maintaining the pacemaking function of the human SN. A high expression of hsa-miR-486-3p in the blood plasma of COVID-19 patients [20] could result in the reduced expression of hsa-TPSAB1 and abnormal functioning of immune cells in the SN. Based on this information, hsa-miR-486-3p could be a promising target in the treatment of bradycardia that is experienced by COVID-19 patients [18,19].

The high expression of immune cells in the SN could slow down the development of effective biological pacemakers. It has been supposed that immune cells contribute to SN functioning. For example, Hu et al. (2014) reported that when an adenoviral vector of TBX18 was delivered to a swine model of total heart block, it affected not only the heart rhythm but also caused an immune response [30].

4.5. *Hsa-miR-938*

We have previously reported that hsa-miR-938 is one of the novel microRNAs that is uniquely expressed in the human right atrium and is predicted to inhibit Ca_v1.3 [4]. Now, following our luciferase assay experiments, we observed a significant decrease in the

luciferase activity of the mRNA encoding for $Ca_v1.3$ when hsa-miR-938 is added (Figure 4). This observation suggests there is interaction between hsa- $Ca_v1.3$ and hsa-miR-938. The function of this microRNA in the cardiovascular system is unknown, but this microRNA is known to promote cell proliferation [31] and is linked to the development of gastric [32] and pancreatic cancer [33].

5. Conclusions

With the growing occurrence of cardiovascular disease, particularly sinus node dysfunction (SND), as the global ageing population increases, it is important for us to identify new therapeutic targets and to further understand the complex mechanisms that regulate the SN's pacemaking function. We hereby provide novel insights into the interacting between key microRNAs and ion channels and immune cell markers in H9C2 cells by further exploring our previous predicted interactions (as described in Petkova et al. (2020) [4] and Aminu et al. (2021) [10]). Using luciferase assay experiments, our observation of significant reduction of luciferase activity suggests there is interaction between miR-486-3p and three mRNAs ($Ca_v1.3$, $Ca_v3.1$, and TPSAB1) and between miR-938 and $Ca_v1.3$ mRNA. These observations allow room for further explorations of how these microRNAs can be used for ex vivo and in vivo experiments to study their effect on cardiac function/dysfunction, as previously shown by Yanni et al., who injected an anti-miR to miR-370 into heart failure mice and restored HCN4 mRNA and protein expression in the SN, thus increasing the beating rate [34], and recently by Petkova et al., who injected miR-486-3p into the rat SN tissue and observed a reduced heart rate [4].

Author Contributions: Methodology, manuscript planning, writing and editing, data curation and analysis, and creating and formatting figures and tables, A.J.A. (Abimbola J Aminu); methodology, data curation, and analysis for $Ca_v1.3$, M.P.; methodology and manuscript editing, W.C.; methodology, Z.Y.; manuscript editing, V.S.K.; supervision, A.J.A. (Andrew J Atkinson); conceptualization, funding acquisition, supervision, manuscript planning, data analysis, figures and tables formatting, and manuscript review and editing, H.D. All authors have read and agreed to the published version of the manuscript.

Funding: This research was funded by the BRITISH HEART FOUNDATION, grant number FS/17/67/33483 and the Leducq Foundation (THE FANTACY 19CVD03).

Data Availability Statement: All data related to this study is contained within the article.

Acknowledgments: We acknowledge the technical support provided by Gabrielle Forte and Cali Anderson from Alicia D'Souza's research group, University of Manchester.

Conflicts of Interest: The authors declare no conflict of interest. The funders had no role in the design of the study; in the collection, analyses, or interpretation of data; in the writing of the manuscript, or in the decision to publish the results.

References

1. Chandler, N.J.; Greener, I.D.; Tellez, J.O.; Inada, S.; Musa, H.; Molenaar, P.; DiFrancesco, D.; Baruscotti, M.; Longhi, R.; Anderson, R.H.; et al. Molecular architecture of the human sinus node insights into the function of the cardiac pacemaker. *Circulation* **2009**, *119*, 1562–1575. [[CrossRef](#)]
2. Stephenson, S.R.; Atkinson, A.; Kottas, P.; Perde, F.; Jafarzadeh, F.; Bateman, M.; Iaizzo, P.A.; Zhao, J.; Zhang, H.; Anderson, R.H.; et al. High resolution 3-dimensional imaging of the human cardiac conduction system from microanatomy to mathematical modeling. *Sci. Rep.* **2017**, *7*, 1–13. [[CrossRef](#)] [[PubMed](#)]
3. Dobrzynski, H.; Anderson, R.H.; Atkinson, A.; Borbas, Z.; D'Souza, A.; Fraser, J.F.; Inada, S.; Logantha, S.J.; Monfredi, O.; Morris, G.; et al. Structure, function and clinical relevance of the cardiac conduction system, including the atrioventricular ring and outflow tract tissues. *Pharmacol. Ther.* **2013**, *139*, 260–288. [[CrossRef](#)] [[PubMed](#)]
4. Petkova, M.; Atkinson, A.J.; Yanni, J.; Stuart, L.; Aminu, A.J.; Ivanova, A.D.; Pustovit, K.B.; Geraghty, C.; Feather, A.; Li, N.; et al. Identification of Key Small Non-Coding MicroRNAs Controlling Pacemaker Mechanisms in the Human Sinus Node. *J. Am. Hear. Assoc.* **2020**, *9*, e016590. [[CrossRef](#)]
5. Zhang, H.; Holden, A.V.; Kodama, I.; Honjo, H.; Lei, M.; Varghese, T.; Boyett, M. Mathematical models of action potentials in the periphery and center of the rabbit sinoatrial node. *Am. J. Physiol. Circ. Physiol.* **2000**, *279*, H397–H421. [[CrossRef](#)]

6. Thum, T.; Galuppo, P.; Kneitz, S.; Fiedler, J.; Van Laake, L.; Mummery, C.; Ertl, G.; Bauersachs, J. WITHDRAWN: MicroRNAs in the Human Heart: A Clue to Fetal Gene Reprogramming in Heart Failure. *J. Mol. Cell. Cardiol.* **2007**, *17*, 258–267. [[CrossRef](#)]
7. Boettger, T.; Braun, T. A new level of complexity the role of micrnas in cardiovascular development. *Circ. Res.* **2012**, *110*, 1000–1013. [[CrossRef](#)]
8. Romaine, S.P.R.; Tomaszewski, M.; Condorelli, G.; Samani, N.J. MicroRNAs in cardiovascular disease: An introduction for clinicians. *Heart* **2015**, *101*, 921–928. [[CrossRef](#)]
9. Torrente, A.G.; Mesirca, P.; Neco, P.; Rizzetto, R.; Dubel, S.; Barrere, C.; Sinegger-Brauns, M.; Striessnig, J.; Richard, S.; Nargeot, J.; et al. L-type Cav1.3 channels regulate ryanodine receptor-dependent Ca²⁺ release during sino-atrial node pacemaker activity. *Cardiovasc. Res.* **2016**, *109*, 451–461. [[CrossRef](#)]
10. Aminu, A.J.; Petkova, M.; Atkinson, A.J.; Yanni, J.; Morris, A.D.; Simms, R.T.; Chen, W.; Yin, Z.; Kuniewicz, M.; Holda, M.K.; et al. Further insights into the molecular complexity of the human sinus node—The role of ‘novel’ transcription factors and microRNAs. *Prog. Biophys. Mol. Biol.* **2021**, *166*, 86–104. [[CrossRef](#)]
11. Riolo, G.; Cantara, S.; Marzocchi, C.; Ricci, C. miRNA Targets: From Prediction Tools to Experimental Validation. *Methods Protoc.* **2020**, *4*, 1. [[CrossRef](#)] [[PubMed](#)]
12. Li, N.; Artiga, E.; Kalyanasundaram, A.; Hansen, B.J.; Webb, A.; Pietrzak, M.; Biesiadecki, B.; Whitson, B.; Mokadam, N.A.; Janssen, P.M.L.; et al. Altered microRNA and mRNA profiles during heart failure in the human sinoatrial node. *Sci. Rep.* **2021**, *11*, 1–15. [[CrossRef](#)]
13. Hsu, A.; Chen, S.-J.; Chang, Y.-S.; Chen, H.-C.; Chu, P.-H. Systemic Approach to Identify Serum microRNAs as Potential Biomarkers for Acute Myocardial Infarction. *BioMed Res. Int.* **2014**, *2014*, 418628. [[CrossRef](#)] [[PubMed](#)]
14. Zhang, R.; Lan, C.; Pei, H.; Duan, G.; Huang, L.; Li, L. Expression of circulating miR-486 and miR-150 in patients with acute myocardial infarction. *BMC Cardiovasc. Disord.* **2015**, *15*, 51. [[CrossRef](#)] [[PubMed](#)]
15. Lange, S.; Banerjee, I.; Carrion, K.; Serrano, R.; Habich, L.; Kameny, R.; Lengenfelder, L.; Dalton, N.; Meili, R.; Börgeson, E.; et al. miR-486 is modulated by stretch and increases ventricular growth. *JCI Insight* **2019**, *4*, 125507. [[CrossRef](#)]
16. Mukai, N.; Nakayama, Y.; Murakami, S.; Tanahashi, T.; I Sessler, D.; Ishii, S.; Ogawa, S.; Tokuhira, N.; Mizobe, T.; Sawa, T.; et al. Potential contribution of erythrocyte microRNA to secondary erythrocytosis and thrombocytopenia in congenital heart disease. *Pediatr. Res.* **2018**, *83*, 866–873. [[CrossRef](#)]
17. Hulsmans, M.; Clauss, S.; Xiao, L.; Aguirre, A.D.; King, K.R.; Hanley, A.; Hucker, W.J.; Wülfers, E.M.; Seemann, G.; Courties, G.; et al. Macrophages Facilitate Electrical Conduction in the Heart. *Cell* **2017**, *169*, 510–522.e20. [[CrossRef](#)]
18. Amaratunga, E.A.; Corwin, D.S.; Moran, L.; Snyder, R. Bradycardia in Patients With COVID-19: A Calm Before the Storm? *Cureus* **2020**, *12*, e8599. [[CrossRef](#)]
19. Capoferri, G.; Osthoff, M.; Egli, A.; Stoeckle, M.; Bassetti, S. Relative bradycardia in patients with COVID-19. *Clin. Microbiol. Infect.* **2020**, *27*, 295–296. [[CrossRef](#)]
20. Tang, H.; Gao, Y.; Li, Z.; Miao, Y.; Huang, Z.; Liu, X.; Xie, L.; Li, H.; Wen, W.; Zheng, Y.; et al. The noncoding and coding transcriptional landscape of the peripheral immune response in patients with COVID-19. *Clin. Transl. Med.* **2020**, *10*, 200. [[CrossRef](#)]
21. Platzer, J.; Engel, J.; Schrott-Fischer, A.; Stephan, K.; Bova, S.; Chen, H.; Zheng, H.; Striessnig, J. Congenital Deafness and Sinoatrial Node Dysfunction in Mice Lacking Class D L-Type Ca²⁺ Channels. *Cell* **2000**, *102*, 89–97. [[CrossRef](#)]
22. Zhang, Z.; Xu, Y.; Song, H.; Rodriguez, J.; Tuteja, D.; Namkung, Y.; Shin, H.-S.; Chiamvimonvat, N. Functional roles of Cav1.3 (alpha1D3) calcium channel in sinoatrial nodes. *Circ. Res.* **2002**, *90*, 981–987. [[CrossRef](#)] [[PubMed](#)]
23. Mangoni, M.E.; Traboulsie, A.; Leoni, A.L.; Couette, B.; Marger, L.; Le Quang, K.; Kupfer, E.; Cohen-Solal, A.; Vilar, J.; Shin, H.-S. Bradycardia and slowing of the atrioventricular conduction in mice lacking Cav3.1/alpha(1G) T-type calcium channels. *Circ. Res.* **2006**, *98*, 1422–1430. [[CrossRef](#)]
24. Zimmer, A.; Bagchi, A.K.; Vinayak, K.; Bello-Klein, A.; Singal, P.K. Innate immune response in the pathogenesis of heart failure in survivors of myocardial infarction. *Am. J. Physiol. Circ. Physiol.* **2019**, *316*, H435–H445. [[CrossRef](#)]
25. Swirski, F.K.; Nahrendorf, M. Cardioimmunology: The immune system in cardiac homeostasis and disease. *Nat. Rev. Immunol.* **2018**, *18*, 733–744. [[CrossRef](#)] [[PubMed](#)]
26. Lazzerini, P.E.; Laghi-Pasini, F.; Boutjdir, M.; Capecci, P.L. Cardioimmunology of arrhythmias: The role of autoimmune and inflammatory cardiac channelopathies. *Nat. Rev. Immunol.* **2018**, *19*, 63–64. [[CrossRef](#)] [[PubMed](#)]
27. Lyons, J.; Yu, X.; Hughes, J.D.; Le, Q.T.; Jamil, A.; Bai, Y.; Ho, N.; Zhao, M.; Liu, Y.; O’Connell, M.; et al. Elevated basal serum tryptase identifies a multisystem disorder associated with increased TPSAB1 copy number. *Nat. Genet.* **2016**, *48*, 1564–1569. [[CrossRef](#)]
28. Antoniak, S.; Sparkenbaugh, E.M.; Tencati, M.; Rojas, M.; Mackman, N.; Pawlinski, R. Protease activated receptor-2 contributes to heart failure. *PLoS ONE* **2013**, *8*, e81733. [[CrossRef](#)]
29. Chen, C.; Darrow, A.L.; Qi, J.S.; D’Andrea, M.R.; Andrade-Gordon, P. A novel serine protease predominantly expressed in macrophages. *Biochem. J.* **2003**, *374*, 97–107. [[CrossRef](#)] [[PubMed](#)]
30. Hu, Y.-F.; Dawkins, J.F.; Cho, H.C.; Marbán, E.; Cingolani, E. Biological pacemaker created by minimally invasive somatic reprogramming in pigs with complete heart block. *Sci. Transl. Med.* **2014**, *6*, 245ra94. [[CrossRef](#)]
31. Li, C.-F.; Li, Y.-C.; Jin, J.-P.; Yan, Z.-K.; Li, D.-D. miR-938 promotes colorectal cancer cell proliferation via targeting tumor suppressor PHLPP2. *Eur. J. Pharmacol.* **2017**, *807*, 168–173. [[CrossRef](#)]

32. Wu, Y.; Jia, Z.; Cao, D.; Wang, C.; Wu, X.; You, L.; Wen, S.; Pan, Y.; Cao, X.; Jiang, J. Predictive Value of MiR-219-1, MiR-938, MiR-34b/c, and MiR-218 Polymorphisms for Gastric Cancer Susceptibility and Prognosis. *Dis. Markers* **2017**, *2017*, 4731891. [[CrossRef](#)] [[PubMed](#)]
33. Cao, Z.; Feng, M.; Yang, G.; Zhang, T. Plasma miRNAs Effectively Distinguish Patients with Pancreatic Cancer from Controls: A Multicenter Study. *J. Am. Coll. Surg.* **2017**, *225*, e125. [[CrossRef](#)]
34. Yanni, J.; D'Souza, A.; Wang, Y.; Li, N.; Hansen, B.J.; Zakharkin, S.O.; Smith, M.; Hayward, C.; Whitson, B.A.; Mohler, P.J.; et al. Silencing miR-370-3p rescues funny current and sinus node function in heart failure. *Sci. Rep.* **2020**, *10*, 1–23. [[CrossRef](#)] [[PubMed](#)]

5.5 Limitations

Out of 21 predicted mRNA-miRNA interactions, only 4 were validated through luciferase reporter gene assay experiments. More surprisingly, LZTS1 mRNA was predicted to have 12 binding sites for miR-486-3p (Table 1 in Paper 3, Chapter 5); however, there was no decrease in bioluminescence to indicate a reduction in LZTS1 mRNA expression (Figure 10 in Appendix). The exact reason why some predicted mRNA-miRNA interactions were not experimentally verified is unclear. However, further experimental routes can be explored to verify these predicted interactions further. For example, both strands of the miRNAs (for example, both miR-486-3p and miR-486-5p) could be explored. Also, western blot analysis could be conducted to confirm the expression level of the genes in the H9C2 cells. The number of prediction tools could be increased to narrow down the binding sites predictions.

In addition, rat cells do not contain the biological machinery to process the human miRNAs and mRNAs that were transfected into them. Therefore, using H9C2 (rat cardiac cells) could have played a role in the lack of experimental verifications. It would be ideal to carry out these experimental verifications in human cardiomyocytes (such as HL-1 or AC16 cell lines).

Finally, it would be beneficial to use qPCR to confirm the sequencing data and the expression levels of mRNAs and miRNAs that were transfected into the H9C2 cells, as gene expression levels do not always correlate with protein expression levels. To further validate that expression is altered at the protein level, *in vitro* analysis in human cell lines would be ideal.

Appendix

Luciferase assay experiments to validate previously predicted interactions between key mRNAs and miRNAs

In addition to what is presented in Aminu et al. 2022, other luciferase assay experiments were conducted.

In our previous studies [32, 44], we predicted interactions between microRNAs and mRNAs that play a role in the function of the sinus node (SN) (see Table 5 of Paper 2, Chapter 4 in chapter 5 and Table 1 of Paper 3, Chapter 5). Some of these microRNAs (miR-486-3p and miR-938) significantly decreased the luciferase activity of some of their target mRNAs (TPSAB1, Ca_v1.3, and Ca_v3.1) (see Paper 3, Chapter 5).

Luciferase assay experiments were conducted on all the interactions presented in Table 5 of Paper 2, Chapter 4 and Table 1 of Paper 3, Chapter 5; however, significant downregulation of luciferase activity was not observed for all interactions. Of the 12 hsa-mRNAs that had been predicted to be inhibited by their respective hsa-miRNAs (Table 1 of Paper 3, Chapter 5), I did not observe a significant decrease in luciferase activity with 8 hsa-mRNAs and their respective hsa-miRNAs (Table 2 of Paper 3, Chapter 5).

The non-significant downregulations are presented here. The statistical test was an unpaired t-test, and the non-significance was $p \geq 0.05$. Grubbs test was used to identify and eliminate outliers. It should be noted that the two control groups were not used for all the experiments because the downregulations (or lack thereof) were not significant.

Even after conducting 3-6 batches of experiments, significant downregulation was not observed. This shows that the prediction of binding sites on the target mRNA (as shown in Table 1 of Paper 3, Chapter 5) does not always mean that binding of the microRNA (or even significant binding) will occur. Reasons for this observation are provided in the Discussion section of Paper 3, Chapter 5. One of these reasons is binding site accessibility: the predicted binding sites on the 3'UTR of the target mRNA should be accessible to the miRNA. Some algorithms and software can predict the binding site accessibility and rank this based on a specific score [110] or free energy [111]. Another reason could be the proximity of the binding sites. Another reason is the thermodynamic stability of the miRNA-mRNA complexes. The free

energy of the predicted interaction is used to assess the thermodynamic stability of the miRNA-mRNA complex – a lower (i.e., more negative) free energy means the complex is more thermodynamically stable. Therefore, the miRNA-mRNA binding is stronger. When this is stronger, significant downregulation in the luciferase activity of the target mRNA will be observed. Hence, it can be predicted that the non-significant reported in this Appendix occurred due to the low thermodynamic stability of the miRNA-mRNA complex.

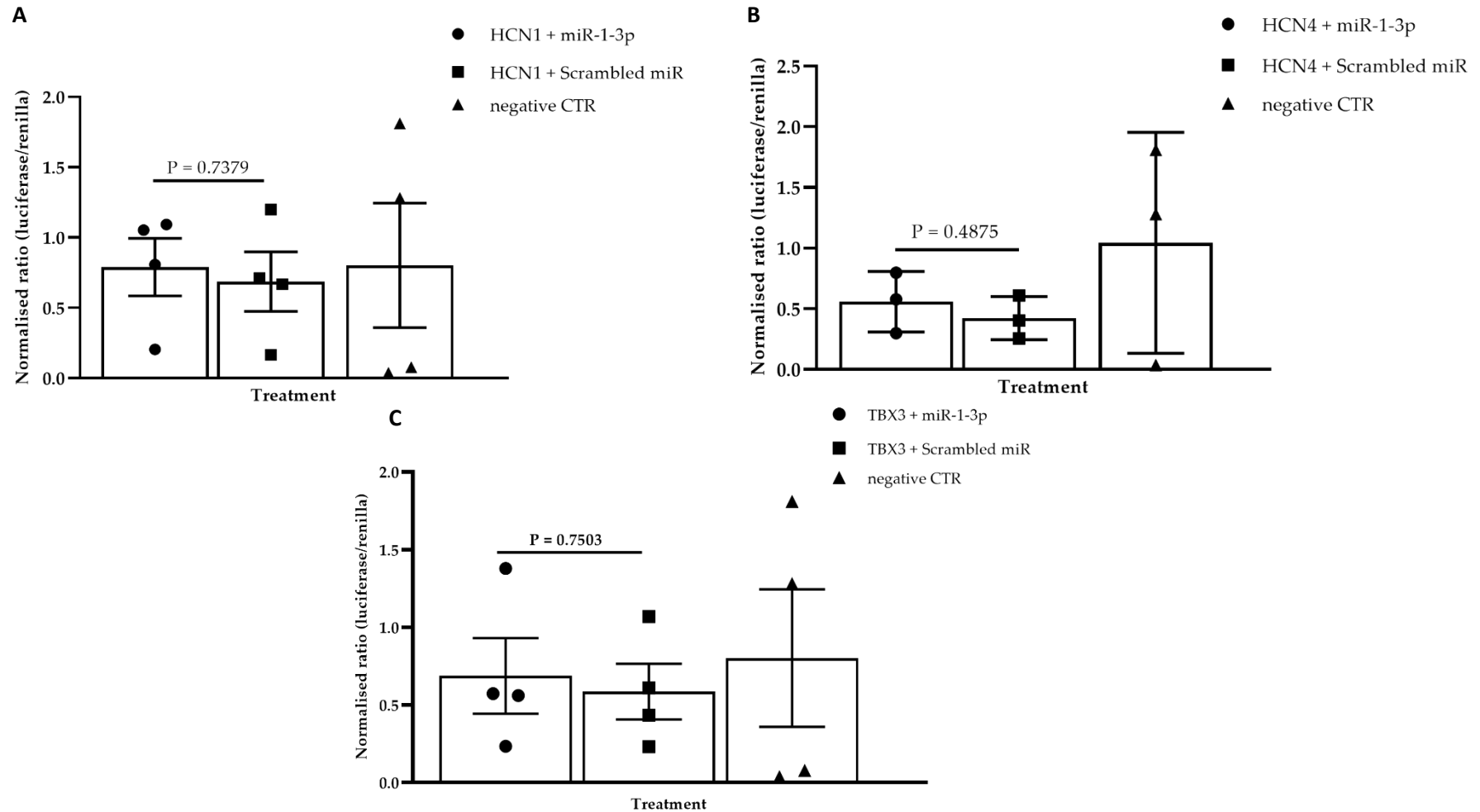


Figure 1. Luciferase bioluminescence after transfection of H9C2 cells with hsa-miR-1-3p and plasmids. Bioluminescence was recorded 24 hours after transfecting H9C2 cells with 0.25 μ g (A) HCN1, (B) HCN4, or (C) TBX3 - 3'- untranslated region-containing plasmid and 5 μ M hsa-miR-1-3p or scrambled hsa-miRNA. Two control groups did not include the luciferase reporter gene and cells were transfected with only hsa-miR-1-3p or remained untransfected (i.e., contained an equivalent volume of culture medium to replace the hsa-miRNAs or 3'-untranslated region-containing plasmid). Data are shown as mean \pm SEM shown (n=4 batches of experiments were plotted for HCN1 and TBX3; n=3 batches of experiments were plotted for HCN4).

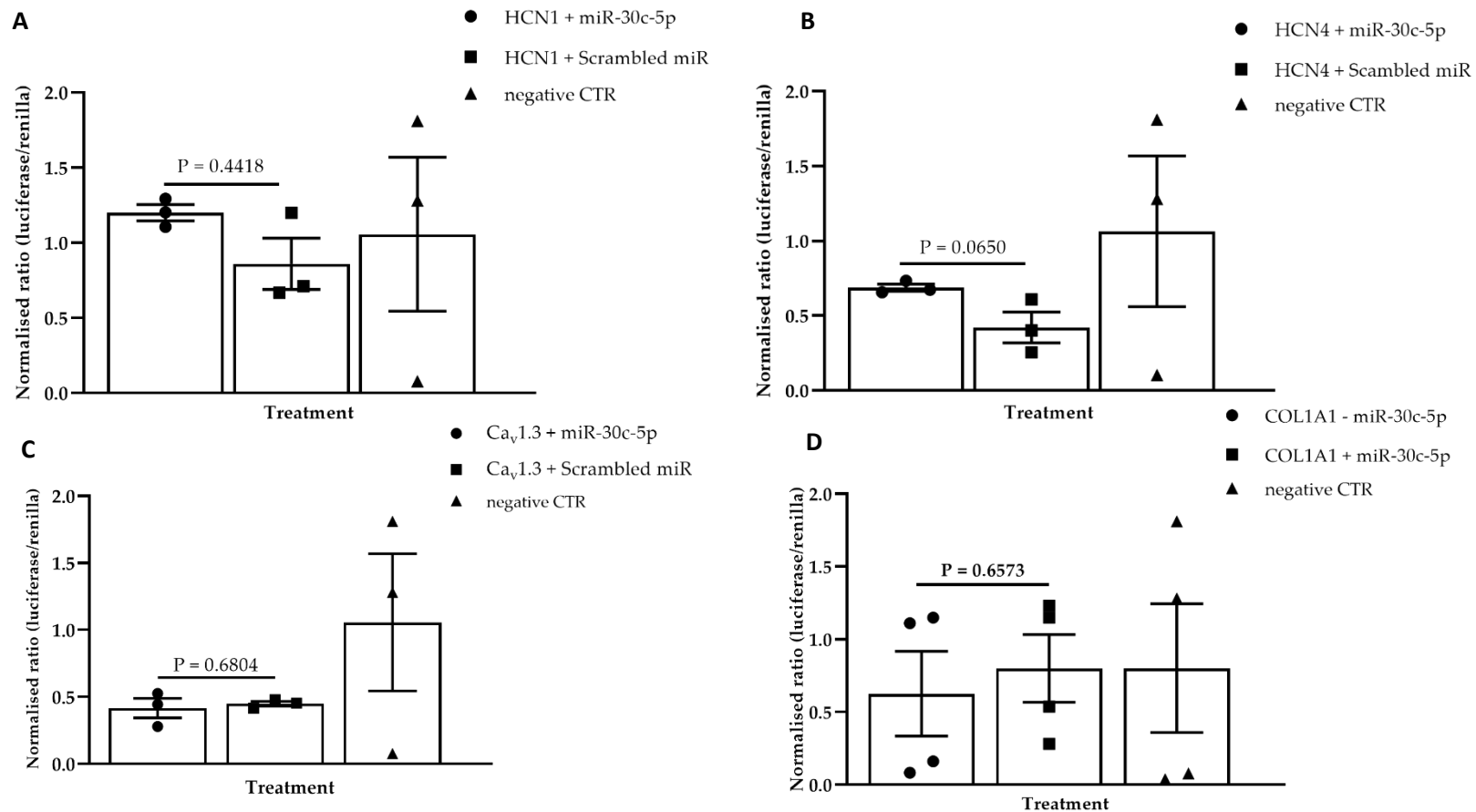


Figure 2. Luciferase bioluminescence after transfection of H9C2 cells with hsa-miR-30c-5p and plasmids. Bioluminescence was recorded 24 hours after transfecting H9C2 cells with 0.25 μ g (A) HCN1, (B) HCN4, (C) $Ca_v1.3$ or (D) COL1A1 - 3'- untranslated region-containing plasmid and 5 μ M hsa-miR-30c-5p or scrambled hsa-miRNA. Two control groups did not include the luciferase reporter gene and cells were transfected with only hsa-miR-30c-5p or remained untransfected (i.e., contained an equivalent volume of culture medium to replace the hsa-miRNAs or 3'-untranslated region-containing plasmid). Data are shown as mean \pm SEM shown (n=3 batches of experiments were plotted for HCN1, HCN4, and $Ca_v1.3$; n=6 batches of experiments were plotted for COL1A1).

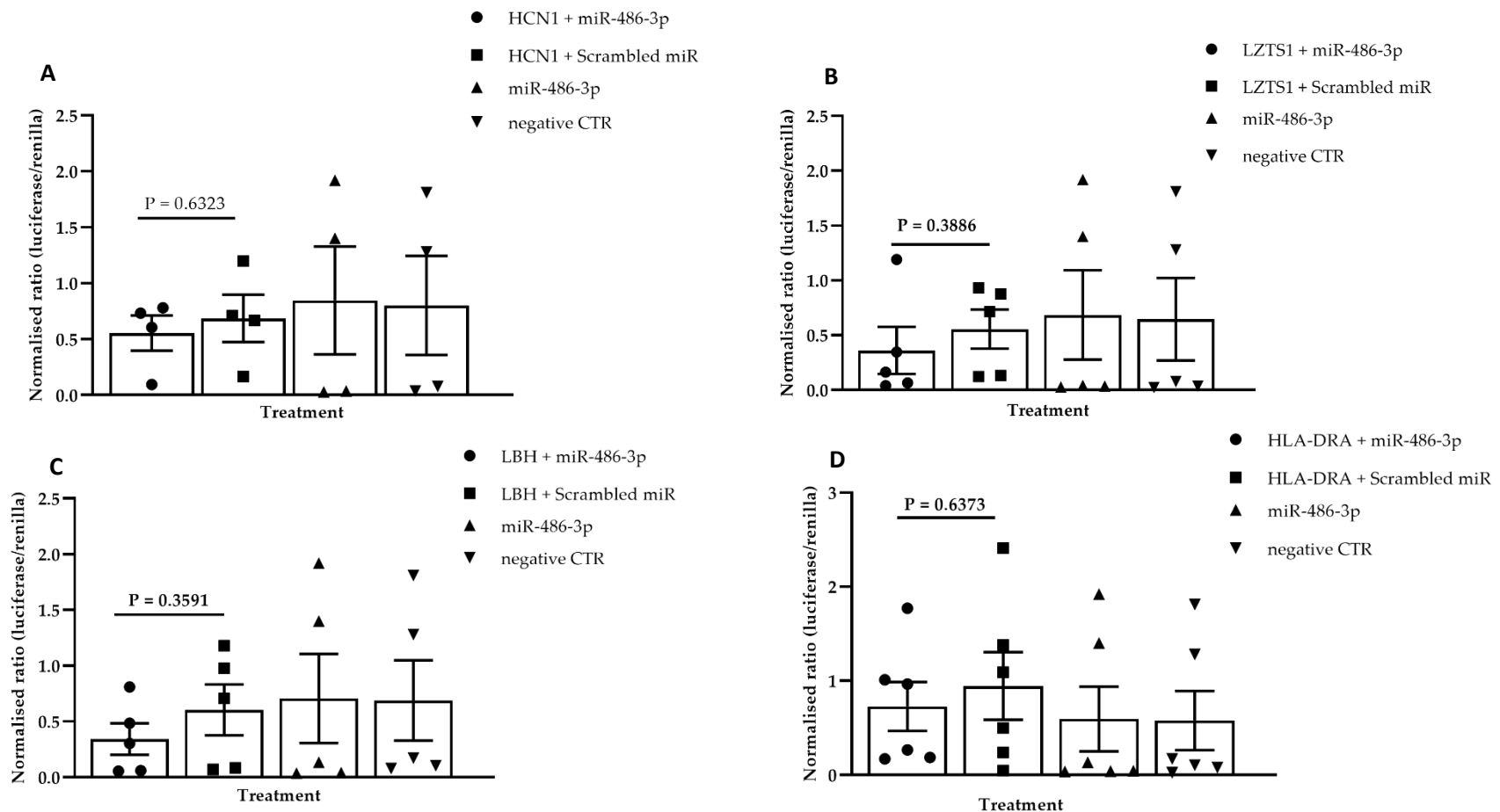


Figure 3. Luciferase bioluminescence after transfection of H9C2 cells with hsa-miR-486-3p and plasmids. Bioluminescence was recorded 24 hours after transfecting H9C2 cells with 0.25 μ g **(A)** HCN1, **(B)** LZTS1, **(C)** LBH or **(D)** HLA-DRA - 3'- untranslated region-containing plasmid and 5 μ M hsa-miR-486-3p or scrambled hsa-miRNA. Two control groups did not include the luciferase reporter gene and cells were transfected with only hsa-miR-486-3p or remained untransfected (i.e., contained an equivalent volume of culture medium to replace the hsa-miRNAs or 3'-untranslated region-containing plasmid). Data are shown as mean \pm SEM shown (n=4 batches of experiments were plotted for HCN1; n=5 batches of experiments were plotted for LZTS1 and LBH; n=6 batches of experiments were plotted for HLA-DRA).

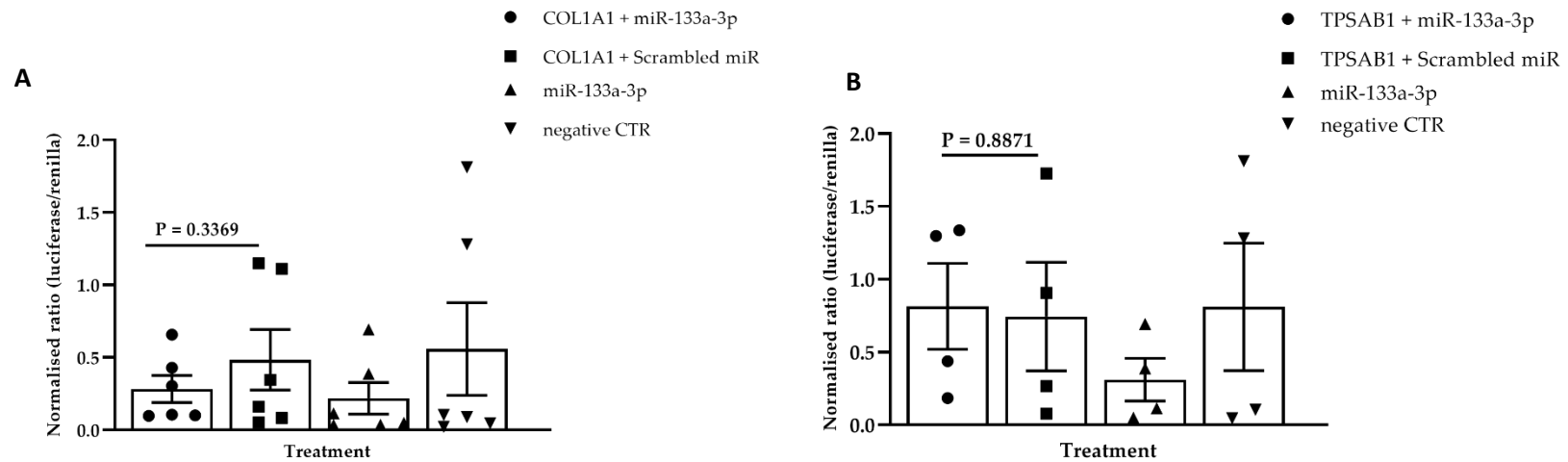


Figure 4. Luciferase bioluminescence after transfection of H9C2 cells with hsa-miR-133a-3p and plasmids. Bioluminescence was recorded 24 hours after transfecting H9C2 cells with 0.25 μ g **(A)** COL1A1 or **(B)** TPSAB1 - 3'- untranslated region-containing plasmid and 5 μ M hsa-miR-133a-3p or scrambled hsa-miRNA. Two control groups did not include the luciferase reporter gene and cells were transfected with only hsa-miR-133a-3p or remained untransfected (i.e., contained an equivalent volume of culture medium to replace the hsa-miRNAs or 3'-untranslated region-containing plasmid). Data are shown as mean \pm SEM shown (n=6 batches of experiments were plotted for COL1A1; n=4 batches of experiments were plotted for TPSAB1).

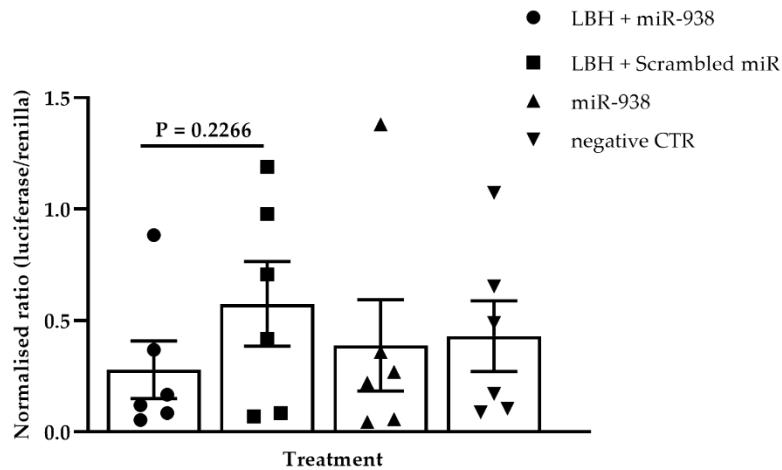


Figure 5. Luciferase bioluminescence after transfection of H9C2 cells with hsa-miR-938 and LBH. Bioluminescence was recorded 24 hours after transfecting H9C2 cells with 0.25µg LBH 3'-untranslated region-containing plasmid and 5 µM hsa-miR-938 or scrambled miRNA. Two control groups did not include the luciferase reporter gene, and cells were transfected with only hsa-938 or remained untransfected (i.e., contained an equivalent volume of culture medium to replace the miRNAs or LBH). Data are shown as mean±SEM shown (n=3 batches of experiments). Data are shown as mean±SEM shown (n=6 batches of experiments).

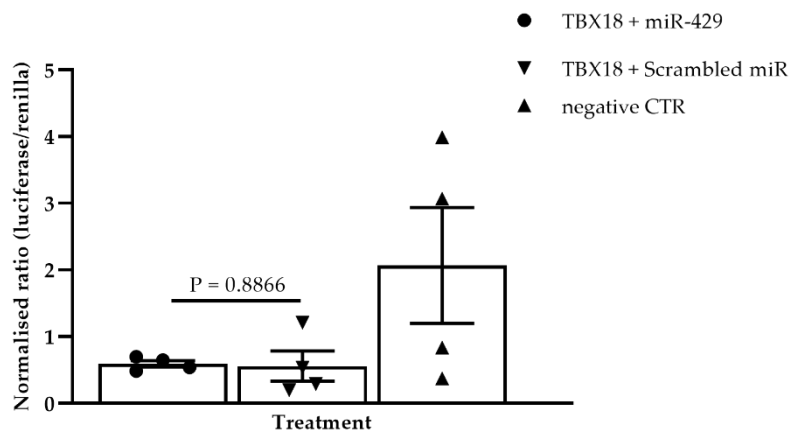


Figure 6. Luciferase bioluminescence after transfection of H9C2 cells with hsa-miR-429 and TBX18. Bioluminescence was recorded 24 hours after transfecting H9C2 cells with 0.25µg TBX18 3'-untranslated region-containing plasmid and 5 µM hsa-miR-429 or scrambled miRNA. Two control groups did not include the luciferase reporter gene, and cells were transfected with only hsa-miR-429 or remained untransfected (i.e., contained an equivalent volume of culture medium to replace the miRNAs or TBX18). Data are shown as mean±SEM shown (n=4 batches of experiments).

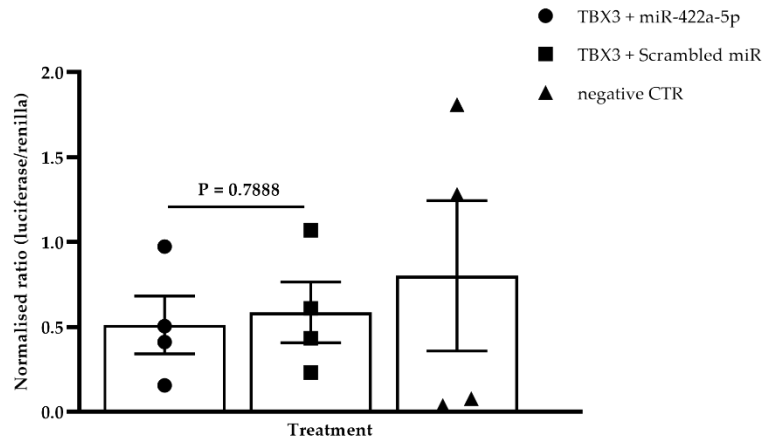


Figure 7. Luciferase bioluminescence after transfection of H9C2 cells with hsa-miR-422a-5p and TBX3. Bioluminescence was recorded 24 hours after transfecting H9C2 cells with 0.25 μ g TBX3 3'-untranslated region-containing plasmid and 5 μ M hsa-miR-422a-5p or scrambled miRNA. Two control groups did not include the luciferase reporter gene, and cells were transfected with only hsa-miR-422a-5p or remained untransfected (i.e., contained an equivalent volume of culture medium to replace the miRNAs or TBX3). Data are shown as mean \pm SEM shown (n=4 batches of experiments).

CHAPTER 6) IDENTIFICATION OF KEY SMALL NON-CODING MICRORNAS CONTROLLING PACEMAKER MECHANISMS IN THE HUMAN SINUS NODE⁴

The first three chapters of this thesis describe studies published as papers in which I am the first author. The study described in this last chapter is published as a paper in which I am a co-author. Some of the data obtained from the study described in this chapter were preliminary data for the study described in chapter 4. However, this study has been added to the last chapter for consistency.

While we know that microRNAs inhibit gene expression, the role of microRNAs in regulating the expression profile of the human SN pacemaking and conduction genes are not well known. This chapter explores the unique expression profile of microRNAs in the adult human sinus node (SN) compared with the right atrial muscle.

Using quantitative polymerase chain reactions (qPCR) and bioinformatics software, out of 754 microRNAs, those that control the expression of SN pacemaker genes were identified. 14 microRNAs were significantly more, and 48 were significantly less expressed in the SN than in the right atrium. Among these 48 was miR-486-3p, which was predicted to inhibit key pacemaking channels such as HCN4, Ca_v1.3, and Ca_v3.1. This makes miR-486-3p a potential therapeutic target in the treatment of SN dysfunction. An interesting interaction pathway is also presented in this chapter.

⁴ This chapter is directly from the publication: Petkova, M., Atkinson, A. J., Yanni, J., Stuart, L., **Aminu, A. J.**, Ivanova, A. D., Pustovit, K. B., Geraghty, C., Feather, A., Li, N., Zhang, Y., Oceandy, D., Perde, F., Molenaar, P., D'Souza, A., Fedorov, V. V., Dobrzynski, H., *Identification of key small non-coding microRNAs controlling pacemaker mechanisms in the human sinus node.* J. Am. Heart Assoc., 2020. **9**: p. e016590




6.1 Contribution to the paper

As a co-author, my contribution to this paper were:

- Masson's trichrome staining of SN tissue section (Figures 1C and 1D)
- Creation of heatmaps and the graph of normalised TFs count (Figure 6)
- Contributed to creating the interaction network (Figure 7)

ORIGINAL RESEARCH

Identification of Key Small Non-Coding MicroRNAs Controlling Pacemaker Mechanisms in the Human Sinus Node

Maria Petkova, PhD*; Andrew J. Atkinson, PhD*; Joseph Yanni, PhD; Luke Stuart, MRes; Abimbola J. Aminu, MRes; Alexandra D. Ivanova, MSc; Ksenia B. Pustovit, PhD; Connor Geraghty, MBChB; Amy Feather, MRes; Ning Li, PhD; Yu Zhang, PhD; Delvac Oceandy, PhD; Filip Perde, PhD; Peter Molenaar , PhD; Alicia D'Souza, PhD; Vadim V. Fedorov , PhD†; Halina Dobrzynski , PhD†

BACKGROUND: The sinus node (SN) is the primary pacemaker of the heart. SN myocytes possess distinctive action potential morphology with spontaneous diastolic depolarization because of a unique expression of ion channels and Ca²⁺-handling proteins. MicroRNAs (miRs) inhibit gene expression. The role of miRs in controlling the expression of genes responsible for human SN pacemaking and conduction has not been explored. The aim of this study was to determine miR expression profile of the human SN as compared with that of non-pacemaker atrial muscle.

METHODS AND RESULTS: SN and atrial muscle biopsies were obtained from donor or post-mortem hearts (n=10), histology/immunolabeling were used to characterize the tissues, TaqMan Human MicroRNA Arrays were used to measure 754 miRs, Ingenuity Pathway Analysis was used to identify miRs controlling SN pacemaker gene expression. Eighteen miRs were significantly more and 48 significantly less abundant in the SN than atrial muscle. The most interesting miR was miR-486-3p predicted to inhibit expression of pacemaking channels: HCN1 (hyperpolarization-activated cyclic nucleotide-gated 1), HCN4, voltage-gated calcium channel (Ca_v)1.3, and Ca_v3.1. A luciferase reporter gene assay confirmed that miR-486-3p can control HCN4 expression via its 3' untranslated region. In *ex vivo* SN preparations, transfection with miR-486-3p reduced the beating rate by $\approx 35 \pm 5\%$ ($P < 0.05$) and HCN4 expression ($P < 0.05$).

CONCLUSIONS: The human SN possesses a unique pattern of expression of miRs predicted to target functionally important genes. miR-486-3p has an important role in SN pacemaker activity by targeting HCN4, making it a potential target for therapeutic treatment of SN disease such as sinus tachycardia.

Key Words: ion channels ■ microRNAs ■ pacemaker of the heart ■ sinus node disease

The sinus node (SN) is the primary pacemaker of the heart and is located at the junction of the superior vena cava with the right atrium (RA). It is an extensive crescent shaped structure and its 3-dimensional anatomy has recently been shown within the whole *ex vivo* human heart.¹⁻⁴ The SN myocytes possess distinctive action potential morphology, with

a phase (phase 4) of slow, spontaneous, diastolic depolarization ultimately responsible for pacemaking. A unique expression of ion channels and Ca²⁺-handling proteins in the SN (described in the human by Chandler et al⁵) is responsible for 2 main mechanisms that synergistically generate this pacemaker potential during phase 4—the membrane voltage and Ca²⁺ clocks.⁶

Correspondence to: Halina Dobrzynski, PhD, University of Manchester, CTF building, 46 Grafton Street, Manchester M13 9NT, United Kingdom. E-mail: halina.dobrzynski@manchester.ac.uk

Supplementary Material for this article is available at <https://www.ahajournals.org/doi/suppl/10.1161/JAHA.120.016590>

*Dr Petkova and Mr Atkinson are co-first authors.

†Dr Fedorov and Dr Dobrzynski are co-last authors.

For Sources of Funding and Disclosures, see page 14.

© 2020 The Authors. Published on behalf of the American Heart Association, Inc., by Wiley. This is an open access article under the terms of the Creative Commons Attribution-NonCommercial License, which permits use, distribution and reproduction in any medium, provided the original work is properly cited and is not used for commercial purposes.

JAHA is available at: www.ahajournals.org/journal/jaha

CLINICAL PERSPECTIVE

What Is New?

- This is the first study to investigate the expression of key microRNAs and their predicated targets important for pacemaking in the human heart.
- MicroRNA-486-3p directly inhibits hyperpolarization-activated cyclic nucleotide-gated 4 and thereby reduces action potential generation by the sinus node.

What Are the Clinical Implications?

- MicroRNA expression has an important role in establishing tissue-specific gene expression profiles in the sinus node and enhances our understanding of the molecular makeup of the human sinus node and its function in health and disease.
- The effect of microRNA-486-3p on sinus node beating rate makes it a potential target for manipulating pacemaking and could have therapeutic implications for the treatment of inappropriate sinus node tachycardia and for biological pacemaker development.

Nonstandard Abbreviations and Acronyms

AP	action potential
HCN	hyperpolarization-activated cyclic nucleotide-gated
IPA	Ingenuity Pathway Analysis
miR	microRNA
qPCR	quantitative polymerase chain reaction
RA	right atrium
SN	sinus node
Tbx	T-box
3'-UTR	3 prime untranslated region

Recent extensive work on non-coding molecules has begun to recognise their robust gene regulatory functions. One family of non-coding molecules are the microRNA (miR) family. miRs are ≈18 to 24 nucleotide single stranded RNAs, which regulate mRNA translation into functional protein through post-transcriptional repression⁷ by complementary nucleotide binding to the 3 prime untranslated region (3'UTR) recruiting the target gene into RNA-induced silencing complexes to be rendered translationally incompetent. miRs negatively regulate gene expression at the post-transcriptional level by degradation of mRNA

or translational repression,⁸ and have been implicated in cardiac development and pathophysiological processes such as cardiac hypertrophy, fibrosis, arrhythmias, and heart failure.^{9–13} There is some evidence that miRs are involved in the SN function: in the mouse, the key pacemaker gene, HCN4 (hyperpolarization-activated cyclic nucleotide-gated 4), is under the control of miRs following athletic training.¹⁴ The aim of this work was to determine if differences in miR expression between the SN and neighboring atrial muscle in the human can explain the differences in the expression of pacemaker genes in the 2 tissues and why the SN shows pacemaking and the atrial muscle does not.

METHODS

The data that support the findings of this study are available from the corresponding author upon reasonable request.

Human Tissue

The human specimens used in this study are described in detail in Table S1. They were obtained, dissected and frozen by co-authors in Australia (PM) and Romania (FP) under their local ethical approval procedures. No informed consent was required. Specimens were stored under the Human Tissue Act 2004.

Upon arrival of donor hearts to the Prince Charles Hospital (in a cardiologic solution on ice) and cadavers (10–35 hours from death) to National Institute of Legal Medicine right atrial/venocaval blocks (an example is shown in Figure 1C) were removed and trimmed, immediately frozen in liquid nitrogen or –60°C liquid isopentane and stored in freezers (–60° to –80°C). Specimens were transported on dry ice to the University of Manchester where the frozen samples were stored at –80°C.

Animal Tissue

Male Wistar-Hanover rats (Charles River UK Ltd.; 230–250 g) were euthanized in accordance with the guidelines of the Animal (Scientific Procedures) Act 1986 and the local ethical committee of the University of Manchester.

Histology

To identify the location of the SN, histology was performed on 10- to 30-μm thick cryosections, which were cut perpendicular to the crista terminalis from each specimen listed in Table S1. The cryosections were stained with Masson trichrome to identify the location of the SN as previously described^{15,16} (Figure 1).

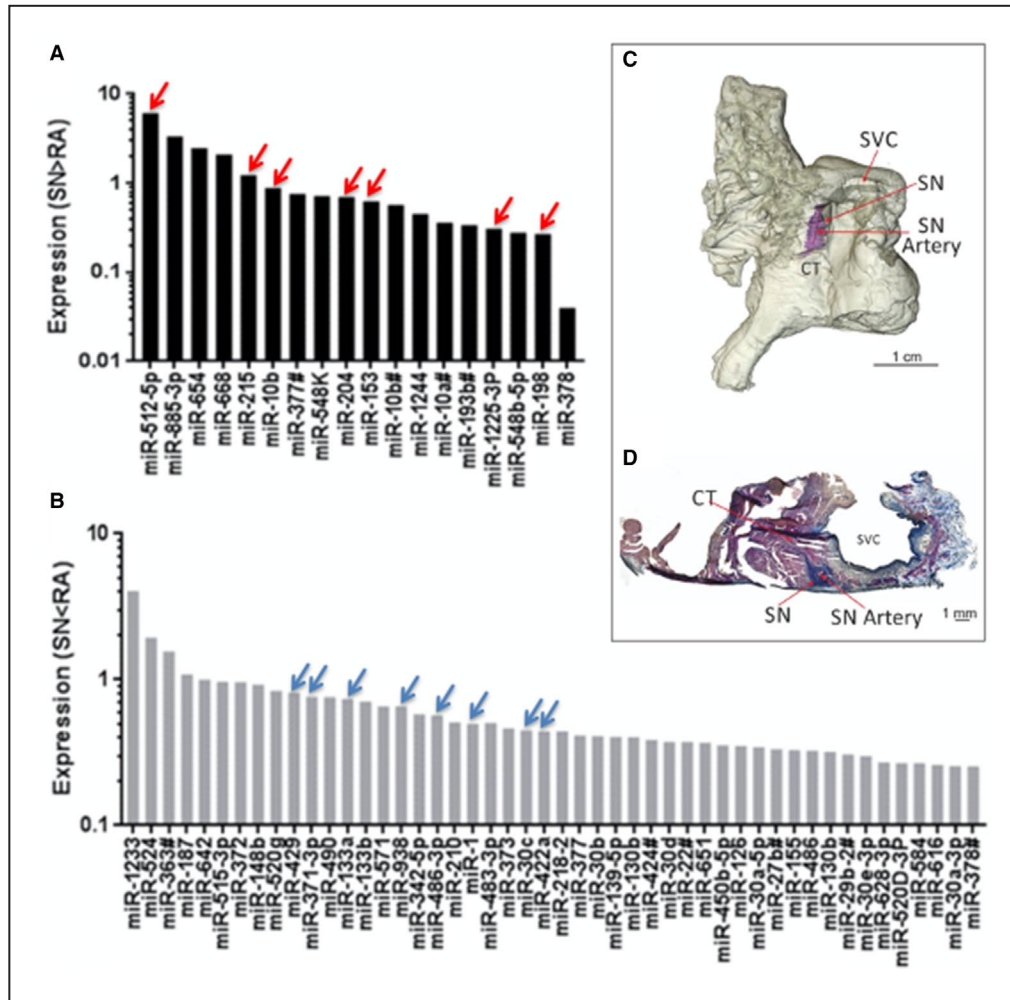


Figure 1. MicroRNAs significantly more or less expressed in the human SN in comparison with right atrial muscle.

A, Expression of 18 microRNAs that are significantly more abundant in the sinus node (SN) compared with atrial muscle. **B**, Expression of 48 microRNAs that are significantly less abundant in the SN compared with atrial muscle ($n=7$; $P<0.05$). **C**, Three-dimensional model of the human right atrium showing the location of the SN around the SN artery (similar to Stephenson et al, 2017 study).¹ The SN is stained blue by the Masson trichrome stain, because of its high content of fibrous tissue. **D**, Masson trichrome stained section through the SN cut perpendicular to the crista terminalis showing the location of the SN around the SN artery. See Table for key microRNAs indicated by red and blue arrows. CT indicates crista terminalis; miR, microRNA; SN, sinus node; and SVC, superior vena cava.

Sections were fixed overnight at room temperature in Bouin solution (Sigma) and then rinsed 3 times in 70% alcohol for 10 minutes. Sections were: stained with Celestine blue for 5 minutes and washed in tap water for 10 minutes; stained with Cole alum hematoxylin for 10 minutes and washed for 15 minutes in tap water; stained with acid fuchsin for 5 minutes and washed for 30 minutes in tap water; and placed in phosphomolybdic acid for 5 minutes, drained and then stained with methyl green for 1 minute and washed for 20 minutes in tap water. Sections were then dehydrated using a graded series of alcohol as follows: 70% alcohol (1 minute), 90% alcohol (1 minute), 100% alcohol (twice for 2 minutes).

Finally, sections were placed in histoclear solution for 5 minutes and mounted with distyrene, plasticizer, and xylene (Thermo Fisher). Histological sections were visualized with a light microscope (Zeiss LSM5) and an AxioCam camera (Zeiss) and collected with Axiovision software (Zeiss).

Immunohistochemistry

To further confirm the location of the SN, immunohistochemistry experiments were performed on sections neighbouring those used for histological verification. Tissue sections were fixed in 10% neutral buffer formalin (Sigma) for 30 minutes and washed

3 times for 10 minutes in 0.01 mol/L PBS (Sigma). Tissue sections were then treated with 0.1% Triton X-100 for 30 minutes, washed 3 times for 10 minutes in PBS and then blocked with 1% bovine serum albumin (Sigma) in PBS for 1 hour at room temperature. Sections were then incubated overnight at room temperature with primary antibodies diluted in 1% bovine serum albumin in PBS. The antibodies used in immunohistochemical experiments are listed in Table S2. Sections were washed 3 times in PBS after incubation with the primary antibody and then incubated with a secondary antibody conjugated to fluorescence markers diluted 1:100 in 1% bovine serum albumin in PBS for 2 hours at room temperature. The sections were washed 3 times in PBS and mounted using Vectashield mounting medium (Vector Laboratories) and coverslips sealed. Immunofluorescence was detected by a confocal microscope (Zeiss LSM5, Zeiss Microscopy) and images were taken with Pascal software (Zeiss Microscopy).

Tissue Sampling and RNA Extraction

The SN area was identified by the presence of the SN artery, a large amount of connective tissue, positive staining for HCN4. After identification of the location of the SN by histology and immunohistochemistry, total RNA was isolated from small SN biopsies taken around the SN artery and an area of right atrial pectinate muscle remote from the SN and flash frozen in liquid N₂.² The tissue biopsies from the SN and atrial muscle were homogenized with an Ika T10 homogenizer (Ika Werke) for 1 minute, and the miRvana miRNA Isolation Kit (Applied Biosystems) with phenol (Life Technologies) was used for RNA isolation according to the manufacturer's instructions. RNA was treated with deoxyribonuclease (Ambion), and RNA purity (260/280 ratio), concentration, and RNA integrity number were measured using Agilent 2100 Bioanalyzer (Agilent). Quality and quantity of RNA extracted from each specimen can be found in Table S1.

Reverse Transcription, Preamplification, and Quantitative Polymerase Chain Reaction for miRs

One-hundred and eighty-five nanograms RNA from each sample were reverse-transcribed using the TaqMan microRNA Reverse Transcription Kit (ThermoFisher). The product of this reaction (2.5 µL) was preamplified with Megaplex PreAmp Primers (ThermoFisher). The primers were divided into pool A and B, each pool containing 380 stem-looped reverse transcription primers and TaqMan PreAmp Master Mix (Applied Biosystems) in a 25-µL polymerase chain reaction. The preamplification cycles were

run as follows: 95°C (10 minutes), 55°C (2 minutes), and 75°C (2 minutes) followed by 12 cycles of 95°C (15 seconds) and 60°C (4 minutes). The cDNA products for each sample were diluted to 100 µL with 0.1x Tris buffer and EDTA, ethylenediaminetetraacetic acid, molecule (pH=8.0). Ten microliters of the diluted cDNA were used for quantitative polymerase chain reaction (qPCR) using TaqMan Array Human MicroRNA A+B Cards Set v3.0 (ThermoFisher) for 754 human microRNAs. 7900HT Fast Real-Time PCR System (Applied Biosystems) was used for qPCR. The reaction conditions were as follows: 92°C for 10 minutes, 40 cycles of 97°C for 1 second, 60°C for 20 seconds. RQ Manager (Applied Biosystems) was used to obtain the average threshold cycle values. RealTime StatMiner (Integromics) was used for differential expression analysis. GeNorm stability assessment of the suitability of the housekeepers for the analysis of cards A and B was used. Housekeepers RNU44 and RNU48 were selected to analyze card A; RNU44 and U6 small nuclear RNA were used for card B. Statistical analysis of the expression levels was performed using Benjamini-Hochberg test and $P < 0.05$ values were assumed as significant.

Reverse Transcription and qPCR for mRNAs

Total RNA was extracted using RNeasy Micro Kit (Qiagen) according to manufacturer's instructions. Two hundred and fifty-four ng RNA from each sample was reverse transcribed to cDNA with SuperScript VILO cDNA Synthesis Kit (ThermoFisher) in 20 µL reactions. The cDNA samples were run on a qPCR Veriti 96-well thermal cycler (Life Technologies) in accordance with the manufacturer's recommended protocol. HCN4 and voltage-gated calcium channel (Ca_v)_{1.3} Quantitect primers were used (Qiagen) for qPCR using a 7900HT Fast Real-Time PCR System (Applied Biosystems). The reaction conditions were as follows: 50°C for 2 minutes, 95°C for 10 minutes, 40 cycles of 95°C for 15 seconds, 60°C for 1 minute. mRNA expression was analyzed using the delta threshold cycle method. RQ Manager (Applied Biosystems) was used to obtain the average threshold cycle values and GAPDH was used for normalization.

Ingenuity Pathway Analysis Bioinformatics

Sixty-six miRs listed in Table S3 were joined with the mRNA data for the SN and atrial muscle from the study by Chandler et al,⁵ and analyzed using Ingenuity Pathway Analysis (IPA, Qiagen) to identify potential interactions and relationships between the miRs and mRNAs involved in the membrane and Ca²⁺ clock pacemaker mechanisms. IPA uses data from TarBase database, miRecords (mirecords.biolead.org),

TargetScan (www.targetscan.org/) and rna22 (cm.jefferson.edu/rna22) to predict if any of the miRs potentially target the mRNAs based on conserved 8mer (≥ 0.8 conserved branch length) and 7mer sites that match the seed region of each miR.

Next Generation Sequencing

Next generation sequencing was performed at the Genomic Technologies Core Facility at the University of Manchester on RNA samples collected from frozen human SN preparations. SN samples were collected from the area around the SN artery and right atrial muscle samples from the pectinate muscles remote from the SN region. Samples were collected from 3 human specimens (Specimens 8, 9, 10 in Table S1). Quantity and integrity of the RNA samples were measured using a 2200 TapeStation (Agilent Technologies) to ensure their suitability. Subsequently, TruSeq Stranded mRNA assays (Illumina) were used to produce libraries of more stable, single-stranded cDNA as follows. Total RNA was purified to polyadenylated mRNA via magnetic separation technology, which works through hybridization of covalent interactions of oligo d(T)₂₅ to poly (A) regions present in most eukaryotic mRNA. The mRNA sequences were fragmented into parts via divalent cations at higher temperature, and random primers were used to reverse transcribe the mRNA fragments into single-stranded cDNA. DNA polymerase and ribonuclease H-mediated the synthesis of the second cDNA strand produced from RNA oligonucleotides, originating from the 5' end of the mRNA. The final cDNA library was generated by an addition of a single "A" base, binding of adapters to the fragments and purification and enrichment via a polymerase chain reaction. The cDNA libraries were incorporated into a multiplex system using the adapters; they were then pooled and clustered using a cBot instrument (Illumina). Optical flow-cells containing the mRNA samples were then paired-end sequenced and mRNA was quantified through repeating 76 cycles twice, using a HiSeq4000 instrument (Illumina). Bcl2fastq software (2.17.1.14) was used to generate an mRNA expression database for each individual SN versus atrial muscle and calculate fold difference in expression between the 2 regions.

Luciferase Reporter Gene Assay

Rat cardiac H9C2 cells (ATCC, UK) were maintained in DMEM (Invitrogen), containing 10% fetal bovine serum, and 1% penicillin-streptomycin. H9C2 cells were seeded at a density of 5×10^5 cells per well in 24-well plates 24 hour before the transfection experiment. Cells were transfected with 500 ng HCN4 or Ca_v1.3 3'UTR-containing plasmid (see below for description of the

plasmid) and 1 μ g miR-486-3p, scrambled miR, or culture media only. Lipofectamine 2000 (Invitrogen, UK) transfection agent was used in accordance with the manufacturer's instructions. The DNA-lipofectamine transfection complex was incubated for 20 minutes at room temperature and then 37°C and 5% CO₂ for 24 hours, followed by washing with PBS and lysis via passive lysis buffer (Promega) on a rocker for 20 minutes. Luciferase reporter gene activity, which is directly proportional to mRNA expression of the target gene, was assessed using the luciferase assay system (Promega). A Lumat LB9507 luminometer (Berthold Technologies) was used to measure the bioluminescent activity in 10 μ L cell lysate. Each assay was performed in quadruplicate and repeated 3 independent times. The luciferase assay activity was normalised to Renilla (Promega) activity and expressed as a ratio.

Sinus Node Preparations Used for Extracellular Potential Recording

Three-month-old male Wistar–Hannover rats weighing 230 to 250 g were used. Animals had free access to food and water and were maintained under standard laboratory conditions in a temperature-controlled room (22°C) with a 12:12 hour light:dark lighting regime. Animals were humanely euthanized by a Schedule 1 procedure (concussion and cervical dislocation) in accordance with UK Home Office regulations under the Animals (Scientific Procedures) Act 1986 under an institutional licence held at the University of Manchester.

Rats were humanely euthanised via CO₂ inhalation and cervical dislocation. The heart was dissected out and placed in 37°C Tyrode's solution (containing NaCl 120 mmol/L, CaCl₂ 1.2 mmol/L, KCl 4 mmol/L, MgSO₄·7H₂O 1.3 mmol/L, NaH₂PO₄·2H₂O 1.2 mmol/L, NaHCO₃ 25.2 mmol/L, glucose 5.8 mmol/L). The entire right atrium was then dissected and opened along the anterior atrial wall and anterior superior vena cava so that the posterior intercaval region remained intact (Figure 2A).

The dissection medium was changed to Modified Eagle's Minimum Essential Medium, containing 5% fetal bovine serum (Life Technologies), and preparations incubated at 37°C/5% CO₂. The culture medium was changed 8 hours after injection (see below) to Advanced DMEM/F-12 medium (Life Technologies), containing 10% fetal bovine serum and 1% penicillin-streptomycin (Sigma). Preparations were kept for 24 hours.

Sinus Node Preparations Used for Sharp Microelectrode Recordings

Ten-week-old male Wistar rats weighing 280 to 300 g were used. Animals were kept in an animal house and

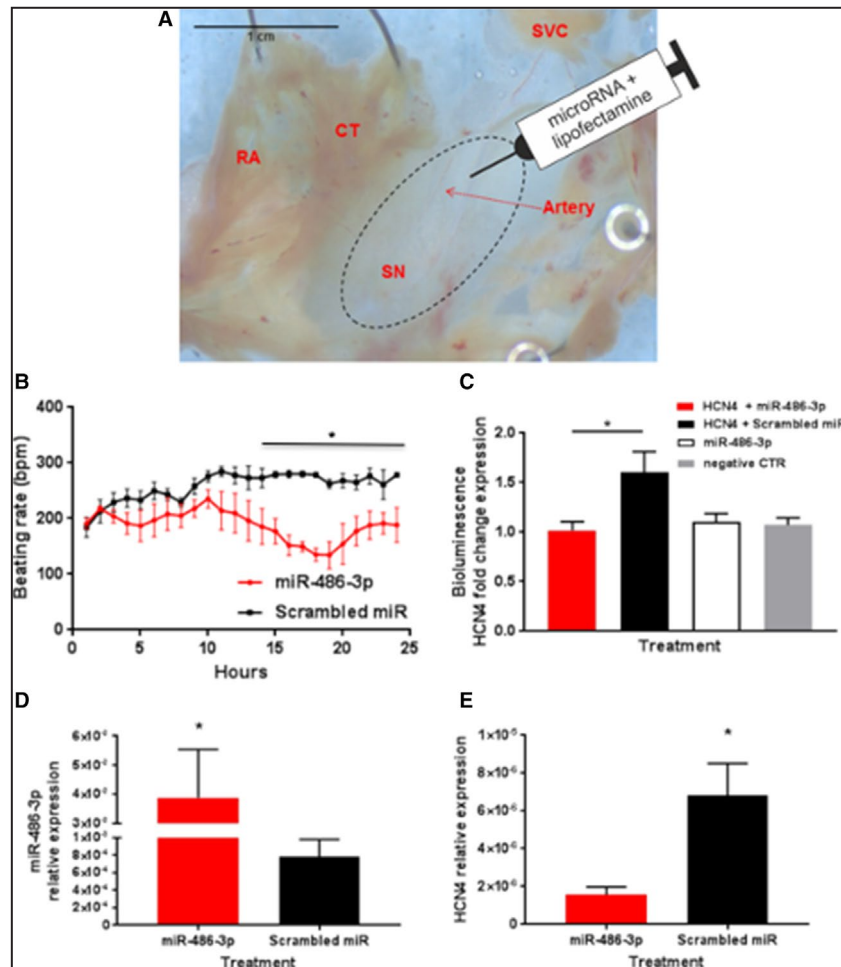


Figure 2. Functional effects of microRNA-486-3p transfection of ex vivo rat sinus node preparations.

A, Typical sinus node (SN) preparation. Site of injection around the SN artery shown. **B**, Beating rate of SN preparations in the 24 hours after injection with microRNA-486-3p or scrambled microRNA (means±SEM, n=9). **C**, Luciferase bioluminescence recorded 24 hours after transfection of H9C2 cells with 500 ng with HCN4 3 prime untranslated region -containing plasmid and 1 µg microRNA-486-3p or scrambled microRNA. As 2 control groups, cells were transfected with microRNA-486-3p alone or remained untransfected (ie, an equivalent volume of culture medium was added in place of transfected oligos or 3 prime untranslated region plasmid). These 2 control groups did not include the luciferase reporter. Means±SEM shown (n=3 batches of cells with 4 replicates; *P<0.05). **D** and **E**, Quantitated polymerase chain reaction experiments showing expression of microRNA-486-3p, (**D**) and HCN4 (hyperpolarization-activated cyclic nucleotide-gated). (**E**) mRNA in SN preparations 24 hours after microRNA-486-3p transfection (means±SEM; n=4; *P<0.05). CT indicates crista terminalis; HCN4, hyperpolarization-activated cyclic nucleotide-gated; miR, microRNA; SN, sinus node; and SVC, superior vena cava.

had free access to food and water and were maintained under standard laboratory conditions with a 12:12 hour light:dark lighting regime. Animals were humanely culled. They were heparinized (100 IU/100 g, intraperitoneal injection), anesthetized with isoflurane (3.5%) and decapitated in accordance with European Convention for the Protection of Vertebrate Animals used for Experimental and other Scientific Purposes (Council of Europe No 123, Strasbourg 1985) and

approved by the Ethics Committee of the National Medical Research Center of Cardiology Institute of Experimental Cardiology.

The chest was opened RA with intercaval SN region was rapidly excised and pinned with endocardial side up to the bottom of a 5 mL perfusion chamber filled with physiological (Tyrode) solution of the following composition (in mmol/L): NaCl 118.0, KCl 2.7, NaH₂PO₄ 2.2, MgCl₂ 1.2, CaCl₂ 1.2, NaHCO₃ 25.0, glucose 11.0, pH

7.4±0.2 bubbled by 95% O₂ and 5% CO₂ gas mixture. The constant perfusion with flow rate of 10 mL/min at 37°C was started immediately after the preparation.

Spontaneously evoked SN pacemaker derived action potentials (APs) were recorded with glass microelectrodes (10–20 MΩ) filled with 3 mol/L KCl, connected to Warner intracellular electrometer (IE-210, Warner Instruments, USA) from the endocardial side of the preparations. Signal was digitized at 10 kHz sampling rate with analog-digital converter (E-154, ADC L-card, Russia). The rate of spontaneous AP was calculated using PowerGraph (PowerGraph 3.3 Professional, version 3.3.8, DISoft) and MiniAnalysis software (Synaptosoft, USA, version 6.0.7). The preparations were equilibrated for 30 minutes before recording of control APs in 3 to 4 mm² region surrounding SN artery bifurcation. Only APs with a diastolic depolarization (35–55 mV/s) and a slow rate of the AP upstroke (<15 V/s) were considered as pacemaker.

After the control recording, the SN region was injected with Tyrode solution (control), lipofectamine or miR-486-3p transfection mixture. The 5 μL of transfection mixture was delivered via glass microelectrode (tip diameter <50 μm) connected to Narishige micromanipulator and microinjection syringe pump (Harvard Apparatus, PHD ultra) with a constant rate 1 μL/min, the injection was repeated for 5 times to cover the 2 to 4 mm² of SN region and to deliver 25 μL of the transfection mixture in total. Pacemaker APs from the same sites in SN preparations were recorded at least for 5 minutes immediately, 2, 4, and 6 hours after the injections. The rate of spontaneous APs as beats per minute was calculated.

Transfection Injection

≈2 μL transfection mixture, containing 6 μL 1x Modified Eagle's Minimum Essential Medium, reduced serum medium (Life Technologies), 1.5 μL Lipofectamine RNAmix (Life Technologies), and 2.5 μL miR-486-3p (MC12986; Life Technologies), was injected at the bifurcation of the SN artery with a 10 μL NanoFil syringe (World Precision Instruments). Control preparations were transfected with Cy3-labeled pre-miR negative control (ThermoFisher). All transfection was performed immediately after dissection of the preparations at the time of the initial culture. The beating rate was measured 24 hours later, ie, post injection.

Plasmids

Human HCN4 (NCBI Reference Sequence: NM_005477.2; HmiT088528-MT06) and Ca_v1.3 (NCBI Reference Sequence: NM_000720.2; HmiT054373-MT06) 3'UTR-containing plasmids were purchased from GeneCopoeia (Rockville, MD, USA).

The pEZX-MT06 luciferase miR expression vector contained reporter genes for luciferase and Renilla luciferase. The amplification of the plasmids was performed as follows: DH5α *Escherichia coli* cells (Sigma) were transformed with the plasmids. A single bacterial colony transfected with the plasmid was incubated in 2 mL LB medium, containing 100 μg/mL ampicillin overnight at 37°C, shaking at 150 rpm. Plasmid DNA was purified from the transduced *E coli* using PureLink Plasmid Kit (Thermo Fisher) according to the manufacturer's protocol. Restriction digest, to confirm the presence of the correct ligation of the miR 3'UTR inserts in the pEZX-MT06 vector, was then performed. One microgram of each plasmid was incubated with restriction endonuclease enzymes EcoRV and HindIII (New England Biolabs) overnight at 37°C. DNA gel electrophoresis was then performed to confirm the presence of the expected DNA fragments.

Extracellular Potential Recording

To record and monitor automaticity of the *ex vivo* SN preparations, extracellular potentials were recorded from the right atrial appendage using 2 0.15-mm diameter stainless steel electrodes (ADInstruments) as previously described by Morris et al.¹⁷ In addition, the culture medium surrounding the preparation was grounded with a 0.15 mm wire earth electrode. Extracellular potentials were continuously recorded using PowerLab 4/35, 4-channel recorder, and LabChart v7 software (ADInstruments). The average beating rate of the SN preparation was calculated via the detection of a deflection >2 SD of a paced beat. Recordings were collected for 24 hours and the SN preparation retained for further experiments.

Statistical Analysis

Mean±SEM values are shown. Significant differences were identified with 1-way ANOVA and/or paired *t* tests. A difference was assumed to be significant at *P*≤0.05 or *P*≤0.001.

The authors had full access to and take full responsibility for the integrity of the data. All authors have read and agree to the article as written.

The presented data can be available from the corresponding author upon request.

RESULTS

Differential MicroRNA Expression in Human Sinus Node and Atrial Muscle

The expression profile of miRs in the SN and neighboring right atrial muscle was mapped using qPCR and a TaqMan assay for human miRs. Out of the 754 human miRs examined, 18 were significantly more

abundant (Figure 1A) and 48 significantly less abundant (Figure 1B) in the SN than the atrial muscle. The location of the SN tissue in which the miR expression was measured is shown in Figure 1C and 1D and the miRs that are significantly differentially expressed in the SN and atrial muscle are summarized in Table S3.

Ingenuity Pathway Analysis

IPA software was used to predict which of the miRs that are differentially expressed between the SN and atrial muscle may be involved in the differential expression of key ion channels, Ca²⁺-handling molecules and connexins involved in the regulation of the membrane,

and Ca²⁺ clock pacemaker mechanisms. The predictions were based on miR-to-mRNA sequence binding probability, in combination with miR expression data for the human SN and atrial muscle from this study (Table S3) and expression of mRNA for key ion channels, Ca²⁺-handling proteins and connexins for the human SN, and atrial muscle from Chandler et al, 2009; upregulation of an miR is expected to lead to downregulation of its target mRNA and vice versa. TargetScan Human and/or TarBase software was used to predict target mRNA; rna22 software was used to predict the number of binding sites for an miR on an mRNA. The predicted miR-mRNA relationships are summarized in Table and are shown graphically

Table. Summary of Predicted MicroRNA-mRNA Interactions in the Human Sinus Node

miR	Expression of miR in Sinus Node (vs Right Atrial Muscle)	Predicted Target	Expression of Target mRNA in Sinus Node (vs Right Atrial Muscle)	No. of Binding Sites for miR on Predicted Target mRNA
miR 1-3p	↓	Tbx3	↑	1
		HCN1	↑	1
		HCN4	↑	1
miR 10b-5p	↑	Gja5 (Connexin 40)	↓	1
miR 30c-5p	↓	HCN1	↑	1
		HCN4	↑	1
		Cacna1g Ca _v 1.3	↑	1
miR 133a-3p	↓	HCN4	↑	5
miR 153-3p	↑	Scn5a (Na _v 1.5)	↓	1
		Cacna1c (Ca _v 1.2)	↓	1
		RyR2	↓	2
miR 198	↑	Cacna1c (Ca _v 1.2)	↓	2
		Kcnh2 (ERG)	↓	7
		RyR2	↓	1
miR 204-5p	↑	Cacna1c (Ca _v 1.2)	↓	1
miR 215-5p	↑	Kcna4 (K _v 1.4)	↓	1
miR 371-3p	↓	Cacna1d (Ca _v 1.3)	↑	1
		Gjc1 (Connexin 45)	↑	5
miR 422a	↓	Tbx3	↑	1
miR 429	↓	Tbx18	↑	1
miR 486-3p	↓	HCN1	↑	6
		HCN4	↑	7
		Cacna1d (Ca _v 1.3)	↑	6
		Cacna1g (Ca _v 3.1)	↑	1
miR 512-5p	↑	Gja1 (Connexin 43)	↓	1
miR 938	↓	Cacna1d (Ca _v 1.3)	↑	9
miR 1225-3p	↑	Scn5a (Na _v 1.5)	↓	2

The data are based on the expression of miRs (microRNAs) from this study and the expression of selected mRNAs important for pacemaking from Chandler et al.⁹ The columns from left to right show the miRs, expression of the miRs in the sinus node vs the right atrial muscle, the gene names (ion channel names shown in parenthesis) of targets predicted by TargetScan Human and/or TarBase software, expression of the predicted targets in the sinus node vs the atrial muscle, and the number of potential binding sites on the target for each miR (predicted by rna22 software). Note that upregulation of an miR is expected to result in a downregulation of the target and vice versa. ERG indicates ether-a-go-go-related gene; Gja, gap junction protein alpha 5; HCN1, hyperpolarization-activated cyclic nucleotide-gated, miR, microRNA; RyR, ryanodine receptor 2; and Tbx, t-box.

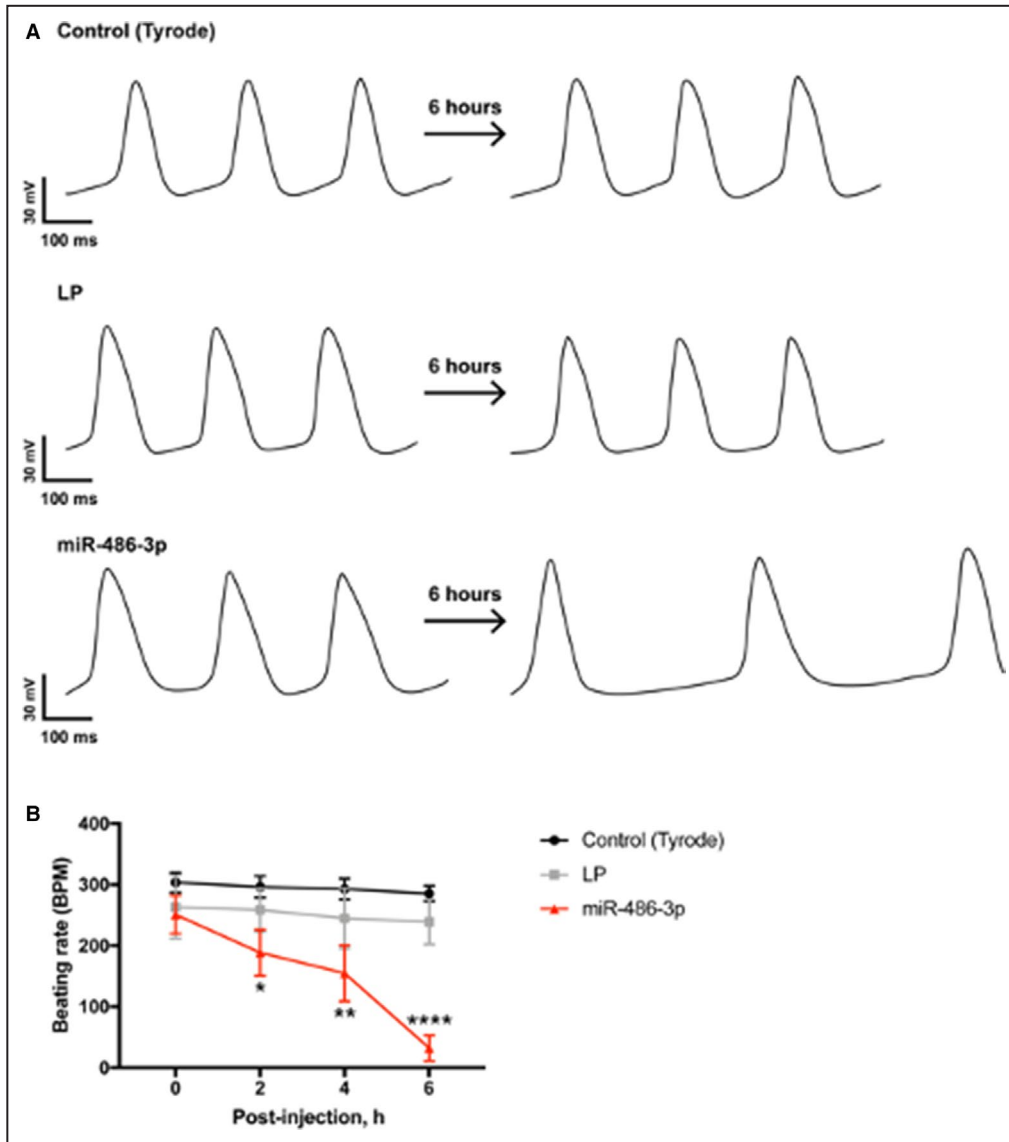


Figure 3. The intracellular recordings of action potentials from rat sinus node preparations after microRNA-486-3p transfection *ex vivo*.

A, Representative example of action potentials recorded intracellularly in the sinus node before and 6 hours after injection with Tyrode (control), lipofectamine, and microRNA-486-3p transfection mixture. **B**, Beating rate of sinus node preparations in 6 hours after the injection (means±SEM, n=5 for each group). AP indicates action potential; LP, lipofectamine; and miR, microRNA. **P*<0.05, ***P*<0.005, *****P*<0.0001 (2-way ANOVA with Tukey multiple comparison test).

in Figure 1 (arrows). Of the 18 miRs that were more abundant in the SN than the atrial muscle, 7 were predicted to target physiologically relevant pacemaker mRNAs that were expressed at lower levels in the SN compared with the atrial muscle (Figure 1 arrows; Table). The 7 miRs were: miR-10b-5p, predicted to target connexin 40; miR-153, predicted to target $Ca_v1.2$, ryanodine receptor 2, and $Na_v1.5$; miR-198, predicted to target $Ca_v1.2$, ryanodine receptor 2, and ether-a-go-go-related gene (ERG); miR-204, predicted to target $Ca_v1.2$; miR-215, predicted to target $K_v1.4$; miR-512-5p, predicted to target connexin

43; and miR-1225-3p, predicted to target $Na_v1.5$ (Figure 1, arrows). Of the 48 miRs that were more abundant in the atrial muscle than the SN, 8 were predicted to target physiologically relevant pacemaker mRNAs that were expressed at lower levels in the atrial muscle compared with the SN (Figure 1, arrows; Table). The 8 miRs were: miR-1-3p, predicted to target HCN1, HCN4 and T-box (Tbx)3; miR-30c, predicted to target HCN1 and $Ca_v1.3$; miR-133a, predicted to target HCN4; miR-371-3p, predicted to target $Ca_v1.3$ and connexin 45; miR422a, predicted to target Tbx3; miR-429, predicted to target Tbx18; miR-486-3p,

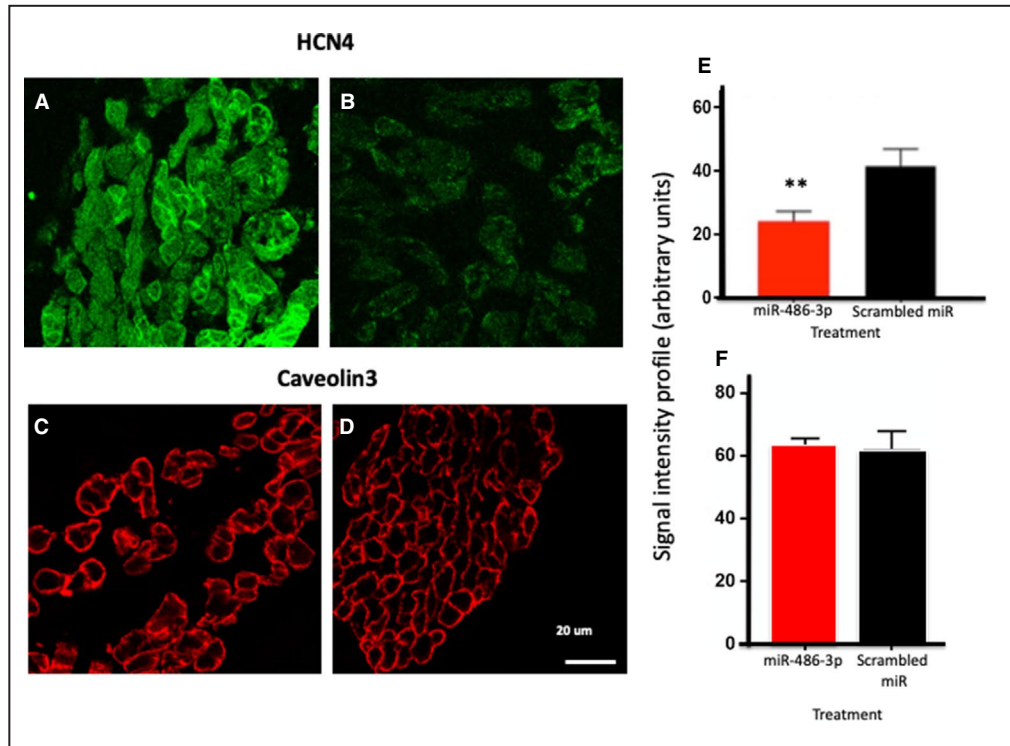


Figure 4. Effect of exogenous expression of microRNA-486-3p on HCN4 protein expression in the rat sinus node.

A and **B**, Immunolabeling of HCN4 (hyperpolarization-activated cyclic nucleotide-gated) protein in the rat sinus node before (**A**) and after (**B**) 24 hours after transfection with microRNA-486-3p. **C** and **D**, Immunolabeling of Caveolin-3 (plasma membrane marker) in the rat sinus node before (**A**) and after (**B**) 24 hours after transfection with scrambled microRNA. **E**, HCN4 protein signal intensity in the rat sinus node 24 hours after transfection with microRNA-486-3p or scrambled microRNA (means \pm SEM; n=5; ** $P\leq 0.005$). **F**, Caveolin-3 protein signal intensity in the rat sinus node 24 hours after transfection with microRNA-486-3p or scrambled microRNA (means \pm SEM; n=4; no significance difference was observed). HCN4 indicates hyperpolarization-activated cyclic nucleotide-gated; and miR, microRNA.

predicted to target $Ca_v1.3$, HCN1, and HCN4; and miR-938, predicted to target $Ca_v1.3$ (Figure 1, arrows).

miR-486-3p Effect on SN Beating Rate

Four miRs were predicted to target the pacemaker channel, HCN4, and the L-type Ca^{2+} channel, $Ca_v1.3$, (Table) and this may reflect the importance of these pacemaker channels. Three miRs were predicted to target the alternative pacemaker channel, HCN1, and the alternative L-type Ca^{2+} channel, $Ca_v1.2$ (Table). Two miRs were predicted to target the Na^+ channel, $Na_v1.5$, the ryanodine receptor, ryanodine receptor 2, and the SN transcription factor, Tbx3 (Table). Finally, 1 miR was predicted to target a T-type Ca^{2+} channel, $Ca_v3.1$, 2 K^+ channels (Kv1.4 and ERG), 3 connexins (40, 43, and 45) and the SN transcription factor, Tbx18 (Table). Arguably the most important pacemaker channel in the SN is HCN4 and consequently it was of special interest. Of the miRs potentially targeting HCN4, miR-486-3p was of special interest, because it was predicted by IPA to have 7 binding

sites on HCN4 mRNA in the human (Table). To confirm that miR-486-3p can target HCN4, experiments were performed on the *ex vivo* rat SN preparation. McGahon et al showed that the human miR-486-3p sequence is conserved in other species, including the rat.¹⁸ Also analysis showed that rat HCN4 mRNA has predicted binding sites for miR-486-3p. This suggests that the *ex vivo* rat SN preparation is suitable to validate HCN4 mRNA as a target of miR-486-3p. miR-486-3p (in a transfection mixture) was injected into the SN (Figure 2A) and the preparation was maintained in culture for 24 hours. Preparations injected with a non-functional scrambled miR were used as controls. miR-486-3p significantly reduced the beating rate of the *ex vivo* rat SN preparations by $\approx 35\%$ 15 hours after transfection and this change was maintained over the rest of the 24-hour period of culture (Figure 2B). The effect of miR-486-3p on SN beating rate appeared to develop a few hours after transfection (Figure 2B).

In another set of experiments, using sharp micro-electrode recordings of the electrical activity in the

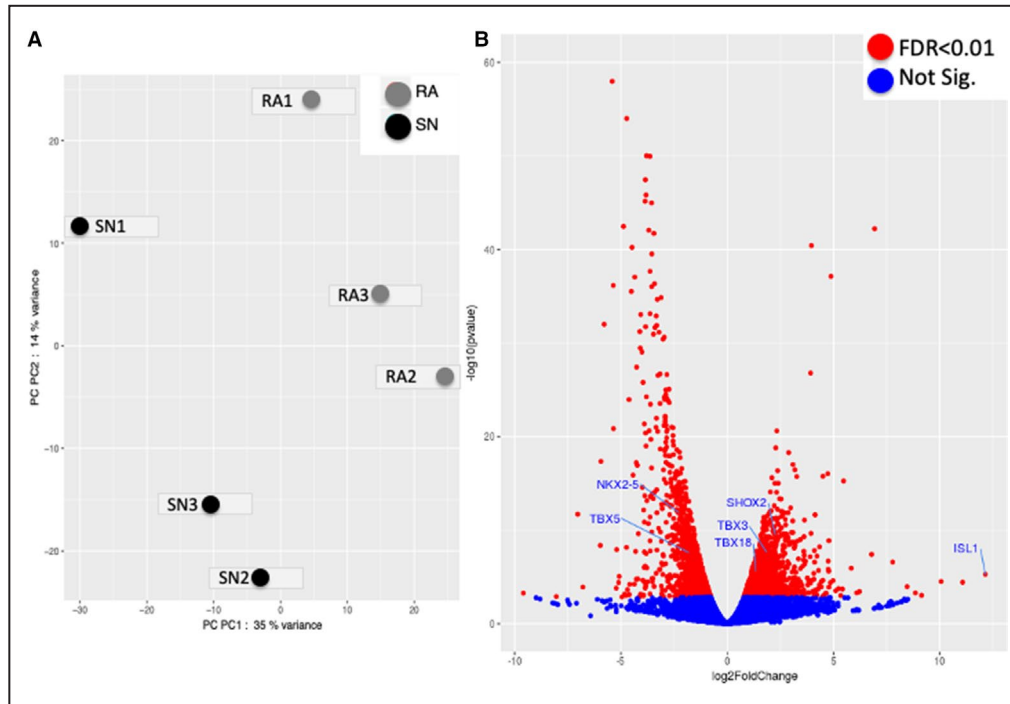


Figure 5. Next generation sequencing for RNAseq data of 3 human sinus node and 3 right atria specimens from the same hearts.

A, Principal component (PC) analysis scatter-plot of RNAseq data from 3 human sinus node (SN) (black dots) and 3 right atrium (RA) (grey dots) specimens. The graph shows that there are 2 distinct groups of tissue, namely the SN (SN1 to SN3) cluster close on the left of x-axis and RA (RA1 to RA3) cluster closer close on the right of x-axis, that have significant differential gene expression. **B**, Volcano plot of all RNAseq data with 6 “embryonic” transcription factors annotated on the plot. Log₂FoldChange $P \leq 0$ indicates genes less expressed in the SN vs RA and vice versa. RA indicates right atrium; and SN, sinus node. Significantly more/less expressed genes (illustrated in red) based on false discover rate < 0.01. FDR indicates false discovery rate; RA, right atrium; and sinus node.

RA/SN preparations, we observed that after injections of the SN region ($n=5$) with miR-486-3p, the rate of the SN-derived spontaneous APs in the RA decreased gradually from 250 ± 30 down to 32 ± 21 beats per minute \pm SEM (Figure 3). This gradual reduction was observed from 2 hours after injection and was maximal at 6 hours post-injection. The rate of APs was only $13 \pm 9\%$ ($P < 0.0001$, $n=5$) of the initial rate before injections calculated both on the basis of the SN or RA recordings (Figure 3). After injections with Tyrode ($n=5$) and lipofectamine ($n=5$) there was no change to the rate of the SN-derived spontaneous APs (Figure 3).

miR-486-3p Effect on HCN4 Expression

To investigate whether miR-486-3p can affect HCN4 expression as predicted, a luciferase reporter gene assay was performed. The predicted binding sites for miR-486-3p are in the 3'-UTR of human HCN4. Therefore, the 3'-UTR of human HCN4 was introduced as the 3'-UTR of the luciferase gene. The resulting plasmid was transfected into rat cardiac

H9C2 cells. Following transcription and translation, the expression of the luciferase protein (surrogate of HCN4 expression) was measured by the resulting luciferase bioluminescence. Bioluminescence was significantly less from cells transfected with the plasmid and miR-486-3p than from cells transfected with the plasmid and scrambled (non-functional) miR (Figure 2C). As expected, bioluminescence was also low if the cells were not transfected with the HCN4 plasmid but only transfected with miR-486-3p or neither transfected with the plasmid nor miR-486-3p (Figure 2C). This suggests that miR-486-3p can control HCN4 expression.

To confirm that miR-486-3p can affect HCN4 expression, experiments were conducted on the *ex vivo* rat SN preparation. Preparations were injected (Figure 2A) with miR-486-3p or scrambled miR. As expected, miR-486-3p expression was greater in preparations in which the SN was transfected with miR-486-3p rather than scrambled miR (Figure 2D). HCN4 mRNA expression was significantly reduced in preparations injected with miR-486-3p (as compared with preparations injected with the scrambled miR).

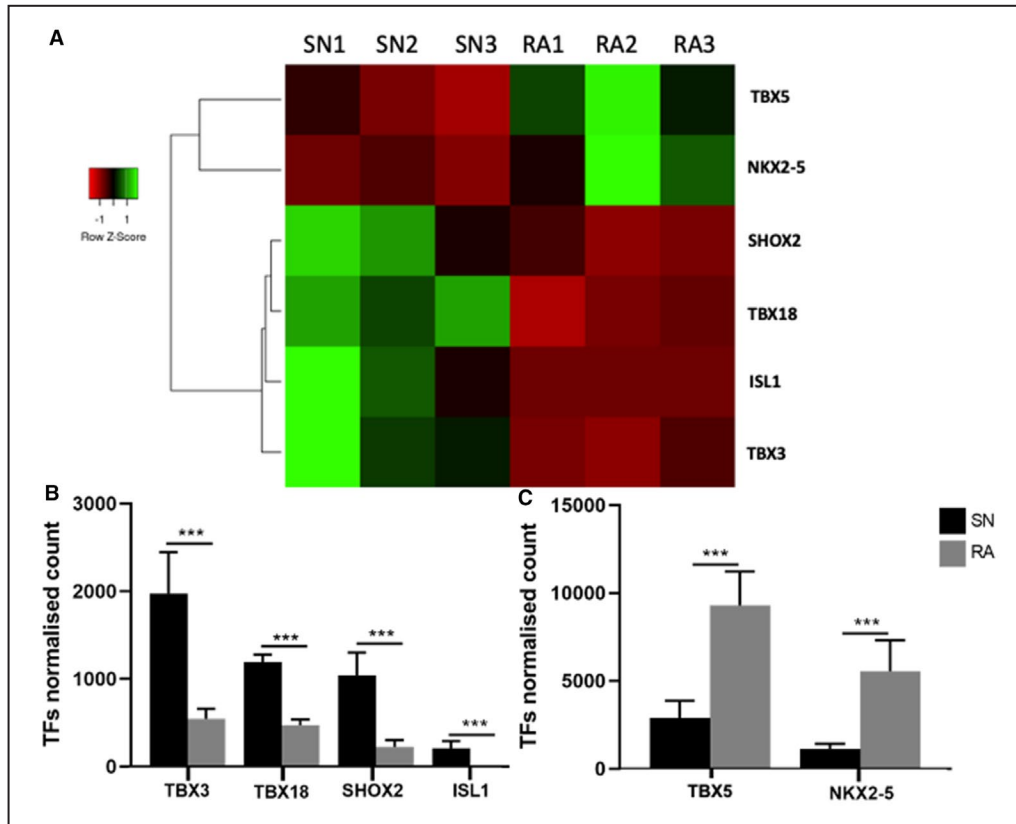


Figure 6. “Embryonic” transcription factors significantly more or less expressed in the human adult sinus node in comparison with right atrial muscle.

Data were analyzed via Bcl2fastq software (2.17.1.14). Transcription factors (TFs) normalized counts are the mean of the DESeq2 normalized read counts for each TF in the sinus node (SN) and right atrium (RA). **A**, Heat maps showing relationship across 6 SN and RA samples (SN1–SN3 and RA1–RA3) for the expression of 6 TFs. Three SNs cluster together and 3 RAs cluster together for the expression of these 6 TFs. **B** and **C**, Means±SEM; n=3; ***P≤0.001 of 6 TFs in SN and RA. Graphs were created via GraphPad Prism 7.0. Nkx2-5 indicates NK2 homeobox 5; RA, right atrium; Shox; short stature homeobox; SN, sinus node; Tbx, T-box; and TF, transcription factor.

This shows that miR-486-3p controls HCN4 mRNA expression in the sinus node (miR-486-3p must promote HCN4 mRNA degradation). In the same *ex vivo* rat SN preparations, HCN4 protein expression was assessed by immunolabeling of HCN4 protein in thin cryosections through the SN (Figure 4A, 4B, and 4E). Labeling was significantly reduced in preparations injected with miR-486-3p (as compared with preparations injected with the scrambled miR) (Figure 4A, 4B, and 4E). Cell membrane preservation and integrity over the 24-hour incubation period was confirmed by Caveolin-3 immunolabeling (Figure 4C, 4D, and 4F).

Transcription Factors are Also Involved in Differential Gene Expression Between the Human Sinus Node and Atrial Muscle

Differential gene expression between the human sinus node and atrial muscle will not exclusively be the result of a differential expression of miRs—a differential

expression of transcription factors will also be involved. Expression of transcription factors was investigated using next generation sequencing. The transcriptomes of 3 human SN and corresponding right atrial muscle samples were sequenced. The expression of the 3060 most abundant human mRNAs was investigated and principal component analysis confirmed distinct SN and atrial muscle mRNA profiles (Figure 5A); 1238 mRNAs had significantly higher expression in the SN (\log_2 fold change >1, $P < 0.05$), 1357 had significantly higher expression in the atrial muscle (\log_2 fold change <1, $P < 0.05$), and 465 were not significantly different between the 2 tissues ($-1 < \log_2$ fold change <1) (Figure 5B, red dots). IPA software was used to identify transcription factors and potential relationships with either miRs or mRNAs in this study; 68 transcription factors were significantly more expressed in the SN, and 60 were more significantly expressed in the atrial muscle. Six of the differentially expressed transcription factors have potential relationships with either the miRs

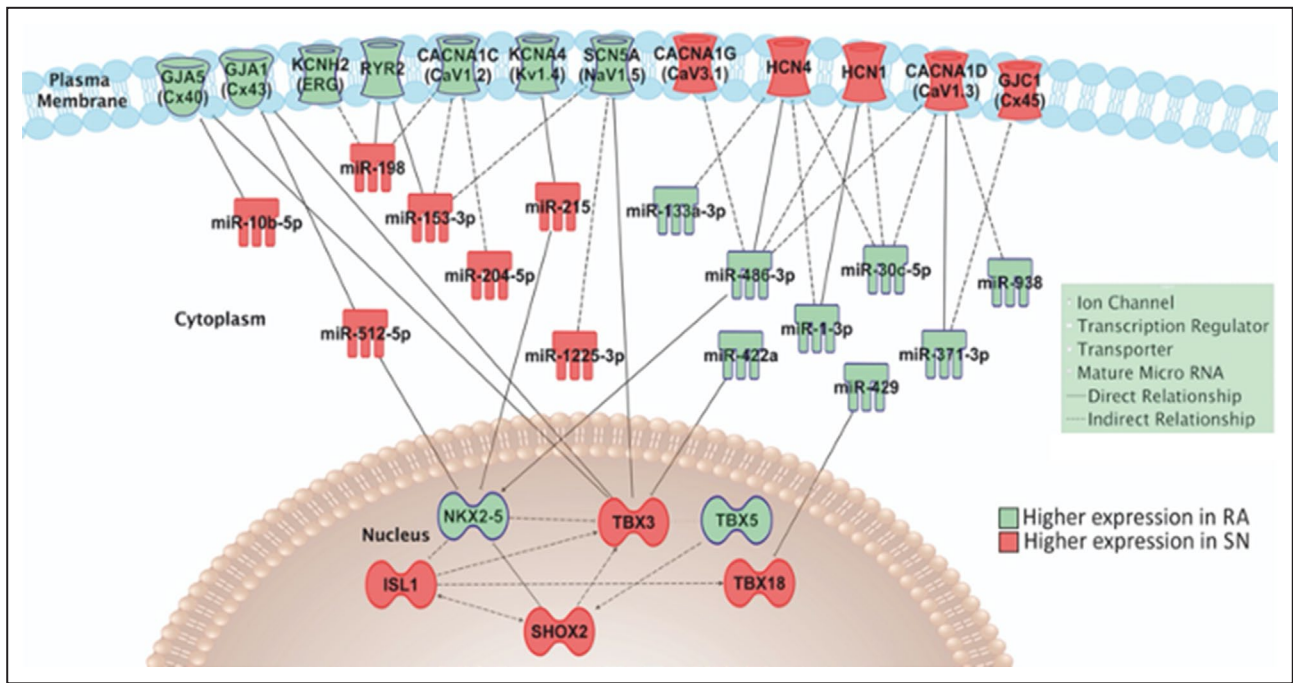


Figure 7. Ingenuity Pathway Analysis predictions of interactions between “embryonic” transcription factors, microRNAs, ion channels, and gap junction subunits.

Transcription factors are shown in the nucleus, microRNAs in the cytoplasm, and ion channels in the surface membrane. For simplicity, RYR2 (ryanodine receptor 2) is shown in the surface membrane rather than the sarcoplasmic reticulum. HCN4 indicates hyperpolarization-activated cyclic nucleotide-gated; miR, microRNA; NKX2-5, NK2 homeobox 5; RA, right atrium; SHOX; short stature homeobox; SN, sinus node; and TBX, T-box.

or mRNAs in this study. These are Islet1, short stature homeobox 2, Tbx3, and Tbx18, which were significantly more highly expressed in the SN, and Tbx5 and NK2 homeobox 5, which were significantly more highly expressed in the atrial muscle (Figures 5B and 6). The predicted relationships between these transcription factors and either miRs or mRNAs are shown in Figure 7. This network shows 24 potential links (direct or indirect) between miRs and ion channels, but only 3 between transcription factors and ion channels. This raises the question of whether much of the ion channel regulation occurs at the post-transcriptional level via miRs. However, miRs themselves are under the control of transcription factors as shown in Figure 7.

DISCUSSION

This study shows, for the first time, a distinct expression pattern of miRs in the human SN compared with that of the right atrial muscle that is predicted to affect the expression of target molecules responsible for the pacemaker mechanisms in the heart. This study shows 66 differentially expressed miRs (Figure 1). The differentially expressed miRs are predicted to target mRNAs that have been reported to be differentially expressed in these tissues.⁵

In this study, we found 7 miRs (miR-10b-5p, miR-153-3p, miR-198, miR-204-5p, miR-215-5p, miR-512-5p, and miR-1225-3p) expressed at higher levels in the SN compared with atrial muscle that are predicted to bind to and thus downregulate molecules that are known to be expressed at lower levels in the SN⁵: the Na⁺ channel, Na_v1.5, the L-type Ca²⁺ channel, Ca_v1.2, 2 K⁺ channels (Kv1.4 and ERG), the RYR2 (ryanodine receptor 2), and 2 connexins (40 and 43). The absence of Na_v1.5 (and the corresponding absence of the Na⁺ current, I_{Na}) in the SN explains why the upstroke of the SN action potential is slow and the absence of the 2 high conductance connexins, 40 and 43, in the SN explains the poor electrical coupling in the SN (essential to protect the SN from the hyperpolarizing influence of the neighboring atrial muscle).¹⁹

Eight miRs (miR-1-3p, miR-30c-5p, miR-133a-3p, miR-371-3p, miR-422a, miR-429, miR-486-3p, and miR-938) that were expressed at higher levels in the atrial muscle compared with the SN are predicted to inhibit molecules that are important for pacemaking: 2 pacemaker HCN channels (HCN1 and HCN4), 2 pacemaker Ca²⁺ channels (Ca_v1.3 and Ca_v3.1), and the low conductance connexin isoform, connexin 45. If the predicted actions of the miRs are correct, this helps to explain why the atrial muscle does not normally show pacemaker activity; conversely, the low

expression of these miRs in the SN helps to explain why the SN does show pacemaking. Of these miRs and their predicted effects, miR-486-3p and its predicted effect on HCN4 were the focus, because of the importance of HCN4 and the number of predicted binding sites on HCN4 for miR-486-3p. A luciferase reporter gene assay confirmed that miR-486-3p can potentially control expression of HCN4 (Figure 2), and miR-486-3p, when ectopically expressed in the SN, reduced HCN4 mRNA and protein levels (Figures 2 and 4), and reduced the SN beating rate (Figure 2). In a recent study, we showed that miR-486-3p is upregulated in the SN in a mouse model of athletic training.¹⁴ Following athletic training, the downregulation of HCN4 and the corresponding ionic current (I_i) in the SN and the consequent sinus bradycardia was attributed to an upregulation of miR-486-3p and miR-423-5p¹⁴; in this study, a luciferase reporter gene assay showed that miR-486-3p was able to regulate mouse HCN4 expression—therefore, miR-486-3p is able to regulate both human (this study) and mouse¹⁴ HCN4 expression.

In this study, we also identified key “embryonic” transcription factors that are differentially expressed in the adult human SN versus atrial muscle and with predicted links to either the miRs or ion channels of interest in the SN (Figures 5, 6, and 7). This suggests that both transcription factors and miRs are responsible for the unique gene expression pattern of the SN. Furthermore, transcription factors may frequently act via miRs.

CONCLUSIONS

The human SN possesses a unique pattern of expression of miRs. Some of the differentially expressed miRs are predicted to target genes that are important for pacemaking, such as HCN1, HCN4, $Ca_v1.3$, and $Ca_v3.1$. The action of miRs is complex with interactions between multiple miRs, transcription factors, and target genes. It has been confirmed that miR-486-3p has an important role in regulating SN pacemaker activity. miR-486-3p directly inhibits HCN4 and thereby reduces action potential generation by the SN, making it a potential target for manipulating pacemaking in therapeutic treatment of sinus node disease. For example, inappropriate sinus node tachycardia is currently treated using ivabradine to block HCN4²⁰ and use of miR-486-3p could be alternative strategy. This study provides novel insights into the mechanisms controlling SN gene expression vital for its role as the primary pacemaker in the heart.

ARTICLE INFORMATION

Received March 23, 2020; accepted August 27, 2020.

Affiliations

From the Division of Cardiovascular Sciences, University of Manchester, United Kingdom (M.P., A.J.A., J.Y., L.S., A.J.A., C.G., A.F., Y.Z., D.O., A.D., H.D.); Physiology and Cell Biology Department, The Bob and Corrine Frick Center for Heart Failure and Arrhythmia, The Ohio State University Wexner Medical Center, Columbus, OH (N.L., V.V.F.); National Institute of Legal Medicine, Bucharest, Romania (F.P.); School of Biomedical Sciences, Queensland University of Technology, Brisbane, Australia (P.M.); Cardiovascular Molecular & Therapeutics Translational Research Group, The Prince Charles Hospital, Brisbane, Australia (P.M.); Department of Human and Animal Physiology, Lomonosov Moscow State University, Moscow, Russia (A.D.I., K.B.P.); and Department of Anatomy, Jagiellonian University Medical College, Krakow, Poland (H.D.).

Sources of Funding

This work was supported by Leducq Foundation (THE FANTASY 19CVD03), the British Heart Foundation program grant RG/18/2/33392; National Institutes of Health (grants HL115580 and HL135109); Russian Science Foundation grant 19-15-00163.

Disclosures

None.

Supplementary Material

Tables S1–S3

REFERENCES

- Stephenson RS, Atkinson A, Kottas P, Perde F, Jafarzadeh F, Bateman M, Iazzo PA, Zhao JC, Zhang HG, Anderson RH, et al. High resolution 3-dimensional imaging of the human cardiac conduction system from microanatomy to mathematical modeling. *Sci Rep*. 2017;7:7188.
- Li N, Csepe TA, Hansen BJ, Dobrzynski H, Higgins RS, Kilic A, Mohler PJ, Janssen PM, Rosen MR, Biesiadecki BJ, et al. Molecular mapping of sinoatrial node HCN channel expression in the human heart. *Circ Arrhythm Electrophysiol*. 2015;8:1219–1227.
- Csepe TA, Zhao J, Hansen BJ, Li N, Sul LV, Lim P, Wang Y, Simonetti OP, Kilic A, Mohler PJ, et al. Human sinoatrial node structure: 3d microanatomy of sinoatrial conduction pathways. *Prog Biophys Mol Biol*. 2016;120:164–178.
- Li N, Hansen BJ, Csepe TA, Zhao J, Ignozzi AJ, Sul LV, Zakharkin SO, Kalyanasundaram A, Davis JP, Biesiadecki BJ, et al. Redundant and diverse intranodal pacemakers and conduction pathways protect the human sinoatrial node from failure. *Sci Transl Med*. 2017;9:eaam5607.
- Chandler NJ, Greener ID, Tellez JO, Inada S, Musa H, Molenaar P, DiFrancesco D, Baruscotti M, Longhi R, Anderson RH, et al. Molecular architecture of the human sinus node insights into the function of the cardiac pacemaker. *Circulation*. 2009;119:1562–1575.
- Lakatta EG, DiFrancesco D. What keeps us ticking: a funny current, a calcium clock, or both? *J Mol Cell Cardiol*. 2009;47:157–170.
- Griffiths-Jones S, Grocock RJ, van Dongen S, Bateman A, Enright AJ. miRBase: microRNA sequences, targets and gene nomenclature. *Nucleic Acids Res*. 2006;34:D140–D144.
- Filipowicz W, Bhattacharyya SN, Sonenberg N. Mechanisms of post-transcriptional regulation by microRNAs: are the answers in sight? *Nat Rev Genet*. 2008;9:102–114.
- Boettger T, Braun T. A new level of complexity the role of micromRNAs in cardiovascular development. *Circ Res*. 2012;110:1000–1013.
- Romaine SPR, Tomaszewski M, Condorelli G, Samani NJ. MicroRNAs in cardiovascular disease: an introduction for clinicians. *Heart*. 2015;101:921–928.
- Torrente AG, Mesirca P, Neco P, Rizzetto R, Dubel S, Barrere C, Sinegger-Brauns M, Striessnig J, Richard S, Nargeot J, et al. L-type Cav1.3 channels regulate ryanodine receptor-dependent Ca^{2+} release during sino-atrial node pacemaker activity. *Cardiovasc Res*. 2016;109:451–461.
- Thum T, Catalucci D, Bauersachs J. MicroRNAs: novel regulators in cardiac development and disease. *Cardiovasc Res*. 2008;79:562–570.
- Farh KK, Grimson A, Jan C, Lewis BP, Johnston WK, Lim LP, Burge CB, Bartel DP. The widespread impact of mammalian microRNAs on mRNA repression and evolution. *Science*. 2005;310:1817–1821.

14. D'Souza A, Pearman CM, Wang YW, Nakao S, Logantha S, Cox C, Bennett H, Zhang Y, Johnsen AB, Linscheid N, et al. Targeting miR-423-5p reverses exercise training-induced HCN4 channel remodeling and sinus bradycardia. *Circ Res*. 2017;121:1058–1068.
15. Chandler N, Aslanidi OV, Buckley D, Inada S, Birchall S, Atkinson A, Kirk D, Monfredi O, Molenaar P, Anderson R, et al. Computer three-dimensional anatomical reconstruction of the human sinus node and a novel paranodal area. *Anat Rec (Hoboken)*. 2011;294:970–979.
16. Sanchez-Quintana D, Cabrera JA, Farre J, Climent V, Anderson RH, Ho SY. Sinus node revisited in the era of electroanatomical mapping and catheter ablation. *Heart*. 2005;91:189–194.
17. Morris GM, D'Souza A, Dobrzynski H, Lei M, Choudhury M, Billeter R, Kryukova Y, Robinson RB, Kingston PA, Boyett MR. Characterization of a right atrial subsidiary pacemaker and acceleration of the pacing rate by HCN over-expression. *Cardiovasc Res*. 2013;100:160–169.
18. McGahon MK, Yarham JM, Daly A, Guduric-Fuchs J, Ferguson LJ, Simpson DA, Collins A. Distinctive profile of isomir expression and novel microRNAs in rat heart left ventricle. *PLoS One*. 2013;8:e65809.
19. Dobrzynski H, Anderson RH, Atkinson A, Borbas Z, D'Souza A, Fraser JF, Inada S, Logantha SJ, Monfredi O, Morris GM, et al. Structure, function and clinical relevance of the cardiac conduction system, including the atrioventricular ring and outflow tract tissues. *Pharmacol Ther*. 2013;139:260–288.
20. Baruscotti M, Bucchi A, Milanese R, Paina M, Barbuti A, Gneccchi-Ruscione T, Bianco E, Vitali-Serdoz L, Cappato R, DiFrancesco D. A gain-of-function mutation in the cardiac pacemaker HCN4 channel increasing cAMP sensitivity is associated with familial inappropriate sinus tachycardia. *Eur Heart J*. 2017;38:280–288.

SUPPLEMENTAL MATERIAL

Table S1. Human specimen information.

Number	Age	Sex	Cause of death	RNA amount (ng/μl) SN/RA	RNA quality (RIN) SN/RA	Use
1	29	M	Road accident	100.60/231.90	6.1/7.6	qPCR
2	22	M	Road accident	30.98/301.40	8.0/7.7	qPCR
3	66	M	Suicide	47.48/285.70	5.2/4.7	qPCR
4	19	M	Suicide	114.11/389.00	6.4/7.2	qPCR
5	60	M	Sudden death	25.4/123.25	7.2/6.5	qPCR
6	54	M	Intracranial haemorrhage	164.67/400.00	8.3/8.8	qPCR
7	42	M	Subarachnoid haemorrhage	173.65/423.00	8.5/9.1	qPCR
8	19	M	Suicide	114.11/389.00	-	NGS
9	21	M	Suicide	35.3/59.66	-	NGS
10	54	M	Intracranial haemorrhage	45.35/91.77	-	NGS

- data not available but total RNA isolated from samples 8-10 passed their quality for NGS experiments

Table S2. Summary of primary antibodies.

Protein	Company	Catalogue #	Source	Dilution
Cx43	Millipore	MAB3068	Mono - Ms	1:50
HCN4	Alomone	APC-052	Poly - Rbt	1:50
Caveolin3	Transduction	310421	Poly-Ms	1:50

Table S3. Significantly up- or down- regulated miRs in the SN vs. RA. Mean relative miR expression and SEM in SN and RA, fold change and log fold change, and P values shown.

miR	SN mean	SN SEM	RA mean	RA SEM	Fold change	Log fold change	P value
hsa-miR-1-3p	6.00E-02	3.00E-02	2.00E-01	8.00E-02	-1.40E-01	-5.00E-01	3.00E-02
hsa-miR-10a-5p	1.00E-04	2.00E-05	3.00E-05	1.00E-05	3.50E-05	3.60E-01	5.00E-02
hsa-miR-10b-5p	5.00E-02	2.00E-03	1.00E-02	1.00E-03	4.00E-02	8.90E-01	1.00E-03
hsa-miR-10b-3p	1.00E-02	1.00E-02	2.00E-03	2.00E-03	5.34E-03	5.70E-01	1.00E-02
hsa-miR-126-3p	3.41E+00	8.90E-01	7.65E+00	1.31E+00	-4.24E+00	-3.50E-01	4.00E-02
hsa-miR-130b-3p	2.00E-03	1.00E-03	1.00E-02	1.00E-03	-3.00E-03	-4.00E-01	5.00E-02
hsa-miR-130b-5p	3.00E-03	4.00E-04	1.00E-02	1.00E-03	-3.00E-03	-3.20E-01	2.00E-02
hsa-miR-133a-3p	9.25E+00	1.77E+00	5.05E+01	1.13E+01	-4.12E+01	-7.40E-01	1.00E-03
hsa-miR-133b	3.00E-02	8.00E-03	1.62E-01	6.20E-02	-1.30E-01	-7.10E-01	5.36E-02
hsa-miR-139-5p	1.70E-01	3.00E-02	4.40E-01	6.00E-02	-2.70E-01	-4.10E-01	9.00E-03
hsa-miR-148b-3p	3.00E-03	1.00E-03	2.00E-02	1.00E-02	-2.00E-02	-8.90E-01	4.00E-02
hsa-miR-153-3p	2.00E-05	1.00E-05	4.00E-06	3.00E-06	1.00E-05	5.90E-01	5.00E-02
hsa-miR-155-5p	2.00E-02	1.00E-02	4.00E-02	6.00E-03	-2.00E-02	-3.10E-01	5.00E-02
hsa-miR-187-3p	3.00E-03	1.00E-03	4.00E-02	1.00E-02	-4.00E-02	-1.09E+00	1.00E-03
hsa-miR-193b-3p	2.00E-03	4.00E-04	1.00E-03	2.00E-04	1.00E-03	3.40E-01	2.00E-02
hsa-miR-198	1.00E-03	3.00E-04	4.00E-04	3.00E-04	3.00E-04	2.70E-01	4.00E-02
hsa-miR-204-5p	8.10E-01	2.10E-01	1.60E-01	3.00E-02	6.50E-01	7.00E-01	2.00E-03
hsa-miR-210-3p	4.00E-02	1.00E-02	1.30E-01	3.00E-02	-9.00E-02	-5.10E-01	1.00E-02
hsa-miR-215-5p	3.00E-03	1.00E-03	2.00E-04	1.00E-04	3.00E-03	1.23E+00	1.00E-03
hsa-miR-218-5p	2.00E-04	4.00E-05	1.00E-03	2.00E-04	-4.00E-04	-4.40E-01	5.00E-02
hsa-miR-22-3p	1.00E-02	3.00E-03	2.00E-02	2.00E-03	-1.00E-02	-3.70E-01	5.00E-03
hsa-miR-27b-3p	1.00E-02	1.00E-03	1.00E-02	1.00E-03	-6.00E-03	-3.30E-01	6.00E-03
hsa-miR-29b-3p	1.00E-03	3.00E-04	2.00E-03	2.00E-04	-8.00E-04	-3.10E-01	3.00E-02
hsa-miR-30a-3p	2.90E-01	6.00E-02	5.20E-01	7.00E-02	-2.30E-01	-2.60E-01	3.00E-02
hsa-miR-30a-5p	2.40E-01	6.00E-02	5.40E-01	7.00E-02	-3.00E-01	-3.50E-01	2.00E-02
hsa-miR-30b-5p	9.10E-01	2.30E-01	2.35E+00	5.30E-01	-1.43E+00	-4.10E-01	3.00E-02
hsa-miR-30c-5p	1.69E+00	4.30E-01	4.76E+00	1.14E+00	-3.07E+00	-4.50E-01	4.00E-02
hsa-miR-30d-5p	8.00E-02	2.00E-02	1.90E-01	3.00E-02	-1.10E-01	-3.80E-01	1.00E-02
hsa-miR-30e-3p	2.60E-01	6.00E-02	5.20E-01	7.00E-02	-2.60E-01	-3.00E-01	2.00E-02
hsa-miR-342-5p	4.00E-04	2.00E-04	2.00E-03	1.00E-03	-1.00E-03	-5.80E-01	2.00E-02
hsa-miR-363-5p	3.00E-07	1.00E-07	1.00E-05	7.00E-06	-1.00E-05	-1.56E+00	4.00E-02
hsa-miR-371-3p	3.00E-05	1.00E-05	2.00E-04	8.00E-05	-1.00E-04	-7.60E-01	4.00E-02
hsa-miR-372-3p	1.00E-03	3.00E-04	1.00E-02	3.00E-03	-5.00E-03	-9.60E-01	2.00E-02
hsa-miR-373-3p	3.00E-05	2.00E-05	1.00E-04	2.00E-05	-1.00E-04	-4.60E-01	3.00E-03
hsa-miR-377-3p	6.90E-01	1.00E-05	1.47E+00	4.00E-06	-7.80E-01	-3.30E-01	4.00E-02
hsa-miR-377-5p	3.00E-05	5.20E-01	5.00E-06	5.40E-01	2.00E-05	7.60E-01	4.00E-02
hsa-miR-378a-3p	3.00E-02	1.00E-02	6.00E-02	1.00E-02	-3.00E-02	-3.40E-01	2.00E-02
hsa-miR-378a-5p	4.00E-04	1.00E-04	1.00E-03	1.00E-04	-3.00E-04	-2.60E-01	5.00E-02
hsa-miR-422a	3.00E-03	1.00E-03	1.00E-02	2.00E-03	-5.00E-03	-4.40E-01	2.00E-02
hsa-miR-424-5p	1.00E-03	3.00E-04	3.00E-03	1.00E-03	-2.00E-03	-3.90E-01	3.00E-02
hsa-miR-429	2.00E-04	2.00E-04	2.00E-03	1.00E-03	-2.00E-03	-9.10E-01	4.00E-02

miR	SN mean	SN SEM	RA mean	RA SEM	Fold change	Log fold change	P value
hsa-miR-450b-5p	1.00E-04	1.00E-04	3.00E-04	1.00E-04	-1.00E-04	-3.60E-01	4.00E-02
hsa-miR-483-3p	1.40E-02	4.00E-03	5.00E-02	1.00E-02	-3.00E-02	-5.10E-01	4.00E-03
hsa-miR-486	6.00E-03	2.00E-03	1.00E-02	2.00E-03	-7.00E-03	-3.30E-01	5.00E-02
hsa-miR-486-3p	3.00E-04	1.00E-04	1.00E-03	3.00E-04	-8.00E-04	-5.70E-01	1.00E-02
hsa-miR-490-3p	9.00E-04	2.00E-04	1.00E-02	1.00E-03	-4.00E-03	-7.60E-01	4.00E-02
hsa-miR-512-5p	1.83E+01	1.16E+01	1.00E-05	9.00E-06	1.83E+01	6.10E+00	3.00E-02
hsa-miR-515-3p	3.00E-07	1.00E-07	3.00E-06	2.00E-06	-3.00E-06	-9.70E-01	4.00E-02
hsa-miR-520d-3p	9.00E-05	4.00E-05	2.00E-04	3.00E-05	-8.00E-05	-2.70E-01	5.00E-02
hsa-miR-520g-3p	6.00E-06	1.00E-05	0.00E+00	2.00E-05	-3.00E-05	-8.40E-01	5.00E-02
hsa-miR-524-3p	5.00E-06	2.00E-06	4.00E-04	2.00E-04	-4.00E-04	-1.95E+00	4.00E-02
hsa-miR-548b-5p	1.00E-04	1.00E-04	1.00E-04	6.00E-05	6.00E-05	2.80E-01	4.00E-02
hsa-miR-548k	2.00E-06	1.00E-06	0.00E+00	8.00E-08	2.00E-06	7.20E-01	5.00E-02
hsa-miR-571	8.00E-05	2.00E-05	4.00E-04	2.00E-04	-3.00E-04	-6.60E-01	3.00E-02
hsa-miR-584-5p	6.00E-04	1.00E-04	1.00E-03	1.00E-04	-5.00E-04	-2.70E-01	4.00E-02
hsa-miR-616-5p	2.00E-04	4.00E-05	3.00E-04	4.00E-05	-1.00E-04	-2.60E-01	4.00E-02
hsa-miR-628-3p	3.00E-03	1.00E-03	5.00E-03	1.00E-03	-2.00E-03	-2.70E-01	4.00E-02
hsa-miR-642a-5p	3.00E-03	1.00E-03	3.00E-02	1.00E-02	-2.00E-02	-1.00E+00	4.00E-04
hsa-miR-651-5p	2.00E-05	1.00E-05	4.00E-05	9.00E-06	-2.00E-05	-3.70E-01	4.00E-02
hsa-miR-654-5p	1.00E-04	1.00E-04	4.00E-07	6.00E-08	1.00E-04	2.48E+00	3.00E-02
hsa-miR-668-3p	5.00E-05	2.00E-05	4.00E-07	8.00E-08	5.00E-05	2.11E+00	3.00E-02
hsa-miR-885-3p	1.00E-03	1.00E-03	4.00E-07	7.00E-08	1.00E-03	3.45E+00	2.00E-02
hsa-miR-938	2.00E-06	1.00E-06	1.00E-05	1.00E-06	-1.00E-05	-6.60E-01	3.00E-03
hsa-miR-1225-3p	3.00E-02	1.00E-02	1.00E-02	1.00E-02	1.00E-02	3.10E-01	3.00E-02
hsa-miR-1233-3p	5.00E-04	5.00E-04	5.38E+00	4.35E+00	-5.38E+00	-4.05E+00	3.00E-02
hsa-miR-1244-3p	3.00E-04	1.00E-04	1.00E-04	4.00E-05	2.09E-04	4.50E-01	1.00E-02

miRs with significant higher expression in SN highlighted in bold.

CHAPTER 7) GENERAL DISCUSSIONS, CONCLUSIONS, LIMITATIONS, FUTURE WORK, AND LIST OF PUBLICATIONS

There are five parts to this chapter. The first summarises the main discussions, the second summarises the main conclusions, and the third summarises the limitations of this dissertation. The next section provides directions for future research, and the final section provides a list of publications at the time of this thesis submission.

7.1 Discussion

Micro-CT is being used to optimise cardiac devices. In patient-specific studies, micro-CT is used to predict post-TAVI aortic regurgitation (a common post-TAVI risk) [112] and improve the position accuracy of the left atrial pressure sensor device [113] in aged and diseased human hearts. However, the studies mentioned did not use contrast agents and were of lower resolution. The contrast-enhanced micro-CT data collected from healthy, aged, and obese cardiac tissue presented in this thesis provides high-resolution insights into the anatomical structures and variation of valves in these three heart groups. Thus, it can contribute to the further improvement of the devices used to treat cardiac dysfunctions.

The anatomical reconstructions and novel imaging techniques reported in this thesis can aid in developing computational models and biophysical simulations of aged and diseased hearts. This can contribute to further understanding, diagnosis, and treatment of CVDs such as cardiac arrhythmia, hypertrophy, and fibrosis.

Anatomical observations are a result of underlying molecular mechanisms. Ageing is correlated with an increase in cardiac fibrosis and loss of nodal cells (as observed in Figure 12Aii in Paper 1, Chapter 3), and extensive fibrosis is a structural remodelling resulting from increased myofibroblast activity. It can lead to dysfunction of the SN, heart failure and death [114, 115]. The loss of nodal myocytes could suggest the loss of pacemaking ion channels (e.g., HCN4) and immune cell markers (e.g., TPSAB1). Different cells and molecules are involved in the development of myocardial fibrosis. In the development of cardiac fibrosis, myofibroblasts are recruited and activated to express ECM-related genes that synthesise collagen 1 – amongst other types of collagens [101]. As mentioned in Paper 2, Chapter 4, COL1A1 (a marker for collagen 1) is more expressed in the healthy SN than in the right atrium.

It has been reported that the increased production of collagen 1 during fibrosis leads to rigid myocardial walls and increased wall tension [116]. With collagen deposition increasing with age and subsequently leading to reduced diastolic function, we know that the structural remodelling caused by cardiac fibrosis in the aged heart results from underlying molecular remodelling. Hence, exploring the interaction pathways of cardiac molecules (such as COL1A1) can enhance our anatomical observations and understanding – and perhaps identify molecular targets for potential drug therapies. Does this raise the question: “can the

introduction of key microRNAs reverse fibrosis”? Table 1 in Paper 2, Chapter 4 showed that COL1A1 is a predicted target for miR-30c-5p and miR-133a-3p. I assume that the increase in the expression of COL1A1 in the SN region during fibrosis means a decrease in the expression of miR-30c-5p. So, the introduction of miR-30c-5p or miR-133a-3p could subsequently reduce the expression of COL1A1 and, therefore ‘reverse’ the development of fibrosis or stop the further loss of SN myocytes. As mentioned previously, Yanni et al. injected a miR-370 anti-miR into heart failure mice to restore the expression of HCN4 in the SN [69] and Petkova et al. injected miR-486-3p into healthy rat tissue to reduce HCN4 expression and thus reduced heart rate [44].

Cardiac hypertrophy – particularly ventricular hypertrophy – is a pathological response to various stimuli such as volume and pressure overload and prolonged cardiac hypertrophy can result in heart failure or eventually cardiac arrest. The heart of the obese individual used in my project was hypertrophic due to its thick ventricular walls and large atrial and ventricular cavities (Figures 1, 2, 5C, 6Ci, 6Cii from Chapter 3). Apart from increased fibrosis, a common feature of cardiac hypertrophy is the activation of inflammatory signalling and immune cells, encouraging inflammation [117, 118]. Inflammatory cytokines such as tumour necrosis factor alpha (TNF- α) are upregulated during cardiac hypertrophy and heart failure [119, 120]. A study by Bozkurt et al. 1998 showed that the continuous infusion of TNF- α into the peritoneal cavity of rats resulted in cardiac dysfunction [121]. This could be reversed through treatment with a TNF- α antagonist [121]. Another study by Sun et al. 2007 showed that the knockout of TNF- α in mice reduced fibrosis, hypertrophy and cardiac dysfunction [122]. Even though the inhibition of TNF- α reduces/reverses cardiac hypertrophy and dysfunction in animal studies, this was not observed in clinical studies of patients with chronic heart failure [123, 124]. Therefore, new molecular targets are required.

In Paper 2, Chapter 4, I show that immune cell markers (i.e., TPSAB1, a mast cell marker; CD209, a macrophage cell marker; and HLAs, human leukocyte antigen markers) are more expressed in the SN, compared to the right atrium, and are predicted to be inhibited by miR-486-3p - thus confirming their importance in maintaining the healthy SN’s function. When miR-486-3p was introduced in H9C2 cells, the expression of TPSAB1 was significantly downregulated (Figure 5, Paper 2, Chapter 5). The fact that an immune response is induced

during the development of cardiac hypertrophy makes these markers (particularly TPSAB1) potential therapeutical targets in treating this structural abnormality.

The number of electronic cardiac pacemaker implantations is increasing; however, they are still significantly limited regarding clinical applications. The challenges of electronic pacemakers involve lead failure/repositioning, electronic interference, and relatively short battery life [125]. In addition, other cardiac dysfunctions (such as congenital heart block) cannot be treated using electronic pacemakers and require other non-device approaches. Therefore, biological pacemakers could be a favourable therapeutic alternative. A gene- and cell-based approach for the generation of biological pacemakers is currently being studied.

The gene-based approach relies on the delivery/overexpression of ion channel-encoding genes or other proteins through viral or non-viral techniques. The delivery of ion channel encoding genes (e.g., HCN ion channels), microRNAs (e.g., miR-486-3p and miR-938) or other proteins into the SN for biopacemaking can be used in the treatment of SN dysfunctions and subsequently, heart failure. In 2013, Morris et al. carried out an adenovirus-mediated gene transfer of HCN2 and HCN212, which increased SN pacemaking rate [126]. In 2017, D'Souza et al. showed that the introduction of the anti-miR-423-5p reversed bradycardia through the restoration of HCN4 [127]. In 2020, Yanni et al. showed that the injection of anti-miR-370-3p in mice models of heart failure with sinus bradycardia led to the restoration of HCN4 [69]. Additionally, Petkova et al. injected miR-486-3p in the SN tissue of a healthy rat and observed a reduction in heart rate due to HCN4 downregulation. All these studies show that the regulation of specific microRNAs make them potential pharmacological targets in treating SN dysfunction.

The cell-based approach relies on sinus nodal cells or pluripotent stem cells (PSCs) and induced PSCs (iPSCs)-derived cardiomyocytes. Lin et al. injected human sinus nodal cells (mixed with atrial cells) into the left ventricles of pigs and observed functional junctions and pacemaker activity [128]. Zhang et al. injected sinus nodal cells into the myocardial wall of the right ventricle in a canine model of complete heart block with electronic pacemaker implantation and observed preserved electrical activity [129]. Some research groups have observed biological pacemaker ability *in vitro* and *in vivo* after transplanting hiPSCs-derived cardiomyocytes into animal hearts [130, 131]. Others have derived SN-like cells from the

cardiac differentiation and pacemaker specification of hiPSCs [132-134]. Results from Chapter 4 show the downregulation of key mRNAs and an immune cell marker by key microRNAs in H9C2 (rat myoblast cell line). It would be interesting to confirm these observations in SAN-like cells derived from hiPSCs.

While this PhD project has identified miRNAs as potential novel therapeutic targets, using miRNAs as therapeutic targets are met with some difficulties. A single miRNA can be predicted to target tens to hundreds of genes, as mentioned earlier in the introduction chapter [49]. Another challenge is that miRNAs are prone to non-specifically binding to blood proteins, consequently reducing their urinary clearance [135]. Therefore, it is almost impossible to specifically inject miRNAs into the SN because these miRNAs could have off-target effects in the surrounding atria or ventricles. This is a challenge that further research is required to overcome.

As mentioned in the limitations section of Chapter 5, H9C2 rat cells do not contain the biological machinery to process the human miRNAs and mRNAs that were transfected into them. Therefore, it would be ideal to out these experimental verifications in human cardiomyocytes such as hiPSCs. Following the transfection of these molecules into stem cells, the cells can then be transferred into aged or diseased cardiac tissue.

The expression profile of miRNAs that are up-regulated or down-regulated in the healthy human SN is presented in this thesis (Paper 2, Chapter 4). This can be used to treat cardiac dysfunction – particularly CCS dysfunction. Ageing is a common risk factor of heart failure, and the dysfunction of the SN positively correlates with the development of heart failure. A 2021 study by Li et al. on human heart failure hearts showed the expression profile of key microRNAs (such as miR-486-3p, miR-133a-3p, and miR-1-3p) are significantly upregulated in the SN during heart failure [136]. These significantly upregulated miRNAs were predicted to inhibit ion channels that regulate SN automaticity (such as HCN1 and HCN4) [136]. This observation provides insight into the CCS remodelling and abnormal SN automaticity observed during heart failure in humans.

7.2 Conclusions

To conclude, this PhD project has shown how various methods such as contrast-enhanced micro-CT imaging; 3D reconstruction, NGS for RNA-seq; and luciferase assay experiments can be used to further understand anatomical and molecular mapping of the human CCS.

The current understanding of the various anatomical structures (such as the CCS, aortic and pulmonary trunk, and coronary arteries) and their structural variations in aged and obese hearts is currently limited. The results presented in this thesis show the useful applications of GO – a novel contrast agent and I₂KI for micro-CT imaging. This has the potential to improve the current treatments for cardiovascular diseases, such as the implantation of electronic pacemakers, ablation, and TAVI procedures. The data obtained can also aid in developing computational/mathematical models of aged and diseased hearts.

With electronic pacemakers costing the National Health Service approximately £75.6 million annually [137] and the device sometimes failing after implantation in patients, it is important to identify alternative therapies for treating cardiac arrhythmias. The molecular mechanisms responsible for the SN's pacemaking function is incredibly complicated. The results from this PhD project shed some light on this complex mechanism. I have shown that, uniquely, there is a high abundance of immune cell markers in the SN, compared to the surrounding atrial tissue – providing further explanation for why the development of biological pacemakers is very difficult. By identifying 'novel' TFs and markers as targets for key microRNAs, I have presented potential therapeutic targets and biopacemakers for treating SN disease – a prevalent disease in our increasingly ageing population.

Results from luciferase assay experiments suggest an interaction between miR-486-3p and three key mRNAs (Ca_v1.3, Ca_v3.1, and TPSAB1) and between miR-938 and the Ca_v1.3 mRNA. Again, these are presented as potential therapeutic targets in the treatment of SND.

Essentially, the results obtained from this project allow us to appreciate the intricate complexity of the whole heart – particularly the SN. Doing so provides further understanding of cardiac anatomical variations in aged and diseased situations and insights into alternative treatments of cardiovascular diseases, potentially reducing health care costs, cardiac morbidities, and patient death rate.

7.3 Limitations

Limitations specific to each study are provided in each of the previous chapters. However, further general limitations are mentioned below.

During the first lockdown of 2020, laboratory work was suspended as access to the University was prohibited for approximately eight months. As a result, I could not carry out experiments such as luciferase assay and qPCR. In addition, further micro-CT scanning of tissue samples could not occur, and I could not analyse previous micro-CT images because I had no access to the computers in the University that had the Amira v6.5 software. Therefore, during the eight months, I primarily focused on the bioinformatics aspect of my PhD project (as I had the software downloaded on my laptop) – allowing me to analyse the NGS for RNA-seq dataset and use IPA to carry out various studies. Furthermore, the funding for this project was exhausted – further preventing the possibility of further experimental validations.

As mentioned in Chapter 3, it was difficult to categorically segment the SN and AVN region within the aged and obese right atrium tissue blocks. This was because the attenuation difference between these regions and the surrounding atrial tissue was not as distinct as within the healthy/normal tissue blocks.

Cardiac glycogen is an important source of glucose for the myocardium's high energy demand. Therefore, glycogen is more localised in the working myocardium compared to the CCS. I₂KI has a high binding capacity for glycogen and accumulates in regions of high glycogen content [138]. Because of the working myocardium's high attenuation of I₂KI, the atrial tissue appears lighter grey in 2D ortho slices. Because of the SN and AV region's low attenuation of I₂KI, this region appears darker grey in 2D ortho slices.

Low glycogen content and reduced glycolysis process are associated with increased cardiac hypertrophy and fibrosis [139, 140]. The aged specimen used for this project was fibrotic, and the obese specimen was hypertrophied. Therefore, the nodal regions of these specimens contained much less-than-normal glycogen content. This explains why these regions in the aged and obese specimens appeared very dark and difficult to distinguish from the surrounding tissue confidently.

It would be ideal to analyse at least n=3 hearts from each group (normal, aged, and obese) to properly investigate and compare anatomical variations and draw more confident

conclusions. However, at the time of this project, only 5 specimens were available, as *ex-vivo* human hearts are very challenging to obtain.

7.4 Future work

The Dobrzynski laboratory has obtained more normal, aged, and obese human heart samples – colleagues in the laboratory are conducting various analyses on these samples to draw more robust conclusions. This also allows for semi-quantitative and statistical analysis of the 3 different heart groups.

***In vivo* morphological analysis of aged hearts and obese hearts**

The hearts used for micro-CT analysis were *ex-vivo*. It would be interesting and ideal to determine if the reported findings (e.g., loss of nodal cells and increased epicardial fat) are observed and are reproducible *in-vivo* in ageing patients and obese patients. Another thing to explore in the future is how the loss of nodal cells observed in aged and obese heart tissues (Figure 11, 12, Chapter 3) leads to reduced heart rate because of slowed/reduced conduction. The risk of thromboembolism and the long-term stability of artificial heart valves remains an issue. Therefore, in the future, the anatomical variations of the myocardial walls and valves in the normal, aged, and obese hearts reported in this thesis can improve the current design of artificial valves. This can enhance the variability in artificial valve designs to accommodate the hearts of aged patients and obese patients.

NGS for RNA-seq on aged nodal and atrial tissues

For the project reported in this thesis, NGS for RNA-seq was performed on 3 healthy SN and 3 healthy RA samples. More healthy samples would be used to carry out statistical analysis and make more comparisons. With an increasingly ageing population, NGS for RNA-seq would also be performed on aged SN and RA samples. This will allow the comparison of mRNAs, miRNAs, TFs, and immune cell markers expression profiles in healthy/young samples vs aged samples. In the project documented in this thesis, the expression of key molecules was studied at the messenger level. The next steps would be to study the expression of these molecules at the protein level using proteomics.

Further validation of luciferase assay experiments

It would be useful to analyse if the miRNA and markers expression observed in H9C2 cells is also observed in SAN-like cells derived from hiPSCs. This could be done by transfecting key molecules (such as miR-486-3p, miR-938, Cav1.3, Cav3.1, and TPSAB1), as previously shown by Müller et al. where they introduced ISL1 and MYH6 to pluripotent stem cells to cause an increase in HCN4 expression [132].

To further validate the results obtained from luciferase assay experiments, qPCR experiments will be performed.

Testing microRNAs for gene-based biopacemaking

As mentioned in the Discussion, studies show that the regulation of specific microRNAs makes them potential pharmacological targets in treating SN dysfunction. I also mentioned that an immune response is activated during cardiac hypertrophy. This PhD project identified TPSAB1 (a mast cell marker) as a target for miR-486-3p. Therefore, further studies could be conducted that involve the introduction of the TPSAB1-encoding gene into hypertrophied hearts or into cardiac tissue of COVID-19 patients to restore the normal functioning of immune cells in the SN, and therefore restore normal pacemaking function.

7.5 List of publications

The following are the papers published, as the first author, at the time of the thesis submission:

- **Aminu, A. J.**, Chen, W., Yin, Z., Kuniewicz, M., Walocha, J., Perde, F., Molenaar, P., laizzo, P. A., Dobrzynski, H., Atkinson., *Novel micro-computed tomography contrast agents to visualise the human cardiac conduction system and surrounding structures in hearts from normal, aged, and obese individuals*. TRIA. 2022. **27**: p. 100175. (<https://doi.org/10.1016/j.tria.2022.100175>).
- **Aminu, A. J.**, Petkova, M., Atkinson, A. J., Yanni, J., Morris, A. D., Simms, R. T., Chen, W., Yin, Z., Kuniewicz, M., Holda, M. K., Kuzmin, V. S., Perde, F., Molenaar, P., Dobrzynski, H., *Further insights into the molecular complexity of the human sinus*

node – the role of ‘novel’ transcription factors and microRNAs. Prog. Biophys. Mol. Biol. 2021. **166**: p. 86-104. (<https://doi.org/10.1016/j.pbiomolbio.2021.04.008>).

- **Aminu, A. J.**, Petkova, M., Chen, W. C., Yin, Z., Kuzmin, V. S., Atkinson, A. J., Dobrzynski, H., *MiR-486-3p and miR-938-important inhibitors of pacemaking ion channels and/or markers of immune cells.* Prog. Biophys. Appl. Sci., 2021. **11**: p. 11366. (<https://doi.org/10.3390/app112311366>).

The following are the papers published, as a co-author, at the time of the thesis submission:

- Petkova, M. P., Atkinson, A. J., Yanni, J., Stuart, L., **Aminu, A. J.**, Ivanova, A. D., Pustovit, K. B., Geragthy, C., Feather, A., Li, N., Zhang, Y., Oceandy, D., Perde, F., Molenaar, P., D’Souza, A., Fedorov, V. V., Dobrzynski, H. 2020. **9**: p. e016590. (<https://doi.org/10.1161/JAHA.120.016590>)
- Kuzmin, V. S., Malykhina, I. A., Pustovit, K. B., Ivanova, A. D., Kuniewicz, M., Walocha, J., Atkinson, A., **Aminu, A. J.**, Dobrzynski, H., *Inflammatory degranulation of the cardiac resident mast cells suppresses the pacemaking and affects activation pattern in the sinoatrial node.* TRIA. 2022. **26**: p. 100170. (<https://doi.org/10.1016/j.tria.2022.100170>).

The following are presentations delivered (both oral and poster) at the time of the thesis submission:

- Further insights into the molecular complexity of the human sinus node – the role of ‘novel’ transcription factors and microRNAs. *Northern Cardiovascular Research Group Meeting, Leeds.* 2021. (Oral presentation).
- Identifications of key transcription factors in the adult human sinus node. *Life Sciences: Post-Translational Modifications and Cell Signalling Conference, Nottingham.* 2019. (Oral and poster presentations).
- Identifications of key transcription factors in the adult human sinus node. *Northern Cardiovascular Research Group Meeting, Leeds.* 2019. (Poster presentation).
- The anatomical and molecular mapping of the human cardiac conduction system – advancing our knowledge and treatment of cardiovascular disease. *Seminar session at University of Lagos, Nigeria.* 2019. (Oral presentation).

- The anatomical and molecular mapping of the human cardiac conduction system – advancing our knowledge and treatment of cardiovascular disease. *Seminar session at Federal University of Technology, Akure, Nigeria. 2019. (Oral presentation).*

References

1. BHF. *UK Factsheet*. 2021 [2nd December 2021]; Available from: <https://www.bhf.org.uk/-/media/files/research/heart-statistics/bhf-cvd-statistics-uk-factsheet.pdf?la=en&rev=5a5bd97afcd140ccb37564b8818168f5&hash=049B98DC2A875F6DD6CE33A203582FEE9E161BD3>.
2. UN, *Department of Economic and Social Affairs, Population Division (2019)*. in *World Population Ageing 2019: Highlights (ST/ESA/SER.A/430)* 2019.
3. Kenchaiah, S., et al., *Obesity and the risk of heart failure*. *N Engl J Med.*, 2002. **347**: p. 305-313.
4. Novo, G., et al., *The role of the renin-angiotensin system in atrial fibrillation and the therapeutic effects of ACE-Is and ARBS*. *Br J Clin Pharmacol.*, 2008. **66**: p. 345-351.
5. Abel, E.D., S.E. Litwin, and G. Sweeney, *Cardiac remodeling in obesity*. *Physiol Rev.*, 2008. **88**: p. 389-419.
6. Seidman, G.J. and C. Seidman, *The genetic basis for cardiomyopathy: from mutation identification to mechanistic paradigms*. *Cell*, 2001. **104**: p. 557-567.
7. Stephenson, S.R., et al., *High resolution 3-dimensional imaging of the human cardiac conduction system from microanatomy to mathematical modeling*. *Sci Rep.*, 2017. **7**: p. 1-13.
8. Boyett, R.M., 'And the beat goes on' *The cardiac conduction system: the wiring system of the heart*. *Exp Physiol*, 2009. **94**: p. 1035-1049.
9. Sanchez-Qunitana, D. and H.S. Yen, *Anatomy of cardiac nodes and atrioventricular specialized conduction system*. *Rev Esp Cardiol. (English Version)*, 2003. **56**: p. 1085-1092.
10. Yiu, K.H. and H.F. Tse, *Hypertension and cardiac arrhythmias: a review of the epidemiology, pathophysiology and clinical implications*. *J Hum Hypertens.*, 2008. **22**: p. 380-388.
11. Roh, J., et al., *The role of exercise in cardiac aging*. *Circ Res.*, 2016. **118**: p. 279-295.
12. Song, Y., et al., *Age-related variation in the interstitial tissues of the cardiac conduction system; and autopsy study of 230 Han Chinese*. *Forensic Sci Int.*, 1999. **104**: p. 133-142.
13. Logantha, S.J.R.J., et al., *Remodeling of the purkinje network in congestive heart failure in the rabbit*. *Circulation: Heart Failure*, 2021. **14**: p. e007505.
14. Zhang, H., et al., *Mathematical models of action potentials in the periphery and center of the rabbit sinoatrial node*. *Am J Physiol.*, 2000. **279**: p. 397-421.
15. Stephenson, S.R., et al., *Contrast enhanced micro-computed tomography resolves the 3-dimensional morphology of the cardiac conduction system in mammalian hearts*. *PLoS One*, 2012. **7**: p. e35299.
16. Schram, G., et al., *Differential distribution of cardiac ion channel expression as a basis for regional specialization in electrical function*. *Circ Res.*, 2002. **90**: p. 939-950.
17. Ben, C., E., et al., *Role of subendocardial Purkinje network in triggering torsade de pointes arrhythmia in experimental long QT syndrome*. *Eurospace*, 2008. **10**: p. 1218-1223.
18. Keith, A. and M. Flack, *The form and nature of the muscular connections between the primary divisions of the vertebrate heart*. *J Anat Physiol.*, 1907. **41**: p. 172-189.
19. Chandler, J.N., et al., *Molecular architecture of the human sinus node insights into the function of the cardiac pacemaker*. *Circulation*, 2009. **119**: p. 1562-1575.
20. Dobrzynski, H., et al., *Structure, function and clinical relevance of the cardiac conduction system, including the atrioventricular ring and outflow tract tissues*. *Pharmacol Therapeut.*, 2013. **139**: p. 260-288.
21. Csepe, T.A., et al., *Fibrosis: a structural modulator of sinoatrial node physiology and dysfunction*. *Front Physiol*, 2015. **6**: p. 37.

22. Abbara, S., et al., *Mapping epicardial fat with multi-detector computed tomography to facilitate percutaneous transeptal arrhythmia ablation*. Eur J Radiol., 2006. **57**: p. 417-422.
23. Brown, H.F., D. Difrancesco, and S.J. Noble, *How does adrenaline accelerate the heart?*. Nature, 1979. **280**: p. 235-236.
24. Baruscotti, M., A. Bucchi, and D. Difrancesco, *Physiology and pharmacology of the cardiac pacemaker ("funny") current*. Pharmacol Ther, 2005. **107**: p. 59-79.
25. Bartos, C.D., E. Grandi, and M.C. Ripplinger, *Ion channels in the heart*. Compr. Physiol., 2015. **5**: p. 1423-1464.
26. Miake, J., E. Marban, and H.B. Nuss, *Biological pacemaker created by gene transfer*. Nature, 2002. **419**: p. 132-133.
27. Joung, B., P.-S. Chen, and S.-F. Lin, *The role of the calcium and the voltage clocks in sinoatrial node dysfunction*. Yonsei Med J., 2011. **52**: p. 211-219.
28. Latchman, D.S., *Transcription factors: an overview*. Int J Biochem Cell Biol., 1997. **29**: p. 1305-1312.
29. Sun, Y.F., X.Q. Liang, and S.M. Evans, *Islet1 progenitors in developing and postnatal heart*. Cardiovascular Development, 2008. **18**: p. 153-165.
30. Sun, Y.F., et al., *Islet 1 is expressed in distinct cardiovascular lineages, including pacemaker and coronary vascular cells*. Developmental Biology, 2007. **304**: p. 286-296.
31. Wilson, V. and L.F. Conlon, *The T-box family*. Genome Biol., 2002. **3**: p. 3008.1-3008.7.
32. Aminu, A.J., et al., *Further insights into the molecular complexity of the human sinus node - The role of 'novel' transcription factors and microRNAs*. Prog. Biophys. Mol. Biol., 2021. **21**: p. 1-19.
33. Harrelson, Z., et al., *Tbx2 is essential for patterning the atrioventricular canal and for morphogenesis of the outflow tract during heart development*. Development, 2004. **131**: p. 5041-5052.
34. Singh, R., et al., *Tbx2 and Tbx3 induce atrioventricular myocardial development and endocardial cushion formation*. Cell Mol Life Sci., 2012. **69**: p. 1377-1389.
35. Banerjee-Basu, S. and A.D. Baxevanis, *Molecular evolution of the homeodomain family of transcription factors*. Nucleic Acid Res., 2001. **29**: p. 3258-3269.
36. Park, D.S. and G.L. Fishman, *Development and function of the cardiac conduction system in health and disease*. J Cardiovasc Dev Dis., 2017. **2017**.
37. Lyons, I., et al., *Myogenic and morphogenetic defects in the heart tubes of murine embryos lacking the homeo box gene Nkx2-5*. Genes Dev, 1995. **9**: p. 1654-1666.
38. Tanaka, M., et al., *The cardiac homeobox gene Csx/Nkx2.5 lies genetically upstream of multiple genes essential for heart development*. Development, 1999. **126**: p. 1269-1280.
39. Vedentham, V., et al., *RNA sequencing of mouse sinoatrial node reveals an upstream regulatory role for Islet-1 in cardiac pacemaker cells*. Circ Res., 2015. **116**: p. 797-803.
40. Liang, X., et al., *Transcription factor ISL1 is essential for pacemaker development and function*. J Clin Invest., 2015. **125**: p. 3256-3268.
41. Espinoza-Lewis, R.A., et al., *Shox2 is essential for the differentiation of cardiac pacemaker cells by repressing Nkx2-5*. Dev Biol., 327. **327**: p. 376-385.
42. Kharche, R.S., et al., *Computational assessment of the functional role of sinoatrial node exit pathways in the human heart*. PLoS One, 2017. **12**: p. e0183727.
43. Maisch, B. and A.D. Risti ć, *Immunological basis of the cardiac conduction and rhythm disorders*. Eur Heart J., 2001. **22**: p. 813-824.
44. Petkova, M., et al., *Identification of key small non-coding microRNAs controlling pacemaker mechanisms in the human sinus node*. J Am Heart Assoc., 2020. **9**: p. e016590.
45. Pasquinelli, A.E., et al., *Conservation of the sequence and temporal expression of let-7 heterochronic regulatory RNA*. Nature, 2000. **408**: p. 86-89.

46. Davis-Dusenbery, B.N. and A. Hata, *Mechanisms of control of microRNA biogenesis*. J Biochem., 2010. **148**: p. 381-392.
47. Mukai, N., et al., *Potential contribution of erythrocyte microRNA to secondary erythrocytosis and thrombocytopenia in congenital heart*. Pediatr. Res., 2018. **83**: p. 865-873.
48. Thum, T., et al., *MicroRNAs in the human heart: a clue to fetal gene reprogramming in heart failure*. Circulation, 2007. **17**: p. 258-267.
49. van Rooij, E., *The art of microRNA research*. Circ Res., 2011. **108**: p. 219-234.
50. Brummer, A. and J. Hausser, *MicroRNA binding sites in the coding region of mRNAs: extending the repertoire of post-transcriptional gene regulation*. Bioessays., 2014. **36**: p. 617-626.
51. Pillai, R.S., C.G. Artus, and W. Filipowicz, *Tethering of human Ago proteins to RNA mimics the miRNA-mediated repression of protein synthesis*. RNA, 2004. **10**: p. 1518-1525.
52. Geary, R.S., et al., *Pharmacokinetics, biodistribution and cell uptake of antisense oligonucleotides*. Adv Drug Deliv Rev., 2015. **87**: p. 46-51.
53. Dhuri, K., et al., *Therapeutic potential of chemically modified, synthetic, triplex peptide nucleic acid-based oncomir inhibitors for cancer therapy*. Cancer Res, 2021. **81**: p. 5613-5624.
54. Elmen, J., et al., *LNA-mediated microRNA silencing in non-human primates*. Nature, 2008. **452**: p. 896-899.
55. Zhao, Y., et al., *Dysregulation of cardiogenesis, cardiac conduction, and cell cycle in mice lacking miRNA-1-2*. Cell, 2007. **129**: p. 303-317.
56. Zhao, Y., S. E., and D. Srivastava, *Serum response factor regulates a muscle-specific microRNA that targets Hand2 during cardiogenesis*. Nature, 2005. **436**: p. 214-220.
57. van Rooij, E., et al., *Control of stress-dependent cardiac growth and gene expression by a microRNA*. Science, 2007. **316**: p. 575-579.
58. Chen, J.-F., et al., *The role of microRNA-1 and microRNA-133 in skeletal muscle proliferation and differentiation*. Nat Genet., 2006. **38**: p. 228-233.
59. Cordes, R.K. and D. Srivastava, *MircoRNA regulation of cardiovascular development*. Circ Res., 2009. **104**: p. 724-732.
60. Liu, N. and E.N. Olson, *MicroRNA regulatory networks in cardiovascular development*. Dev Cell, 2010. **18**: p. 510-525.
61. Porrello, E.R., *MicroRNAs in cardiac development and regeneration*. Clin Sci., 2013. **125**: p. 151-166.
62. Wojciechowska, A., A. Braniewska, and K. Kozar-Kaminska, *MicroRNA in cardiovascular biology and disease*. Adv Clin Exp Med., 2017. **26**: p. 865-874.
63. Tritsch, E., et al., *An SRF/miR-1 axis regulates NCX1 and annexin A5 protein levels in the normal and failing heart*. Cardiovasc Res., 2013. **98**: p. 372-380.
64. Smith, T., et al., *MicroRNAs in congenital heart disease*. Ann Transl Med., 2015. **3**: p. 333.
65. Wang, G.-K., et al., *Circulating microRNA: a novel potential biomarker for early diagnosis of acute myocardial infarction in humans*. Eur Heart J., 2010. **31**: p. 659-666.
66. Sun, T., et al., *The role of microRNAs in myocardial infarction: from molecular mechanism to clinical application*. Int J Mol Sci., 2017. **18**: p. 745.
67. Car è, A., et al., *MicroRNA-133 controls cardiac hypertrophy*. Nat Med., 2007. **13**: p. 613-618.
68. Lu, Y., et al., *MicroRNA-328 contributes to adverse electrical remodeling in atrial fibrillation*. Circulation, 2010. **122**: p. 2378-2387.
69. Yanni, J., et al., *Silencing miR-370-3p rescues funny current and sinus node function in heart failure*. Sci Rep., 2020. **10**: p. 1-23.
70. Hindso, L., et al., *Normal values of regional left ventricular myocardial thickness, mass and distribution-assessed by 320-detector computed tomography angiography in the Copenhagen General Population Study*. Int J Cardiovasc Imaging, 2017. **33**: p. 421-429.
71. Badea, T.C., et al., *Left ventricle measurements in cardiac micro-CT*. Comput Med Imaging Graph., 2008. **32**: p. 239-250.

72. Kawel, N., et al., *Normal left ventricular myocardial thickness for middle aged and older subjects with SSFP cardiac MR: The Multi-Ethnic Study of Atherosclerosis*. *Circ Cardiovasc Imaging*, 2012. **5**: p. 500-508.
73. Kou, S., et al., *Echocardiographic reference ranges for normal cardiac chamber size: results from the NORRE study*. *Eur Heart J Cardiovasc Imaging*, 2014. **15**: p. 680-690.
74. Leibowitz, D., et al., *Measurement of wall thickness alone does not accurately assess the presence of left ventricle hypertrophy*. *Clin Exp Hypertens*, 2006. **29**: p. 119-125.
75. Rodrigues, L.C.J., et al., *The relationship between left ventricular wall thickness, myocardial shortening, and ejection fraction in hypertensive heart disease: insights from cardiac magnetic resonance imaging*. *Hypertens*, 2016. **18**: p. 1119-1127.
76. Tsuda, T., et al., *Echocardiographic measurement of right ventricular wall thickness in adults by anterior approach*. *Br Heart J*, 1980. **44**: p. 55-61.
77. Webb, J., et al., *Usefulness of cardiac magnetic resonance imaging to measure left ventricular wall thickness for determining risk scores for sudden cardiac death in patients with hypertrophic cardiomyopathy*. *J Cardiol*, 2017. **119**: p. 1450-1455.
78. Ho, Y.S., *Anatomy and myoarchitecture of the left ventricular wall in normal and in disease*. *Eur J Echocardiogr*, 2009. **10**: p. 113-117.
79. Black, J., *Microbiology: Principles and exploration*. 8th ed. 2012: John Wiley Sons.
80. Titford, M., *Progress in the development of microscopical techniques for diagnostic pathology*. *J. Histotechnol*, 2009. **32**: p. 9-19.
81. Ueno, H., et al., *Comparison of echocardiographic and anatomic measurements of the left ventricular wall thickness*. *Kobe J Med Sci*, 1991. **37**: p. 273-286.
82. Badea, C.T., et al., *4-D micro-CT of the mouse heart*. *Mol Imaging*, 2005. **4**: p. 110-116.
83. Kathria, N.N., et al., *Assessment of left ventricular enlargement at multidetector computed tomography*. *J Comput Assist Tomogr*, 2015. **39**: p. 794-796.
84. Metscher, B.D., *MicroCT for developmental biology: a versatile tool for high-contrast 3D imaging at historical resolutions*. *Dev Dyn*, 2009. **238**: p. 632-640.
85. Metscher, B., *MicroCT for comparative morphology: simple staining methods allow high-contrast 3D imaging of diverse on-mineralized animal tissues*. *BMC Physiology*, 2009. **9**: p. 11.
86. Atkinson, A., et al., *Anatomical and molecular mapping of the left and right ventricular His-Purkinje conduction networks*. *J Mol Cell Cardiol*, 2011. **51**: p. 689-701.
87. Aslanidi, O.V., et al., *Application of micro-computed tomography with iodine staining to cardiac imaging, segmentation, and computational model development*. *IEEE Trans Med Imaging*, 2012. **32**: p. 8-17.
88. Nakao, S., et al., *Common arterial trunk in a cat: a high-resolution morphological analysis with micro-computed tomography*. *J Vet Cardiol*, 2021. **34**: p. 8-15.
89. Aurigemma, C., et al., *Persistent enhanced platelet activation in patients with acute myocardial infarction and coronary microvascular obstruction: clinical implications*. *Thromb Haemost*, 2014. **111**(1): p. 122-30.
90. Csige, I., et al., *The impact of obesity on the cardiovascular system*. *J Diabetes Res*, 2018. **2018**: p. 3407306.
91. Coleman, D.L., *Obese and diabetes: two mutant genes causing diabetes-obesity*. *Diabetologia*, 1978. **14**: p. 141-148.
92. Larsson, C.A., et al., *Clusters of AMI risk factors and their association with left ventricular hypertrophy: a population-based study within Skaraborg Project, Sweden*. *Int J Cardiol*, 2013. **168**: p. 5416.
93. Kaltoft, M., A. Langsted, and B.G. Nordestgaard, *Obesity as a casual risk factor for aortic valve stenosis*. *J Am Coll Cardiol*, 2020. **75**: p. 163-176.
94. Lavie, C.J., et al., *Obesity and atrial fibrillation prevalence, pathogenesis, and prognosis: effects of weight loss and exercise*. *J Am Coll Cardiol*, 2017. **70**: p. 2022-2035.

95. Magnani, J.W., E.M. Hylek, and C.M. Apovian, *Obesity begets atrial fibrillation: a contemporary summary*. *Circulation*, 2013. **128**: p. 401-405.
96. Biernacka, A. and G.N. Frangogiannis, *Aging and Cardiac Fibrosis*. *Aging Dis*, 2011. **2**: p. 158-173.
97. Peters, C.H., E.J. Sharpe, and C. Proenza, *Cardiac pacemaker activity in aging*. *Annu Rev Physiol.*, 2020. **82**: p. 21-43.
98. Dakkak, W. and R. Doukky, *Sick Sinus Syndrome*. 2022, Treasure Island (FL): StatPearls Publishing.
99. Jones, S.A., M.K. Lancaster, and M.R. Boyett, *Ageing-related changes of connexins and conduction within the sinoatrial node*. *J Physiol.*, 2004. **560(Part 2)**: p. 429-437.
100. Agrawal, T. and S.F. Nagueh, *Changes in cardiac structure and function with aging*. *J Cardiovasc Aging*, 2022. **2**: p. 1-13.
101. Grilo, G.A., et al., *Age- and sex-dependent differences in extracellular matrix metabolism associate with cardiac functional and structural changes*. *J Mol Cell Cardiol.*, 2020. **139**: p. 62-74.
102. Cole, M.A., et al., *Extracellular matrix regulation of fibroblast function: redefining our perspective on skin aging*. *J Cell Commun Signal.*, 2018. **12**: p. 35-43.
103. LabCE. *Tissue Fixation*. 8th February 2022]; Available from: https://labce.com/spg2715129_tissue_fixation.aspx#:~:text=As%20defined%20by%20Freida%20Carson,that%20the%20specimen%20is%20diagnostic.
104. Boerckel, J.D., et al., *Microcomputed tomography: approaches and applications in bioengineering*. *Stem Cell Res. Ther.*, 2014. **5**: p. 1-12.
105. Suvarna, S.K., C. Layton, and J.D. Bancroft, *Bancroft's Theory and Practice of Histological Techniques*. 2019: Elsevier.
106. Illumina. *An introduction to next-generation sequencing technology*. 2017 16/12/2021]; Available from: https://www.illumina.com/content/dam/illumina-marketing/documents/products/illumina_sequencing_introduction.pdf.
107. Qiagen. *Qiagen ingenuity pathway analysis (IPA)*. 2021 16/12/2021]; Available from: <https://www.qiagen.com/us/products/discovery-and-translational-research/next-generation-sequencing/informatics-and-data/interpretation-content-databases/ingenuity-pathway-analysis/>.
108. Lin, X., et al., *A chemical genomics screen highlights the essential role of mitochondria in HIF-1 regulation*. *PNAS*, 2008. **105**: p. 174-179.
109. Chandler, N.A., O., et al., *Computer three-dimensional anatomical reconstruction of the human sinus node and a novel paranodal area*. *Anat Rec.*, 2011. **294**: p. 970-979.
110. Robins, H., Y. Li, and R.W. Padgett, *Incorporating structure to predict microRNA targets*. *Proc Natl Acad Sci USA.*, 2005. **102**: p. 4006-4009.
111. Long, D., et al., *Potent effect of target structure on microRNA function*. *Nat Struct Mol Biol.*, 2007. **14**: p. 287.
112. Tanaka, Y., et al., *Quantitative assessment of paravalvular leakage after transcatheter aortic valve replacement using a patient-specific pulsatile flow model*. *Int J Cardiol.*, 2018. **258**: p. 313-320.
113. Roberts, A., et al., *Integrated microscopy techniques for comprehensive pathology evaluation of an implantable left atrial pressure sensor*. *J Histotechnol.*, 2013. **36**: p. 17-27.
114. Sanders, W.E.J., et al., *Catheter ablation of sinoatrial node reentrant tachycardia*. *J Am Coll Cardiol.*, 1994. **23**: p. 926-934.
115. Liu, T., et al., *Current understanding of the pathophysiology of myocardial fibrosis and its quantitative assessment in heart failure*. *Front Physiol.*, 2017. **8**: p. 328-373.
116. Segura, A.M., O.H. Frazier, and L.M. Buja, *Fibrosis and heart failure*. *Heart Fail Rev.*, 2014. **19**: p. 173-185.

117. Siwik, D.A., D.L. Chang, and W.S. Colucci, *Interleukin-1 beta and tumor necrosis factor-alpha decrease collagen synthesis and increase matrix metalloproteinase activity in cardiac fibroblasts in vitro*. *Circ Res.*, 2000. **86**: p. 1259-1265.
118. Yokoyama, T., et al., *Tumor necrosis factor-alpha provokes a hypertrophic growth response in adult cardiac myocytes*. *Circulation*, 1997. **95**: p. 1247-1252.
119. Testa, M., et al., *Circulating levels of cytokines and their endogenous modulators in patients with mild to severe congestive heart failure due to coronary artery disease or hypertension*. *J Am Coll Cardiol.*, 1996. **28**: p. 964-971.
120. Kubota, T., et al., *Dilated cardiomyopathy in transgenic mice with cardiac-specific overexpression of tumor necrosis factor-alpha*. *Circ Res.*, 1997. **81**: p. 627-635.
121. Bozkurt, B., et al., *Pathophysiologically relevant concentrations of tumor necrosis factor-alpha promote progressive left ventricular dysfunction and remodeling in rats*. *Circulation*, 1998. **97**: p. 1382-1391.
122. Sun, M., et al., *Tumor necrosis factor-alpha mediates cardiac remodeling and ventricular dysfunction after pressure overload state*. *Circulation*, 2007. **115**: p. 1398-1407.
123. Bozkurt, B., et al., *Results of targeted anti-tumor necrosis factor therapy with etanercept (ENBREL) in patients with advanced heart failure*. *Circulation*, 2001. **103**: p. 1044-1047.
124. Chung, E.S., et al., *Randomized, double-blind, placebo-controlled, pilot trial of infliximab, a chimeric monoclonal antibody to tumor necrosis factor-alpha, in patients with moderate-to-severe heart failure: Results of the anti-TNF therapy against congestive heart failure (ATTACH) trial*. *Circulation*, 2003. **107**: p. 3133-3140.
125. Nishii, N., *Arrhythmia management after device removal*. *J Arrhythmia.*, 2016. **32**: p. 287-292.
126. Morris, G.M., et al., *Characterization of a right atrial subsidiary pacemaker and acceleration of the pacing rate by HCN over-expression*. *Cardiovasc Res.*, 2013. **100**: p. 160-169.
127. D'Souza, A., et al., *Targeting miR-423-5p reverses exercise training-induced HCN4 channel remodeling and sinus bradycardia*. *Circ Res*, 2017. **121**: p. 1058-1068.
128. Lin, G., et al., *Biological pacemaker created by fetal cardiomyocyte transplantation*. *J Biomed Sci.*, 2005. **12**: p. 513-519.
129. Zhang, H., et al., *Implantation of sinoatrial node cells into canine right ventricle: biological pacing appears limited by the substrate*. *Cell Transpl.*, 2011. **20**: p. 1907-1914.
130. Protze, S.I., et al., *Sinoatrial node cardiomyocytes derived from human pluripotent cells function as a biological pacemaker*. *Nat Biotechnol.*, 2017. **35**: p. 56-68.
131. Chauveau, S., et al., *Induced pluripotent stem cell-derived cardiomyocytes provide in vivo biological pacemaker function*. *Circ Arrhythmia Electrophysiol.*, 2017. **10**: p. 4502.
132. Müller, M., et al., *Ca²⁺ activated K channels-new tools to induce cardiac commitment from pluripotent stem cells in mice and men*. *Stem Cell Rev Rep.*, 2012. **8**: p. 720-740.
133. Birket, M.J., et al., *Expansion and patterning of cardiovascular progenitors derived from human pluripotent stem cells*. *Nat Biotechnol.*, 2015. **33**: p. 970-979.
134. Zhang, J. and C. Huang, *A new combination of transcription factors increases the harvesting efficiency of pacemaker-like cells*. *Mol Med Rep.*, 2019. **19**: p. 3584-3592.
135. Momin, M.Y., et al., *The challenges and opportunities in the development of microRNA therapeutics: a multidisciplinary viewpoint*. *Cells*, 2021. **10**: p. 3097.
136. Li, N., et al., *Altered microRNA and mRNA profiles during heart failure in the human sinoatrial node*. *Sci Rep.*, 2021. **11**: p. 1-15.
137. Brooks, A. *Me and my operation: pacemaker*.
138. Lecker, D.N., S. Kumari, and A. Khan, *Iodine binding capacity and iodine binding energy of glycogen*. *J Polym Sci A Polym Chem.*, 1997. **35**: p. 1409-1412.
139. Jain, M., et al., *Glucose-6-phosphate dehydrogenase modulates cytosolic redox status and contractile phenotype in adult cardiomyocytes*. *Circ Res.*, 2003. **93**: p. e9-e16.
140. Hecker, P.A., et al., *Glucose-6-phosphate dehydrogenase deficiency increases redox stress and moderately accelerates the development of heart failure*. *Circ Heart Fail.*, 2013. **6**: p. 118-126.

